Fully-Resolved Simulations of Ignition and Combustion of Single Coal Particles and Coal Particle Clouds

von der
Fakultät Energie-, Verfahrens- und Biotechnik
der Universität Stuttgart
zur Erlangung der Würde eines
Doktors der Ingenieurwissenschaften
(Dr.-Ing.) genehmigte Abhandlung

vorgelegt von
Giovanni Luigi Tufano
aus Avellino, Italien

Hauptberichter:	Prof. Dr. Andreas Kronenburg
Mitberichter:	Prof. Dr. Andreas Markus Kempf
Tag der mündlichen Prüfung:	19. Mai 2021

Institut für Technische Verbrennung
der Universität Stuttgart
2021

Erklärung

Hiermit versichere ich:

1. dass ich meine Arbeit selbständig verfasst habe,
2. dass ich keine anderen als die angegebenen Quellen benutzt und alle wörtlich oder sinngemäß aus anderen Werken übernommenen Aussagen als solche gekennzeichnet habe,
3. dass die eingereichte Arbeit weder vollständig noch in wesentlichen Teilen Gegenstand eines anderen Prüfungsverfahrens gewesen ist,
4. dass ich die Arbeit noch nicht vollständig veröffentlicht habe und,
5. dass das elektronische Exemplar mit den anderen Exemplaren übereinstimmt.

Ingolstadt, Mai 31, 2021

Giovanni Luigi Tufano

„Considerate la vostra semenza:
fatti non foste a viver come bruti,
ma per seguir virtute e canoscenza.“

Consider your origins:
you were not made to live as brutes,
but to follow virtue and knowledge.

Dante Alighieri, Inferno (Canto XXVI)

In Memory of my Grandfather Luigi

Preface

Parts of this thesis have been presented at conferences and published in the archival literature. The background and theoretical developments given in chapters 2 and 3 have been modified with respect to the originally published texts and been significantly extended to ensure completeness, coherence and consistency of the present manuscript.

The relevant papers are:

1. G.L. Tufano, O.T. Stein, A. Kronenburg, A. Frassoldati, T. Faravelli, L. Deng, A.M. Kempf, M. Vascellari, C. Hasse, Resolved flow simulation of pulverized coal particle devolatilization and ignition in air- and O_2/CO_2-atmospheres, *Fuel* 186:285-292 (2016), https://doi.org/10.1016/j.fuel.2016.08.073

   - Data and results discussed in this paper are presented in chapter 5.
   - Author's contribution: Programming (100%), data generation (100%), scientific originality (35%)

2. G.L. Tufano, O.T. Stein, B. Wang, A. Kronenburg, M. Rieth, A.M. Kempf, Coal particle volatile combustion and flame interaction. Part I: Characterization of transient and group effects, *Fuel* 229:262-269 (2018), https://doi.org/10.1016/j.fuel.2018.02.105

   - Data and results discussed in this paper are presented in chapter 6.
   - Author's contribution: Programming (100%), data generation (95%), scientific originality (70%)

3. G.L. Tufano, O.T. Stein, B. Wang, A. Kronenburg, M. Rieth, A.M. Kempf, Coal particle volatile combustion and flame interaction. Part II: Effects of particle Reynolds number and turbulence, *Fuel* 234:723-731 (2018), https://doi.org/10.1016/j.fuel.2018.07.054

   - Data and results discussed in this paper are presented in chapter 7.
   - Author's contribution: Programming (100%), data generation (95%), scientific originality (70%)

4. G.L. Tufano, O.T. Stein, A. Kronenburg, G. Gentile, A. Stagni, A. Frassoldati, T. Faravelli, A.M. Kempf, M. Vascellari, C. Hasse, Fully-resolved simulations of coal particle combustion using a detailed multi-step approach for heterogeneous kinetics, *Fuel* 240:75-83 (2019), https://doi.org/10.1016/j.fuel.2018.11.139

    - Data and results discussed in this paper are presented in chapter 8.
    - Author's contribution: Programming (30%), data generation (100%), scientific originality (50%)

Acknowledgements

The present dissertation successfully concludes my research activity at the Institute for Combustion Technology (ITV) of the University of Stuttgart. It is my greatest achievement and I would like to share the joy as well as the credit with several people that supported me along the way, making it a tough but wonderful journey.

First and foremost, I would like to thank Prof. Dr. Andreas Kronenburg for taking a chance on me, giving me the opportunity to be part of his research group. The very first time we met he gave me what helped me the most: a vision of where hard work and commitment in research could have brought me. In the following years he truly supported me, trusting me to work independently but always being there when I needed his precious help. I will be always grateful for the possibilities he opened in my life, allowing me to reach my professional and life goals, making that vision come true.

In addition, I would like to acknowledge Prof. Dr. Andreas Kempf for being the second examiner and providing me useful insights on pulverized coal combustion. I had the chance of collaborating with his institute and I am grateful for the simulations data that I could use as input during my studies.

I would also like to thank Dr. Oliver Stein for his constant dedication, guidance and, most of all, his kindness. He taught me to aim at perfection and not to settle for less. This encouraged me to use my creativity and to push myself beyond limits, which is something I treasure for the next professional challenges. Moreover I had the pleasure to experience him as a neighbor, a travel companion to the institute and a coffee enthusiast, really appreciating our pleasant discussions as well as his advices. Now that our professional collaboration has come to an end I am glad I can still count on his friendship.

I am grateful for the time shared at ITV with very nice people and committed researchers: Gregor Olenik, Niko Seubert, Satoshi Ukai, Gizem Inci, Santanu De, Son Vo, Dirk Dietzel, Gregor Neuber, Carmen Straub, Milena Smiljanic, Bosen Wang, Jonas

Kirchmann, Daniel Loureiro, Jan Gärtner and Marvin Sontheimer.

In particular, Sato made me feel welcome from the very beginning and made sure I spent enough time watching VfB (not always memorable) performances. Son brought friendship to the whole new level of non spoken words, still managing to provide tons of original theories and surprisingly useful advices. A great THANK YOU goes to Dirk, we shared the office and filled it with loud laughs during the highs and truly supported each other to overcome the deep lows we faced during research. We also shared our free-time collecting outstanding memories so that our friendship deserves a very special place in my heart.

I would also like to thank Ricarda Schubert for her kind support in making everything run smoothly during my time at ITV, and for her nice and encouraging words in every occasion.

The collaboration with the CRECK Modeling Group in Milano is also gratefully acknowledged. I really appreciated Prof. Dr. Tiziano Favarelli for his hospitality and Dr. Giancarlo Gentile for kindly sharing his codes and helping me adapt them for my needs. I am also grateful for the collaboration with the research group of Prof. Dr. Christian Hasse in Freiberg (currently in Darmstadt). There I had the pleasure to meet Dr. Michele Vascellari which enlightened me with the theory of flamelet modeling and with which I shared great time during several conferences.

I owe everything I am to my family. My mother Gina shared with me the brain and the passion to succeed in my educational path. She decided to sacrifice most of her ambitions to fully dedicate to the family. She truly supported me, believed I could succeed in everything I started and has been the safe harbor where I found rescue every time I needed. My father Carmine passed down to me his humor and creativity but especially he provided me a powerful example of generosity, commitment and hard work. I am aware of the amount of pain I caused moving far away from my parents. Everyday I hope to make them proud with the person I became to make all their sacrifices worthwhile.
A special thanks goes to my sister Katia for her heart-warming affection and encouraging smile, to her husband Mimmo and to their wonderful kids Christian and Carlotta which have filled my life with joy and have comforted me in countless occasions.

Last but not least, my deepest gratitude goes to a very special person which has been by my side for the past years, unconditionally supporting me, ultimately making all this come true: I feel blessed to have you in my life, Laura.

Inhaltsverzeichnis

List of figures

List of tables

Nomenclature

Roman Symbols

A	aromatic nuclei	[-]
A	air mass	[kg]
A_j	pre-exponential factor (Arrhenius rate of reaction j)	
A_c	pre-exponential factor (Arrhenius rate of char conversion)	[s/m]
A_v	pre-exponential factor (Arrhenius rate of devolatilization)	[1/s]
A_τ	autocorrelation time scaling factor	[-]
B	labile bridges	[-]
b_0	fraction of intact bridges	[-]
C	char links	[-]
C_D	drag coefficient	[-]
C_{dev}	devolatilization progress	[-]
C_{diff}	diffusion rate constant	[s/K$^{0.75}$]
Co	Courant number	[-]
c_p	specific heat capacity (at constant pressure)	[J/(kg·K)]
$c_{p,c}$	coal specific heat capacity (at constant pressure)	[J/(kg·K)]
c_i	i-th species molar concentration	[kmol/m^3]
D	molecular diffusivity	[m^2/s]
D_g	gas-mixture diffusivity	[m^2/s]
D_p	coal particle diameter	[m]
D_Z	scalar dissipation diffusion coefficient	[m^2/s]
D^{Kn}	Knudsen diffusivity	[m^2/s]
$\boldsymbol{Da}$	Darcy tensor	[1/m^2]
d_{por}	mean pore diameter	[m]
E	specific turbulent energy spectrum	[m^3/s^2]
E_{aj}	activation energy (Arrhenius rate of reaction j)	[J/mol]
E_c	activation energy (Arrhenius rate of char conversion)	[J/mol]
E_v	activation energy (Arrhenius rate of devolatilization)	[J/mol]

$\boldsymbol{F}$	Forchheimer tensor	[1/m]
F	fuel mass	[kg]
F_k	ordinary differential equation system	[-]
FI	flame index	[1/m^2]
G_p	particle incident radiation	[W/m^2]
$\boldsymbol{g}$	gravity vector	[m/s^2]
h	absolute enthalpy	[J/kg]
h_f^0, $\overline{h}_f^0$	enthalpy of formation	[J/kg], [kJ/mol]
h_s	sensible enthalpy	[J/kg]
$\boldsymbol{I}$	unity tensor	[-]
K_j	j-th reaction equilibrium constant	[-]
k	turbulent kinetic energy	[m^2/s^2]
$k_{c,i}$	char conversion intrinsic rate of reaction	[1/s]
k_j	j-th reaction rate coefficient	[1/s]
k_v	Arrhenius rate constant of devolatilization	[1/s]
L	characteristic length scale	[m]
L_{int}	turbulent integral length scale	[m]
L_x	particle spacing	[m]
M	molar mass	[kg/kmol]
M_{cl}	average molar mass per aromatic cluster	[kg/kmol]
M_δ	average side-chain molar mass	[kg/kmol]
$\mathbb{M}$	total number of chemical reactions	[-]
$\mathcal{M}_i$	i-th reactant/product species	[-]
m	mass	[kg]
m_c	mass of char	[kg]
m_p	particle mass	[kg]
m_v	mass of volatile matter	[kg]
m_v^*	asymptotic mass of volatile matter	[kg]
$\dot{m}$	mass release rate	[kg/s]
$\dot{m}_v$	devolatilization rate	[kg/s]
N	total number of chemical species	[-]
n	normal coordinate	[m]
Nu	Nusselt number	[-]
p	pressure	[Pa]
p_0	atmospheric pressure	[Pa]
Pr	Prandtl number	[-]
q_j	rate of progress of reaction j	[kmol/m^3/s]
$Q_{r,p}$	particle surface radiative heat flux	[W/m^2]

R_{diff}	char conversion diffusion reaction rate coefficient	[s/m]
R_c	char conversion chemical reaction rate coefficient	[s/m]
R_p	particle radius	[m]
R_u	universal gas constant	[J/mol/K]
r	radial coordinate	[m]
Re	Reynolds number	[-]
Re_p	particle Reynolds number	[-]
$\boldsymbol{S}$	porous media momentum source term	[kg/m^2/s^2]
S	peripheral groups	[-]
S	surface	[m^2]
S_a	specific internal surface area	[m^2/kg]
S_p	particle surface area	[m^2]
$\mathcal{S}$	solid	[-]
Sc	Schmidt number	[-]
T	temperature	[K]
T_g	gas-phase temperature	[K]
T_p	coal particle temperature	[K]
$T_{p,s}$	coal particle surface temperature	[K]
$\overline{T}_p$	(spatial) mean particle temperature	[K]
T_{ref}	standard temperature	[K]
t	time	[s]
$\boldsymbol{U}$	velocity vector (U_i, U_j, U_k)	[m/s]
U	characteristic velocity	[m/s]
U_{rel}	gas-particle relative velocity	[m/s]
$\overline{\boldsymbol{U}}$	mean velocity	[m/s]
$\overline{U}$	inlet mean orthogonal velocity	[m/s]
U'	root-mean-square velocity	[m/s]
$\boldsymbol{u}'$	fluctuating velocity vector	[m/s]
$\boldsymbol{u}'_{sgs}$	sub-grid scale velocity vector	[m/s]
u'_{sgs}	sub-grid turbulence intensity	[m/s]
$\hat{u}$	Fourier mode velocity amplitude	[m/s]
$\mathcal{V}$	volatile matter	[-]
V	volume	[m^3]
V_p	coal particle volume	[m^3]
V_{sphere}	spherical particle volume	[m^3]
$\boldsymbol{v}$	diffusion velocity	[m/s]
$\boldsymbol{v}^c$	diffusion velocity correction factor	[m/s]

$\boldsymbol{x}$	reference coordinate vector (x_i, x_j, x_k)	[m]
X	species molar fraction	[-]
Y	species mass fraction	[-]
y	elemental mass fraction	[-]
Z	mixture fraction	[-]

Greek Symbols

α	thermal diffusivity	[m^2/s]
α_e	wave number scaling factor	[-]
α_{v1},α_{v2}	Kobayashi volatile yield factors	[-]
β	temperature exponent (Arrhenius rate of reaction)	[-]
Δ	variation/interval	[-]
Δh_v	heat of devolatilization	[J/kg]
ΔH_R	enthalpy of reaction	[kJ]
δ	boundary layer thickness	[m]
ϵ	turbulent energy dissipation rate	[m^2/s^3]
ϵ_p	particle emissivity	[-]
ε	coal particle porosity	[-]
η	Kolmogorov length scale	[m]
η_p	pore resistance effectiveness factor	[-]
Θ	angular coordinate	[rad]
$\boldsymbol{\kappa}$	wave number vector	[1/m]
κ	wave number	[1/m]
κ_e	most energetic eddy wave number	[1/m]
κ_η	Kolmogorov eddy wave number	[1/m]
λ	thermal conductivity	[W/(m·K)]
λ_c	coal thermal conductivity	[W/(m·K)]
λ_g	gas-mixture thermal conductivity	[W/(m·K)]
μ	dynamic viscosity	[Pa·s]
ν	kinematic viscosity	[m^2/s]
ν'_{ij}	stoichiometric reactant coefficient (species i, reaction j)	[-]
ν''_{ij}	stoichiometric product coefficient (species i, reaction j)	[-]
ρ	density	[kg/m^3]
ρ_c	coal particle density	[kg/m^3]
ρ_g	gas-mixture density	[kg/m^3]

$\boldsymbol{\sigma}$	Fourier mode velocity direction	[-]
σ	Stefan-Boltzmann constant	[W/(m^{2}K^4)]
$\sigma + 1$	average number of attachments per cluster	[-]
$\boldsymbol{\tau}$	viscous stress tensor	[Pa]
τ	coal particle tortuosity	[-]
τ_a	autocorrelation time interval	[s]
τ_{ign}	ignition delay time	[s]
τ_η	Kolmogorov time scale	[s]
υ_η	Kolmogorov velocity scale	[m/s]
ϕ	general scalar	
ϕ_{global}	global equivalence ratio	[-]
χ	scalar dissipation rate	[1/s]
χ	coal particle conversion	[-]
ψ	Fourier mode velocity phase	[-]
ψ_c	char particle surface factor	[-]
$\dot{\omega}$	mass consumption/production rate	[kg/m^3/s]
$\dot{\omega}^m$	molar consumption/production rate	[kmol/m^3/s]
$\dot{\omega}_{h,het}$	sensible energy heterogeneous source	[J/m^3/s]
$\dot{\omega}_{h,che}$	sensible energy (homogeneous) chemical source	[J/m^3/s]
$\dot{\omega}_{h,rad}$	sensible energy radiative source	[J/m^3/s]
$\dot{\omega}_{i,het}$	species mass fraction heterogeneous source	[kg/m^3/s]
$\dot{\omega}_{i,hom}$	species mass fraction homogeneous source	[kg/m^3/s]
$\dot{\omega}_{\rho,het}$	mass heterogeneous source	[kg/m^3/s]
$\dot{\omega}_{\rho U,het}$	momentum heterogeneous source	[kg/m^2/s^2]
$\dot{\omega}_{Z,het}$	mixture fraction heterogeneous source	[kg/m^3/s]

Superscripts

N	total number of Fourier modes
N	total number of chemical species
n	n-th Fourier mode
S, G	solid and gas state in multiphase flow problem
$(\dot{\cdot})$	first time derivative

Subscripts

cum	cumulative
eff	effective
i, j	indices for solid/gas chemical species
int	interface
st	stoichiometric conditions
0	initial conditions
ϕ	general scalar

Acronyms

BC	boundary condition
CDF	cumulative distribution functions
CFD	computational fluid dynamics
CFL	Courant-Friedrichs-Lewy criterion
CGC	critical group combustion
CPD	chemical percolation devolatilization model
CPU	central processing unit
DNS	direct numerical simulation
FG-DVC	functional group-depolymerization vaporization cross-linking
FVM	finite-volume method
GPL	general public license
HLRS	High-Performance Computing Center Stuttgart
IFC	individual flame combustion
IGC	incipient group combustion
LES	large-eddy simulation
LHS	left hand side of an equation
NMR	nuclear magnetic resonance
PCC	pulverized coal combustion
PDF	probability density function
PGC	partial group combustion
PIMPLE	Pressure Implicit Method for Pressure-Linked Equations
PISO	Pressure-Implicit with Splitting of Operators
PKP	pyrolysis kinetic preprocessor
PSIC	particle source in cell approach

RANS	Reynolds averaged Navier Stokes/simulation
RHS	right hand side of an equation
SFOR	single first order rate reaction rodel
ST	synthetic turbulence
TVD	total variation diminishing
UDS	upwind differencing scheme

Abstract

The objective of the present work is to develop a comprehensive CFD model for the simulation of pulverized coal combustion (PCC). In particular, a direct numerical simulation framework for the OpenFoam CFD package is developed and successfully applied to predict pulverized coal particle devolatilization, burning and char conversion. The fully resolved approach along with the use of detailed chemical kinetic models allows for accurate predictions that improve the available database on coal particle ignition and combustion, providing reliable reference data, which are fundamental for the development of more simplified numerical methods.

The first part of this thesis presents the research context of coal combustion. The physical and chemical fundamentals involved in PCC are then introduced, along with the main modeling approaches, with a special focus on those on which the developed simulation framework relies. Thereafter, in the results chapters different configurations are investigated exploring a broad range of parameters that can affect coal combustion characteristics, progressively adding complexity to the computational setup and the modeling technique. In particular two main approaches with different levels of detail are developed.

The first approach relies on a fully-resolved description of the gas mixture carrying the coal particles that affect the gas phase by means of boundary conditions at the interface. The heating rate history of the particles is obtained by solving for intra-particle heat transfer and heat exchange between the particle and the surroundings. The time evolution of volatile release is captured by using the particle temperature to calculate the devolatilization rate from a single kinetic rate law relying on parameters either provided by a coal pre-processing network model or fitted to pyrolysis kinetics measurements. In order to describe the release of the volatiles at the obtained rate, a species transport boundary condition is introduced at the coal surface, accounting for both convective and diffusive phenomena during pyrolysis. The assumed volatile composition includes light gases and hydrocarbons up to C_6H_6 to represent tars. This permits to accurately describe homogeneous chemistry using a reduced version of a general detailed kinetic mechanism for pyrolysis and oxidation of hydrocarbon and oxygenated fuels. This allows to limit the computational cost associated with 3D fully resolved simulations and offers the possibility to investigate a broad range of coal particle configurations.

This approach is validated investigating the effect of enhanced oxygen levels on single coal particle ignition, by means of resolved laminar flow simulations. The numerical results are compared to experimental data for well-defined conditions (Molina & Shaddix, 2007). Particle heat-up, pyrolysis, ignition and envelope flame stabilization are characterized in four gas atmospheres differing in oxygen content and the use of either N_2 or CO_2 as balance gas. In agreement with the experimental evidence, enhanced oxygen levels shorten ignition delay time τ_{ign} and result in a higher combustion temperature and radical production for all studied mixtures. For the studied oxy-mixtures the presence of CO_2 in substitution of N_2 delays ignition. The observed behavior is coherent with the different thermo-physical properties of the gas mixtures. The sensitivity of ignition delay to a set of uncertainties is also discussed. While the absolute values of predicted ignition delay time are functions of potential particle preheating, particle Reynolds number Re_p and the chosen reference quantity to extract ignition delay, the relative trends among the gas mixtures remain in line with the experimental evidence.

The same modeling approach is used to extend the investigation of the heat-up, devolatilization, ignition and volatile combustion from single coal particles to particle arrays in laminar but also turbulent flow. The gas phase and particle conditions are extracted from an existing large eddy simulation (LES) of a semi-industrial coal furnace (Rieth *et al.*, 2016). Direct numerical simulation (DNS) is performed by fully resolving the particle boundary layers, the flame thickness and the smallest flow scales within the computational domain that represents a characteristic LES cell. The transient evolution and group effects in laminar flows are considered at first. The analysis of arrays of infinite particle layers in laminar flow shows a strong dependence of the flame interaction on the inter-particle distance L_x. In particular, different combustion regimes are observed for different L_x (for a fixed particle Reynolds number Re_p), ranging from isolated burning of the particles for large L_x to group combustion for small L_x, and spanning a wide range of global equivalence ratios from very lean (large L_x) to very rich (small L_x). The regime transition affects the surface temperature and devolatilization rate history of the particles. Models for the mixture fraction distributions in the particle wake are provided based on the analogous problem of droplet evaporation.

The effects of particle Reynolds number and turbulence are also investigated. Increasing Re_p in laminar flow leads to delayed ignition of single particles with local extinction due to high upstream scalar dissipation rates and the formation of wake flame structures downstream of the particle. An attempt is made to recover the single particle results with a standard steady laminar flamelet approach, which is shown to work well at low Re_p, but fails at high Reynolds numbers, where multi-dimensional effects occur and must be incorporated into flamelet modeling. It is found that applying standard film theory to model the effect of convection on devolatilization rates can lead to qualitatively wrong trends and peak devolatilization rates compared to the DNS results at high Re_p. The occurrence

of significant levels of turbulence introduces a wide range of additional chemical states due to the randomness of the turbulent fluctuations that can act either to increase or decrease the local strain, in turn weakening or enhancing particle interactions. For the studied conditions, turbulence slightly promotes the mass release from the most upstream particle set, but considerably delays the volatile release from the downstream particles, which is explained by the different extents and degrees of interaction of the up- and downstream volatile flames.

The investigations conducted in the first part of this work rely on a simplified description of the particle interior properties and of the volatile matter released by the coal particle, allowing for the use of a reduced mechanism for the homogeneous chemistry. Due to its limited computational cost, this approach has allowed to extensively perform fully resolved calculations. These simulations have been used to characterize the ignition and volatile burning behavior of single coal particles and particle arrays under different operating conditions. However, the physico-chemical phenomena occurring inside the porous coal particle, the detailed composition of the fuel stream released by the particle and heterogeneous char reactions are not captured by this approach. Therefore the computational framework is extended with regard to the particle description and coal kinetics, alleviating previously made assumptions of single-step pyrolysis, fixed and reduced volatile composition as well as simplified particle interior properties, and allowing for the consideration of char conversion. This second modeling approach is based on a detailed multi-step mechanism for heterogeneous kinetics, coupled to detailed homogeneous chemistry. It considers the elemental analysis of the given coal and interpolates its properties by linear superposition of a set of reference coals, dynamically predicting the mass release rate and species composition of the complex mixture released from the particle. A comprehensive description for the particle interior is also introduced, where a time-evolving porosity and tortuosity control the fluid flow of gas formed inside the coal particle during its thermal conversion. The introduced complexity results in a significantly increased computational cost of the fully resolved simulations. Therefore, this approach is applied to the single particle setup only, attempting to reproduce ignition and volatile flame combustion, as well as to analyze char conversion of single coal particles in convective gas environments, as in the reference experiment (Molina & Shaddix, 2007). The results this time show that the burning behavior is affected by the oxygen concentration, i.e. for enhanced oxygen levels ignition occurs in a single step, whereas decreasing the oxygen content leads to a two-stage ignition process. Char conversion becomes dominant once the volatiles have been depleted, but also causes noticeable deviations of temperature, released mass, and overall particle conversion during devolatilization already, indicating an overlap of the two stages of coal conversion which are usually considered to be consecutive. The complex pyrolysis model leads to non-monotonous profiles of the combustion quantities which introduce a minor dependency of the ignition delay time τ_{ign} on its definition, slightly affecting the predicted

values and trends. Regardless of the chosen extraction method though, the simulations capture the measured τ_{ign} very well.

This thesis includes pulverized coal combustion simulation results and predictions obtained with the presented model development, through different levels of complexity and fidelity. Therefore, this work provides an overview of benefits and limitations that result from including or neglecting different models for the variety of underlying physical and chemical processes that govern PCC. The findings presented here are useful for the development of LES sub-grid scale combustion models for pulverized coal flames, such as flamelets and others.

Kurzfassung

Das Ziel der vorliegenden Arbeit ist die Entwicklung eines umfassenden CFD-Modells für die Simulation der Kohlestaubverbrennung. Im Speziellen wird ein Framework für die direkte numerische Simulation in OpenFOAM entwickelt und erfolgreich angewendet, um Kohlepartikelpyrolyse und -verbrennung sowie Koksabbrand vorherzusagen. Die vollaufgelöste Methode in Kombination mit den detaillierten Modellen für die chemische Kinetik erlaubt eine genaue Vorhersage, die die vorhandenen Datenbanken für Kohlepartikelzündung und -verbrennung verbessert. Die so generierten Referenzdaten sind für die Entwicklung einfacherer numerischer Methoden von grundlegender Bedeutung.

Im ersten Teil der Arbeit wird der aktuelle Forschungsstand im Bereich Kohleverbrennung vorgestellt. Danach werden die physikalischen und chemischen Grundlagen der Kohlestaubverbrennung sowie die wichtigsten Modellierungsansätze erläutert. Hierbei liegt ein spezieller Fokus auf den Kenntnissen und Methoden, auf denen die hier entwickelte Simulationsumgebung basiert. Die anschließenden Ergebniskapitel betrachten verschiedene Konfigurationen und untersuchen ein breites Spektrum an Parametern, die die Kohleverbrennung charakterisieren. Die Komplexität des Rechensetups und der numerischen Modelle wird dabei schrittweise erhöht. Im Speziellen werden zwei Hauptmodelle mit unterschiedlichem Detailgrad entwickelt.

Die erste Methode basiert auf einer vollständigen Auflösung des Gasgemisches als Trägerphase für die Kohlepartikel, deren Einfluss auf die Gasphase mit Hilfe geeigneter Randbedingungen berücksichtigt wird. Der Wärmetransport im Partikelinneren und der Wärmeübergang zwischen Partikeloberfläche und Umgebung wird aufgelöst, um den zeitlichen Verlauf der Partikelaufheizung zu erhalten. Die zeitliche Entwicklung der Freisetzung flüchtiger Bestandteile wird erfasst, indem die Pyrolysegeschwindigkeit mit Hilfe der Partikeltemperatur bestimmt wird. Die Parameter für das zugrunde liegende kinetische Modell werden entweder durch eine Kohledatenbank bereitgestellt oder mit Hilfe von Pyrolysemessungen gefittet. Eine Speziestransportrandbedingung an der Oberfläche der Kohlepartikel, die Konvektion und Diffusion berücksichtigt, ermöglicht die korrekte Vorgabe der berechneten Freisetzungsrate der flüchtigen Bestandteile. Innerhalb dieses Modellansatzes werden leichte Gase und Kohlenwasserstoffe bis C_6H_6 für die Zusammensetzung der flüchtigen Bestandteile betrachtet. Das ermöglicht eine genaue Beschreibung

homogener Chemie mit einem reduzierten Reaktionsmechanismus für die Pyrolyse sowie für die Oxidation von Kohlenwasserstoffen und mit Sauerstoff angereicherten Brennstoffen. Der reduzierte Reaktionsmechanismus ist die Voraussetzung für eine Begrenzung der Rechenzeiten, die sich für 3D vollaufgelöste Simulationen ergeben, so dass eine große Auswahl an Kohlepartikelkonfigurationen untersucht werden kann.

Dieser Ansatz wird durch die Untersuchung des Einflusses einer erhöhten Sauerstoffkonzentration auf die Zündung einzelner Kohlepartikel mit Hilfe aufgelöster laminarer Simulationen validiert. Die Ergebnisse werden mit experimentellen Daten für definierte Bedingungen verglichen (Molina & Shaddix, 2007). Partikelaufheizung, Pyrolyse, Zündung und Stabilisierung der Hüllflamme werden für vier Gasatmosphären charakterisiert, die sich im Sauerstoffgehalt unterscheiden und bei denen entweder N_2 oder CO_2 die Basis der Gasatmosphäre bilden. In Übereinstimmung mit den experimentellen Ergebnissen verringert ein erhöhter Sauerstoffgehalt die Zündverzugszeit τ_{ign} und erhöht die Flammentemperatur und die Radikalbildung für alle untersuchten Mischungen. Für die betrachteten Sauerstoffgehalte erhöht sich die Zündverzugszeit, wenn N_2 durch CO_2 ersetzt wird. Dieses Verhalten entspricht den unterschiedlichen thermo-physikalischen Eigenschaften der Gasmischungen. Die Sensitivität der vorhergesagten Zündverzugszeit zu verschiedenen Unsicherheitsfaktoren wird ebenfalls diskutiert. Während die Absolutwerte der Zündverzugszeit von einer möglichen Partikelvorheizung, der Partikel-Reynoldszahl und der Referenzgröße zur Bestimmung des Zündverzugs abhängig sind, stimmen die relativen Tendenzen mit den experimentellen Erkenntnissen überein.

Der erste Modellansatz wird dann weiterverwendet, um die Untersuchungen zu Partikelaufheizung, Devolatilisierung, Zündung und Verbrennung flüchtiger Bestandteile von Einzelpartikeln auf Partikelcluster sowie von laminar auf turbulent zu erweitern. Die Bedingungen der Gasphase und der Partikel werden aus vorhandenen Grobstruktursimulationen (LES) eines industrie-relevanten Kohlebrenners extrahiert (Rieth *et al.*, 2016). Die direkten numerischen Simulationen (DNS) in der vorliegenden Arbeit lösen die Partikelgrenzschichten, die Flammendicke und die kleinsten strömungsmechanischen Längenskalen vollständig auf. Das Rechengebiet der DNS repräsentiert eine einzelne Rechenzelle der LES. Die transiente Entwicklung von Partikelgruppen und die Auswirkung der Partikelinteraktion für laminare Bedingungen werden zuerst untersucht. Die Analyse unendlich großer Partikelcluster mittels periodischer Randbedingungen zeigt eine starke Abhängigkeit der Flammeninteraktion vom Partikelabstand L_x. Im Speziellen werden unterschiedliche Verbrennungsregime bei unterschiedlichem L_x (und konstanter Partikel-Reynoldszahl) beobachtet. Diese reichen von einer isolierten Verbrennung der individuellen Partikel im Cluster bei großem Partikelabstand bis zur Gruppenverbrennung bei kleinem Partikelabstand. Sowohl magere (großes L_x) als auch fette (kleines L_x) globale Mischungsverhältnisse treten auf. Der Übergang zwischen den Regimen beeinflusst die Oberflächentemperatur und die Pyrolysegeschwindigkeit der Partikel. Modelle für die Mischungsbruchverteilung im

Nachlauf der Partikel werden auf Basis des analogen Problems der Tropfenverdampfung entwickelt.

Der Einfluss der Partikel-Reynoldszahl und der Turbulenz wird ebenfalls analysiert. Eine Erhöhung von Re_p bei laminarer Strömung führt zu einer verzögerten Zündung einzelner Partikel und stellenweise zur Verlöschung aufgrund hoher skalarer Dissipationsraten stromaufwärts und der Bildung von Flammenstrukturen im Partikelnachlauf. In einem weiteren Schritt wird versucht, diese Ergebnisse mit einem stationären Flamelet-Modell zu reproduzieren. Der Ansatz funktioniert für kleine Re_p gut, versagt aber bei höheren Re_p, wo mehrdimensionale Effekte auftreten, die in das Flamelet-Modell integriert werden müssen. Wenn der Einfluss der Konvektion auf die Pyrolyseraten mit einer Standard-Filmtheorie modelliert wird, ergeben sich qualitativ falsche Verläufe und Höchstwerte der Pyrolyseraten im Vergleich zu den DNS-Ergebnissen bei hohen Re_p. Bei einem signifikanten Turbulenzgrad führt der zufällige Charakter turbulenter Fluktuationen zu einer Vielzahl zusätzlicher chemischer Zustände. Die turbulenten Fluktuationen können die lokalen Fluidspannungen auf die Flamme erhöhen oder verringern und die Partikelinteraktionen damit abschwächen oder verstärken. Bei den untersuchten Bedingungen erhöht die Turbulenz die Massenfreisetzung der am weitesten stromauf gelegenen Partikel geringfügig. Die Freisetzung flüchtiger Bestandteile der am weitesten stromab gelegenen Partikel wird dementgegen durch die Turbulenz erheblich verzögert. Grund hierfür ist die unterschiedlich starke Flammeninteraktion zwischen stromauf und stromab gelegenen Partikeln.

Die Untersuchungen im ersten Teil der Arbeit basieren auf einer vereinfachten Beschreibung der Eigenschaften im Partikelinneren und der freigesetzten flüchtigen Bestandteile, die die Verwendung eines reduzierten Reaktionsmechanismus für die homogene Chemie ermöglichen. Aufgrund des entsprechend begrenzten Rechenaufwands konnten umfangreiche, vollständig aufgelöste Berechnungen durchgeführt werden. Diese Simulationen charakterisieren die Zündung und Verbrennung flüchtiger Bestandteile von Einzelpartikeln und Partikelclustern unter verschiedenen Betriebsbedingungen. Die physikalisch-chemischen Phänomene, die innerhalb der porösen Kohlepartikel auftreten, sowie die detaillierte Zusammensetzung der freigesetzten Brennstoffe und die heterogene Koksabbrandreaktionen werden mit dieser Methode allerdings nicht erfasst. Deshalb wird das Simulationsframework im Hinblick auf die Partikelbeschreibung und chemische Kinetik der Kohle noch erweitert, so dass die zuvor getroffenen Annahmen der einstufigen Pyrolyse, der festen und reduzierten Zusammensetzung der flüchtigen Bestandteile, sowie des vereinfachten Partikelinneren durch genauere Ansätze ersetzt werden und auch Koksabbrand untersucht werden kann. Dieser zweite Modellierungsansatz basiert auf einem detaillierten Mehrschrittmechanismus für die heterogene Reaktionskinetik, der mit detaillierter homogener Chemie gekoppelt wird. Die Methode berücksichtigt eine elementare Analyse der vorgegebenen Kohle und interpoliert die Eigenschaften auf Basis verschiedener Referenzkohlen. Die Massenfreisetzungsrate und die Spezieszusammensetzung der komplexen von einem

Partikel freigesetzten Mischung können damit dynamisch vorhergesagt werden. Darüber hinaus wird eine umfassende Beschreibung des Partikelinneren eingeführt, bei der eine zeitabhängige Porosität und Tortuosität die Gasströmung im Partikel während der thermischen Umwandlung bestimmen. Die erhöhte Komplexität des Modellierungsansatzes führt zu einem signifikant erhöhten Rechenaufwand der voll aufgelösten Simulationen. Deshalb wird diese Methode nur für die Einzelpartikel-Setups verwendet. Dabei ist das Ziel der Untersuchungen die Zündung und Verbrennung flüchtiger Bestandteile zu reproduzieren, sowie Koksabbrand in einer gasförmigen Konvektionsströmung gemäß der Referenzexperimente (Molina & Shaddix, 2007) zu analysieren. Die Ergebnisse bestätigen, dass das Brennverhalten durch die Sauerstoffkonzentration beeinflusst wird. Bei erhöhtem Sauerstoffgehalt tritt die Zündung in einem einzelnen Schritt auf, wohingegen eine verringerte Sauerstoffkonzentration zu einer zwei-stufigen Zündung führt. Koksabbrand wird dominant, sobald die flüchtigen Bestandteile verbraucht sind, führt aber ebenfalls zu einer spürbaren Abweichung der Temperatur, der freigesetzten Masse und der gesamten Partikelumwandlung bereits während der Pyrolyse. Das deutet auf eine Überlappung der beiden Stufen der Kohleumwandlung hin, die üblicherweise als aufeinanderfolgend betrachtet werden. Das komplexe Pyrolysemodell führt zu nicht-monotonen Profilen der Verbrennungsgrößen, was eine geringfügige Abhängigkeit der Zündverzugszeit τ_{ign} von ihrer Definition zur Folge hat. Die vorhergesagten Werte und Trends werden hiervon ebenfalls geringfügig beeinflusst. Unabhängig vom gewählten Ansatz zur Bestimmung von τ_{ign} können die numerischen Simulationen die experimentell gemessenen Werte gut reproduzieren.

Die vorliegende Arbeit beinhaltet Simulationsergebnisse der Kohlestaubverbrennung und Vorhersagen aus Modellen mit unterschiedlichem Komplexitätsgrad und unterschiedlicher Genauigkeit. Deshalb stellt diese Arbeit einen Überblick von Vorteilen und Limitierungen bereit, die sich aus der Verwendung oder Vernachlässigung verschiedener Modelle für die Vielzahl zugrunde liegender physikalischer und chemischer Prozesse ergeben. Die hier präsentierten Erkenntnisse sind für die Entwicklung von LES Feinstrukturmodellen für die Kohlestaubverbrennung, wie zum Beispiel Flamelets, hilfreich.

Chapter 1

Introduction

1.1 Motivation

Fossil fuels represent the major source for power generation and have satisfied in the past decades the continuous increase in energy demand, supplying the required support to the rapid growth of established and rising economies (Figs. 1.1-1.2). The worldwide statistical data collected and published by the U.S. Energy Information Administration reveal how coal reserves have been extensively exploited (Fig. 1.2), primarily to produce electrical base load power (Fig. 1.3), leading to a share of coal in the power mix which has almost remained steady for the past years at around 40% (Fig. 1.2(b)).

On the other hand the ecosystem is suffering the consequences of the incredible development of society worldwide. In fact, pulverized coal combustion (PCC), the key technology to extract energy from fossil coal, not only increases air and water pollution but is also among the primary causes of global warming. When coal burns, its carbon bonds are broken and release energy. Meanwhile other chemical reactions occur most of which release airborne toxic pollutants and heavy metals including nitrogen and sulfur oxides (NO_x and SO_x), mercury, lead and particulate matter (soot) into the environment. This air and water pollution impacts on human health increasing cases of asthma and breathing difficulties, brain damage, heart problems, cancer, neurological disorders and premature death. Even more harmful and irreversible are the consequences of carbon dioxide emissions from fossil fuel combustion on global warming. Released CO_2 acts as a heat-trap leading to an increase in temperature of the earth's surface, melting ice and resulting sea level rise that can eventually drive environmental and human disruption. Figure 1.4 shows the strong correlation between temperature and the concentration of carbon dioxide in the atmosphere

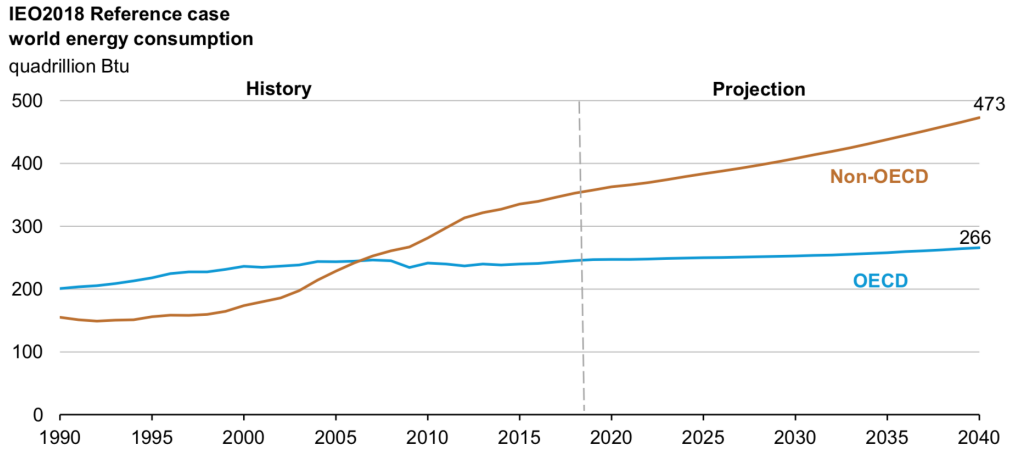

(a) World energy consumption

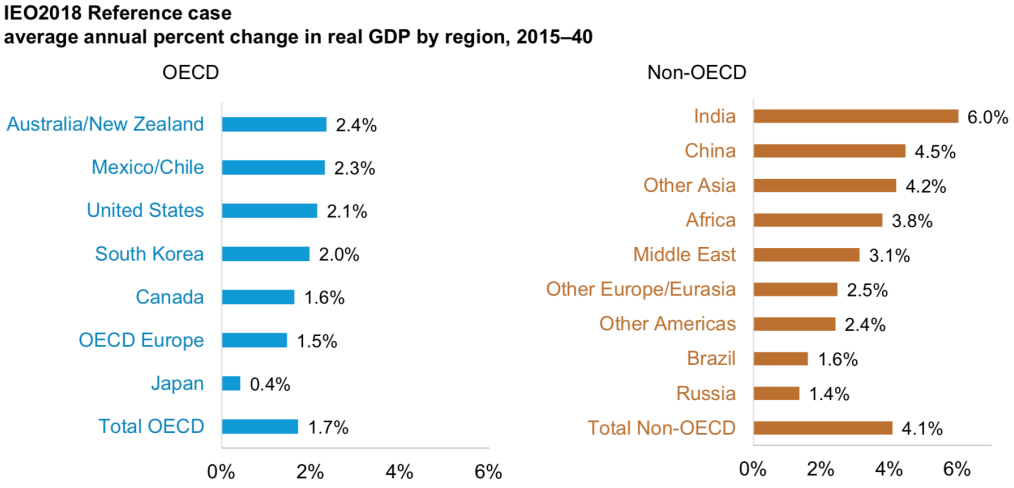

(b) Annual change per region

Abbildung 1.1: World energy consumption (a) and its annual change per region (b) according to the International Energy Outlook 2018 [6]. Countries are split based on their membership to the Organisation for Economic Cooperation and Development (OECD). OECD members are developed countries with a high-income economy that have committed to a sustainable world trade and economic progress.

observed during the glacial cycles of the past several hundred thousand years. At the same time, Fig. 1.5 depicts the severe amount of CO_2 emissions related to coal conversion, in comparison with other fuels. In particular, coal appears to be the most polluting source of energy and it generally emits almost twice as much CO_2 as natural gas, its main competitor. This behavior can be understood considering the stoichiometric reaction equations of coal (mainly carbon, C) and natural gas

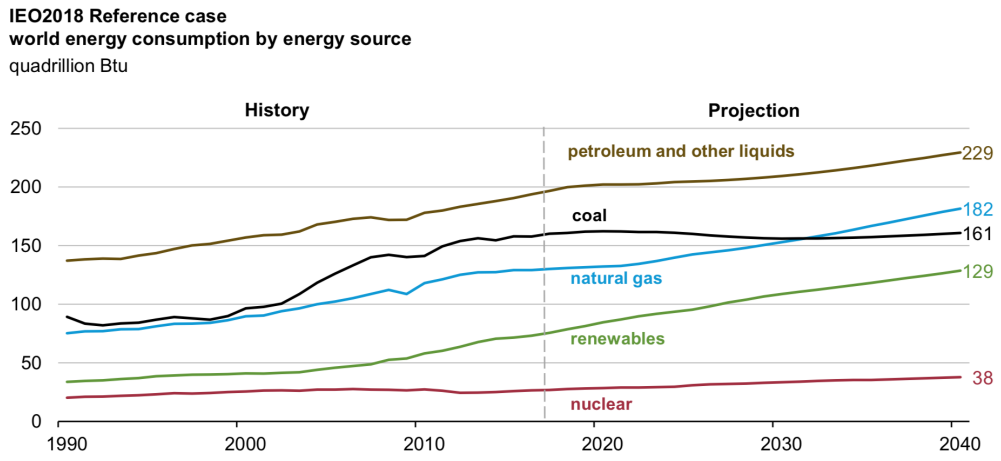

(a) Total energy generation

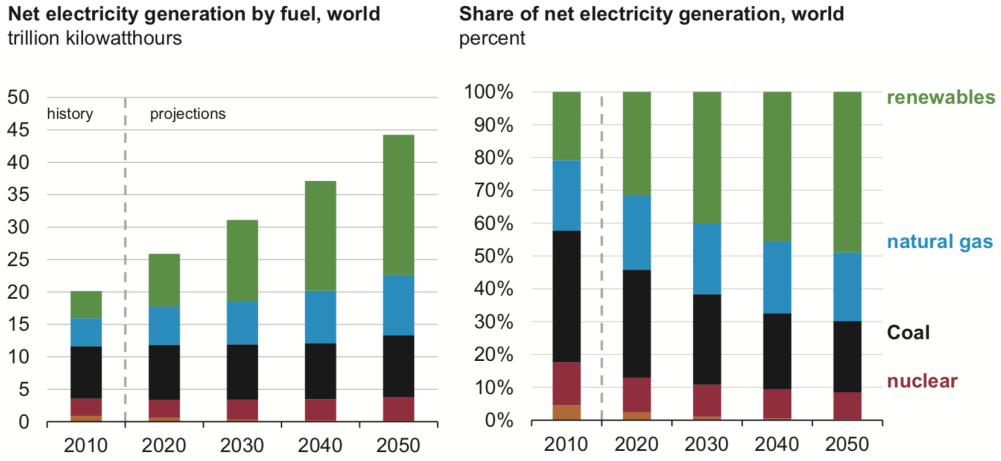

(b) Electricity generation

Abbildung 1.2: Energy consumption by energy source [6].

(mainly methane, CH_4) with oxygen, O_2,

$$C + O_2 \rightarrow CO_2, \tag{1.1}$$

$$CH_4 + 2O_2 \rightarrow CO_2 + 2H_2O, \tag{1.2}$$

and calculating the respective enthalpies of reaction, ΔH_R, i.e. the change in enthalpy between the products and the reactants [131]. Considering the standard enthalpies of formation of the reactants ($\overline{h}^0_{f,O_2} = \overline{h}^0_{f,C} = 0$, $\overline{h}^0_{f,CH_4} = -74.8\ \mathrm{kJ/mol_{CH_4}}$) and of the products ($\overline{h}^0_{f,CO_2} = -393.5\ \mathrm{kJ/mol_{CO_2}}$, $\overline{h}^0_{f,H_2O} = -241.8\ \mathrm{kJ/mol_{H_2O}}$), the energy released during carbon oxidation at standard conditions (298.15 K and 1 atm) for

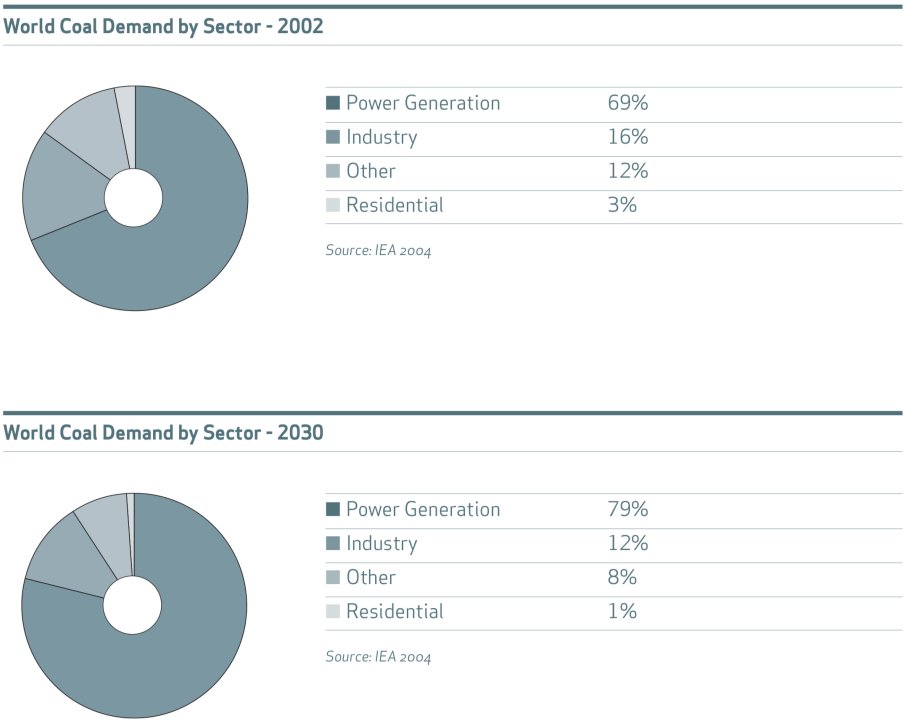

Abbildung 1.3: World coal demand by sector [2].

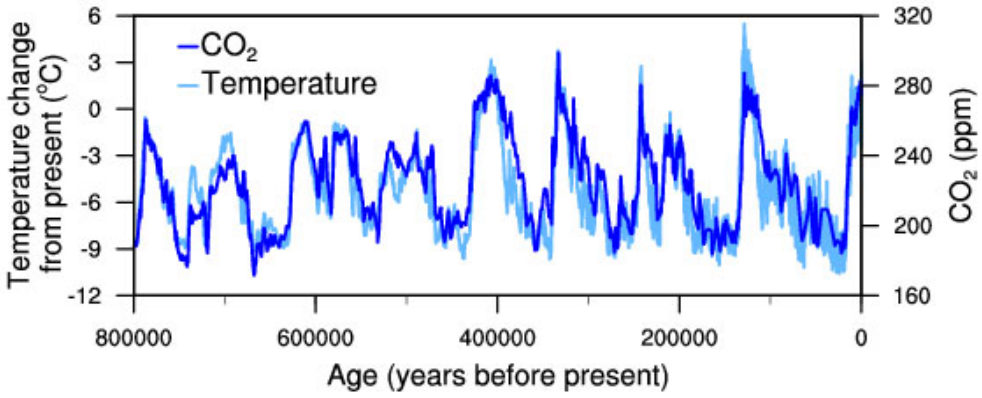

Abbildung 1.4: Temperature change (light blue) and carbon dioxide change (dark blue) measured from the EPICA Dome C ice core in Antarctica [7].

each mole of produced CO_2 can be calculated as

$$\Delta H_R = 1 \text{ mol}_{CO_2} \times (-393.5 \text{ kJ/mol}_{CO_2}) = -393.5 \text{ kJ}.$$

For methane combustion in standard conditions the released energy per each mole

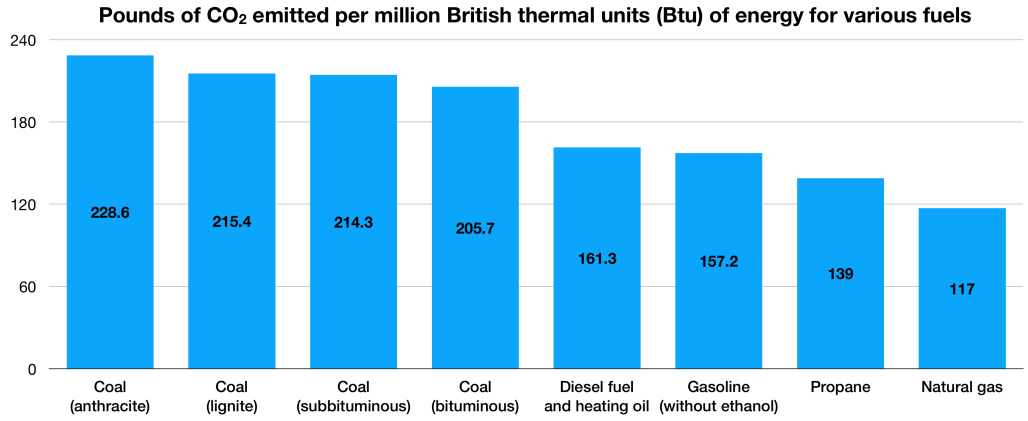

Abbildung 1.5: Specific carbon dioxide emissions of various fuels [8].

of produced CO_2 amounts to

$$\begin{aligned}\Delta H_R = {} & 1\ \mathrm{mol}_{\mathrm{CO_2}} \times (-393.5\ \mathrm{kJ/mol}_{\mathrm{CO_2}}) \\ & + 2\ \mathrm{mol}_{\mathrm{H_2O}} \times (-241.8\ \mathrm{kJ/mol}_{\mathrm{H_2O}}) \\ & - 1\ \mathrm{mol}_{\mathrm{CH_4}} \times (-74.8\ \mathrm{kJ/mol}_{\mathrm{CH_4}}) = -802.3\ \mathrm{kJ},\end{aligned}$$

which approximately doubles the calculated value for carbon, thus explaining the trend of CO_2 emissions per released energy shown in Fig. 1.5.

The environmental risks associated with a fossil fuel based energy system have pushed towards international agreements and national policies promoting renewable energy sources [75]. In this scenario Germany has started remarkably early this transition (*Energiewende*) and has committed to completely phase-out coal fired power plants by 2038 [75, 88]. Despite the anticipated trends in Germany, Fig. 1.2(a) shows how in the past few years the consumption of coal has been even increasing worldwide. The Annual Energy Outlook also attempts to forecast future developments in the energy field and bases its projections on a reference case. The latter is defined assuming that the current improvement expectations in known technologies and the economic and demographic trends remain valid and that current laws and regulations affecting the energy sector are unchanged throughout the projection period. Coal production is expected to decrease only through 2030, in response to shutdowns of coal-fired electric power plants and competitiveness of natural gas and renewables, before stabilizing and owning by 2050 still a 22% share of the global electric power production (Fig. 1.2(b)).

The reason why in this context of climate change coal remains a fundamental energy source to produce electricity is that the world's largest economies are deve-

loping in opposite directions. The efforts and commitments of many countries that are accelerating the phase-out of coal are compromised by a number of countries that have not announced phase-out policies yet and that, by contrast, are increasing the share of coal in their power mix (Fig. 1.6). These trends reveal how difficult

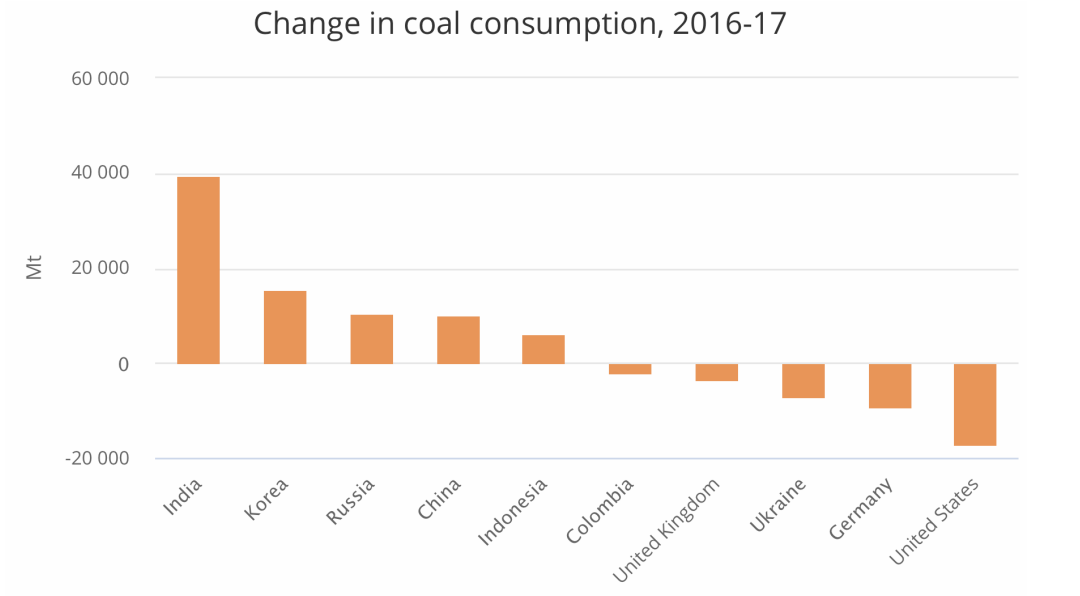

(a)

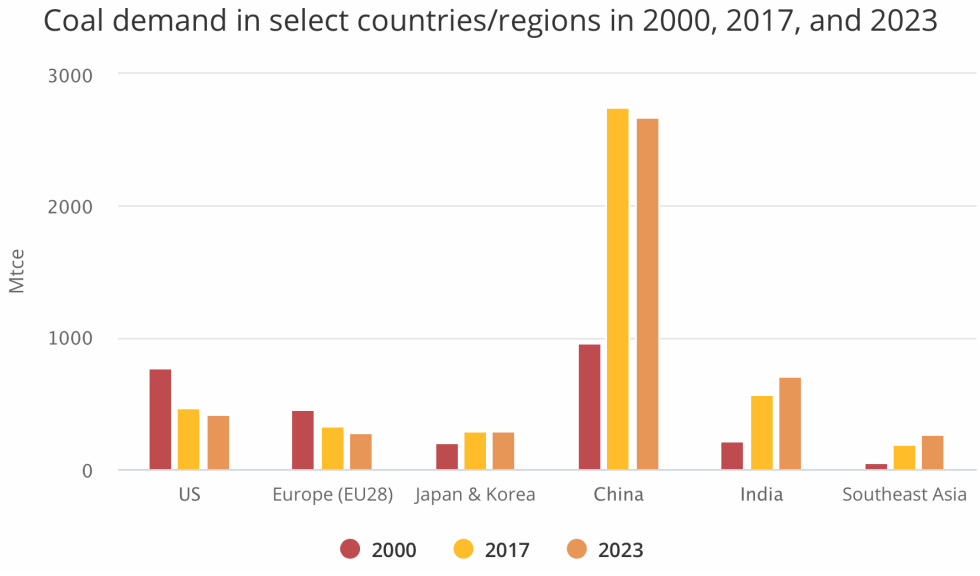

(b)

Abbildung 1.6: Change in coal consumption (a) and demand (b) in selected countries [5].

it is to reduce coal consumption, particularly for major coal-producing countries such as China and India (Fig. 1.7). For these countries the development of rene-

wables is not sufficient to absorb the growth in electricity demand. Moreover, the abundance, convenience and affordability of coal in these regions fits the rush of growing their economies and limits their dependence on oil-/gas-producing countries. In 2050, China is expected to remain the largest consumer and producer of coal in the world. Similarly, in India the incessant industrial growth and the challenge to further electrify the country's rural areas are expected to keep driving the growth of coal consumption. Therefore, notwithstanding the fast-growing distribution of re-

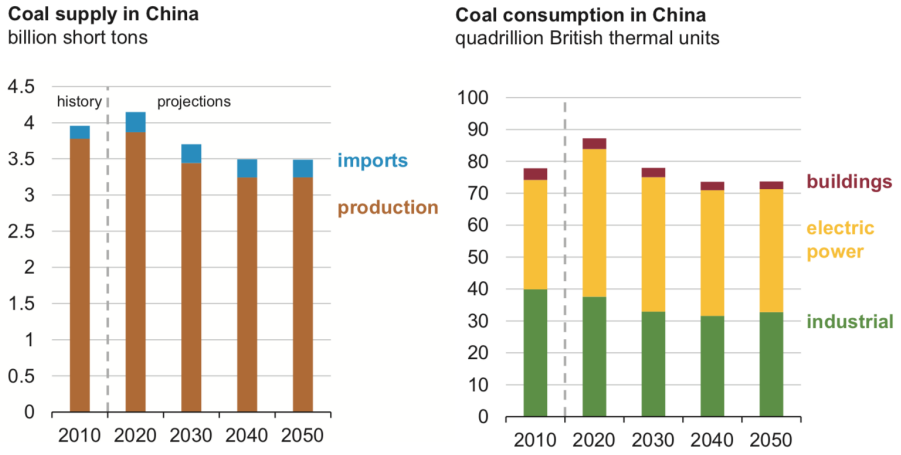

(a)

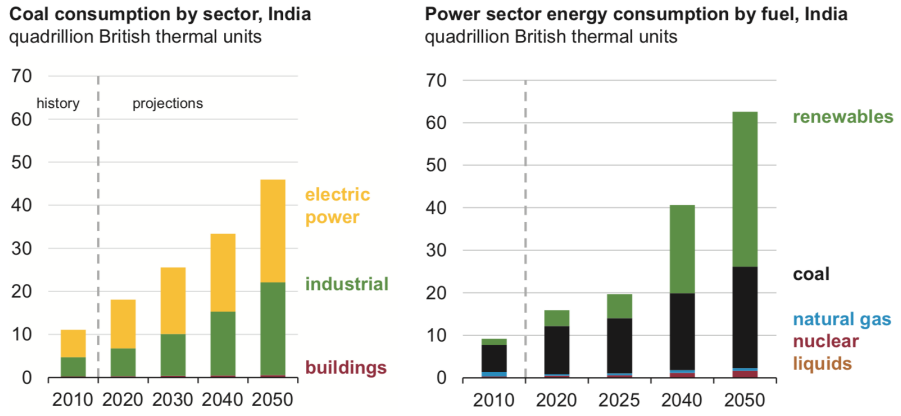

(b)

Abbildung 1.7: Coal supply and consumption in China (a) and India (b) [5].

newable energy, coal is expected to play a fundamental role in generating power for the next decades. For a sustainable coal conversion in the future, pollutants from PCC, i.e. the most commonly used technology in coal-fired power plants, need to be heavily reduced in order to mitigate the environmental threats of air and water pollution as well as climate change. To achieve cleaner and more efficient technologies to burn coal detailed insights in the underlying physical and chemical processes

that govern PCC are required. This leads to the need to keep pursuing innovation in coal research in order to develop less polluting techniques to burn coal. For these reasons, the present work focuses exclusively on PCC.

1.2 Background

PCC is the most widely spread coal conversion method for power generation purposes. Coal is pulverized to a fine powder with an average particle size of about 100μm for bituminous coal. The particles are carried by a hot mixture of combustion gases and injected into a furnace where combustion occurs at temperatures that can be significantly higher than 1000 K, depending on the used coal. The particles burning in suspension release heat which is transferred into a steam cycle driving a generator and a turbine. The residence time of the particle is of a few seconds and their size must be small enough to allow, during this time, for complete burnout. The latter is promoted by the high combustion temperature that on the other hand though, causes high NO_x emissions. Turbulent swirl conditions are created inside the burner to enhance combustion efficiency. Most PCC boilers have outputs between 50 and 500 MWe. However, larger units delivering over 1000 MWe are available [4, 52]. Even though PCC is performed in very large power plants, its characteristics are determined by devolatilization, ignition and combustion of the pulverized coal which occur at the particle size scale. These phenomena are the subject of investigation of the present work. Indeed, in order to improve modern pulverized coal burners a thorough understanding of coal ignition and combustion is fundamental and an improved knowledge of the interacting multi-phase and multi-scale processes is needed to predict PCC characteristics. Devolatilization and ignition influence flame properties in terms of stability, pollutant formation and possible extinction. Detailed state-of-the-art experimental investigations [13, 53, 65, 79, 139, 146, 147] can provide important data on such phenomena, but they are often difficult to perform due to the extreme conditions reached inside coal furnaces that make the application of most measurement techniques prohibitive. Intrusive measurements are relatively robust, but they may interact with the measured flame physics, e.g. act as flame holders. Laser diagnostics are usually more accurate, but the limited optical accessibility in the hostile PCC environments, make comprehensive flame diagnostics studies infeasible, also due to laser light scattering in the presence of coal particles and soot. Therefore, numerical simulations can complement the measurements and provide further insights into the PCC process. A classical and affordable si-

mulation approach is to solve the time-averaged Navier-Stokes equations (RANS) in order to obtain mean property solutions. As the flow conditions in PCC furnaces are typically turbulent, the large eddy simulation (LES) approach is increasingly employed to capture the highly transient processes in pulverized coal flames [20, 59, 68, 81, 89, 91, 98, 108, 121, 140, 150, 156]. LES relies on resolving the large scales of turbulence while reverting to models for the small scale processes near the particle surface and has the potential to offer more refined data compared with RANS. However, the processes in the direct vicinity of individual particles and particle groups ultimately govern PCC flame ignition and stabilization and accurate sub-grid closures for LES are required. Hence fully resolved approaches become increasingly important for providing a detailed description of near-particle processes [80]. This can be achieved performing direct numerical simulations (DNS), i.e. solving the governing balance equations in their general formulation, increasing both the time and space resolutions in order to capture turbulent motion without any modeling. In case of laminar conditions, time and space resolution requirements become less stringent and resolved laminar simulations allow for a full characterization of the flow. Resolved flow simulation studies of PCC have recently been published, focusing on counterflow [77, 149] and suspended particle [60] configurations, solid fuel clouds in turbulent flow [17, 67, 82, 106] and entire turbulent laboratory scale burners [48, 70]. These studies resolve the carrier (gas) phase, but rely on a Lagrangian point-particle framework for the solid phase, which leaves all particle boundary layers unresolved. PCC simulations that fully resolve the boundary layers have been performed assuming quiescent or laminar flow in 1D or 2D configurations. Vascellari *et al.* [135] performed resolved laminar simulation along with flamelet modeling to predict the ignition delay of single coal particles in a non-premixed Hencken burner. The accurate scalar dissipation rate profiles provided by the fully-resolved simulation allowed the laminar flamelet approach to correctly recover the experimental temperature and chemical species distributions as well as the ignition time. Goshayeshi & Sutherland [42] explored the effect of various devolatilization and gas-phase chemistry approaches by performing 1D simulations. They found significant differences in the predicted flame shape and stand-off distance when using different devolatilization models, namely the chemical percolation and devolatilization (CPD) rather than a two-step model, and moving from infinitely-fast chemistry to detailed chemical kinetics models. McConnell *et al.* [76] analyzed the effect of furnace temperature and particle diameter on detailed char burnout calculations to investigate the efficacy of devolatilization and char conversion models. They found that high-fidelity

models are more effective at representing particle temperature and mass data across a wide range of oxygen levels and coal types, and observed a significant overlap in devolatilization and char consumption. Nikrityuk *et al.* [83] analyzed a single carbon particle subject to oxidation in 2D. They found that the temperature, the regime of combustion and the carbon consumption rates of the particle are strongly affected by the heterogeneous kinetics, the particle Reynolds number and the O_2 concentration. Farazi *et al.* [35] used 2D resolved laminar simulation to study char combustion of single particles in various oxidizing environments and Sayadi *et al.* [111] extended the analysis to small particle clusters, exploring the effect of a wide range of parameters on char conversion characteristics. The burning behavior of the particles was found to be strongly dependent on their mutual distance and position, whereas the array arrangement only had a mild influence on the combustion characteristics. Most of the mentioned studies limited their investigation to simple configurations, such as a single coal particle [76, 83, 135], in laminar low Reynolds number flow [83] and employed a gas-phase kinetic model not specificly designed for coal applications [35, 111], e.g. based on GRI 3.0, a natural gas combustion mechanism, or a reduced version of it [76], representing a limit to the complexity of the assumed volatile matter composition. The next section highlights how these limitations have been partially overcome by the present contribution.

1.3 Present Contribution

The aim of this work has been the development of a comprehensive framework for the direct numerical simulation of pulverized coal particle heating, devolatilization, fuel-oxidizer mixing, subsequent ignition, combustion and eventual char conversion in the immediate proximity of single particles and particle arrays. This has been achieved, step by step, starting from a standard approach relying on common assumptions such as pre-fitted single-step devolatilization, a presumed fixed volatile composition based on relatively small hydrocarbons and a simplified description of the particle interior processes. The effects of porosity and char conversion, among others, have been omitted in this first instance. This preliminary modeling technique has been validated performing resolved laminar simulation of a series of particle ignition experiments in various gas atmospheres [79]. Characteristic particle conditions have then been obtained from a reference LES of a semi-industrial coal furnace [108] and fully resolved simulations have been performed, exploring transient effects at low particle Reynolds numbers Re_p and studying arrays of particles with diameter

D_p arranged at inter-particle distance L_x, in order to characterize the various coal combustion regimes that result from a wide range of relative spacings L_x/D_p. The analysis of the reference LES revealed that high Re_p and locally turbulent flow occur in the direct vicinity of coal particles in industrial PCC furnaces. Thus, the effects of high particle Reynolds numbers on single particles and closely spaced particle ensembles have also been explored. This has highlighted the limits of conventional flamelet modeling and standard film theory on highly strained envelope flames. Finally the effect of locally turbulent flow on volatile flame interaction and devolatilization have been investigated by means of DNS. The DNS has covered the volume of a single cell of the reference LES, fully resolving the mixing, the scalar dissipation and the transient evolution of the reacting scalar fields at the particle surface, hence providing important detailed LES sub-grid information. The final part of this work has aimed at alleviating the previous limitations of the model by considering a detailed kinetic model for the heterogeneous particle processes. The employed approach dynamically predicts the volatile release rate and composition, including large hydrocarbons, and accounts for char conversion. Moreover it is based on a detailed description of the particle interior properties such as porosity and particle-internal fluid flow. The robustness of the such-obtained comprehensive approach has been finally demonstrated comparing the predicted particle ignition and combustion behavior against the available experimental data [79].

1.4 Thesis Outline

The present thesis is structured as follows: in Chap. 2 the characteristics of multiphase reacting flows are presented. Chapter 3 focuses on the modeling of turbulent gas phase combustion, as well as the relevant sub-processes of coal pyrolysis such as devolatilization and the subsequent conversion of the residual char. Chapter 4 presents the numerical approach and its implementation based on the open-source CFD code OpenFOAM. In Chap. 5 the suitability of the computational framework is validated reproducing available data on the ignition of single coal particles in laminar air- and oxy-environments. Chapters 6 and 7 aim at characterizing coal particle array volatile combustion and flame interaction for the range of relevant conditions extracted from the reference LES: transient and group effects are investigated in Chap. 6, whereas in Chap. 7 the influence of particle Reynolds Number and turbulence is discussed. In Chap. 8 the model fidelity describing the thermal conversion of coal is enhanced by introducing a detailed multi-step approach for heterogeneous

kinetics. Finally, Chap. 9 provides the main conclusions from the conducted research before giving an outlook on future developments.

Chapter 2

Two-Phase Reacting Flows

This chapter covers the fundamental theoretical principles governing the flows that are investigated in this work. At first the characteristic properties and basic laws of reacting fluid motion are presented as well as the different approaches that can be adopted to solve them. Some insights on the phenomenon of turbulence are also given. Then, the physics of combustion are introduced along with characteristic quantities that are useful for the investigation of reacting flows. Finally, an overview on coal characteristics is provided as coal is the prime object of this investigation.

2.1 Generalities

Multiphase flows consist of two or more phases or components which are characterized by a macroscopical level of separation, i.e. significantly above the molecular scale. A simple classification is commonly based on the physical state of the different phases or components. Two topologies of multiphase flow can be identified, namely separated and disperse flows. The former consist of two or more continuous streams of different phases separated by interfaces. On the other hand dispersed flows present finite particles, drops or bubbles (the disperse phase) which are distributed throughout the continuous phase. The flows in the focus of this work consist of a gas mixture carrying pulverized coal particles, representing an example of two-phase dispersed flow. The latter is therefore the main subject of the following sections.

2.2 Governing Equations of the Fluid Phase

The fluid is assumed to satisfy the *continuum hypothesis* allowing to focus on fluid particles rather than on individual constituent molecules. Its mathematical descrip-

tion is therefore achieved by defining a set of coupled partial differential equations enforcing the conservation of momentum, enthalpy, total and species mass. The set of equations governing the instantaneous fluid properties that describe a reacting gas mixture carrying a dispersed phase can be expressed as follows,

$$\frac{\partial \rho}{\partial t} + \nabla \cdot (\rho \boldsymbol{U}) = \dot{\omega}_{\rho,het}, \tag{2.1}$$

$$\frac{\partial \rho \boldsymbol{U}}{\partial t} + \nabla \cdot (\rho \boldsymbol{U}\boldsymbol{U}) = -\nabla p + \nabla \cdot \boldsymbol{\tau} + \rho \boldsymbol{g} + \dot{\omega}_{\rho U,het}, \tag{2.2}$$

with

$$\boldsymbol{\tau} = \mu \left[\nabla \boldsymbol{U} + (\nabla \boldsymbol{U})^T - \frac{2}{3}(\nabla \cdot \boldsymbol{U})\boldsymbol{I} \right], \tag{2.3}$$

$$\frac{\partial \rho h_s}{\partial t} + \nabla \cdot (\rho h_s \boldsymbol{U}) = \nabla \cdot (\rho \alpha \nabla h_s) + \dot{\omega}_{h,che} + \dot{\omega}_{h,rad} + \dot{\omega}_{h,het}, \tag{2.4}$$

$$\frac{\partial \rho Y_i}{\partial t} + \nabla \cdot (\rho Y_i \boldsymbol{U}) = \nabla \cdot (\rho D_i \nabla Y_i) + \dot{\omega}_{i,hom} + \dot{\omega}_{i,het}, \tag{2.5}$$

where the fluid properties ρ, μ and α are density, dynamic viscosity and thermal diffusivity, respectively. The latter is defined as $\alpha = \lambda / \rho c_p$ with thermal conductivity λ and specific heat capacity c_p. $\boldsymbol{U}$ and $\boldsymbol{g}$ are the velocity and gravity acceleration vectors, p is the pressure, h_s is the sensible enthalpy and Y_i represents the mass fraction of the i-th species. The latter diffuses with molecular diffusivity D_i. For Newtonian fluids as the ones considered in this work, the viscous stress tensor $\boldsymbol{\tau}$ shows the linear dependence on the velocity gradients expressed in Eq. (2.3). The terms $\dot{\omega}_{\rho,het}$ and $\dot{\omega}_{\rho U,het}$ are heterogeneous sources to the total gas mass and momentum, and $\dot{\omega}_{h,che}$, $\dot{\omega}_{h,rad}$ and $\dot{\omega}_{h,het}$ are changes of the sensible energy due to (homogeneous) chemical reaction, radiation and heterogeneous processes. The source terms in Eq. (2.5) for the species mass, $\dot{\omega}_{i,hom}$ and $\dot{\omega}_{i,het}$, are changes of the species mass fractions Y_i due to homogeneous and heterogeneous processes.

2.2.1 Modeling Approaches

The two-phase dispersed flows considered in this work are typically dilute, meaning that they consist of a dominant (by volume) fluid phase carrying the particles, i.e. the dispersed phase. The latter can be described and solved either in a Lagrangian or Eulerian framework.

2.2.1.1 Lagrangian Point-Particle Approach

In the Lagrangian framework the individual particles are tracked as they are transported through the continuous phase. To do that, particle motion is described by balancing the forces acting on the particle, e.g. drag, buoyancy and gravity forces, with the change of momentum, i.e. applying Newton's second law. The evolution of the particle temperature is also captured solving for the heat exchanged with the carrier phase. In case of coal particles the obtained temperature can be easily related to a model in order to describe devolatilization, char conversion and radiation processes. The Euler-Lagrange approach offers the advantage, compared to Euler-Euler methods, to be able to capture the influence of different particle size distributions and trajectories on particle drag and slip velocity as well as devolatilization, char conversion and radiation by accounting for kinetic and thermal non-equilibrium between gas and particles of different size [123]. On the other hand Lagrangian methods are based on solving the evolution of point sources, neglecting the detail and complexity of the particle interior and the phase interface or simplifying their description by means of models. The source terms in the carrier fluid equations (Eqs. (2.1-2.5)) are calculated by the particle source in cell (PSIC) approach [25]. This drastically simplifies the description of the exchange between the continuous and dispersed phases. Moreover, not resolving the boundary layers around the particles allows for using much larger computational cells, significantly reducing the computational cost. For PCC applications the particle size is usually smaller than the grid size, except for very large coal particles in highly turbulent flows. Since this work aims at providing comprehensive predictions of the physical and chemical processes occurring in the direct vicinity of burning coal particles and particle groups, such processes should not be modeled by a Lagrangian point-particle approach, but be resolved, making an Eulerian formulation more adequate.

2.2.1.2 Eulerian Approach

The Eulerian approach is based on the principle of observing the fluid motion focusing on specific locations fixed in space through which the fluid flows. The main fluid properties are functions of space and time. In case of two-phase flows, also the dispersed phase (especially if non-dilute) can be treated as an Eulerian fluid (Euler-Euler approach) modeling the flow of two continuous and fully interpenetrating phases. This requires solving the set of Eqs. (2.1-2.5) for each phase, hence leading to a high computational cost. Moreover with this approach the interface bet-

ween the two fluids that can -in general- be moving is usually not explicitly tracked but instead the volume fraction of each phase is defined and solved for.

In this work a fully-resolved Eulerian approach has been used for the carrier phase in order to resolve the particle boundary layer and accurately capture all transport processes. Particle location and spacing are fixed and the coupling between the two phases is enforced by boundary conditions at the particle surface describing heterogeneous processes such that the heterogeneous source terms in Eqs. (2.1-2.5) reduce to zero. The developed framework will be presented in detail in the following Chap. 3, covering all the adopted techniques to describe coal particle combustion.

2.3 Turbulence

Fluid flows can be either laminar or turbulent. In the first case the motion is well-ordered with several layers sliding on each other as pressure gradients and viscous forces establish. The flows involved in industrial processes, especially for energy conversion, are almost entirely turbulent. Turbulent flows are characterized as chaotic, unstable, three dimensional and dissipative. In 1883, Reynolds characterized for the first time the phenomenon of turbulence by investigating the conditions under which the transition of laminar to turbulent occurred due to non-linear flow instabilities overcoming the stabilizing effect of viscous forces [102]. He defined a dimensionless parameter, today named after him, reflecting the tendency of a flow to become turbulent. The *Reynolds number* is written as

$$Re = \frac{UL}{\nu}, \tag{2.6}$$

where U, L and ν are the characteristic velocity, characteristic length scale and the kinematic viscosity of the fluid, respectively. Considering pipe flow, U is taken as an average velocity over the pipe cross section and L the diameter of the pipe. Values of $Re > 2000$ can be identified as critical with respect to the onset of turbulence [103]. The instantaneous turbulent velocity field $\boldsymbol{U}(\boldsymbol{x}, t)$ can be decomposed in a mean velocity $\overline{\boldsymbol{U}(\boldsymbol{x}, t)}$ and a fluctuating component $\boldsymbol{u}'(\boldsymbol{x}, t)$ so that

$$\boldsymbol{U}(\boldsymbol{x}, t) = \overline{\boldsymbol{U}(\boldsymbol{x}, t)} + \boldsymbol{u}'(\boldsymbol{x}, t). \tag{2.7}$$

If the mean value $\overline{\boldsymbol{U}(\boldsymbol{x}, t)}$ is taken as the temporal average (Reynolds average) this separation is known as *Reynolds decomposition*. In this case inserting the decomposed turbulent velocity into the conservation equations for mass and momentum leads,

through further simplifications, to the so-called *Reynolds Averaged Navier-Stokes (RANS)* system of equations. With this approach the flow unsteadiness is completely averaged out and regarded as part of the turbulence. This leads to additional terms in the conservation equations, e.g. the *Reynolds stresses* and the *turbulent scalar flux* that are unknown and need to be modeled [47]. A similar decomposition is applied in Large Eddy Simulation (LES), where the mean velocity $\overline{\boldsymbol{U}(\boldsymbol{x},t)}$ originates from spatial filtering and includes the large scales of the total field only, i.e. the most energetic components. In this case the temporal dependence is preserved but the fluctuating velocity becomes an unresolved sub-grid scale component $\boldsymbol{u}'_{sgs}$ for which modeling is still required. Alternatively, by solving the instantaneous velocity field directly, therefore not requiring any model or approximation, results in Direct Numerical Simulation (DNS), the method that has been chosen for this work. The mentioned methods considerably differ regarding the turbulent scales that they resolve. More details on the computational approaches follow in the next section.

2.3.1 Modeling of Turbulence

2.3.1.1 Spatial & Temporal Scales in Turbulent Flows

Turbulence is a phenomenon that occurs on multiple scales, both in time and space. Within the chaotic structures that turbulent flows exhibit it is still possible to find regularities, e.g. coherent structures like vortices or eddies. The size of these structures is connected to the level of energy that they carry and the relationship between the largest and the smallest scales of turbulent motion is provided by the concept of the *energy cascade* introduced by Richardson in 1922 [104]. Turbulent kinetic energy is produced at the large scales in locations of mean flow gradients (e.g. shear layers). The most energetic eddies break up due to their intrinsic instability and transfer their energy to smaller eddies, that progressively feed smaller structures until viscous effects become too strong for the smallest scales to survive. This process of dissipation of the large scales of turbulent energy occurs at a rate ϵ which is not affected by viscosity and can be related to the characteristic length L, time t and velocity U

$$\epsilon = \frac{U^2}{t} = \frac{U^3}{L}. \tag{2.8}$$

The smallest scales, i.e. the scales at which turbulent kinetic energy is eventually dissipated by the action of viscosity, were characterized in space and time by

Kolmogorov [63, 64] and are named after him

$$\eta = \left(\frac{\nu^3}{\epsilon}\right)^{1/4}, \tag{2.9}$$

$$\tau_\eta = \left(\frac{\nu}{\epsilon}\right)^{1/2}. \tag{2.10}$$

The scales η and τ_η describe the size and the turnover time of the smallest eddies respectively. Accordingly, a velocity scale can be obtained as

$$\upsilon_\eta = (\nu\epsilon)^{1/4}. \tag{2.11}$$

A turbulent velocity field can be expressed in terms of a Fourier decomposition [47]. This allows to characterize the energy of the turbulent eddies either in physical space or in wave number space. The process of the energy cascade can be visualized by considering the turbulent energy spectrum shown in Fig. 2.1. The intermediate ran-

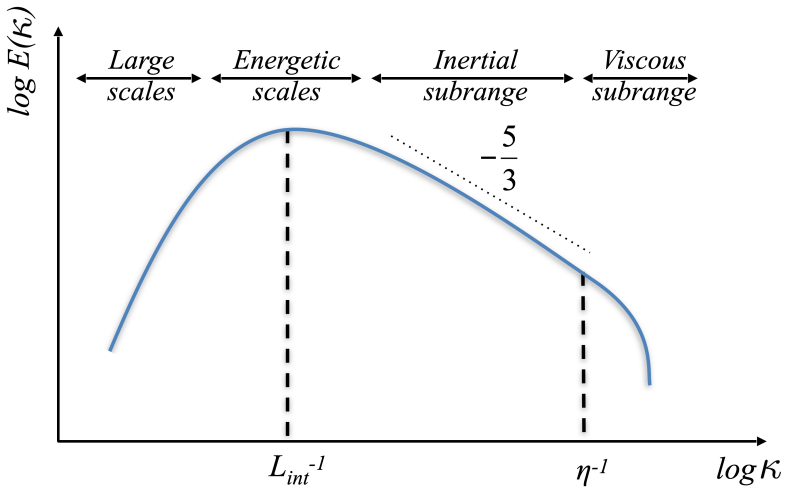

Abbildung 2.1: Sketch of a turbulent energy spectrum showing turbulent kinetic energy $E(\kappa)$ versus wave number κ [94].

ge of turbulent scales (or wave numbers) located in-between the energy-containing eddies and the viscous eddies is known as the inertial subrange. In this region of the spectrum, the net energy coming from the energy-containing eddies is in equilibrium with the net energy cascading to smaller eddies where it is dissipated. Hence the slope of the energy spectrum in this range remains constant. Kolmogorov's hypotheses as well as the experimental evidence set this slope to -5/3 and led to the following

expression for the energy spectrum:

$$E(\kappa) \propto \epsilon^{2/3} \kappa^{-5/3}. \tag{2.12}$$

The equilibrium condition for the formation of the inertial subrange only really establishes at very high Reynolds numbers [125].

2.3.1.2 Reynolds Averaged Navier Stokes (RANS) Approach

The most affordable computational approach for the simulation of turbulence is to solve the time-averaged Navier-Stokes equations in order to obtain mean property solutions. The presence of the unknown *Reynolds stresses* and *turbulent scalar flux* in the conservation equations requires the use of modeling approximations for their closure. These models usually aim at characterizing turbulence by means of its kinetic energy and length scale. Mixing-length models directly prescribe these quantities but they are only effective for simple flows. More sophisticated models introduce partial differential equations to compute the turbulence quantities. For example, the widely used $k-\epsilon$ model introduces two additional equations to calculate the kinetic energy k and the dissipation ϵ (which can be related to the length scale L). By applying RANS, all fluctuations and therefore all the scales of the energy spectrum are modeled. This translates into quick availability of results, characterized though by a significant loss of information. RANS is preferred for industrial, large-scale devices that benefit from the inexpensiveness of the simulations and when focusing on few quantitative properties of the flow only.

2.3.1.3 Large Eddy Simulation (LES)

Large Eddy Simulation only solves the large scales of turbulent motion assuming that those contain most of the energy (low-mid wave numbers range in Fig. 2.1), whereas it reverts to models for the small scales due to their universal character. This is done by spatially filtering the Navier-Stokes equations removing small-scale information from the numerical solution. The filtered equations include the additional *subgrid-scale Reynolds stress* that requires a model for its closure. The most common example of subgrid-scale model is the eddy viscosity model proposed by Smagorinsky [113], which is based on the assumption that the *subgrid-scale Reynolds stress* primarily leads to an increase in transport and dissipation, which can be related to a turbulent eddy viscosity [47]. In LES, turbulent eddies are resolved down to the computational cell size which, in general, is significantly larger

than the Kolmogorov scale. Turbulent scales smaller than the grid size are taken into account by modeling the sub-grid energy dissipation rate. No time-averaging is performed, hence allowing to capture unsteady effects. This aspect, along with the limited computational costs, has made LES increasingly popular for academic and industrially relevant research, finding applications also in realistic PCC configurations [21, 40, 51, 81, 89, 98, 108, 145].

2.3.1.4 Direct Numerical Simulation

The most comprehensive approach for the numerical investigation of turbulent flows is Direct Numerical Simulation. It is based on solving the Navier-Stokes equations, the transport equations of species and enthalpy in their general formulation (Eqs. (2.1)-(2.5)), i.e. without making use of any turbulence model. DNS requires the computational grid to fully resolve all turbulent scales down to Kolmogorov, resulting in a very fine discretization. To achieve such high accuracy of the results, a massive increase of the computational costs has to be accommodated for, making DNS still unaffordable for most of the relevant industrial applications. Its use is therefore limited to research purposes, in particular where experimental data is not available or very difficult to produce as in the case of PCC [48, 70]. This aspect earned DNS the epithet of *numerical experiment*. Model development for RANS and LES approaches can also benefit from reliable DNS data. These can be used as input, as reference for model validation or as supplemental information by providing sub-grid data (e.g. [106, 129, 130, 143] among others).

In the present work DNS is performed to characterize devolatilization and combustion of isolated coal particles and closely spaced particle ensembles in laminar and turbulent flow. The achieved full resolution is fundamental in order to effectively predict the physical and chemical processes occurring in the immediate vicinity of the particles that control the devolatilization and combustion characteristics. Since the experimental conditions that this work aims at reproducing show locally laminar flow around the single particles, many of the performed simulations are fully-resolved simulations of laminar flow. In order to investigate the effect of elevated particle Reynolds number, Re_p, and considerable levels of turbulence on coal particles devolatilization and burning behavior, turbulent flow in the vicinity of the particle surface is also considered. For these simulations artificial turbulence for the DNS inflow is generated based on a von Karman spectrum using inverse Fourier transforms according to the method of Billson *et al.* [16]. Details on the turbulence generation are provided in Appendix A.

2.4 Combustion

Combustion transforms a set of reactants into various chemical species through exothermal reactions, so that the energy contained in the chemical bonds of the reactants is released as thermal energy. This process occurs in several steps involving a number of elementary reactions of various chemical species. Each of these reactions can generally be represented as:

$$\sum_{i=1}^{N} \nu'_{ij} \mathcal{M}_i \rightleftharpoons \sum_{i=1}^{N} \nu''_{ij} \mathcal{M}_i, \tag{2.13}$$

where ν'_{ij} and ν''_{ij} are the stoichiometric reactant and product coefficients of species i denoted as $\mathcal{M}_i$, respectively, and $j = 1, \ldots, \mathbb{M}$ is the reaction index. The molar consumption/production rate of the i-th species $\dot{\omega}_i^m$ is given by

$$\dot{\omega}_i^m = \frac{dc_i}{dt} = \sum_{j=1}^{\mathbb{M}} (\nu''_{ij} - \nu'_{ij})\, q_j, \tag{2.14}$$

where c_i is the molar concentration of the species $\mathcal{M}_i$ and q_j represents the rate of progress of reaction j,

$$q_j = k'_j \prod_{i=1}^{N} c_i^{\nu'_{ij}} - k''_j \prod_{i=1}^{N} c_i^{\nu''_{ij}}. \tag{2.15}$$

The quantities k'_j and k''_j represent the forward and reverse rate coefficient of the j-th reaction, respectively. The forward rate coefficient can be computed with an Arrhenius rate expression

$$k'_j = A_j T^{\beta} \exp\left(-\frac{E_{aj}}{R_u T}\right), \tag{2.16}$$

with the pre-exponential factor A_j, the temperature exponent β, the activation energy E_{aj}, and the universal gas constant R_u. The reverse rate coefficient can be computed from the equilibrium constant

$$K_j = \frac{k'_j}{k''_j}. \tag{2.17}$$

The above relations allow for computing the species production rates required by the species transport equation,

$$\dot{\omega}_i = \dot{\omega}_i^m M_i, \tag{2.18}$$

where M_i is the molar mass of the i-th species. In general, the prediction of the combustion characteristics improves in terms of flame properties and structure the more relevant reactions and species are included in the chemical mechanism. For example detailed chemical kinetics of hydrocarbon combustion can involve hundreds of species and thousands of reactions. However, the use of large mechanisms can become extremely expensive from the computational point of view [69, 95]. Therefore it is crucial to have an efficient strategy for chemistry reduction that can speed up numerical investigations of practical combustion applications. This is achieved by progressively simplifying the chemical mechanism, yet keeping the profiles of some important species or combustion properties, e.g. ignition delay times, unaltered. Such reductions are complex to perform, and subject to detailed research [3, 100]. The computational load of detailed chemical kinetics can also be reduced using alternative methods, e.g. chemistry tabulation as done in flamelet modeling [94].

2.4.1 Modes of Combustion

For an effective theoretical analysis of combustion problems it is useful to characterize the conditions under which the combustion process occurs. A regime classification can be done considering the status of the reactants before entering the combustion chamber, leading to two limiting cases:

- *Premixed combustion*: Fuel and oxidizer are perfectly mixed before/when entering the combustion chamber. Premixed flames propagate at a flame speed determined by the chemical composition of the reacting mixture, its thermodynamical state (pressure and temperature) and the conditions of the flow (turbulence). The well determined mixture composition leads to cleaner and more efficient combustion. On the other hand, premixed combustion can also result in dangerous combustion instabilities, e.g. flashback that can eventually lead to detonations of the device due to flame propagation against the mean flow direction.

- *Non-premixed combustion*: Fuel and oxidizer enter the combustion chamber separately, where they mix prior to ignition. The mixing process therefore con-

trols the rate of reaction. Non-premixed flames cannot propagate upstream and are hence easier to control and preferred in most practical applications. In non-premixed conditions, insufficient mixing can lead to inefficient and incomplete combustion resulting in the formation of significant amounts of pollutants.

The derivation of modeling formulations differs significantly for the modes of combustion mentioned above. Since in this work predominantly non-premixed combustion is investigated, the theoretical description focuses on non-premixed flame characteristics only.

2.4.2 Mixture Fraction, Scalar Dissipation Rate and the Flamelet Concept

Since non-premixed combustion is governed by the mixing of fuel and oxidizer, it is useful to introduce a parameter describing the degree of mixing between fuel and oxidizer. For a two-streams problem the mixture fraction Z can be defined as a normalized element mass fraction y_i of element i (for example C, O, H, etc.),

$$Z = \frac{y_i - y_{i2}}{y_{i1} - y_{i2}}, \tag{2.19}$$

with indices 1 and 2 denoting the fuel and oxidizer stream, respectively. By this definition, $Z = 1$ in the fuel stream and $Z = 0$ in the oxidizer stream. Since elements are conserved within combustion processes, the mixture fraction transport equation contains no chemical source/sink terms,

$$\frac{\partial \rho Z}{\partial t} + \nabla \cdot (\rho Z \boldsymbol{U}) = \nabla \cdot (\rho D_Z \nabla Z) + \dot{\omega}_{Z,het}. \tag{2.20}$$

The only source term in Eq. (2.20), $\dot{\omega}_{Z,het}$, represents the additional fuel contribution from heterogeneous processes at the particle surface (devolatilization and char conversion in case of coal) to the gas phase. Numerical simulations of non-premixed flames can be interpreted based on the definition of the mixture fraction since it has the advantage of being an inert species. This leads to several benefits when solving Eq. (2.20) for reacting flows. The absence of the chemical source term becomes a considerable advantage when applying the mixture fraction approach to turbulent flows, as the (otherwise unclosed) highly non-linear reaction rates drop out. Mixture fraction is a key quantity in the flamelet model for non-premixed turbulent combustion. The model considers the turbulent flame as an ensemble of stretched laminar flames, the flamelets, located around the thin stoichiometric iso-surface [155]. The

basic assumption is that the flame wrinkling induced by the turbulent flow occurs on a larger scale than the flame thickness, i.e. that the Kolmogorov eddy is much larger than the reaction layer where the chemical conversion occurs [93]. The transport equations of reacting scalars in physical space can be transformed into mixture fraction space [94],

$$\frac{\partial \rho Y_i}{\partial t} = \rho \frac{\chi}{2} \frac{\partial^2 Y_i}{\partial Z^2} + \dot{\omega}_i. \tag{2.21}$$

The scalar dissipation rate χ is defined as

$$\chi = 2 D_Z \left(\nabla Z\right)^2, \tag{2.22}$$

and it is closely related to the chemical reaction rate [15]. In general reaction progress is inversely proportional to χ, i.e. small values of χ indicate near to equilibrium conditions. The scalar dissipation rate can also be seen as a measure of the mixing rate. Scalar dissipation dissipates fluctuations in scalar fields similarly to viscosity that dissipates velocity fluctuations [144]. For non-premixed combustion, solving the flamelet equation, Eq. (2.21), in mixture fraction space allows to establish a relationship between the thermo-chemical properties and the mixture fraction. However, a scalar dissipation rate profile has to be prescribed. The obtained solution can be tabulated in mixture fraction space and then used to recover the chemical state corresponding to a computed mixture fraction field. The main advantage offered by the flamelet concept is the possibility to uncouple the detailed chemistry solution and the turbulent flow calculations. In Chap. 7, the flamelet approach is applied using the chemical state at the mixture fraction bounds and the scalar dissipation rate profiles extracted from the DNS as input. An attempt is made to recover the single coal particle combustion results with the flamelet calculations, investigating the limits of conventional flamelet modeling on highly strained and curved envelope flames.

2.5 Pulverized Coal Combustion

This work focuses on characterizing the devolatilization and combustion of pulverized coal particles immersed in the surrounding gaseous mixture serving as oxidizer. When coal particles are exposed to the hot environment, the temperature of the solid rises and devolatilization occurs. Particles are pulverized in order to enhance mass transfer rates by increasing the surface area for two-phase heat and mass transfer so that combustion efficiency is strongly improved. Reducing the size of

the coal particles also results in shorter devolatilization and ignition delay times. The mixing of the released volatiles and the surrounding mixture is controlled by diffusion (both laminar and turbulent) and it is fundamental in order to achieve flammability conditions for the mixture, such that combustion takes place. The investigated multi-phase flows are therefore characterized by a continuous exchange of total and species mass, momentum and energy at the interface between the solid and the gas-phase.

2.5.1 Burning of Coal

Thermal conversion of coal includes complex multi-scale processes involving several species and kinetic steps, the first being coal pyrolysis that has a strong influence on the subsequent phenomena. Pyrolysis starts with changes of the original coal structure upon heating. Subsequently, devolatilization begins and a wide range of chemical compounds are released, such as light gases, heavier species known as tars and the solid char. These compounds, once produced, can react with oxygen-containing species, either homogeneously or heterogeneously, in a fashion that strongly depends on the operating conditions and the carbon content of the coal. Given its sedimentary nature, resulting from organic materials undergoing decomposition as they are subjected to geologic heat and pressure over millions of years, coal is porous and highly heterogeneous with a composition that significantly varies from one type of coal to another. Closely related to the carbon content is the coal "rank" depending on specific H/C and O/C ratios. The aging process of coal, starting from its organic precursor peat, can be followed in van Krevelen's diagram in Fig. 2.2.

The reported coal ranks can be also interpreted and classified on the basis of moisture and volatile matter content or the calorific value resulting in the so-called *proximate analysis*. Lignite coals are very young from a geological perspective and are therefore soft, presenting a woody structure. They appear brown and are characterized by high moisture and volatile matter content but relatively low calorific value. They are not particularly suited for fine pulverization and show a tendency to fragment when burning. Sub-bituminous coals are black, dull and lack woody structures. They exhibit slightly higher calorific values than lignite coals. Bituminous coals are intensively employed for energy generation purposes due to their high calorific value. Their volatile matter content can be further distinguished between high, medium and low. Finally anthracite coals are hard, black and lustrous. They represent the highest rank and calorific values, being characterized by only minimal amounts of volatiles and moisture [9].

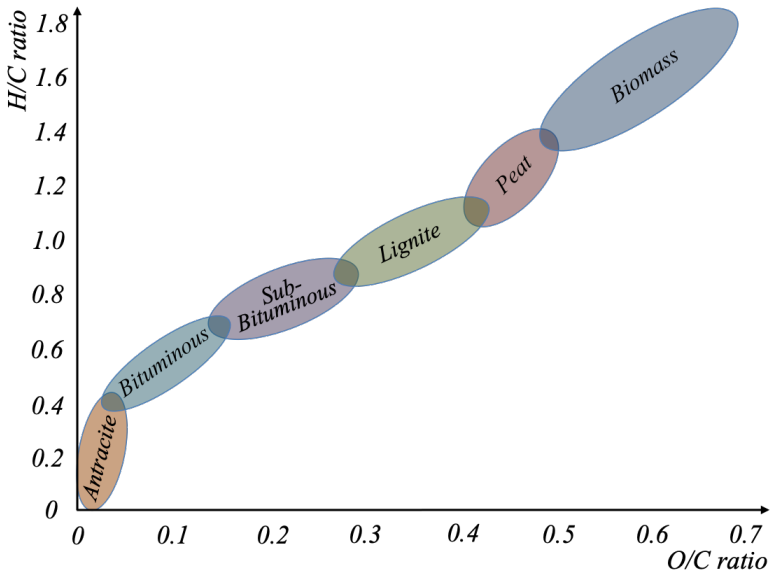

Abbildung 2.2: Coal ranks in van Krevelen's diagram [132]

The elemental breakdown of the coal composition is referred to as *ultimate analysis*. It is widely variable for the different coals due to their heterogeneous nature, complicating a general description of coal and a characterization of its combustion. However, heating up pulverized coal inside a furnace, a classical scheme can be detected: at first the moisture is extracted during the drying process, immediately after that, devolatilization starts releasing light gases and tars. The heating rate of the coal affects both the volatile composition and the rate at which volatile species are released. As they mix with the surrounding gas phase they might ignite and burn homogeneously, further increasing the temperature of the coal. Heterogeneous or mixed heterogenous/homogeneous coal ignition can also occur. As volatile matter is driven off, coal may swell and increase its porosity. After depletion of volatiles the solid residue consists of char. At this point heterogeneous reactions consume the char with a lower rate than devolatilization, transforming it into ash, slag and various fine particulate fumes [131].

2.5.2 Modeling of Coal Devolatilization Kinetics

This section briefly reviews some of the most important models developed for the pyrolysis of pulverized coal with a special focus on devolatilization. In order to predict coal devolatilization, two main approaches can be pursued leading to two general categories, namely detailed network models and reduced/empirical models. The first category relies on building a complex model that accounts for the decomposition

of the coal matrix as the particle heats up. For this approach, detailed chemical engineering knowledge and experimental data are required for the specific coal in order to accurately describe its initial matrix structure as well as the release of the gases and tars during pyrolysis. The devolatilization models of the second category use generalized expressions relying on a reduced set of reactions modeling the release process by low order kinetics. The coal properties data and the experimental data on pyrolysis have to be carefully selected with the aim of generating simple and promptly available models, capable of reliable predictions notwithstanding coal heterogeneity. More detailed information on coal pyrolysis kinetics can be found in [71, 153]. For CFD purposes reduced/empirical models are usually preferred due to the considerable computational cost that the inclusion of detailed coal matrix pyrolysis would add to a numerical code. This work offers useful insights on both approaches. It explores the circumstances under which complex models can significantly improve the prediction of homogeneous and heterogeneous burning behavior (providing a strong incentive for the higher CPU cost) and when instead simpler model descriptions suffice to recover the experimental evidence.

2.5.2.1 Detailed Network Models

The development of coal devolatilization computational models has aimed at being able to predict the coal devolatilization behavior, at least in some limited regime of temperature and heating rate, by means of a preprocessing computer subroutine, only requiring the input of the coal properties and the furnace operating conditions. Such models are for example the functional group-depolymerization vaporization cross-linking (FG-DVC) [116–118], the FLASHCHAIN [87] and the chemical percolation devolatilization (CPD) model [44].

2.5.2.1.1 Functional Group (FG), Depolymerization, Vaporization, and Crosslinking (DVC) Model

The FG-DVC model by Solomon *et al.* [118] consists of two stages and it is designed to predict the rates and yields of all the major gaseous species and the yields and elemental compositions of tars and char from a coal undergoing pyrolysis. The model is particularly accurate in predicting slow heating rates and it is suitable up to 40,000 K/s. The first stage of the model considers the functional groups (aromatic and hydroaromatic clusters linked by aliphatic bridges) and it is based on the premise that a fraction of the total gases is produced as the weakest bridges break up separating some functional groups from the macromolecular network. Some other

functional groups remain attached to the coal matrix and are eventually released along with tar molecules. The amount of functional groups resulting in gases is closely related to the heating rate, the final temperature, the density of the functional group and the structure of the specific coal. The second stage considers thermal breakdown of the macromolecular network. Starting from an approximation of the network and its structural attributes, the decomposition and fragmentation of the network is predicted on the basis of a Monte-Carlo method. Evaporating gases and tars originate from the smaller fragments, whereas the residuals of the macromolecule constitute the char [154]. FG-DVC relies on a database of coal-specific libraries describing the structural, chemical and kinetic properties of the specific coal. This circumstance represents the greatest limitation of the method as its capability of accurately predicting the yields and volatile composition during pyrolysis can only be exploited for coals within the available database or by interpolating their properties. New libraries are indeed difficult to generate due to the complexity and limited availability of the required information. Further details on FG-DVC can be found in [116–118].

2.5.2.1.2 FLASHCHAIN Theory for Rapid Coal Devolatilization Kinetics

The FLASHCHAIN model was originally formulated by Niksa and Kerstein [87]. The model represents the macromolecular structure of coal as a mixture of chain fragments of different sizes. These structural components can be classified in aromatic nuclei (A), labile bridges (B), char links (C), and peripheral groups (S). During devolatilization, the fragments disintegrate as bridges break and reintegrate as char links form. Chain statistics provide the chemical kinetic rates of conversion and recombination of the fragments in order to describe their size distributions. A main four-step reaction mechanism controls bridge conversions that are not unimolecular scissions but complex chemical processes involving numerous steps and species. First order rate expressions with distributed activation energies establish the temperature dependence of bridge conversion. Finally, species conservation laws predict the yields of individual gases whereas the release rate of tars is determined with the flash distillation analogy, in which a phase equilibrium relates at each instant the fragment concentrations in the tar vapor and in the condensed phase [85].

Following its introduction, the model was further developed with several publications collected in [86], refining the theory and extending its practical application. It has been proved to be able to predict with good accuracy the product yield variation

with pressure (ranging from vacuum to 6.9MPa), heating rates (from 1 to 10^4K/s) and coal rank. Still, this model requires extensive effort and research into the properties of many different coals, especially by means of nuclear magnetic resonance (NMR) in order to build an effective database, which again represents a limit to its applicability.

2.5.2.1.3 Chemical Percolation for Coal Devolatilization (CPD)

The chemical percolation devolatilization model presented by Grant *et al.* [44] also requires experimental data in order to characterize the diversity of the possible coal structures. The model relies on the percolation theory providing the size distribution of discrete coal clusters, joined together by intact bridges and isolated from others by broken bridges. The theory also provides mathematical expressions in closed form to account for the lattice statistics, which are important for the modeling of the devolatilization process. The use of percolation expressions avoids computationally expensive Monte-Carlo techniques not affecting though the accuracy of the statistical information. CPD distributes devolatilization products into char, tar, and light gas which are, however, not further assigned to individual components. The model is based on the following key elements:

- a description of the target coal by means of NMR measurements,
- a reaction mechanism for the linking bridges along with kinetics,
- a set of reaction parameters for the activation energy and frequency factor for light gas release,
- percolation lattice statistics in order to predict bridge breaking and characterize the distribution of the detached fragments which eventually result in tars,
- a liquid-vapor equilibrium mechanism able to describe the fraction of liquid that vaporizes as tar,
- a cross-linking mechanism for heavy tar precursors reconsolidating into char.

The required data, including M_{cl} (the average molar mass per aromatic cluster), M_δ (the average side-chain molar mass), $\sigma + 1$ (the average number of attachments per cluster), and b_0 (the fraction of intact bridges), can be obtained from NMR analysis of a given coal and be directly used as input for the CPD. This represents a big

advantage for CPD since other models obtain these parameters as empirical fitting coefficients. Genetti *et al.* [38] developed a correlation between the chemical structure input parameters and the elemental composition and volatile matter content of the coal, allowing for the determination of CPD input parameters for quite a wide range of coals without any further NMR data required. Moreover, they proposed an algorithm able to provide a detailed composition for the light gas released during devolatilization, overcoming the CPD limitation of predicting a global volatile release only. Vascellari *et al.* [133] developed a similar tool, namely a pyrolysis kinetic preprocessor (PKP), assigning the released volatile matter to pre-selected volatile species.

As it will be discussed in Chap. 3, the coal composition (Tab. 3.3) assumed for the Pittsburgh seam high-volatile bituminous coal and employed in Chap. 5 has been obtained from CPD, where the coal-specific CPD input parameters were obtained according to Genetti [37] and the heating rates were chosen according to the targeted burner experiment [79].

2.5.2.2 Reduced/Empirical Models

The preprocessor methods discussed so far have crucial importance in determining the amount of volatiles and their composition for a coal particle undergoing pyrolysis. Their computational cost, however, has so far prevented their direct application within CFD codes. Even though some CPD applications already exist in DNS [33, 34] and LES [105, 140], direct coupling is not standard yet. Meanwhile, several empirical models have been developed to describe the rate of release of volatiles. Most of these models rely on Arrhenius rate parameters and are capable of reproducing overall weight loss and approximated individual evolution of fixed species.

2.5.2.2.1 Single First Order Rate (SFOR) Reaction Model

The most simplistic employed model is the single first-order reaction model such as the one developed by Badzioch and Hawksley [11]. Devolatilization is assumed to be a first-order reaction depending on the amount of volatiles remaining in the particle. The model provides the rate at which volatiles ($\mathcal{V}$) are driven out of the solid ($\mathcal{S}$) particle as it is heated up, representing the rate of weight loss of the coal sample

$$Coal \xrightarrow{k_v} \mathcal{S} + \mathcal{V}, \tag{2.23}$$

$$\frac{dm_v}{dt} = k_v(m_v^* - m_v), \tag{2.24}$$

$$k_v = A_v e^{-E_v/R_u T_p}, \tag{2.25}$$

with the asymptotic volatile content, m_v^*, and instantaneous mass of volatiles, m_v, released into the gas, respectively. A_v and E_v are Arrhenius parameters, namely the pre-exponential factor and the activation energy, respectively, that along with the universal gas constant, R_u, and the particle pyrolysis temperature, T_p, define the Arrhenius rate constant of devolatilization k_v. All the parameters and factors required for the model depend on the specific coal sample and on the operating conditions, limiting the generality and applicability of the method. The results presented in Chaps. 5, 6 and 7 are all based on the SFOR reaction model which will therefore be further discussed in Chap. 3.

2.5.2.2.2 Two Competing Reactions Model

Kobayashi *et al.* [62] proposed a model based on regarding coal pyrolysis as two simultaneous and competing reactions, one dominating at a low temperatures range, the other dominating at high temperatures instead,

$$Coal \xrightarrow{k_{v1}} (1-\alpha_{v1})\mathcal{S}_1 + \alpha_{v1}\mathcal{V}_1, \tag{2.26}$$

$$Coal \xrightarrow{k_{v2}} (1-\alpha_{v2})\mathcal{S}_2 + \alpha_{v2}\mathcal{V}_2, \tag{2.27}$$

$$\frac{dm_v}{dt} = (\alpha_{v1}k_{v1} + \alpha_{v2}k_{v2})(m_v^* - m_v), \tag{2.28}$$

$$k_{v1} = A_{v1} e^{-E_{v1}/R_u T_p}, \tag{2.29}$$

$$k_{v2} = A_{v2} e^{-E_{v2}/R_u T_p}, \tag{2.30}$$

where α_{v1} and α_{v2} are the mass stoichiometric coefficients or yield factors for each reaction. Therefore, the resulting rate of volatile yield is given by the combination of the different competing rates, allowing for taking into account the influence of different heating rates and temperatures. On the other hand, this type of model still relies on six parameters that depend on the specific coal sample, limiting its applicability to the available data.

2.5.3 Modeling of Char Conversion

This section briefly reviews the classical models describing char conversion, i.e. the burning out process of the carbon residue with the oxygen diffusing into the porous coal structure. Char oxidation occurs once devolatilization has finished and it is

characterized by a slower rate. The char conversion process involves the reacting surface of the porous particle and can be modeled with either a surface-based or an intrinsic approach. The former assumes the heterogeneous reactions to exclusively occur on the outer particle surface, whereas the latter predicts the reaction rates taking into account the complex pore structure of the particle. At the same time different methods can be used to track the development on the inner particle surface, mostly by means of empirical correlations [84].

Baum *et al.* [14] and Field [36] developed a kinetic/diffusion model assuming that the carbon oxidates to CO only, being the related reaction dominant at high temperatures, and that the conversion is governed by the diffusion of oxygen to the particle surface and by the chemical rate of reaction between oxygen and carbon. The model describes char oxidation by means of a global kinetic rate expression,

$$\frac{dm_c}{dt} = \pi D_p^2 p_0 X_{\mathrm{O}_2} \left(R_{diff}^{-1} + R_c^{-1}\right)^{-1}, \tag{2.31}$$

where m_c and D_p are the mass and the diameter of the char particle, whereas p_0 and X_{O_2} are the atmospheric pressure and the fraction of O_2, respectively. R_{diff} and R_c are the bulk gas-phase oxygen diffusion reaction rate coefficient and the chemical reaction rate coefficient, respectively. The original approach uses for the diffusion coefficient the following expression [36],

$$R_{diff} = \frac{C_{diff}}{D_p} \left(\frac{T_g + T_p}{2}\right)^{0.75}, \tag{2.32}$$

where the diffusion rate constant $C_{diff} = 5 \times 10^{-12} s/K^{0.75}$ and T_g and T_p are the bulk gas and particle temperature, respectively. The kinetic rate constant R_c for char oxidation can instead be written as

$$R_c = A_c \psi_c e^{-E_c/R_u T_p}, \tag{2.33}$$

where A_c and E_c are the pre-exponential factor and the activation energy for char combustion, respectively. The model treats internal and external reacting surface equally and as a whole, considering though their development by means of the surface factor ψ_c given by the ratio of the total reacting surface and the external surface area of the particle, that is assumed to be spherical [14]. The presented formulation does not take into account the char pore structure, neglecting the effect of internal pore diffusion on the chemical reaction rate.

The intrinsic model by Smith [115] established a relationship between the pore

structure/diffusion and the char reaction rate coefficient by means of an effectiveness factor η_p accounting for pore diffusion resistance, so that

$$R_c = \eta_p \rho_c S_a k_{c,i} \frac{D_p}{6}. \tag{2.34}$$

In Eq. (2.34) ρ_c is the density of the coal particle and S_a and $k_{c,i}$ are the specific internal surface area and the intrinsic rate of chemical reaction of oxygen with char, respectively. The effectiveness factor represents the ratio of the actual char combustion rate to the rate attainable if no pore diffusion resistance existed [115].

2.5.4 Multi-step Coal Volatile/Char Off-Gas Kinetics

Most of the available models for coal kinetics are effective in predicting the rate of volatile release during pyrolysis, even though they usually limit the composition of the released volatile matter to a few compounds, leading to inaccuracies as additional materials, such as tars, are not included. Moreover, char burn-out, i.e. the heterogeneous reactions that take place on the particle surface, are either neglected or treated separately, especially when focusing on devolatilization, as they usually occur after the volatile matter has been depleted. Future development of coal kinetic models requires thus a more comprehensive approach for devolatilization and char conversion, in which the composition of the volatile matter can include additional materials, tars in particular, and can be effectively predicted for different types of coal and operating conditions.

Sommariva *et al.* [119] presented a multi-step kinetic mechanism, assuming coal as aromatic clusters with several bridges, side chains and functional groups on peripheral positions. Three reference coals were considered representing completely different rank conditions so that the behavior of different coal samples could be obtained, given only its normal chemical analysis, as a combination of the behavior of the reference coals. The model was proved to be reliable as in good agreement with the experimental evidence, and its fundamental strength lies in its predictive capability, not requiring any tuning of the rate parameters and stoichiometry for different coals.

Gentile *et al.* [39] used this approach for porous media with chemical reactions [72, 73] for modeling pyrolysis of anisotropic biomass particles. However, the gas phase outside the particle was not modeled. Tufano *et al.* [126] extended the computational framework for the first time to a multidimensional CFD calculation, including gas-solid interaction processes inside the particle and fully resolving the

surrounding gas phase, with the aim of predicting the ignition delay time of single pulverized coal particle in air- and oxy-atmospheres. The main findings of that work are presented here in Chap. 8, thus the model approach is described in detail in Chap. 3.

Chapter 3

Modeling

In Chap. 2 the characteristics of multiphase reacting flows have been introduced. The present chapter discusses the modeling details and the boundary conditions which have been adopted in order to solve the general equations governing the involved physical/chemical processes.

The current approach is based on the target configuration. This work focuses on single coal particle and particle array ignition and burning. These setups are not only relevant for the prediction of combustion in simplified experimental configurations but can also be representative of local conditions extracted from realistic pulverized coal flames. This is shown in Fig. 3.1 where an example of a computational domain is obtained isolating a single particle from a PCC flame and identifying the gas-mixture and the coal particle regions. In order to solve such a problem, the developed approach has to provide a model for both regions and has to guarantee closure at the interface, where the particle and the surrounding gas-phase interact by means of boundary conditions.

In this work two distinct approaches are used. The first one, modeling coal pyrolysis and volatile combustion, with focus on the initial stages, has led to the results presented in Chaps. 5, 6 and 7. The second one, the comprehensive multi-step approach for heterogeneous coal conversion has led to the results discussed in Chap. 8.

The following sections present in detail both numerical frameworks.

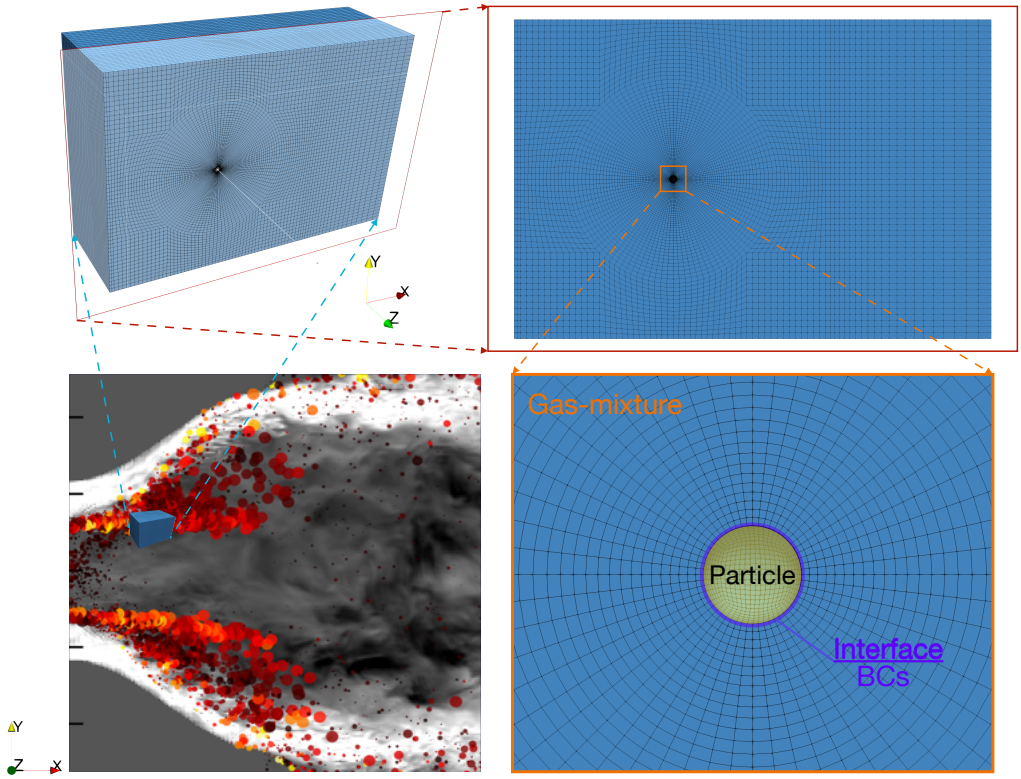

Abbildung 3.1: Example of the computational setup used for the modeling of single coal particle combustion. Simple configurations can be representative of local conditions extracted from industrially relevant PCC flames as the one computed in [108] and taken as reference in Chaps. 6 and 7.

3.1 Modeling of Coal Pyrolysis and Volatile Combustion

3.1.1 Transport Equations and Boundary Conditions

A fully-resolved Eulerian approach (Sec. 2.2.1.2) is used in order to describe the reacting gas mixture carrying pulverized coal particles. The set of equations governing the instantaneous fluid properties is directly derived from Eqs. (2.1-2.5), in which the particle sources become boundary conditions for the gas phase such that the heterogeneous source terms reduce to zero

$$\dot{\omega}_{\rho,het} = \dot{\omega}_{\rho U,het} = \dot{\omega}_{h,het} = \dot{\omega}_{i,het} = 0. \tag{3.1}$$

The final set of equations becomes

$$\frac{\partial \rho}{\partial t} + \nabla \cdot (\rho \boldsymbol{U}) = 0, \tag{3.2}$$

$$\frac{\partial \rho \boldsymbol{U}}{\partial t} + \nabla \cdot (\rho \boldsymbol{U}\boldsymbol{U}) = -\nabla p + \nabla \cdot \boldsymbol{\tau} + \rho \boldsymbol{g}, \tag{3.3}$$

with

$$\boldsymbol{\tau} = \mu \left[\nabla \boldsymbol{U} + (\nabla \boldsymbol{U})^T - \frac{2}{3}(\nabla \cdot \boldsymbol{U})\boldsymbol{I} \right], \tag{3.4}$$

$$\frac{\partial \rho h_s}{\partial t} + \nabla \cdot (\rho h_s \boldsymbol{U}) = \nabla \cdot \left(\frac{\mu}{Pr} \nabla h_s \right) + \dot{\omega}_{h,che} + \dot{\omega}_{h,rad}, \tag{3.5}$$

$$\frac{\partial \rho Y_i}{\partial t} + \nabla \cdot (\rho Y_i \boldsymbol{U}) = \nabla \cdot \left(\frac{\mu}{Sc} \nabla Y_i \right) + \dot{\omega}_{i,hom}. \tag{3.6}$$

For conditional analysis, an additional transport equation for the volatile gas mixture fraction is solved,

$$\frac{\partial \rho Z}{\partial t} + \nabla \cdot (\rho Z \boldsymbol{U}) = \nabla \cdot \left(\frac{\mu}{Sc} \nabla Z \right). \tag{3.7}$$

Assuming low Mach number conditions, the work and the kinetic energy contributions have been neglected in the enthalpy equation. The fluid is also assumed to obey the ideal gas law relating pressure, density and temperature. Fluid absolute enthalpy is defined as

$$h(T) = \sum_{i=1}^{n} Y_i \cdot h_i(T), \tag{3.8}$$

with the species absolute enthalpies h_i given by the sum of the sensible enthalpy and the standard enthalpy of formation, $h^0_{f,i}$,

$$h_i(T) = h^0_{f,i} + \int_{T_{ref}}^{T} c_{p,i}\, dT. \tag{3.9}$$

The temperature dependence of gas phase viscosity is described by Sutherland's law. In Eqs. (3.5-3.7) a single gas diffusion coefficient ($D_i = D$) equal to the thermal diffusivity ($Le = Sc/Pr = 1$) is assumed such that the species diffusional fluxes, expressed within the gas by the Fick's law, rely on the definition of the Schmidt number $Sc = \mu/\rho D$. Prandtl and Schmidt numbers of 0.7 are assumed. Hence the model does not account for differential diffusion, as the latter was found by Tufano *et al.* [127] to have a negligible impact on a similar configuration to the one considered in Chap. 5 and shown here in Fig. 3.1. In [127] resolved simulations of coal particle ignition were performed reproducing available experimental measurements

of the ignition delay time of a single coal particle in a laminar hot co-flow. The effects of a broad range of parameters that affect the prediction of the ignition delay were investigated. In particular, predictions based on a detailed species transport approach were compared to unity Lewis number results. To this end Fig. 3.2 shows the temporal evolution of the maximum temperature inside the domain for both simulation approaches. Ignition can be detected in correspondence of the sudden and steep temperature increase. The results show how detailed transport (blue line) only had a marginal effect (<5%) on the ignition delay time of a single particle in comparison to the unity Lewis number assumption (red line).

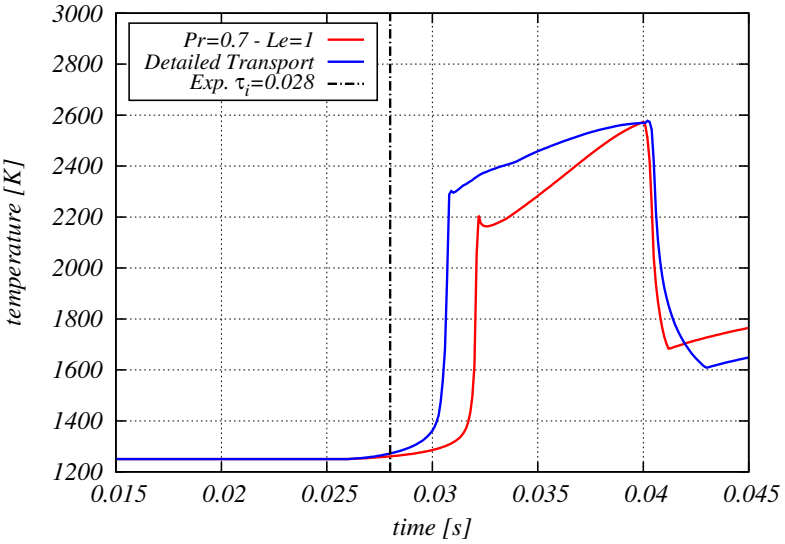

Abbildung 3.2: Resolved laminar simulation of devolatilization and volatile ignition of a single coal particle immersed in a hot-air mixture: maximum temperature inside the domain as a function of time [127].

For the description of the solid, heterogeneous char reactions are ignored based on the assumption of subsequent, independent stages of coal combustion. The coal particle is treated as a solid with a continuous internal structure, i.e. neglecting its porosity, heterogeneity and potential ash layer effects. Hence, heat transfer in the interior of the coal particle is governed by a simple temperature equation for the solid,

$$\rho_c c_{p,c} \frac{\partial T}{\partial t} + \nabla \cdot (-\lambda_c \nabla T) = \frac{\dot{m}_v}{V_p} \Delta h_v, \tag{3.10}$$

where ρ_c, $c_{p,c}$, λ_c, V_p are the density, heat capacity, thermal conductivity and volume of the coal particle, $\dot{m}_v$ is the volatile mass flow rate and Δh_v is the heat of devolatilization. At the particle surface, the following boundary condition describes

the heat exchange between gas and solid phase

$$\lambda_c \frac{\partial T}{\partial r}\bigg|_{\text{coal}} = \lambda_g \frac{\partial T}{\partial r}\bigg|_{\text{gas}} + Q_{r,p}\,, \quad \text{with} \quad Q_{r,p} = -\frac{\epsilon_p}{2(2-\epsilon_p)}(4\sigma T_p^4 - G_p), \quad (3.11)$$

where $Q_{r,p}$ is the surface radiative heat flux, ϵ_p the particle emissivity, σ the Stefan-Boltzmann constant and G_p the incident radiation. Coal particle emissivity is commonly assumed to be near unity during devolatilization and to reduce to approx. 0.5 [108, 122] and lower [43] during char conversion. Sensitivity studies within the full range of $0 \leqslant \epsilon_p \leqslant 1$ did not reveal any significant influence for the particle configurations considered in this work. Thus, the term $Q_{r,p}$ in Eq. (3.11) is omitted from the present DNS. In contrast, gas phase radiation has a (mild) cooling effect [128] and is included here by adopting the P1-approximation [22, 78] assuming unity gas emissivity.

Solution of Eqs. (3.10) and (3.11) yields the radial profile of the intra-particle temperature, which is crucial in determining the rate at which volatiles are released by the particle, $\dot{m}_v = \frac{dm_p}{dt}$. The latter is calculated here by means of a single first order Arrhenius kinetic rate model (Sec. 2.5.2.2.1), using Eqs. (2.24) and (2.25) and considering the spatial mean value of the radial profile of particle temperature, $\overline{T}_p$,

$$\dot{m}_v = A_v e^{-\frac{E_v}{R_u \overline{T}_p}}(m_v^* - m_v). \quad (3.12)$$

An alternative evaluation of Eq. (3.12) based on the particle surface temperature did not strongly affect the results, cf. Sec. 5.2. Due to the small particle size and comparatively low relative velocities in the reference particle configurations and the assumptions inherent in Eq. (3.10) (negligible internal particle structure), particle heating occurs nearly uniformly across the particle volume. Hence, alternatively evaluating the devolatilization rate by integrating Eq. (3.12) over the particle volume and using the local particle temperature does not change the trends that will be observed and discussed in the results chapters.

The model parameters A_v and E_v require adjustment for the given coal and heating rates of the target furnace. They can be determined by parameter fitting, e.g. applying the CPD model (Sec. 2.5.2.1.3), as done here for the Pittsburgh seam high-volatile bituminous coal used in Chap. 5 and Chap. 8, or relying on experimental data, as done here for the Saar hvBb [61], employed in Chap. 6 and Chap. 7. The value of $\dot{m}_v$ affects the gas phase by means of a particle boundary condition for the

species mass transfer across the particle surface [131],

$$\dot{m}_i = Y_i \dot{m}_v - \rho_g S_p D_g \frac{\partial Y_i}{\partial n}, \tag{3.13}$$

which consists of a linear combination of the species mass fraction Y_i and its derivative evaluated normal to the particle surface (third type or Robin boundary [46]). In Eq. (3.13), $\dot{m}_i$ is the total mass flow rate of species i, ρ_g and D_g are the gas density and diffusivity at the particle surface, and S_p is the surface area of the particle, which is assumed to be spherical and of constant size. The latter assumption is deemed suitable given the relatively low heating rates in the reference (mostly laminar) flame configurations that the model attempts to predict, and due to the main focus on the early stages of coal combustion, namely devolatilization, ignition and volatile burning. Solving the above system of equations on an appropriate grid (as the one shown in Fig. 3.1, highly refined in the particle vicinity) ensures that the interface between the two phases is fully resolved and all relevant processes such as temperature and species gradients, devolatilization, volatile mixing with the surrounding gas, subsequent ignition and combustion are directly simulated.

3.1.2 Homogeneous Chemistry

Chapter 2 underlined the importance of having available a comprehensive, yet affordable chemical mechanism. For simulations of PCC the description of the chemical reactions is complicated by the number and the chemical structure of the volatile species and tars that are involved in the combustion reactions. The presence of heavy species that need to be decomposed through different chemical steps limits the simplification of the mechanism, which moreover has to account for the oxidation of all the released species. Section 2.5.1 also discussed how complex and diverse the chemical compounds constituting the volatile matter can be so that the detailed composition of the released species is often unknown. In order to fulfill the requirements of affordable simulations, it is impossible to include a whole variety of species, especially when performing fully resolved simulations which are intrinsically expensive. Therefore, it is fundamental to restrict the number of volatiles released by the particle to a set of significant species without invalidating the prediction of coal combustion characteristics. The assumed volatile composition (especially of the tars) ultimately determines the required homogeneous chemistry mechanism. All the mechanisms used in this work are derived from a general detailed kinetic scheme, consisting of more than 450 species and ≈17,000 reactions referred to as

POLIMI_TOT_1407 and discussed in [100, 109, 110]. This comprehensive low and high temperature kinetic scheme is based on a detailed core mechanism for C_1-C_4 species, a lumped description of the primary propagation reactions of larger species and their primary intermediates. It permits the description of the pyrolysis and oxidation of a variety of hydrocarbons up to C_{16}, as well as the formation paths of major pollutant species, making it suitable up to jet fuels and diesel applications [100]. This kinetic mechanism was validated for a wide range of operating conditions through the comparison with experimental measurements carried out in ideal reactors and laminar flames. The kinetic mechanism and a more exhaustive list of the references for its validation are available online [3].

The two approaches used in this work significantly differ in terms of the solid particle description and assumed volatile composition. This leads to different requirements for the homogeneous chemistry, resulting in two different reductions of the general mechanism. The target coals used in this work are the Pittsburgh seam high-volatile bituminous coal and the Saar hvBb coal, with the proximate and ultimate analysis reported in Tabs. 3.1 and 3.2, respectively.

Tabelle 3.1: Proximate and ultimate analysis (as received) of Pittsburgh seam high-volatile bituminous coal [79]

Proximate Analysis		Ultimate Analysis	
Volatile matter	35.89	C	75.23
Fixed carbon	56.46	H	5.16
Moisture	0.47	O	9.83
Ash	6.95	N	1.43
HHV	30.94 MJ/kg	S	2.00

Tabelle 3.2: Proximate and ultimate analysis (dry, ash-free) of the Saar hvBb coal [146].

Proximate Analysis		Ultimate Analysis	
Volatile matter	37.00	C	79.30
Fixed carbon	52.50	H	4.70
Moisture	2.00	O	13.70
Ash	8.30	N	1.30
LHV	32.32 MJ/kg [92]	S	1.00

When applying the simplified approach described in the current section the assumed compositions for both coals are reported in Tab. 3.3.
The given compositions include light gases and the larger hydrocarbon benzene C_6H_6 that was chosen to represent tars. Common alternatives are the C_2-hydrocarbons

Tabelle 3.3: Assumed volatile matter composition for Pittsburgh and Saar coals (mass %)

	Pittsburgh	Saar
CO	8.81	37.70
C_2H_4	-	37.00
CO_2	3.94	-
CH_4	7.22	0.50
H_2	2.47	0.20
H_2O	13.68	-
N_2	2.92	2.20
C_6H_6	60.96	22.40

such as C_2H_2 which is widely used to model devolatilization [107, 127, 135, 151], but is characterized by faster consumption paths than typical heavier tar molecules, resulting in increased mixture reactivity that can lead to deviations of the predicted ignition delay from the experimental evidence. Additionally, these effects can be enhanced by commonly used mechanisms such as GRI3.0 [114] or the reduced DRM22 [56], which were designed and optimized to model natural gas combustion and lack of complex chemical paths for the oxidation of large hydrocarbon chains. The adopted homogeneous chemistry mechanism has to be capable of describing the oxidation of the chemical compounds included in Tab. 3.3, i.e. up to C_6H_6. Starting from the POLIMI_TOT_1407 detailed kinetic scheme, a skeletal mechanism tractable for CFD calculations of coal volatile oxidation, containing 52 species and 452 reactions, has been obtained. The reduction was performed by the CRECK modeling group to minimize the error in the range of operating conditions (temperature, pressure, and equivalence ratios) of interest for this work. The mechanism was reduced adopting an automatic technique based on the combination of reaction flux analysis and sensitivity analysis as previously described in [101, 120]. The reduction procedure provided an accurate skeletal mechanism, characterized by a maximum error in ignition delays of 10% with an average error of 3.2%, compared to the corresponding complete mechanism. The relevant information on the final reduced mechanism is included in Appendix B.

The presented approach, using an effective but relatively affordable skeletal mechanism to describe the homogeneous chemistry for coal pyrolysis, along with the simplified description of the solid particle, allows to investigate a broad range of coal particle configurations by means of 2D and 3D fully resolved simulations (Chaps. 5, 6 and 7).

The following section introduces the second approach used in this work, i.e. the comprehensive multi-step model for heterogeneous coal conversion. It is based on a detailed description of the solid particle releasing a complex mixture of light gases and heavy tars including much larger hydrocarbons than C_6H_6, therefore requiring a different, more detailed reduction of the general kinetic scheme (Sec. 3.2.4). The added level of detail results in a significantly increased computational cost of the fully resolved simulations. Therefore, this second approach is applied in the present work to laminar, single particle configurations only (Chap. 8).

3.2 Multi-Step Approach for Heterogeneous Coal Conversion

In order to improve the prediction of the thermal degradation of coal also including the conversion of the char, a comprehensive multi-step approach for heterogeneous kinetics is introduced. This requires the formulation of a full two-phase reaction and transport model, achieved with the update of the particle interior and heterogeneous kinetics description. The latter alleviates the previously made assumptions of single-step pyrolysis, fixed volatile composition and simplified particle interior properties. The obtained framework is also capable of predicting char conversion by considering the gas-solid interaction processes inside the particle using a sophisticated model for porous media with chemical reactions.

3.2.1 Transport Equations

The model describes the particle interior and exterior by means of different sets of partial differential equations. The particle is considered as a porous medium bounded by a spherical outer shell that separates it from the exterior gas phase. To describe the exterior gas the conservation equations of momentum, enthalpy, total and species mass in their variable density formulation are solved as previously presented in Sec. 2.2 and applying Eq. (3.1).

The particle interior volume is split into a gas (superscript G) and solid (superscript S) contribution, where the gas and solid volumes can be calculated from the porosity ε

$$V^G = V_{sphere} \cdot \varepsilon, \tag{3.14}$$

$$V^S = V_{sphere} \cdot (1 - \varepsilon), \tag{3.15}$$

and $V_{sphere} = V^G + V^S$. Total and individual species mass conservation is considered for the particle interior *solid phase* as

$$\frac{\partial[\rho^S(1-\varepsilon)]}{\partial t} = \sum_{i=1}^{N^S} \dot{\omega}_i^S, \tag{3.16}$$

$$\frac{\partial[\rho^S(1-\varepsilon)Y_i^S]}{\partial t} = \dot{\omega}_i^S, \tag{3.17}$$

with time t, density ρ, reaction rate $\dot{\omega}$, number of species N and species mass fraction Y. Similarly, for the particle interior *gas phase* applies

$$\frac{\partial(\rho^G\varepsilon)}{\partial t} + \nabla\cdot(\rho^G\boldsymbol{U}) = \sum_{j=1}^{N^G} \dot{\omega}_j^G, \tag{3.18}$$

$$\frac{\partial(\rho^G\varepsilon Y_j^G)}{\partial t} + \nabla\cdot(\rho^G Y_j^G\boldsymbol{U}) = -\nabla\cdot(\rho^G Y_j^G\boldsymbol{v}_j^c) + \dot{\omega}_j^G, \tag{3.19}$$

with the local density of the gas enclosed inside the particle ρ^G (varying with the ideal gas law), the local intra-particle velocity $\boldsymbol{U}$ [45] and the correction diffusion velocities $\boldsymbol{v}_j^c$. Note that the subscripts i and j have been used to distinguish between solid and fluid species. The correction diffusion velocities are introduced to enforce mass conservation according to [23],

$$\boldsymbol{v}_j^c = \boldsymbol{v}_j + \boldsymbol{v}^c, \tag{3.20}$$

$$\boldsymbol{v}_j = -\frac{D_{eff,j}}{Y_j^G}\nabla Y_j^G, \tag{3.21}$$

$$\boldsymbol{v}^c = -\sum_{j=1}^{N^G} \boldsymbol{v}_j, \tag{3.22}$$

where $\boldsymbol{v}_j$ includes both bulk and pore diffusion by considering an effective diffusion coefficient $D_{eff,j}$ and $\boldsymbol{v}^c$ is a velocity correction factor as introduced in [39]. The momentum conservation equation for the particle interior gas phase reads

$$\frac{\partial\rho^G\varepsilon\boldsymbol{U}}{\partial t} + \nabla\cdot(\rho^G\boldsymbol{U}\boldsymbol{U}) = -\nabla p + \nabla\cdot\boldsymbol{\tau} + \rho^G\boldsymbol{g} + \boldsymbol{S}, \tag{3.23}$$

with pressure p, gravity vector $\boldsymbol{g}$ and

$$\boldsymbol{\tau} = \mu^G\left[\nabla\boldsymbol{U} + (\nabla\boldsymbol{U})^T - \frac{2}{3}(\nabla\cdot\boldsymbol{U})\boldsymbol{I}\right], \tag{3.24}$$

where μ^G denotes dynamic viscosity. The momentum source term for porous media $\boldsymbol{S}$ in Eq. (3.23) is calculated according to the Darcy-Forchheimer law

$$\boldsymbol{S} = -\left(\mu^G \boldsymbol{Da} + \frac{1}{2}\rho^G ||\boldsymbol{U}|| \boldsymbol{F}\right) \boldsymbol{U}, \tag{3.25}$$

and affects the pressure drop inside the particle by means of a viscous and an inertial contribution, which are characterized by the Darcy $\boldsymbol{Da}$ and Forchheimer $\boldsymbol{F}$ tensors, respectively. Due to the low particle Reynolds numbers considered when applying the model in this work, the inertial contribution is ignored [39]. $\boldsymbol{Da}$ represents the resistance against the flow of gas produced inside the porous medium, which enhances the intra-particle pressure gradients. Ranzi *et al.* [99] reported how the full momentum equations (Eq. (3.23)) can be simplified under the assumptions of steady-state and very low flow velocity, obtaining the widely used Darcy law for porous media. Here, the more general approach is employed to characterize the evolution of a solid fuel particle, which is governed by the fundamental conservation equations of mass, momentum, and energy, and accounts for porous media effects via porosity and Darcy-Forchheimer source terms. Particle interior heat transfer occurs by conduction and (gas) convection. The amount of gas instantaneously contained inside the particle pores is limited and, considering the very large surface area of the porous medium, it is reasonable to consider that the gas instantaneously reaches the temperature of the solid. This assumption does not imply that the particle internal thermal gradients are neglected, but only that locally the temperature of the solid and the gas contained inside the pores is the same. In fact, the heat capacity $\rho^S c_p^S$ of the solid is much larger than that of the gas formed inside the particle. Thus, local thermal equilibrium is assumed between the co-existing solid and gas phase and a unique temperature field for the porous medium is obtained solving the equation

$$c_p^G \frac{\partial(\rho^G \varepsilon T)}{\partial t} + c_p^G \nabla \cdot (\rho^G \boldsymbol{U} T) + c_p^S \frac{\partial[\rho^S (1-\varepsilon) T]}{\partial t} = \nabla \cdot (\lambda_{eff} \nabla T) + \dot{Q}_R\,, \tag{3.26}$$

with temperature T, heat capacity c_p, effective thermal conductivity λ_{eff} and heat release by chemical reaction $\dot{Q}_R$. The density of the gas mixture ρ^G is calculated from the perfect gas law and all other transport properties are evaluated by applying the mixture averaging rules [27].

3.2.2 Boundary Conditions

A set of boundary conditions at the (spherical) interface between the particle interior and exterior needs to be applied. Atmospheric conditions for total pressure and the equivalence of the convective fluxes at both sides of the interface are enforced. The gaseous species mass fractions and temperature need to satisfy the following equivalence of fluxes at both sides of the interface

$$\rho^G D_{eff,j} \frac{\partial Y_j^G}{\partial r}\bigg|_{\text{int}} = \rho^G D_j \frac{\partial Y_j^G}{\partial r}\bigg|_{\text{ext}}, \tag{3.27}$$

and

$$\lambda_{eff} \frac{\partial T}{\partial r}\bigg|_{\text{int}} = \lambda^G \frac{\partial T}{\partial r}\bigg|_{\text{ext}} + Q_{r,p}, \quad \text{with} \quad Q_{r,p} = -\frac{\epsilon_p}{2(2-\epsilon_p)}(4\sigma T_p^4 - G_p). \tag{3.28}$$

As discussed in Sec. 3.1.1, a sensitivity study within the full range $0 \leqslant \epsilon_p \leqslant 1$ did not reveal any significant influence for the studied particle configurations. Moreover, for this detailed model, test runs including $Q_{r,p}$ have been conducted and did not show any significant role of it for ignition since, up to the ignition point, temperature levels in the particle vicinity are comparatively low. After ignition, radiative effects become more important, especially in the presence of heterogeneous chemistry. In this work though, the detailed model is applied attempting at reproducing experimental measurements which are available only for the ignition delay, whereas no reference data is available for the subsequent combustion phase. Therefore, also for the detailed, multi-step approach the term $Q_{r,p}$ in Eq. (3.28) has been omitted from the DNS. Gas phase radiation is again included by the P1-approximation [22, 78], using absorption and emission coefficients for the continuous phase. By imposing the equivalence of the convective fluxes across the interface, the convective contributions on both sides cancel out and therefore do not directly appear in Eqs. (3.27) and (3.28). A reaction source term is also not included in Eqs. (3.27) and (3.28) since reactions do not occur on the surface but are purely volume-based instead.

3.2.3 Physical Properties

The thermophysical and transport properties of all species involved in the conversion process are obtained from established databases [18] as previously reported in [39, 72]. Due to the limited availability of experimental data regarding the heat capacity, thermal and (effective) mass diffusivity of the solid phase, simple models are assumed

here. The heat capacity c_p^S of the solid species contained in the coal is assumed to be constant and equal to the nominal value for the coal of interest. The effective thermal conductivity λ_{eff} of the porous medium is obtained as a linear combination of the gas and solid contributions

$$\lambda_{eff} = \varepsilon\lambda^G + (1-\varepsilon)\lambda^S, \tag{3.29}$$

where for λ^S the nominal value of the given coal is considered. The effective pore diffusion coefficients are evaluated as in [73]

$$D_{eff,j} = \left[\frac{1}{D_j} + \frac{1}{D_j^{Kn}}\right]^{-1} \cdot \frac{\varepsilon}{\tau^2}, \tag{3.30}$$

where D_j and D_j^{Kn} are the molecular and Knudsen diffusivities and τ is the local tortuosity. The Knudsen diffusivity is calculated as

$$D_j^{Kn} = \frac{d_{por}}{3}\sqrt{\frac{8R_uT}{\pi M_j}}, \tag{3.31}$$

with the mean pore diameter $d_{por} = 0.3\mu$m as estimated in [73] for bituminous coal, the universal gas constant R_u and species j molar mass M_j.

During pyrolysis the solid particle undergoes radical changes of its internal structure due to drying, devolatilization and char conversion. A pyrolysis regime analysis was conducted based on Biot and Pyrolysis numbers according to Paulsen *et al.* [90] for the investigated case. For the sake of simplicity, the rate of the initial decomposition of reference COAL1 (see Sec. 3.2.4) was used as being representative of coal pyrolysis. The analysis revealed that the pyrolysis regime for the present case is *kinetically-limited isothermal*, but very close to the boundary of the region where internal temperature gradients begin to become important. In the *kinetically-limited isothermal* regime a thermally thin particle has limited internal temperature gradients during pyrolysis and the chemical reactions take place uniformly throughout its volume. For these conditions the mass loss results in an increase of the porosity ε without variations of the particle size [39]. This assumption is sufficiently robust in the case of coal particles which are subjected to modest shrinking during devolatilization. Therefore mass loss is included by assuming a linear increase of the particle porosity ε with particle conversion χ [73]

$$\chi = 1 - \frac{m^S}{m_0^S}, \tag{3.32}$$

$$\varepsilon = \varepsilon_0 + \chi(1 - \varepsilon_0), \tag{3.33}$$

where m^S and m_0^S are the current and initial mass of the solid phase and ε_0 is the initial porosity. The solid mass varies according to

$$\frac{dm^S}{dt} = \sum_{i=1}^{N^S} \dot{\omega}_i^S V^S, \tag{3.34}$$

Conversely, the tortuosity decreases linearly with particle conversion [73]

$$\tau = \tau_0 - \chi(\tau_0 - 1)\ . \tag{3.35}$$

3.2.4 Kinetic Model

A predictive, multi-step kinetic model for coal pyrolysis [119] and char conversion [73] is applied. The model is able to predict the thermal degradation of different coals across a wide range of operating conditions only requiring the elemental composition of the coal. While the physical properties are assigned to the coal as a whole, the chemical-kinetic properties of the coal of interest for a given problem are obtained by linear interpolation of the kinetic properties of three reference coals, i.e. three separate species evolving simultaneously. Here, Pittsburgh seam high-volatile bituminous coal is considered, the properties of which have been reported in Tab. 3.1. Table 3.4 shows its composition in terms of the reference coals COAL1, COAL2 and COAL3 defined in [119].

Tabelle 3.4: Reference coal distribution for the Pittsburgh bituminous coal [mass-%].

COAL1	COAL2	COAL3	ASH
27.90	49.41	12.69	10.00

The kinetic sub-mechanism describing the pyrolysis of the reference coals is based on the previous work of Sommariva *et al.* [119] and composed of 32 species and 36 reactions. The sub-mechanism for heterogeneous char reactions considers char combustion, char gasification and thermal annealing in a set of 8 species and 14 reactions with rates and heats of reaction based on the work of Maffei *et al.* [73]. The latter represents a volume-based approach. For the sake of simplicity, even the gasification reactions are volume-based as already pointed-out in [73]. The model also accounts for particle drying by means of a single kinetic rate law. The heterogeneous mechanisms are made available in Appendix B. The volatile matter released during pyrolysis is a complex mixture of light gases and heavy tars, the latter of which

are modeled as lumped species [119]. According to the different molecular structure and atomic composition, each of the lumped tar species released during coal devolatilization is split up into a limited number of compounds already available inside the detailed kinetic mechanism for the gas phase. Aromatic and oxygenated aromatic species are adopted: Methyl-naphthalene, Tetralin, Acenaphthylene, Coumaryl, Sinapaldehyde and a large PAH species, see Tab. 3.5. These species are selected in order to have the same chemical functionalities of the original tar species and their relative amount is calculated by solving a linear system representing the conservation of the C, H, O atomic balances.

Tabelle 3.5: Assignment of the lumped tar species from [119] to hydrocarbon species in the gas phase mechanism [mass-%].

VTAR1	25.8 $C_{10}H_{12}$ + 74.2 $C_{12}H_8$
VTAR2	22.4 $C_{10}H_7CH_3$ + 50.8 $C_{20}H_{10}$ + 26.8 $C_{11}H_{12}O_4$
VTAR3	9.7 $C_{10}H_7CH_3$ + 22.1 $C_{20}H_{10}$ + 27.3 $C_9H_{10}O_2$ + 40.8 $C_{11}H_{12}O_4$
BTX2	41.8 $C_{10}H_7CH_3$ + 58.2 $C_{10}H_{12}$

Finally, as mentioned in Sec. 3.1.2, the homogeneous gas-phase kinetics are described by using the POLIMI_TOT_1407 kinetic model. To limit the computing demand of the fully-resolved simulation, the complete mechanism was reduced by the CRECK group following a multi-step algorithm, based on flux and sensitivity analysis [120], which led this time to a final skeletal scheme with 76 species and 973 homogeneous reactions. The homogeneous reaction scheme is referenced in Appendix B as well.

3.2.5 Model Fidelity

It shall be noted here that the modeling approach described in Sec. 3.2, is relatively complex and that simpler model descriptions may suffice to recover experimental particle ignition delay times [128]. However, the results produced in Chap. 8 applying the comprehensive approach will show that even though the temperature is mostly uniform when moving from the particle core to its outer layers, temperature differences of up to 400K may be encountered near the surface (Fig. 8.4). Therefore, it seems reasonable to neglect particle shrinking since the reactions occur throughout the entire particle volume, leading to an increase in particle porosity at constant particle diameter, cf. Sec. 3.2.3. Yet, significant temperature and oxygen gradients (Fig. 8.4) can establish inside the particle and have an impact on the homogeneous and heterogeneous burning behavior. Therefore, the introduced model complication

can be fundamental for accurately modeling the physico-chemical phenomena occurring in- and outside the particle already for the conditions that will be presented in Chap. 8 (particle diameter $D_p = 0.1\text{mm}$). Moreover, even bigger effects are expected for larger particles, giving stronger incentives for the higher CPU cost of the detailed multi-step model for coal heterogeneous kinetics compared with simpler models.

Chapter 4

Numerical Approach

All data presented in this work have been generated with the CFD library OpenFOAM which has been extended to account for the coal models. This chapter provides a brief overview of the toolbox and of how the models described in Chap. 3 have been implemented in order to perform the DNS computations. In addition the OpenSMOKE++ library, used to interpret the thermophysical and transport properties of all species included in the detailed kinetic mechanisms, is is briefly introduced.

4.1 Open Source Library OpenFOAM

OpenFOAM is a C++ library developed in the 1990's at Imperial College London to numerically solve continuum mechanics problems [55, 148]. The name stands for "Open Source Field Operation and Manipulation" referring to the general public license (GPL) under which it is distributed. The free availability, along with the possibility to access and modify the source code, has made the toolbox particularly appealing both for industrial and research purposes. The CFD code uses the finite volume method (FVM) and is based on a variety of well established libraries for fluid dynamics problems, including combustion or turbulence modeling, starting from which users and developers can build suitable applications. These applications can be either solvers to run the calculations, or utilities for pre- or post-processing that allow for data manipulation enabling fast and flexible simulation preparation and results analysis. A schematic view of the overall structure of OpenFOAM is provided in Fig. 4.1. In particular the *templates* and *classes* structure available in C++ allows for the implementation of new models, combining existing modules and routines or creating new ones without altering the functionality and the structure of the existing models. Moreover OpenFOAM can deal with complex geometries as the

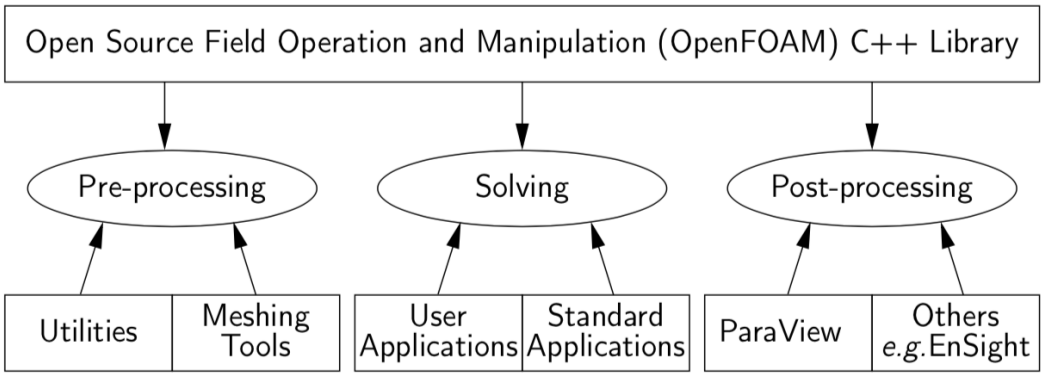

Abbildung 4.1: Overview of OpenFOAM structure [1]

discretization and parallelization are based on unstructured meshes that can also be subject to local refinement. For all the above reasons OpenFOAM has become increasingly popular and suitable for a wide range of studies, from pure research to industrially relevant applications.

4.1.1 OpenFOAM Standard Classes, Solvers and Utilities

OpenFOAM profits from the object-orientation of C++, since solvers and utility applications are based on the underlying *classes* and are coded with a syntax that reflects the actual differential equations that need to be solved. For example the balance equation of mixture fraction

$$\frac{\partial(\rho Z)}{\partial t} + \frac{\partial}{\partial x_i}(\rho U_i Z) = \frac{\partial}{\partial x_i}\left(\rho D_Z \frac{\partial Z}{\partial x_i}\right), \tag{4.1}$$

is implemented in OpenFOAM as

```
#include "fvCFD.H"
solve
(
fvm::ddt(rho,Z)
+ fvm::div(phi,Z)
- fvm::laplacian(rho*Dif,Z)
);
```

Here *fvm* represents the 'finite volume method' class that includes the numerics, handled by the member functions of the class, *ddt*, *div* and *laplacian*.

4.2 The OpenSMOKE++ Library

OpenSMOKE++ [26] is a numerical framework developed by the CRECK modeling group for the simulation of reacting systems with detailed kinetic mechanisms, including thousands of chemical species and reactions. It is implemented in object-oriented C++ and provides *classes* representing different components of a simulation, such as gas mixtures, reactors, kinetics models, equations of state, ODE integrators and reaction path diagrams. Profiting from a modular approach, the physical models can be assembled intuitively by creating and combining different *classes*. This leads to big advantages in terms of usability and extension of OpenSMOKE++ that can be easily customized for specific tasks and coupled to existing programs and CFD codes. OpenSMOKE++ capabilities range from the solution of ideal chemical reactors (plug-flow, batch, and jet stirred reactors), shock-tubes, rapid compression machines, to the modeling of multi-dimensional reacting flows for complex practical systems. The framework adopts advanced numerical techniques, e.g. efficient algorithms to evaluate reaction and formation rates, in order to reduce the computational cost of solving large kinetic mechanisms, without sacrificing the accuracy and the robustness of the calculations.

In the present work OpenSMOKE++ is used in the multi-step approach for heterogeneous coal conversion described in Sec. 3.2, to calculate the thermophysical and transport properties of all species involved in the conversion process (Sec. 3.2.3) and to interpret the detailed kinetic mechanism and solve the resulting system of reactions (Sec. 3.2.4).

In particular, a kinetic pre-processor reads a symbolic description of a reaction mechanism and extracts the needed thermodynamic and transport data for each species and the kinetic data for each reaction. The kinetic mechanism is then rewritten in an XML format which can be efficiently accessed and used while simulating the chemical reactor with an OpenSMOKE++ solver.

The thermodynamic properties of single chemical species, namely the specific heat, enthalpy and entropy, are calculated at constant pressure as functions of temperature with polynomial correlations following the approach proposed by Gordon and McBride [41]. The thermodynamic properties of the mixture are then evaluated by averaging the contributions of all species, weighted by their molar fraction, according to the Gibbs theorem.

The transport properties of the species are computed by using standard kinetic theory expressions, using a 4^{th}-order polynomial fitting to express the temperature

dependence, in order to speed up the evaluation of viscosity, thermal conductivity and mass diffusion [57].

Finally OpenSMOKE++ is also able to manage the elementary chemical reactions included in the detailed kinetic mechanism, both reversible and irreversible, providing reaction rates as well as formation rates for the individual species, counting on a wide range of ODE solvers, which are also suitable for stiff problems.

More information on the OpenSMOKE++ structure, its functionalities and procedures can be found in [26].

4.3 Customized Code for Coal Pyrolysis & Combustion

In this section the CFD codes used to perform DNS of pulverized coal particle devolatilization and combustion are presented. Two modeling approaches have been introduced in Chap. 3, mainly differing for the description of the solid particle and coal kinetics, which have led to the development of two different numerical codes.

In the first approach the carrier gas mixture is fully resolved, whereas the coal particles affect the gas phase by means of boundary conditions at the interface. Devolatilization is described by a single kinetic rate law and the particle is assumed to release a simplified mixture of light gases and tars up to C_6H_6. As discussed in Sec. 3.1.2, this allows to use a significantly reduced version of the comprehensive POLIMI_TOT_1407 kinetic model. The code based on this simplified approach is validated in Chap. 5 against available experimental data and is then used in Chaps. 6 and 7 to investigate particle arrays in laminar and turbulent flow, extracting characteristic particle conditions from a reference LES of a semi-industrial coal furnace.

The second approach alleviates the assumptions of single-step pyrolysis, fixed volatile composition and simplified particle interior properties, and it allows for the consideration of char conversion. The mass release rate and composition of species released from the particle are dynamically predicted. A detailed description of the particle interior is introduced, based on time-evolving porosity and tortuosity which control the gas flow formed inside the particle during the thermal conversion of the coal. This is achieved by using a multi-region code, fully resolving both the solid particle and the surrounding gas phase. In order to handle the complex homogeneous and heterogeneous kinetics, the code is coupled to OpenSMOKE++. Due to the resulting complexity and computational cost, the comprehensive code is applied in Chap. 8 to a relatively simple setup, attempting to predict ignition, volatile flame

combustion and char conversion of single coal particles in laminar flow.

The respective mathematical models behind the two approaches have been described in Sec. 3.1 and Sec. 3.2. In the following sections, details on the implementation of both systems of equations are provided and the code flow is shown, highlighting the order in which operations are executed.

4.3.1 *coalReactingFoam*

As first OpenFOAM implementation example, the user-defined solver and libraries based on the model introduced in Sec. 3.1 are considered here. These have been used to produce the results discussed in Chaps. 5, 6 and 7.

Figure 4.2 provides a flow chart for the solver with some linked routines, both from standard OpenFOAM as well as user-defined libraries. After the initialization of the geometry, of the simulation time settings, and of the computational fields with the local discretization of all physical quantities, the solver starts with the evaluation of the reaction rates and the solution of the system of differential equations that provides the source terms for species and sensible enthalpy transport equations.

After that, the momentum (Eq. (3.3)), mass continuity (Eq. (3.2)), species mass fractions (Eq. (3.6)), mixture fraction (Eq. (3.7)) and sensible enthalpy (Eq. (3.5)) equations are solved, without any modeling, using the finite volume method. Pressure-velocity (and -density) coupling is performed using OpenFOAM's *hybrid approach* [50].

According to the purely Eulerian formulation introduced in Sec. 3.1, the coupling between the different phases (gas and solid) is enforced by boundary conditions at the particle surface describing heterogeneous processes. Therefore, the momentum equation requires the velocity at the particle surface which corresponds to the rate of release of the volatile matter. This is expressed via the single first order rate presented in Eq. (3.12).

In Eq. (3.12) the devolatilization rate is a function of the temperature of the particle T_p. The latter is calculated by solving Eq. (3.10) along with Eq. (3.11) which also sets the particle boundary condition for the enthalpy equation. The obtained devolatilization rate is then used to update the species mass fractions at the particle surface according to Eq. (3.13). Moreover, the solver keeps track of the mass of volatiles which has been released comparing it to the available volatile mass in Eq. (3.12), leading to the end of the volatile yield once the volatile matter has been fully depleted.

Once the instantaneous mass fractions, enthalpy/temperature and other thermo-

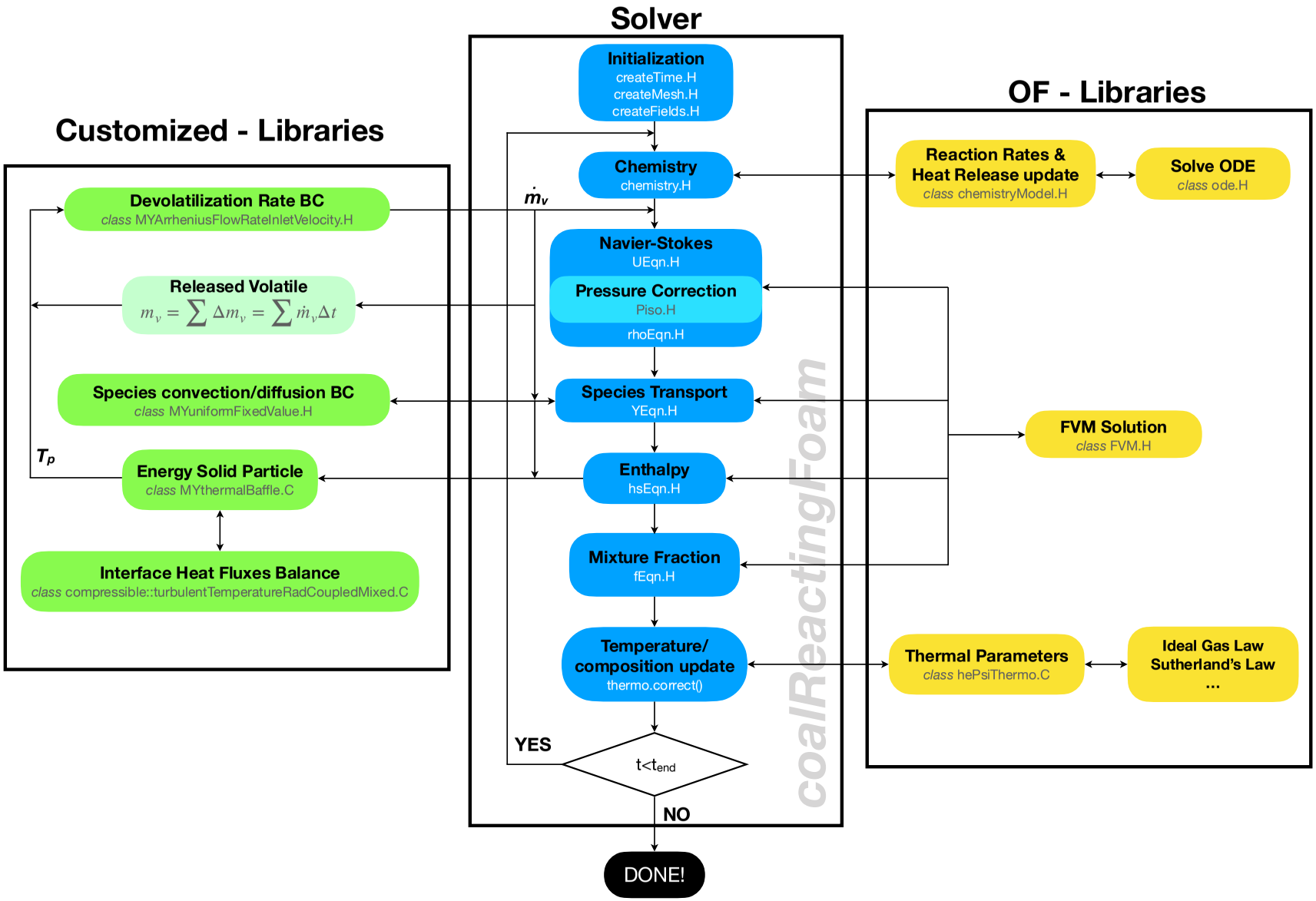

Abbildung 4.2: A simplified diagram of the *coalReactingFoam* solver for the DNS of pulverized coal devolatilization and volatile combustion

physical parameters have been calculated, density and viscosity are updated by means of the ideal gas law and Sutherland's law, respectively. The time loop iterates until the prescribed end time is reached.

Further details on the OpenFOAM implementation of the customized libraries shown in Fig. 4.2 are provided in Appendix C.

4.3.2 *coalSMOKE-MR*

The solver structure described above represents the basic logic with which also the solver *coalSMOKE-MR* (Multi-Region) is implemented, by including all the equations introduced in Sec. 3.2 and combining elements from both OpenFOAM and OpenSMOKE++. Figure 4.3 shows the solver flow chart. The multi-phase solver operates now on two different regions, solid and gaseous. The governing equations are enforced equally on both sides, so that the particle does not only provide boundary conditions for the fluid by means of simplified models (as in *coalReactingFoam*) but it is fully resolved instead. Therefore, the solid description is much more complex and includes detailed physical properties of the particle, such as porosity and tortuosity, that the solver calculates in *propertiesSolidRegions.H* by means of Eqs. (3.33) and (3.35), respectively. Moreover, the thermophysical and transport properties of all solid and gaseous species involved in the coal conversion process are calculated and updated by OpenSMOKE++ which interprets the *ThermodynamicsMap* and *TransportMap*, produced beforehand by its kinetic pre-processor. This leads, for example, to the calculation of the effective thermal conductivity λ_{eff} and pore diffusion coefficients $D_{eff,j}$ for the solid region according to Eqs. (3.29) and (3.30), respectively. This information made available by OpenSMOKE++ is then passed to the OpenFOAM solver to be used in the following equations. The chemistry for both the homogeneous and heterogeneous reactions is modeled with batch reactors for the solid and the fluid. OpenSMOKE++ provides at each state the reaction rates and the species production rates interpreting the *KineticsMap*. In the solid region the chemical reactions convert the solid mass either into other solid species, eventually forming char, or into volatile matter, leading to an increase of the mass of gas in the solid region. These species are transported through the porous particle via pressure gradients and the Darcy-Forchheimer source terms which are calculated by the corresponding OpenFOAM porosity model as defined in Eq. (3.25). Volatiles can be released in the fluid region surrounding the particle as they reach the interface. Since both the fluid and solid regions are fully resolved and mutually exchange mass, momentum and energy, the interface boundary conditions reduce to mass and heat

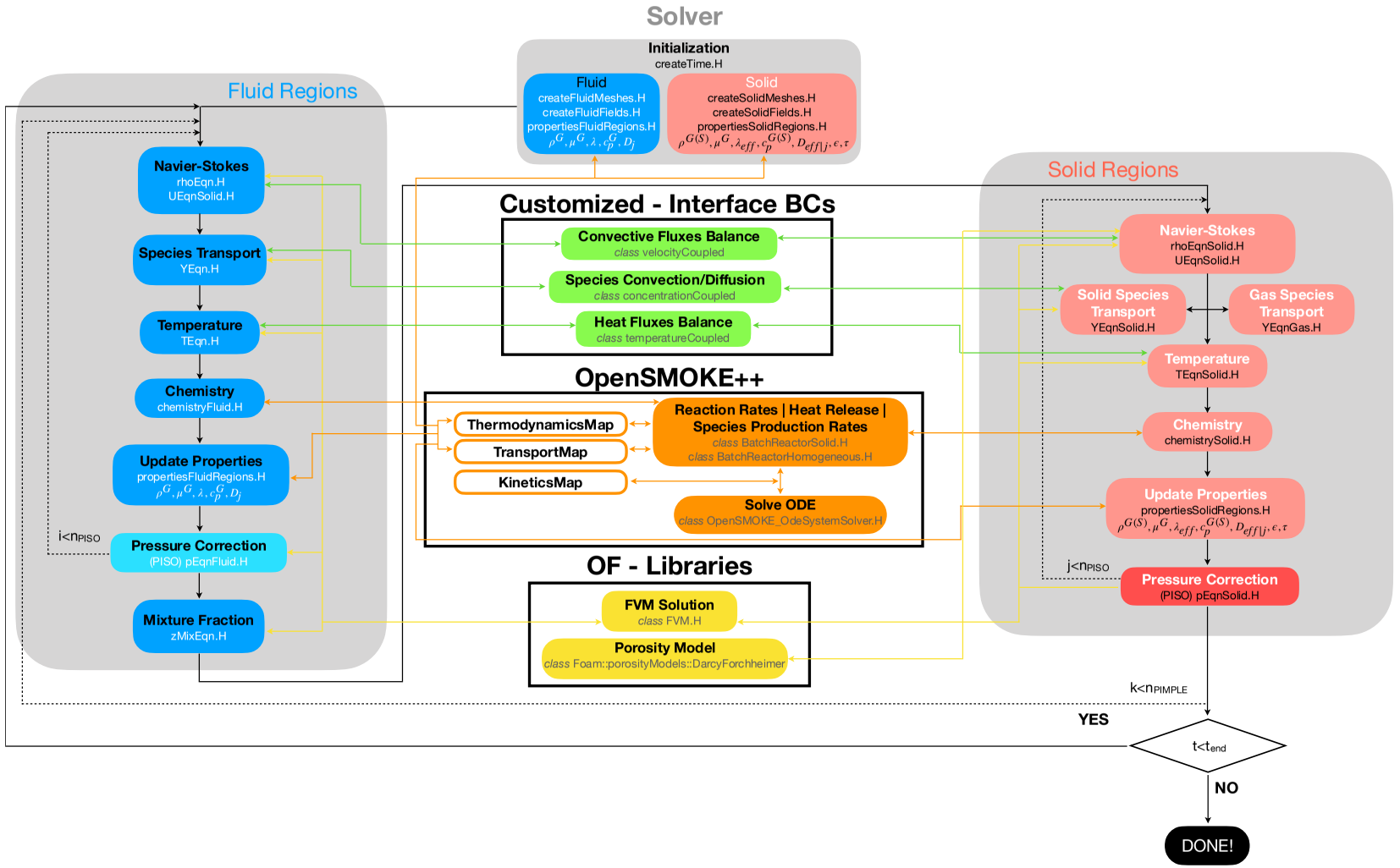

Abbildung 4.3: A simplified diagram of the *coalSMOKE-MR* multi-region solver for the DNS of pulverized coal combustion

flux balances. The numerical solution of all transport equations is left to standard OpenFOAM. The pressure correction occurs inside each region by means of a PISO (Pressure Implicit Splitting Operator) loop until pressure and velocity converge, whereas a PIMPLE (Pressure Implicit Method for Pressure-Linked Equations) loop ensures the consistency of the boundaries [136].

4.4 Numerical Discretization

The governing equations are discretized on a structured three-dimensional hexahedral grid by means of a finite volume method (FVM) [31, 136]. The such obtained algebraic system of equations is then solved in each cell. The cell value of a certain variable represents the value assumed in the center of the cell. Interpolation schemes are required to obtain the variable values at the cell surface that are necessary for the calculation of the fluxes. For a generic variable ϕ the integral form of its balance equation over a control volume V reads

$$\int_V \frac{\partial(\rho\phi)}{\partial t} dV + \int_V \frac{\partial(\rho U_i \phi)}{\partial x_i} dV = \int_V \frac{\partial}{\partial x_i} \left(\rho D_\phi \frac{\partial \phi}{\partial x_i} \right) dV + \int_V \omega_\phi dV, \tag{4.2}$$

with D_ϕ being the diffusivity and ω_ϕ the source term of the scalar ϕ. Using the Gauss theorem, volume integrals of convection and diffusion can be transformed into surface integrals of fluxes across the surface delimiting the control volume. Moreover, the last term on the RHS can be approximated by the product of the cell averaged source term and the cell volume. Hence Eq. (4.2) can be rewritten as

$$\int_V \frac{\partial(\rho\phi)}{\partial t} dV + \int_S (\rho U_i \phi) n_i dS = \int_S \left(\rho D_\phi \frac{\partial \phi}{\partial x_i} \right) n_i dS + \omega_\phi V, \tag{4.3}$$

where n_i is the normal vector to the cell face. The first term on the LHS of Eq. (4.3) is the unsteady term and temporal discretization schemes are necessary in order to solve it. For the calculations performed in the present work, first order implicit Euler and second order backward time discretization schemes [96] are employed, along with a variable time step controlled by the Courant-Friedrichs-Lewy (CFL) criterion for stability and accuracy [47].

The surface integrated convection and diffusion contributions are discretized by second order total variation diminishing (TVD) and central difference (CDS) spatial schemes [47, 49]. In particular the adopted TVD scheme is stabilized with the introduction of a Sweby limiter [55, 124]. Specialized limited TVD is required for

bounded scalars like the species mass fractions.

Most of the results presented in this work are for laminar flow such that the typical numerics requirements of DNS do not fully apply, as long as full resolution of all relevant scales is ensured. For the turbulent results presented in Sec. 7.2.2 great care has been taken to also sufficiently resolve the Kolmogorov scales and previous work [137] has shown that OpenFOAM's second order numerics are good enough to capture turbulence compared with high order codes as long as the grid is sufficiently refined. The turbulent calculations performed in this work fully resolve the thin boundary layer surrounding the particles, which is much thinner than the estimated Kolmogorov length scale. Hence, the latter does not represent the limiting factor in terms of resolution requirements. The DNS setup and the resolution requirements for the turbulent cases will be discussed in detail in Secs. 6.1.2 and 7.1.

Chapter 5

Single Particle Ignition in Air- and Oxy-Atmospheres

In this chapter the results of resolved laminar flow simulations are presented in order to discuss the effect of enhanced oxygen levels on single coal particle ignition. The numerical results are compared against available experimental data from the literature [79]. The reference experiment is presented at first, then the numerical configuration reproducing the experimental setup is described. The modeling approach validated in this chapter is the one presented in Sec. 3.1. Devolatilization is described by a generic boundary condition at the particle surface that accounts for both convective and diffusive phenomena during pyrolysis (Eq. (3.13)). The heating rate history of the particle is obtained by solving for intra-particle heat transfer and heat exchange between the particle and its surroundings (Eqs. (3.10) and (3.11)). The time evolution of volatile release is captured by using the particle mean temperature to calculate the devolatilization rate from a single kinetic rate law with CPD-fitted parameters (Eq. (3.12)). The assumed volatile composition includes light gases and larger hydrocarbons up to C_6H_6 to represent tars as shown in Tab. 3.3. A skeletal kinetic mechanism for pyrolysis and oxidation of hydrocarbon and oxygenated fuels containing 52 species and 452 reactions is used to describe homogeneous chemistry (Sec. 3.1.2 and Appendix B). Particle heat-up, pyrolysis, ignition and envelope flame stabilization are characterized in four gas atmospheres differing in oxygen content and the use of either N_2 or CO_2 as balance gas. The results presented in this chapter have been published in *Fuel* 186:285-292 (2016) [128].

5.1 Experimental and Numerical Configuration

5.1.1 Experimental

In the experiments by Molina & Shaddix [79] particles of Pittsburgh seam high-volatile bituminous coal with a mean diameter of 0.1mm were injected in the laminar co-flow of combustion products from a Hencken burner at a nominal feeding rate of 0.02g/min. The burner dimensions and main operating parameters are given in [79]. The proximate and ultimate analysis of the Pittsburgh seam high-volatile bituminous coal have been already provided in Tab. 3.1. The effect of CO_2 on coal ignition was evaluated by performing experiments in mixtures with N_2 or CO_2 as a balance gas at oxygen concentrations of 21 and 30% by volume. Table 5.1 shows the set of gas compositions.

Tabelle 5.1: Experimental balance gas compositions (mol%) [79]. The stoichiometric mixture fraction Z_{st} following from the assumed volatile matter composition of Tab. 3.3 is also given.

Case	N_2-21	N_2-30	CO_2-21	CO_2-30
O_2	21.00	30.00	21.00	30.00
N_2	65.08	56.00	0.00	0.00
CO_2	1.65	1.65	65.31	57.02
H_2O	12.27	12.34	13.69	12.98
Z_{st}	0.091	0.1238	0.0686	0.2197

Solid fuel particles were released at the furnace centerline and, due to the very slow coal supply, the experimentalists assumed that there was no interaction between individual particles and that single-particle ignition and combustion phenomena occurred. Ignition delay time was derived based on ensemble-averaged images of experimental CH* chemiluminescence.

5.1.2 Computational Configuration

To model the experimental campaign, simulations of particle heating, devolatilization, ignition and envelope flame stabilization are performed. A characteristic cell width of 0.02 particle diameters (D_p=0.1mm) in the vicinity of the particle ensures that the boundary layer is well resolved and all transport processes are accurately captured. Figure 5.1 shows the two-dimensional axisymmetric domain, which is 100

particle diameters long and extends 1/3 of its length in the cross-stream direction. The particle is positioned at 1/3 of the total length of the domain, which is

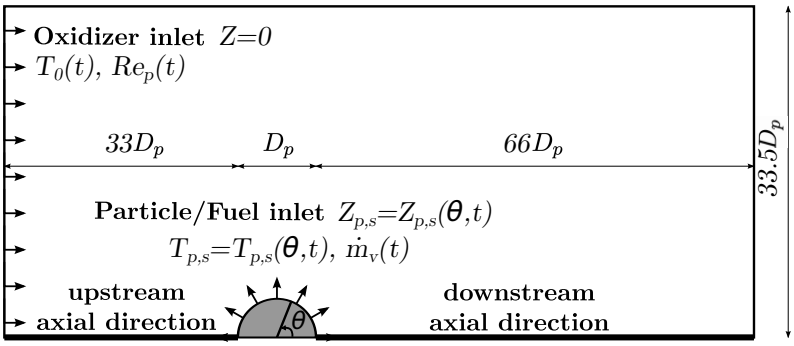

Abbildung 5.1: Computational domain for the resolved laminar simulation.

a 5° wedge. The wedge geometry was chosen to recover a fully spherical particle upon rotation about the axis of symmetry of the (laminar) flow. A computational grid containing 34,000 hexahedral cells produced consistent results with respect to both modified domain dimensions and mesh refinement. Simulations using twice the number of grid points resulted in changes of absolute ignition delay time below 1%, whereas a reduction to 1/10 of the present resolution resulted in differences of less than 5%. The domain and grid resolution used for the reacting case was additionally validated by calculating the drag coefficient C_D of the laminar flow of cold air past a sphere. The results showed the correct scaling of C_D with inverse Reynolds number for the range of Re_p relevant for the reacting case. The interior of the solid particle is meshed with 4,800 cells and further grid refinement of the solid region did not change the results. The mixture of hot products enters the domain at the left boundary with a prescribed constant composition (Tab. 5.1) and time-variant temperature and relative velocity. Vascellari *et al.* [135] performed a separate Euler-Lagrange simulation of the particle trajectory and the particle heating for the same burner configuration. The results were used in [127, 135] as transient boundary conditions for the particle Reynolds number $Re_p = U_{rel}\, D_p/\nu$, particle surface temperature $T_{p,s}$, oxidizer temperature T_0 and devolatilization rate $\dot{m}_v$ for a subsequent resolved laminar simulation. Here, T_0 and $Re_p = f(U_{rel})$ (i.e. the time-variant gas phase environment) are taken from the same Euler-Lagrange simulation of the burner [135], see Fig. 5.2, and set uniformly across the inlet plane of the simulation domain. The particle temperature T_p (therefore $T_{p,s}$ and $\overline{T}_p$) and $\dot{m}_v$ are, however, directly calculated from Eqs. (3.10)-(3.13) at runtime of the resolved simulation. An alternative, simplified estimation of Re_p based on the relative velocity taken as the

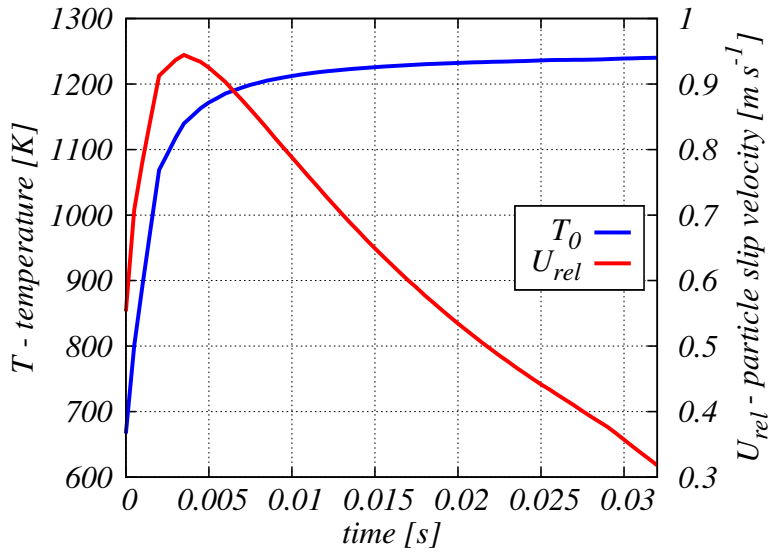

Abbildung 5.2: Particle slip velocity U_{rel} and oxidizer temperature T_0 from the Euler-Lagrange simulation of the burner [135], which are used as transient inlet conditions for the resolved laminar simulation.

terminal slip velocity of a particle in Stokes flow was also tested, but resulted in substantially lower relative velocities and in turn slower particle heating and substantial over-predictions of ignition delay. The initial conditions for the interior of the simulation domain are obtained by setting the values from the inlet boundary condition for the gas species concentrations (Tab. 5.1), temperature and velocity (Fig. 5.2, t=0) uniformly inside the domain, where the axial velocity component is set to U_{rel} and the cross-stream component is equal to zero. The actual value of the transient T_0 reaches the particle surface in less than 5ms. Since after about 15ms, T_0(t) has already reached an asymptotic value, this delay does not affect the ignition delay time predicted for the particles. The total mass of volatiles that the particle can release has been calculated based on $\rho_c = 1400$ kg/m^3 and the coal's proximate analysis (Tab. 3.1). However, the CPD results used to determine the total volatile yield at high temperature give a substantially higher value than the proximate analysis with its significantly different standard heating conditions. The CPD value of 54.75% (daf) volatile matter is used to calculate m_v^*. The devolatilization rate parameters $A_v = 72054.9$ s^{-1} and $E_v = 54.285$ kJ/mol are obtained by fitting the CPD volatile release curves to the functional form of Eq. (3.12). For the solid coal particle $c_{p,c} = 1680$ J/(kg·K) and $\lambda_c = 0.3$ W/(m·K) are considered, with a heat of devolatilization of Δh_v=0.267 MJ/kg. The initial particle temperature T_p^0 is set to 500K to account for pre-heating by the flame as the particle is injected into the burner. This temperature is assumed in the absence of a measured value and the sensitivity of

the results to T_p^0 are reported in Sec. 5.2.2. The simulations are performed using the in-house solver based on OpenFOAM v2.4.x, presented in Sec. 4.3.1. After testing a wide range of both fixed and variable time step sizes (Courant numbers, Co) a variable time step is used and $Co \leqslant 0.3$ is enforced for stability and accuracy in all simulations. The chemistry solver is however subject to further sub-stepping and not directly affected by Co. Simulations are typically run on 48 Opteron cores over the course of approximately 20 hours to reach ignition.

5.2 Results and Discussion

5.2.1 Experimental and Numerical Comparison

The discussion of the results is centered around a reference case defined as the experimental condition N_2-21 of [79]. Some of the aspects showed and discussed during the analysis of this reference case also characterize the other three cases that differ only regarding their mixture composition as described in Sec. 5.1. Figure 5.3 shows temperature, CH mass fraction contours and iso-lines of mixture fraction at selected characteristic times from the resolved laminar simulation of the reference case N_2-21. For N_2-21 ignition occurs at around 28ms, which is consistent with the experimen-

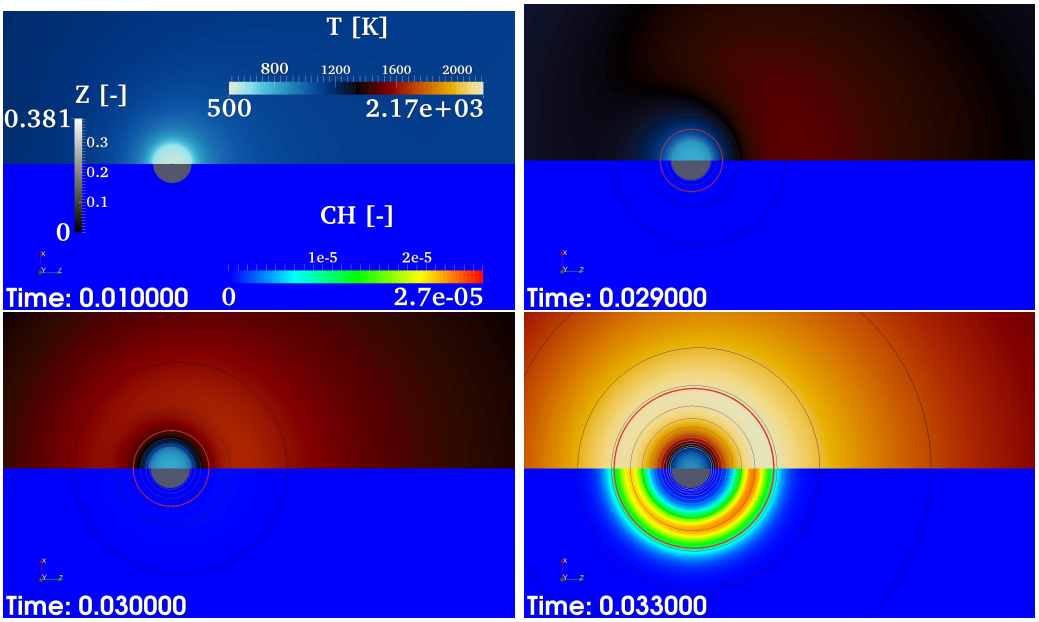

Abbildung 5.3: Temperature (top half of each frame), Y_{CH} (bottom half) contours, and mixture fraction iso-lines in gray-scale (stoichiometric condition, $Z_{st}^{(N_2-21)}$=0.091, in red) at selected times during ignition for case N_2-21.

tally observed ignition delay. During ignition the temperature rapidly increases in the downstream wake region behind the particle, where the gradients of mixture fraction are smaller and therefore scalar dissipation is lower than upstream of the particle. In agreement with previous simulations [127, 135] ignition occurs on the downstream side and for lean conditions, and the flame rapidly propagates towards the richer mixtures in the vicinity of the particle, enveloping the entire particle as shown in the sequence in Fig. 5.3 for the example of N_2-21, but representative for all four cases. As can be seen from Fig. 5.3 at the given Reynolds number (initially $Re_p = 0.8$, further decreasing to zero) the envelope flame is nearly spherical such that after ignition the particle is heated uniformly from all sides. As a result, there is no appreciable dependence of the reacting scalar fields on the angular coordinate Θ near the particle surface and only single surface values are reported. Distributions of temperature and scalar dissipation rate in mixture fraction space, extracted along the downstream axial coordinate at different times, are presented in Fig. 5.4 for the two N_2 atmospheres (similar results are obtained for the two CO_2 cases, but omitted from Fig. 5.4 for legibility).

The data are extracted along the downstream coordinate and plotted for small mixture fractions to allow for a clear description of the devolatilization, ignition and burning process, but this does not limit the analysis as the flame quickly envelopes the particle, cf. Fig. 5.3. In the initial phase of particle heating, volatile matter starts to be released, which can be seen by the appearance of the first non-zero mixture fraction in Fig. 5.4(a). Just before ignition, the far downstream regions of initial heat release correspond to the local temperature peaks at low mixture fraction in Figs 5.4(b) (N_2-30) and 5.4(c) (N_2-21). Lean downstream ignition for both cases can be observed from the rapidly increasing temperature peaks close to Z=0 for ignition temperatures around 1250K and low scalar dissipation rates of the order of $0.1s^{-1}$. The absolute time of this thermal runaway depends on the surrounding gas composition, as discussed below. After ignition, the temperature peaks propagate from the remote particle wake towards the particle surface (i.e. richer mixtures) and the envelope flames stabilize at a stand-off distance of approximately 2 particle diameters from the surface, with their temperature peaks slightly rich of stoichiometric, Fig. 5.4(d). During the subsequent period of stable volatile combustion the temperature peaks remain near Z_{st} and the peaks are higher for higher O_2 concentrations, Fig. 5.4(d). After extinction, which quickly occurs after the particle has fully released its volatile matter content, the (volatile) mixture fraction becomes zero and the profiles collapse towards $Z = 0$ (omitted from Fig. 5.4 as the focus is on ignition).

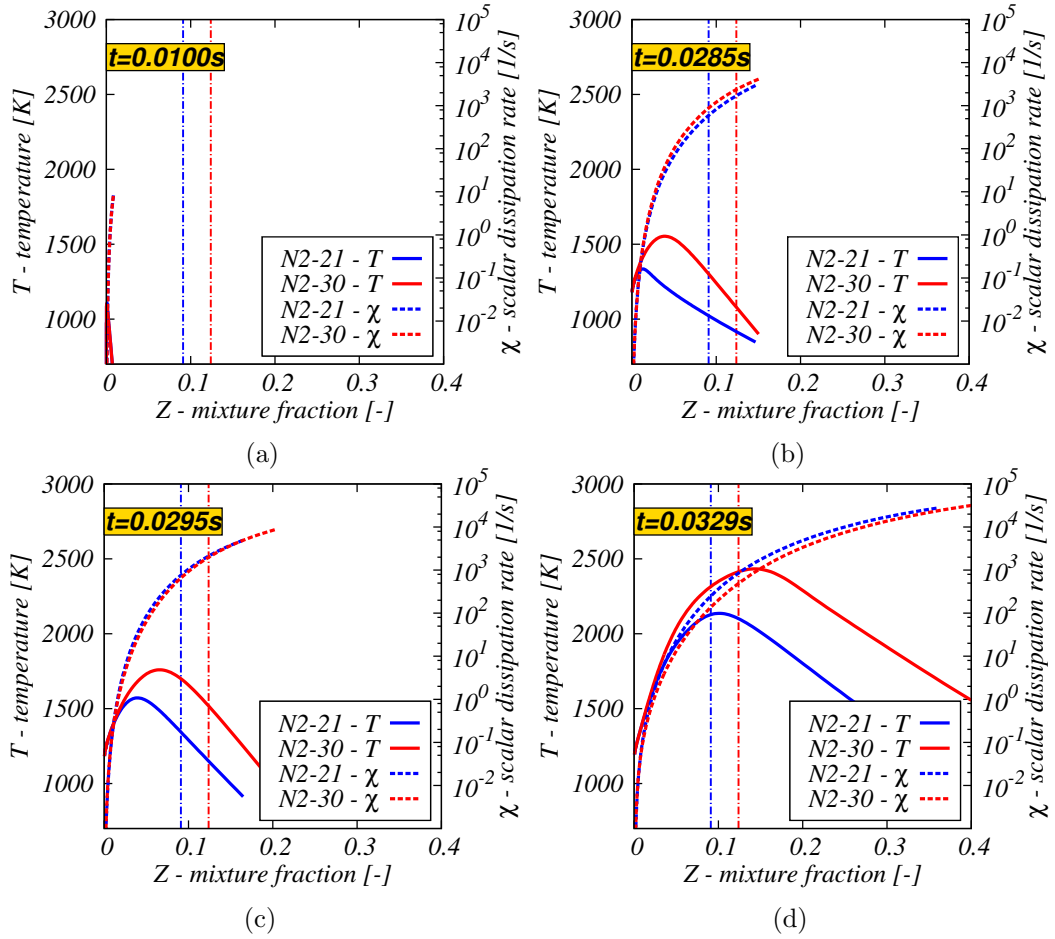

Abbildung 5.4: Profiles of temperature (continuous) and scalar dissipation rate (dashed) across mixture fraction space, extracted along the downstream axial coordinate at selected times for cases N_2-21 (blue) and N_2-30 (red). The vertical dash-dotted lines indicate the corresponding stoichiometric mixture fraction values Z_{st}, (cf. Tab. 5.1).

Numerically calculated ignition delay times are extracted from the resolved laminar simulations similarly to the experimental signal acquisition, where ensemble-averaged CH* profiles along the burner centerline were analyzed and τ_{ign} was extracted as the time of the first significant increase of the averaged CH* signal [79]. Zero-dimensional ignition delay times based on Y_{CH} and Y_{CH*} have been compared and since no significant difference was found, CH is taken as a valid approximation of CH*. In addition to CH, the temporal profiles of Y_{OH} and gas temperature have been considered to represent ignition delay. Two approaches for extracting ignition delay time from the simulation are tested. In the first approach the instantaneous two-dimensional scalar field is searched for the maximum value of the considered key quantity (CH, OH or T). The second approach reflects the fact that the simula-

tion domain corresponds to a numerical observation window following the particle's trajectory. This is accounted for by extracting the values of the key quantity along the centerline of the domain and mapping them in space to reflect their absolute position in the reference frame of the burner. The ensemble of mapped profiles extracted at different simulation times is then superimposed to obtain a cumulative distribution. Figure 5.5 shows temporal profiles of cumulative and maximum Y_{CH} in comparison with similarly extracted Y_{OH} data, along with a profile of the peak temperature within the domain, where all profiles have been normalized to a common peak of one. It can be observed that the cumulative profiles are narrower than the

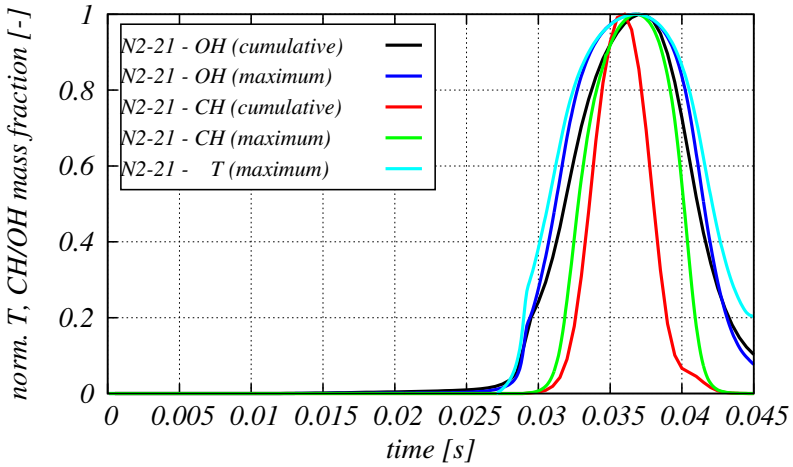

Abbildung 5.5: Comparison of maximum/cumulative CH, OH and peak temperature as indicators of τ_{ign}.

corresponding distributions based on the maximum values and that the time of the first increase of the respective quantity is shifted to slightly later times when using the cumulative perspective. The cross-comparison of CH, OH and T shows that the latter two quantities increase almost simultaneously, whereas the CH profiles increase slightly later. The overall uncertainty of extracting ignition delay based on the considered key quantities is approximately 4ms. To reflect this, the following comparison of ignition delay times for the different gas phase environments considers the bounds of the profiles shown in Fig. 5.5, namely T_{max} and $Y_{CH,cum}$. Experimental CH* signals and distributions of $Y_{CH,cum}$ and T_{max} from the simulations are shown in Fig. 5.6. For better comparability, the simulation data in Fig. 5.6(a) and Fig. 5.6(b) has been normalized by the corresponding experimental peaks, where the latter are no absolute values, but only a measure of relative signal intensity. Comparing Fig. 5.6 with 5.5 shows that the experimental trend of bell-shaped signal curves, with a steep initial increase towards a peak, followed by a gentle decrease when particles

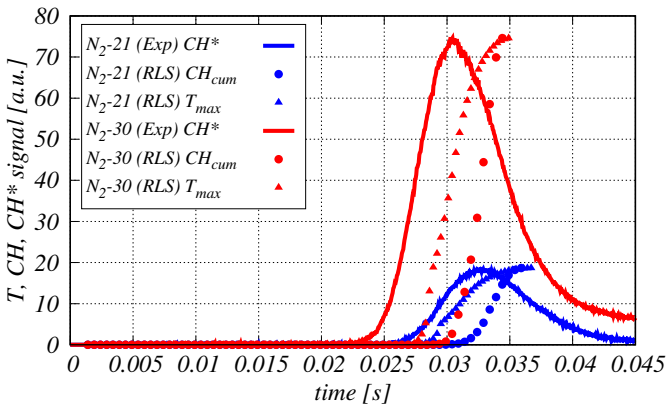

(a)

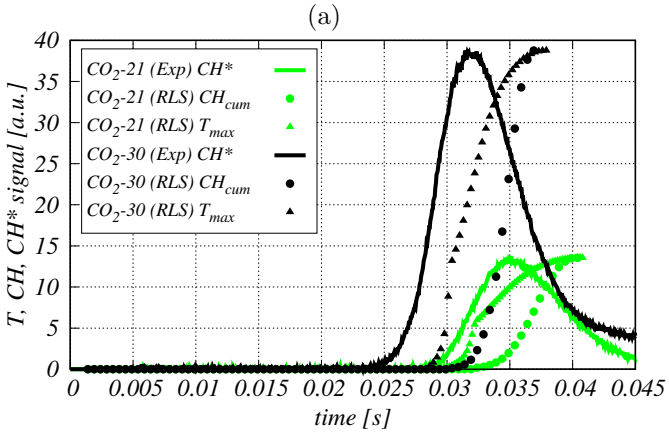

(b)

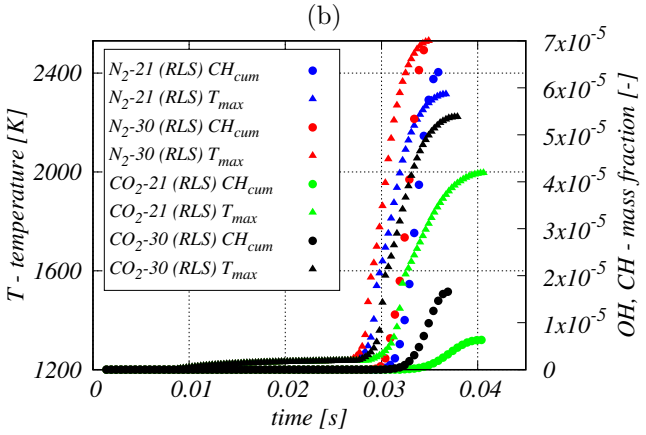

(c)

Abbildung 5.6: Ensemble-averaged experimental CH* signal intensity compared with normalized cumulative Y_{CH} and maximum temperature from the resolved laminar simulation (RLS) as a function of particle residence time for mixtures containing N_2 (a) and CO_2 (b) as balance gas. Original (not scaled) simulation profiles in (c).

cease to burn is captured qualitatively well in the simulation. However, as the exact shape of the experimental signal curves may be affected by more complex effects like char conversion and soot formation (not considered in the simulations), no attempt

is made here to make a quantitative comparison and the numerical profiles are only plotted up to their respective peak values, where ignition is important and secondary effects can be neglected. Figure 5.6 shows that the simulation correctly captures the experimental ignition trends for all four cases, albeit ignition occurs slightly later in the simulation, irrespective of the quantity chosen to determine ignition delay. The trends already shown in Fig. 5.5 for case N_2-21 are corroborated for all considered gas atmospheres, where the numerical CH profiles increase slightly later than temperature. Without scaling to the experimental peaks (Fig. 5.6(c)) the simulation data captures further experimental findings: For both employed balance gases oxygen-richer mixtures have higher temperature and CH* (CH) peaks, suggesting a higher heat release, as expected since enhanced oxygen levels yield more intense combustion. For the same oxygen content, mixtures in which N_2 concentration is predominant are characterized in both the experiments and the simulations by a stronger CH* (CH) production compared to the CO_2 cases. Figure 5.7 compares experimental and numerical values of τ_{ign}. To extract a (single) characteristic ignition delay time from the temporal profiles in Fig. 5.6, the x-intercept of a line tangent to the maximum temporal gradient of T_{max} or $Y_{CH,cum}$ is calculated. The extraction

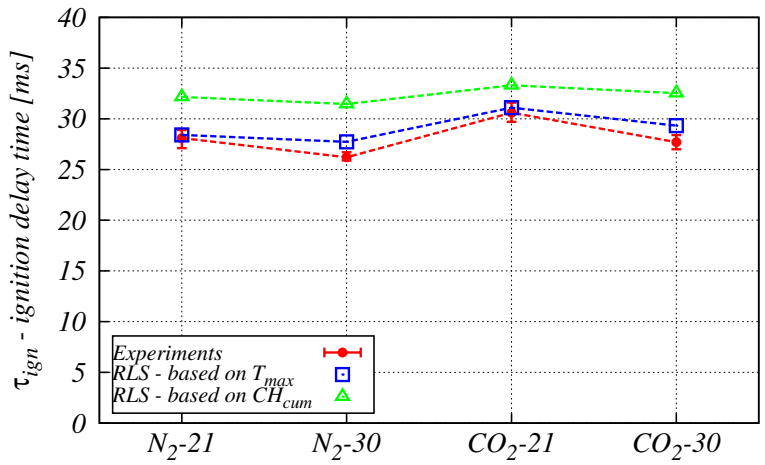

Abbildung 5.7: Ignition delay times measured in [79] and extracted from the resolved laminar simulation (RLS). Vertical bars represent 98% confidence statistical error in the experimental data.

of ignition delay based on T_{max} or $Y_{CH,cum}$ does not affect the relative comparison of the different gas environments. As already discussed for Fig. 5.6 using T_{max} leads to slightly earlier ignition compared to $Y_{CH,cum}$, a trend consistently captured for all four cases. Figure 5.7 shows that independent of the balance gas composition, enhanced O_2-levels lead to earlier ignition. The use of CO_2 instead of N_2 as an inert

gas delays ignition especially for 21%[vol] of oxygen. These trends can be explained by the different thermo-physical properties of the gas mixtures. As reported in [79] ignition delay time decreases as the mixture reactivity and heat release increase and increases in proportion with the product of heat capacity and density. In particular the higher (molar) specific heat and density of CO_2 with respect to N_2 leads to a longer ignition delay in CO_2-based mixtures. Increased O_2-levels correspond to decreased inert gas concentrations, the net effect of which is an increased characteristic reaction rate of the local mixture and shorter ignition delay.

5.2.2 Sensitivities

The absolute values of predicted ignition delay are found sensitive to (i) the gas phase chemistry description, (ii) the (transient) relative velocity/particle Reynolds number, and (iii) the initial temperature of the particle. The sensitivity to homogeneous chemistry was extensively discussed in [127]. Here, the assumptions on volatile composition and homogeneous chemistry have been considerably improved and an accurate, yet tractable skeletal description of gas phase kinetics has been adopted, cf. Sec. 3.1.2. The sensitivity to the relative velocity has been discussed in Sec. 5.1, where the accurate heating rate history of the particle from an auxiliary Euler-Lagrange simulation of the burner, see Fig. 5.2, has been found to be superior to simplified estimates of $Re_p = f(t)$. Figure 5.8 shows the particle surface temperature $T_{p,s}$ and the devolatilization rate as a function of particle residence time based on different initial particle temperatures T_p^0 for reference case N_2-21 during the ignition period. Upon injection into the hot gas mixture the particle surface temperature increases slowly at first, until the point of ignition, which is followed by a sudden increase of T_p due to heating by the envelope flame. The time of ignition corresponds to a rapid increase of devolatilization rate due to the exponential term in Eq. (3.12). Comparing the times of sudden increase of surface temperature and devolatilization rate Fig. 5.8 shows that with a variation of the initial particle temperature across a range $300\text{K} \leqslant T_p^0 \leqslant 500\text{K}$ an up to 25% larger ignition delay can be found when assuming no pre-heating (300K) compared to the assumed $T_p^0 = 500\text{K}$. Further sensitivities of the presented results relate to the coal properties, the assumed volatile matter composition and the rate parameters of the employed single kinetic rate law for devolatilization. Here, care has been taken to assume realistic coal properties, the volatile matter composition has been improved compared to previous work and the devolatilization rate parameters have been obtained by best fits to accurate CPD data. A significant level of model detail and generality will be added in Chap. 8, in

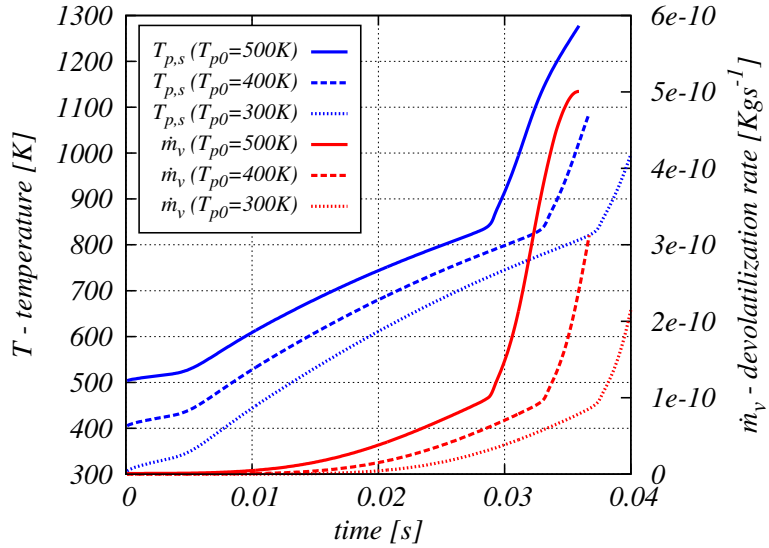

Abbildung 5.8: Particle surface temperature and devolatilization rate as a function of residence time for different initial particle temperatures T_p^0 (case N_2-21).

particular with regard to the particle interior description and heterogeneous kinetics, by applying the detailed kinetic model for the heterogeneous particle processes presented in Sec. 3.2.

5.3 Summary of Single Particle Ignition

An investigation of single coal particle ignition and combustion in four different hot gas environments, for which reliable experimental ignition delay times are available, is conducted by performing resolved laminar simulations of the flow, mixing and gas phase chemistry around the particle, extending the previous analyses in [127, 135].

The fully resolved approach presented in Sec. 3.1 is used in order to capture the phenomena occurring around the particle. A customized pyrolysis BC accounting for both convective and diffusive contributions during devolatilization is employed. Particle heating and devolatilization are described by solving for intra-particle heat transfer and heat exchange between the particle and its surroundings, and by using the particle mean temperature to calculate the devolatilization rate from a single rate kinetic law in the simulation. The assumed volatile composition includes both light gases and larger hydrocarbons to represent tars. Homogeneous chemistry is described by a 52 species/452 reactions chemical mechanism obtained by automated reduction from a detailed kinetic scheme. Results show a good agreement with the experimental ignition delay times, considering the intrinsic uncertainties in both coal experiments

and simulations. The trends of ignition delay times for the investigated mixtures characterized by different oxygen levels and the use of N_2 and CO_2 as balance gas are predicted by the simulation in accordance with the experimental evidence. It is found that absolute values of predicted ignition delay time are functions of potential particle preheating, particle Reynolds number and the reference quantity employed for extraction of ignition delay, but the relative trends for different gas phase environments remain correct.

Therefore, the developed approach has proved to be capable of recovering the experimental evidence and will be further used in the following Chaps. 6 and 7 to characterize coal particle array volatile combustion and flame interaction.

Chapter 6

Characterization of Transient and Group Effects in Coal Particle Volatile Combustion

The analysis of the heat-up, devolatilization, ignition and volatile combustion of single coal particles presented in Chap. 5 is extended in the present and the following chapters to particle arrays in laminar and turbulent flow by means of DNS. As discussed in Sec. 2.3.1.4, DNS refers to applying the Navier-Stokes equations to turbulent flow directly, i.e. without using any model for turbulence. This same approach can be also used in case of laminar flow, as already done in Chap. 5, in order to benefit from the full resolution that the direct solution of the governing equation for a very fine computational grid offers in the absence of any modeling. In this case the DNS reduces to resolved laminar simulation, a definition which has been extensively used in Chap. 5 to address the simulations. For sake of simplicity, in this and the next chapters the performed fully resolved simulations are simply referred to as DNS, in the presence of both laminar and turbulent flow, even though for the latter only the conventional definition fully applies.

The modeling approach presented in Sec. 3.1 has been proved capable of effectively predicting the experimental ignition delay time of single coal particles in hot laminar flows in Chap. 5. In this chapter the same approach is used to investigate the transient evolution and group effects of laminar flows, whereas the following Chap. 7 will report the effects of particle Reynolds number and turbulence. This time the characteristic particle conditions for DNS are extracted from an accompanying LES of a semi-industrial coal furnace [108] (cf. Sec. 6.1.1). The DNS fully resolves the particle boundary layers, the flame thickness and the smallest flow sca-

les. Particle heat-up is captured by solving for intra-particle heat transfer, while devolatilization and volatile combustion are described by specific particle boundary conditions and detailed homogeneous chemistry as described in Sec. 3.1. The transient physico-chemical processes around the particle(s) are characterized for a single particle first, before the interactions of several particles are studied. Transient effects at (mildly) larger particle Reynolds number than the one considered in Chap. 5 are also explored. The DNS covers the volume of a single cell of the reference LES, fully resolving mixing, scalar dissipation and the transient evolution of the reacting scalar fields at the particle surface, and thereby provides detailed LES sub-grid information. Moreover, this study for particle arrays allows for the characterization of coal combustion regimes. In fact, for decreasing inter-particle distance, volatile flame interactions can be observed and related to existing regime classifications [10]. Models for the mixture fraction distributions in the particle wake are also provided, based on the analogous problem of droplet evaporation. The results presented in this chapter have been published in *Fuel* 229:262-269 (2018) [129].

6.1 Computational Configuration

The DNS configuration reproduces the typical conditions that coal particles experience inside a furnace after injection, where they undergo heat-up, devolatilization, ignition and combustion. The volatile combustion regime ranges from single envelope flames around individual particles to group flames around sets of particles or particle clouds. The present DNS considers single particles and sets of particles arranged in regularly spaced arrays.

6.1.1 LES Data Extraction for DNS

To identify relevant conditions for the DNS setup, gas phase statistics and time histories of coal particles are evaluated from the LES of a semi-industrial coal furnace (IFRF furnace #1) by Rieth *et al.* [108]. Figure 6.1 (background) shows a snapshot of gas temperature inside the furnace from LES, with a zoom into the upstream near-quarl region, where axial velocities and gas-particle relative velocities are shown. On the right of Fig. 6.1 the typical quantities extracted from LES and used to set up the DNS are shown schematically. For selected regions of interest, the LES provides information on the typical gas composition around the particles, as well as quantities that characterize gas-particle interactions, such as relative velocities U_{rel}, turbulent sub-grid fluctuations u'_{sgs}, particle Reynolds numbers Re_p, particle

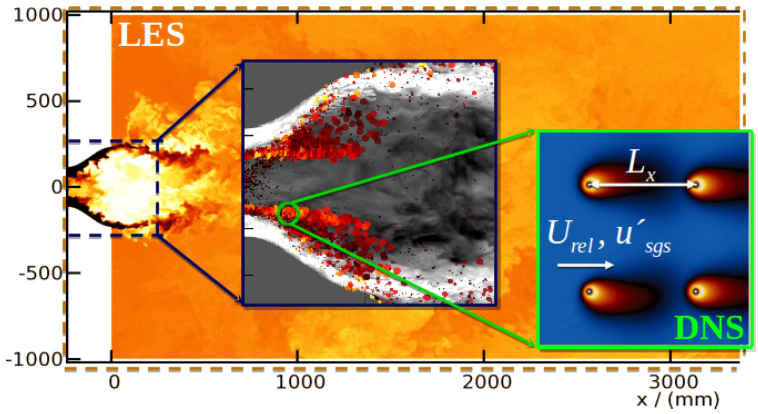

Abbildung 6.1: Data extraction from the LES of IFRF furnace #1 [108] for the DNS. Background, left/middle: Gas temperature contour (black-yellow), axial velocity (black-white) and gas-particle relative velocity (yellow-red) from LES. Foreground, right: Sketch of the DNS.

spacing L_x and heat-up histories of individual particles. The data is used to identify the initial and boundary conditions for the DNS. The main focus is on the early stages of PCC by including (the end of) particle heat-up, devolatilization, volatile flame ignition, stabilization and potential flame interaction. In the LES of the IFRF swirl flame, these processes are largely confined to the burner quarl (region with $x < 0$ in Fig. 6.1), whereas the interior of the furnace ($x > 0$) is dominated by char conversion. As this chapter is focused on volatile combustion, only particles with less than 90% devolatilization progress C_{dev} and located inside the quarl are extracted from the LES. Analysis of the LES data for this region gives a range of inter-particle distances $30\mu\text{m} \leqslant L_x \leqslant 10\text{mm}$ (or $0.3 \leqslant L_x/D_p \leqslant 100$, if normalized by the DNS particle diameter). However, the particle size distribution of the coal exhibits a large number of small particles with $D_p < 10\mu\text{m}$ [146]. Hence, a range of $1 < L_x/D_p \leqslant 1000$ is estimated to occur in the LES and has been considered for DNS.

To judge the occurrence of locally laminar or turbulent flow around the particles, the ratio of the sub-grid turbulence intensity u'_{sgs} to the relative velocity U_{rel} in the LES was inspected. To this end, probability density functions (PDFs) and cumulative distribution functions (CDFs) of u'_{sgs}/U_{rel} for the selected particle ensemble (inside the quarl and with $C_{dev} < 0.9$) were analyzed. It was found that 95% of the particles face ratios u'_{sgs}/U_{rel} of less than 0.97, with a most likely value of 0.25. Hence, the flow around the fully-resolved coal particles is typically laminar, and the present chapter only considers laminar flow conditions. However, some particles travel through furnace regions with considerable sub-grid turbulence intensities (up

to $u'_{sgs}/U_{rel} \approx 15$), and such conditions are considered in Chap. 7.

6.1.2 DNS Setup

The DNS represents a characteristic cell size used for LES. Various different DNS domains are considered, to cover the range from single particles to small particle arrays. Figure 6.2 shows the computational domain for the example of a three particle case comprised of one upstream-, one downstream- and three intermediate particle sections. The central building block is a cubical section of size L_x containing

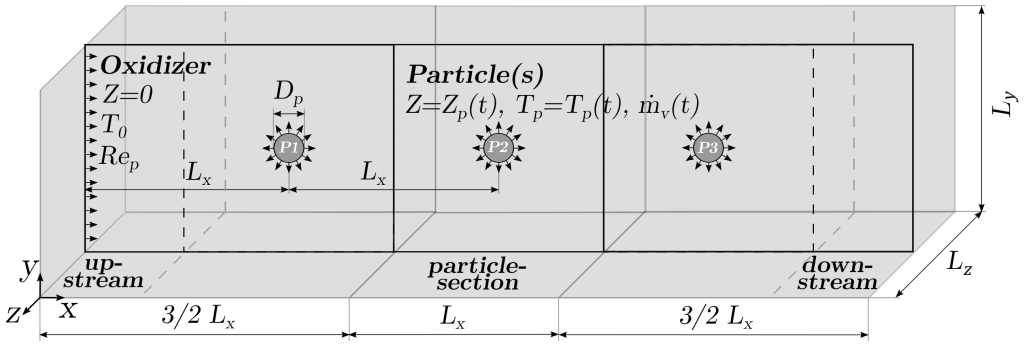

Abbildung 6.2: Schematic of the computational domain(s) used for DNS. The single particle case has one particle section surrounded by one up- and one downstream section, whereas larger cases (here: 3 particles) are generated by adding more particle sections in-between.

a single particle of constant diameter $D_p = 100\mu m$ at its center. The edge length of the particle section is equal to the inter-particle spacing L_x and the up- and downstream sections have dimensions $1/2L_x \times L_y \times L_z$ with $L_x = L_y = L_z$. The inter-particle spacing is a multiple of the particle diameter D_p and varied across a wide range in Sec. 6.2.2.2. The mesh is spherical near the particle and Cartesian close to the boundaries. Local grid refinement allows for an increased resolution in the immediate vicinity of the coal particle, where most of the relevant physico-chemical phenomena occur, yet ensures a smooth transition between the different mesh regions. This mesh structure has previously been used to study mixing phenomena in closely-spaced evaporating droplet arrays and found suitable [142]. By setting periodic boundaries in both the cross-stream and spanwise directions, an infinite layer of equally spaced particles can be simulated.

A fully converted mixture of hot lean combustion products, reproducing the typical bulk flow gases outside of the coal stream, inside a pulverized coal reactor [79], enters the DNS domain with a prescribed constant composition (Tab. 6.1), tempe-

rature and relative velocity. As mentioned in the context of Fig. 6.1 the relevant gas-mixture and particle conditions for the DNS are extracted analyzing the (transient) LES data. The identified conditions are used to initialize the DNS and are then kept constant for the gas-mixture entering the domain (whereas the particle evolution is dynamically predicted by the DNS as described in the following). This allows for the DNS to capture the sensitivities to these conditions by varying them in the different simulations.

Tabelle 6.1: Assumed composition of surrounding gas (mol-%) [79].

O_2	CO_2	H_2O	N_2	Z_{st}
21.00	1.65	12.27	65.08	0.0985

The studied conditions are representative of particles located in the mixing region between the coal carrier gas stream with the secondary oxidizer stream near the quarl wall, and the inner quarl zone governed by the recirculation of hot product gases inside the furnace [108]. As for Chap. 5, the particle temperature T_p (therefore $T_{p,s}$ and $\overline{T}_p$) and $\dot{m}_v$ are directly calculated from Eqs. (3.10)-(3.13) at runtime. Devolatilization is described by Eq. (3.12), where the pre-exponential factor A_v and activation energy E_v have been fitted to pyrolysis kinetics measurements specific to the employed coal (Saar hvBb, Tab. 3.2), resulting in $A_v = 20{,}820\,\mathrm{s}^{-1}$ and $E_v = 46.96\,\mathrm{kJ/mol}$ [74]. The volatile yield is calculated based on $\rho_c = 1000\,\mathrm{kg/m}^3$ and the coal's proximate analysis (Tab. 3.2), and Q-factor correction lead to a final yield of 59.2%. The assumed volatile composition is the one reported in Tab. 3.3 and gas phase chemistry is based on the skeletal mechanism with 52 species and 452 reactions for C_1-C_4 species and C_6H_6 obtained reducing the detailed POLIMI_TOT_1407 scheme as discussed in Sec. 3.1.2.

The interior DNS domain is initialized by the values imposed on the inlet. To characterize the level of reactivity of the various investigated particle arrangements the global equivalence ratio $\phi_{global} = (A/F)/(A/F)_{st}$ is calculated by considering the oxidizer inflow and the total volatile yield contribution from all particles, and relating this air-to-fuel ratio (A/F) to stoichiometric conditions $(A/F)_{st}$ at the time of peak devolatilization rate.

The DNS needs to resolve all relevant scales of the considered problem. With the focus on gas phase mixing and reaction, any process inside the particles is neglected, except for heat conduction (Eq. (3.10)). In the gas phase, the DNS needs to resolve all relevant physics, namely (i) all flow scales including the smallest turbulent scales, (ii) the flame structure and (iii) the particle boundary layers. Since this

chapter only considers laminar flow conditions, the flow scales do not limit the grid resolution. Regarding the flame thickness and boundary layer resolution, the requirements become particularly stringent for high values of the Re_p (up to $Re_p = 8$, as considered in Chap. 7), at which the boundary layer becomes very thin and the flame becomes highly asymmetrical, with the thinner portion located upstream of the particle. Thus the resolution requirements are set for the highest considered value of Re_p. For this limiting condition it is enforced that the number of cells within the minimum thickness of a fully developed flame (at the instant of peak devolatilization rate) is at least 8 and that the number of cells within the boundary layer is at least 6. By jointly fulfilling these requirements it is ensured that the boundary layer is well resolved, and all transport processes are accurately captured. The DNS are performed with the customized OpenFOAM solver presented in Sec. 4.3.1. The effect of time-step width on the results was tested and a Courant number limit of $Co \leqslant 0.5$ was found suitable for achieving stability and accuracy. Chemistry is treated by operator splitting, with further sub-stepping. Simulations are typically run on 64 Opteron cores on local workstations for single particle setups and up to 240 cores on Cray XC40 (HLRS Stuttgart, Hazel Hen) for the largest 3x3x3 particles configuration, requiring 50 to 150 hours of wall time until the volatiles are depleted.

6.2 Results

6.2.1 Single Particle

Figure 6.3 illustrates the transient processes of volatile ignition, envelope flame stabilization and burning, followed by flame extinction for a single particle in laminar flow at $Re_p = 2$. This sequence of events agrees with the observations previously made in Chap. 5, for a low-velocity Hencken burner with an initial $Re_p = 0.8$ that further decreased to zero, resulting in almost spherical envelope flames. Here, the local conditions of a pilot scale PCC flame with significant wake flame structures are simulated, which is mimicked by holding Re_p fixed at 2 throughout the entire process, and even larger Re_p are investigated in Chap. 7. The transients are observed by OH mass fraction and gas temperature contours (left column of Fig. 6.3), scatter plots of temperature vs. mixture fraction colored by Y_{OH} (middle column), and distribution functions of mixture fraction and conditionally-averaged scalar dissipation rates (right column). The distribution functions and conditional means are obtained by binning mixture fraction space and sampling the reacting scalar fields

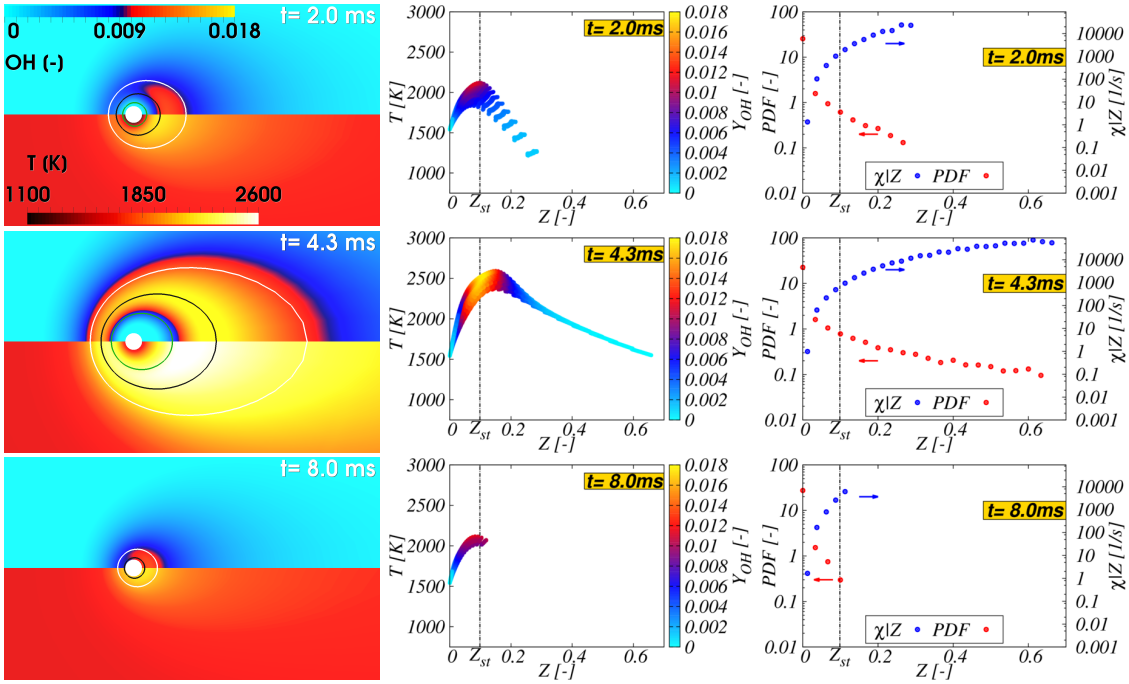

Abbildung 6.3: Results after 2.0ms (top row), 4.3ms (middle row) and 8.0ms (bottom row) during single particle combustion for $Re_p = 2$. **Left:** Mass fraction Y_{OH} (top frames), temperature (bottom frames) contours, and mixture fraction iso-lines at Z_{st} (black), $Z_{st}/2$ (white) and $2Z_{st}$ (green). **Middle:** Scatter plots of gas temperature vs. mixture fraction, colored by Y_{OH}. The vertical dash-dotted lines indicate Z_{st}. **Right:** Distribution functions of mixture fraction (red) and conditional average of scalar dissipation rate (blue).

across the entire DNS domain, where a total number of 30 bins was found ideal in terms of mixture fraction resolution and number of samples per bin.

Ignition occurs in the particle wake at very lean conditions, where scalar dissipation is low, followed by a rapid upstream propagation of the flame towards the particle and around it, as previously observed in Sec. 5.2. Here, at 2 ms (top row of Fig. 6.3), the flame reaches the stoichiometric iso-surface and wraps around the particle. The scatter plot of temperature spans a mixture fraction range of up to $Z = 0.3$. The minimum gas temperatures across mixture fraction space are obtained upstream of the particle, which the envelope flame has not reached yet, whereas the highest values of the gas temperature T_g are found along the downstream $x-$coordinate, where the flame is located at this time instant, and the highest OH mass fractions are located downstream near $Z = Z_{st}$. It can be noted that the oxidizer is at an elevated temperature prior to ignition of the envelope flame, which reflects the presence of nearby flames in the selected furnace region as captured by the LES. The mixture fraction distribution shows a large number of pure oxidizer samples (away

from the particle), whereas the small number of high Z-values corresponds to the particle surface region, to which volatiles are ejected. The scalar dissipation rate is highest near the particle surface ($Z \rightarrow Z_{max}$), and strongly decreases towards the oxidizer side as expected and previously reported in Sec. 5.2. At 4.3 ms (middle row of Fig. 6.3), the envelope flame has triggered a rapid heat transfer from the gas to the particle, and the maximum devolatilization rate is reached. The temperature and OH contours show an elongated wake flame structure, which reaches the highest Y_{OH} roughly between half and twice the stoichiometric mixture fraction Z_{st}. The flame stand-off distance from the particle is determined by the distance of the iso-surface $Z = Z_{st}$ from the particle surface, and has been reported as two particle diameters for a very low Reynolds number (Chap. 5). Here, the stand-off distance is 1.5 and 4.5 particle diameters up- and downstream of the particle, respectively. At 4.3 ms the temperature scatter reaches its maximum extent in mixture fraction space with $Z_{max} \approx 0.7$, and the peak temperatures are found slightly rich of Z_{st}, while the peak OH remains near Z_{st}. The mixture fraction distribution functions and scalar dissipation rates at 4.3 ms follow the same trends as at 2 ms, but span a wider mixture fraction range. The peak scalar dissipation rate has increased due to rapid volatile ejection from the particle, which is now strongly heated by the envelope flame. At 8.0 ms (bottom row of Fig. 6.3), the Z_{st}-iso-line has recessed to the particle surface and, in the absence of char conversion, flame extinction occurs. Thus, the temperature scatter, $Z-$distribution and scalar dissipation rate profiles have reversed towards $Z = 0$. Comparing with the results presented in Chap. 5, the current simulation predicts a similar transient evolution and also a stable envelope flame. The downstream wake formation, however, leads to non-constant, distributed flame stand-off distances.

6.2.2 Particle Array Combustion

To study particle group combustion in closely spaced ensembles, DNS of regularly spaced particle arrays are conducted. A row of three particles arranged in the flow direction is considered, which is extended to three infinite planes of equally spaced particles (inter-particle spacing $L_x = L_y = L_z$) in the two cross-stream directions by the periodic BCs.

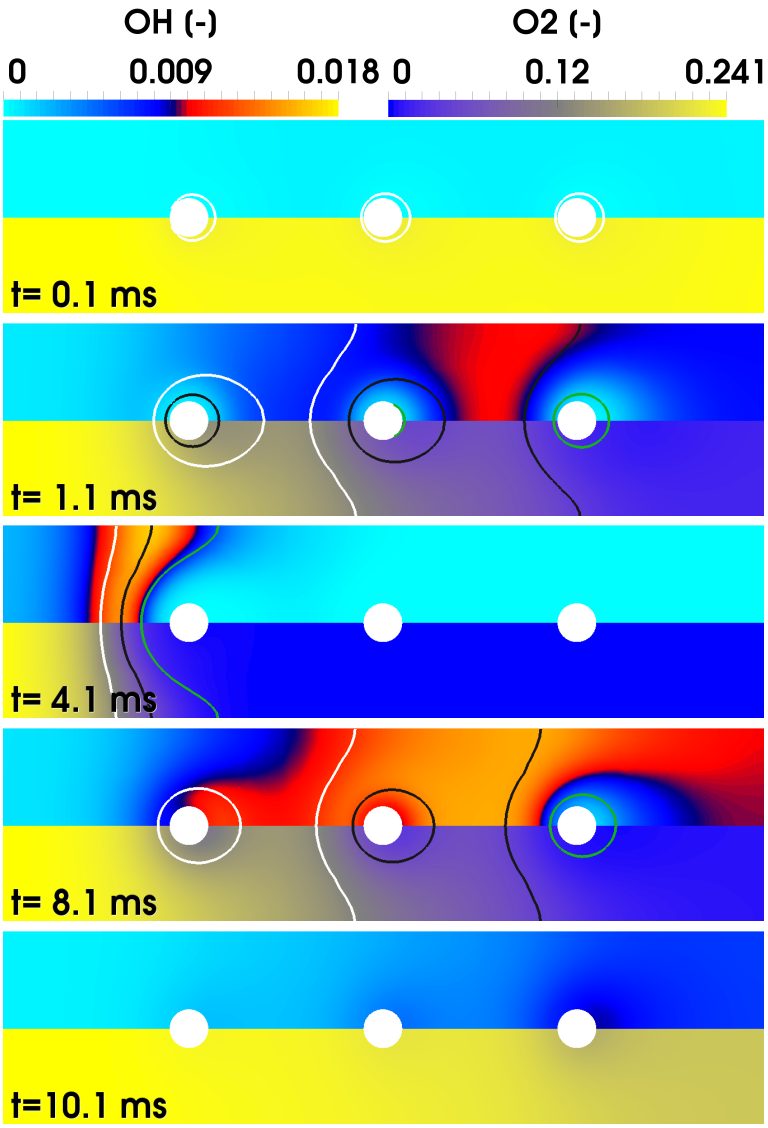

Abbildung 6.4: Mass fraction Y_{OH} (top of each frame) and Y_{O_2} (bottom of each frame) contours at selected times for a particle array with $Re_p = 2$ at inter-particle distance $L_x = 5D_p$. The iso-lines indicate mixture fractions of $Z_{st}/2$ (white), Z_{st} (black) and $2Z_{st}$ (green).

6.2.2.1 Transient Evolution

The transient evolution of a particle array at fixed inter-particle spacing $L_x = 5D_p$ and $Re_p = 2$ is considered first. Figure 6.4 shows OH and O_2 mass fraction contours along with selected mixture fraction iso-lines during devolatilization and volatile combustion. Similar to the single particle case, ignition occurs in the lean region behind the array ($t \approx$1ms), followed by rapid upstream flame propagation (1ms$< t <$4ms). At $t =$4.1ms, the instant of maximum devolatilization rate of

particle 1, the flame has traversed almost the entire domain, and stabilizes upstream of the first particle. The Y_{OH} contours and Z-iso-lines reveal that, during the upstream propagation process, the flame follows the (moving) zone of near-stoichiometric mixture fraction between two neighboring particles, e.g. particles 2 and 3 at $t = 1.1$ms. At $t = 4.1$ms the iso-lines indicate that the entire mixture fraction range $Z_{st}/2 < Z < 2Z_{st}$ (roughly indicating the burning limits) is located upstream of the first particle set, separating a lean upstream zone from an oxygen-starved downstream region, which cannot sustain an envelope flame. Hence, the downstream particles do not burn, reach a lower peak $\dot{m}_v$ and devolatilize more slowly, as can be observed in the temporal history of surface temperature and devolatilization rate for each particle presented in Fig. 6.5. While the third particle

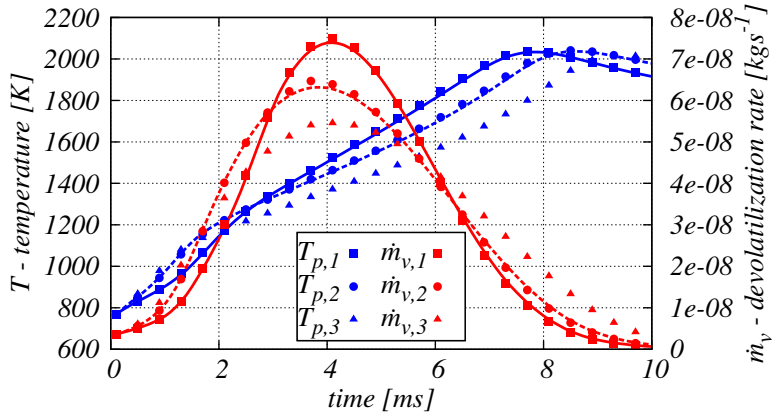

Abbildung 6.5: Particle surface temperature and devolatilization rate vs. residence time for 2 (lines) and 3 (symbols) particles at an inter-particle distance $L_x = 5D_p$ and $Re_p = 2$.

(triangles) shows the earliest increase of the observed parameters due to downstream ignition, followed by particles 2 (circles) and 1 (squares), the flame rapidly propagates upstream and quickly establishes a situation, where particle 1 is heated the most. Hence, both T_p and $\dot{m}_v$ of particle 1 intersect with the corresponding lines of particles 2 and 3 (e.g. at $t \approx 3$ms for $\dot{m}_v$) and the first particle attains the overall highest peak devolatilization rate (at $t = 4.1$ms). Later, $\dot{m}_v$ decreases as the volatiles are depleted, which leads to the flame receding downstream, until no volatiles are left and extinction occurs (see Fig. 6.4, $t = 8.1 \ldots 10.1$ms). As a result, the time histories of particles 1 through 3 in Fig. 6.5 intersect again at late times, with the overall most-heated particle 1 depleted first, followed by the less heated particles 2 and 3. In addition to the three-particle case discussed so far, Fig. 6.5 also shows a corresponding case of only two particles spaced at the same distance $L_x = 5D_p$.

By comparing the two-particle result (lines) to the three-particle case (symbols) it can be observed that the most downstream third particle has no discernible effect on the time history of the two upstream particles, as expected. Following the solid fuel group combustion terminology introduced by Annamalai *et al.* [10] (for particle clouds), the burning mode that establishes once the flame has stabilized (see Fig. 6.4 at $t = 4.1$ms) can be identified as critical group combustion (CGC). In the CGC regime, the high particle number density (small inter-particle spacing) leads to strong interaction, and a volatile flame, located just outside the array, that prevents oxygen from penetrating into it. The gas temperatures within the array are between the particle and flame temperature. Other group combustion regimes are established for different inter-particle spacings (cf. Fig. 6.7, discussed in Sec. 6.2.2.2).

A deeper understanding of particle interaction is obtained from axial profiles of temperature, mixture fraction and scalar dissipation rate for a single, two and three particles with identical inter-particle spacing ($L_x = 5D_p$) at the time of $\dot{m}_{v,max}$, as shown in Fig. 6.6. For the single particle, the gas temperature T_g peaks in the down-

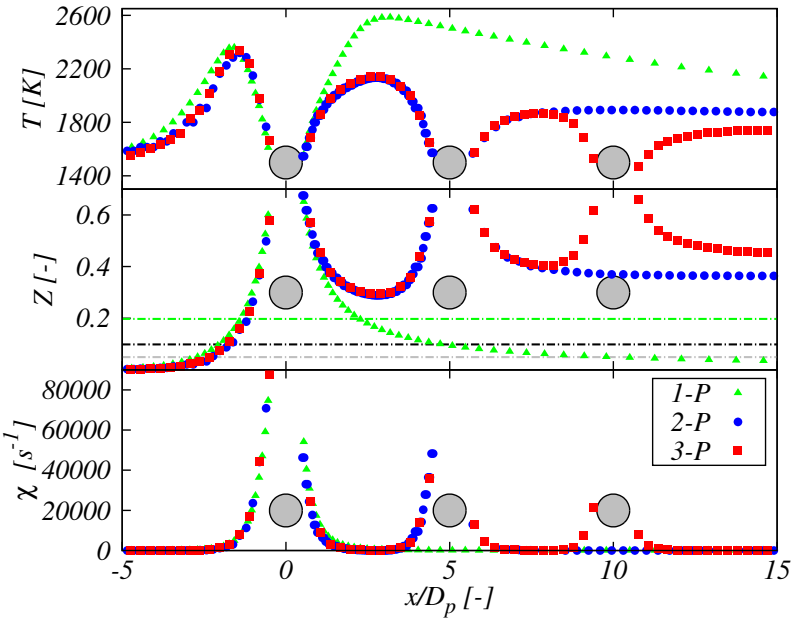

Abbildung 6.6: Streamwise axial profiles of gas temperature, mixture fraction and scalar dissipation rate for 1 (triangles), 2 (circles) and 3 (squares) particles at the time of maximum devolatilization rate of particle 1. The second and third particle are placed at $L_x = 5D_p$. Dashed horizontal lines in the $Z-$frame mark $Z_{st}/2$ (grey), Z_{st} (black) and $2Z_{st}$ (green).

stream region, at a distance of about $2.5D_p$ from the surface. Mixture fraction and dissipation rate reach their peak values at the particle surface, in the downstream

and upstream regions, decaying to zero with increasing distance from the particle. Adding a second particle at $L_x = 5D_p$ leads to the strong interaction that is responsible for the flame to move upstream, as was observed in Fig. 6.4 ($t = 4.1$ms). In Fig. 6.6 the peak gas temperature for two particles is therefore located in the upstream region of particle 1 and corresponds to the value calculated at the same position for a single particle. Despite the lack of O_2 and the corresponding absence of OH between particles 1 and 2 in Fig. 6.4 ($t = 4.1$ms), the gas temperature between particles 1 and 2 remains elevated, but 500K lower than behind a single particle. The downstream Z-values are significantly higher and remain above $2Z_{st}$ if more than one particle contributes to volatile release, again confirming the previous findings from Fig. 6.4. The peak scalar dissipation rate is not much affected by the presence of a second particle, but naturally increases to peak again at particle surface 2. Figure 6.6 also shows that adding a third particle leads to changes in its direct vicinity, but hardly affects the state around the two upstream particles.

6.2.2.2 Effect of Inter-Particle Distance

This section examines the effect of inter-particle spacings L_x ranging from $5D_p$ to $30D_p$, which is well within the span present in the LES and was found wide enough for the transition from single to group combustion. Figure 6.7 shows the same quantities as Fig. 6.4, this time for varying inter-particle distances L_x, extracted at the time of peak devolatilization rate of the respective upstream particle. As expected, increasing L_x decreases the interactions, gradually moving from group combustion towards single particle burning. For a small inter-particle spacing of $L_x = 5D_p$ at 4.1ms, as shown in Fig. 6.4, critical group combustion occurs. Increasing inter-particle distance provides more space in the cross-stream direction -before interfering with the next particle in the infinite array- for some of the incoming oxygen to pass the most upstream flame front, such that the particles positioned in the wake of the first one face favorable conditions for combustion. This is quantified by the global equivalence ratio that, for $L_x = 5D_p$, amounts to (very rich) $\phi_{global} = 7.4$. For $L_x = 10D_p$ (top of Fig. 6.7), a contiguous stoichiometric region forms around particle 1 and extends approximately to the axial location of particle 2, which first narrows behind particle 1 and then widens around particle 2. At the present Re_p this region faces comparatively low scalar dissipation rates, and therefore a widely distributed reaction zone is established, with the highest OH mass fraction on the stoichiometric surface wrapping around particles 1 and 2. The downstream particle is surrounded by a rich region with $Z > 2Z_{st}$, such that no flame can be sustained.

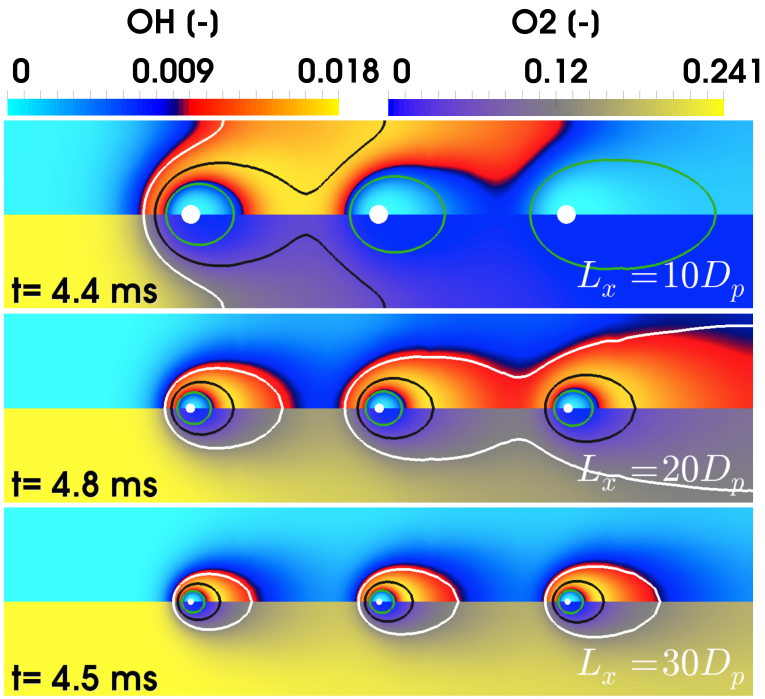

Abbildung 6.7: Mass fractions Y_{OH} and Y_{O_2} contours at the time of maximum devolatilization rate at $Re_p = 2$ for different inter-particle distances L_x. Mixture fraction iso-lines as per Fig. 6.4, which also shows the corresponding situation for $L_x = 5$ (at 4.1ms).

The value of ϕ_{global} is 2.1 at $L_x = 10D_p$. Further increasing L_x to $20D_p$, Fig. 6.7 (middle), leaves yet more space for O_2 to reach the downstream particles, and ϕ_{global} reduces to 0.5. Thus, the single flame observed for $L_x = 10D_p$ is now split into a set of envelope flames around the particles in the most upstream plane, followed by more complex flame structures due to the interaction of particles 2 and 3. The downstream particles interact strongly in the flow direction due to their particle wakes, whereas no overlapping OH contours, and hence significant interactions, are observed in the cross-stream direction. The transition from $L_x = 5D_p$ to $L_x = 20D_p$ corresponds to moving from critical group combustion (CGC) to partial (PGC) and incipient group combustion (IGC) [10]. Further increasing L_x to $30D_p$ (bottom of Fig. 6.7), leads to $\phi_{global} = 0.23$ and to a case, where particles are grouped in a closely spaced ensemble, yet the combustion of each particle is unaffected by the presence of the others and individual flame combustion (IFC) occurs [10]. The transition from group combustion to single particle combustion strongly affects the heating and devolatilization histories of the sets of particles placed at downstream locations. Figure 6.8 presents the particle surface temperature and devolatilization rate vs. time, previously shown for particle spacing $L_x = 5D_p$ in Fig. 6.5, now for

$L_x = 30D_p$. Comparing the two figures shows that, while particles attain distinctly different heating and mass release histories during CGC, Fig. 6.5, the time evolution of all three particle sets is (almost) identical in IFC, where interaction is negligible, Fig. 6.8. A further analysis of the effect of varying L_x on transverse mixture fraction

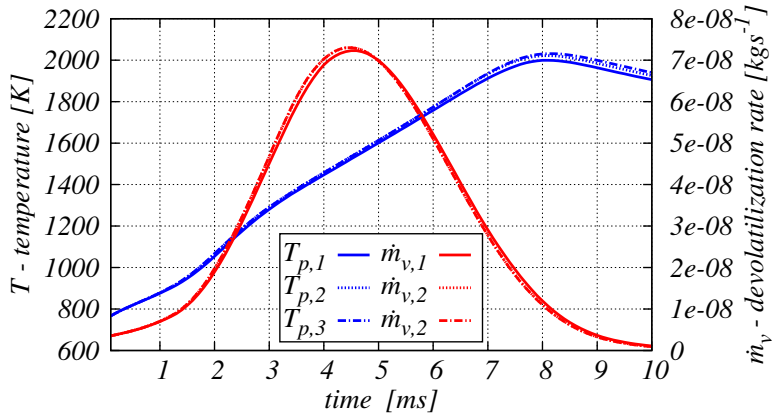

Abbildung 6.8: Particle surface temperature and devolatilization rate vs. residence time for 3 particles aligned with the flow direction at inter-particle distance $L_x = 30D_p$ and $Re_p = 2$.

profiles behind single particles and particle arrays is presented in Sec. 6.3.

6.3 Transverse Mixture Fraction Profiles

This section reports additional results from the present analysis, found by drawing analogies between coal pyrolysis and droplet evaporation. In the context of multi-phase flamelet modeling for LES, the knowledge of sub-grid mixture fraction profiles in the direct vicinity of dispersed fuel sources becomes important (cf. Sec. 2.4.2). For (single) droplet evaporation Klimenko & Bilger [58] derived transverse profiles of mixture fraction at a given axial distance from the droplet using asymptotic analysis, which were shown to be in good agreement with DNS predictions by Zoby *et al.* [158]. The transverse mixture fraction profiles read

$$Z(r) = Z_\infty + Ae^{-\alpha r^2} \tag{6.1}$$

with

$$A = \frac{\dot{m}(Z_d - Z_\infty)}{4\pi\rho Dl}\,, \tag{6.2}$$

$$\alpha = \frac{U_{rel}}{4Dl}\,, \tag{6.3}$$

where r is the transverse coordinate, l is the axial distance from the position of the fuel source, Z_d and Z_∞ are the mixture fraction inside the dispersed phase and in the far free stream along the transverse coordinate, respectively, $\dot{m}$ the fuel mass release rate and U_{rel} the relative velocity between the gas and dispersed phase. The gas density ρ and diffusivity D are calculated as spatial and Favre-averages across the inter-particle space. During the early stages of pulverized coal combustion, where char conversion is not important, the volatile flame around a coal particle is similar to the envelope flame from an evaporating fuel droplet, since both processes are governed by the mixing process of fuel ejected from a dispersed phase with a continuous oxidizing environment. Hence, the transverse profiles described by Eqs. (6.1)-(6.3) should equally hold for droplet evaporation and coal devolatilization. This is illustrated in Fig. 6.9, which compares transverse mixture fraction profiles from asymptotics to results from the current DNS for a single and a row of three particles at different distances L_x. The mixture fraction is extracted at $l = 2D_p$ from each particle and plotted versus the transverse coordinate normalized by the particle spacing L_x (for a single particle L_x refers to the domain extent). For the single particle case an almost perfect match of the asymptotic and DNS solution is obtained, with the remaining uncertainties (near $r/L_x \approx 0.1$), likely to be related to the averaging of the transport properties ρ and D. The transverse profiles in the wakes of the closely-spaced particle array ($L_x = 5D_p$, Fig. 6.9(a)) show similarly good matches between asymptotics and DNS, despite the added complexity of interacting particle wakes at the selected (small) particle distance, which has not been considered in the asymptotic derivation. It can be noted, that transverse profiles corresponding to the three particle array reflect the considerably richer mixtures in closely-spaced fuel clouds, where fuel can accumulate without burning ($Z > 2Z_{st}$, even at the maximum transverse distance). On the other hand, for single particle combustion, mixing states $Z \rightarrow 0$ (pure oxidizer) are obtained along the transverse distance and a flame can be sustained. Analyzing also the transverse mixture fraction profiles for larger particle spacings $L_x = 10D_p$ (Fig. 6.9(b)) and $L_x = 30D_p$ (Fig. 6.9(c)), reveals that the profiles gradually shift from the three separate ones shown for $L_x = 5D_p$ in Fig. 6.9(a), to three identical profiles, corresponding to the single particle result in Fig. 6.9(c) for $L_x = 30D_p$. Thus, it can be concluded that transverse mixture fraction profiles in the wake of laminar coal volatile flames can be recovered by asymptotic expressions, which have been derived for evaporating droplets.

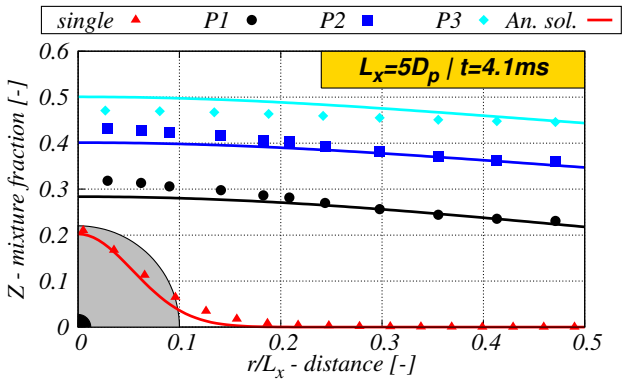

(a)

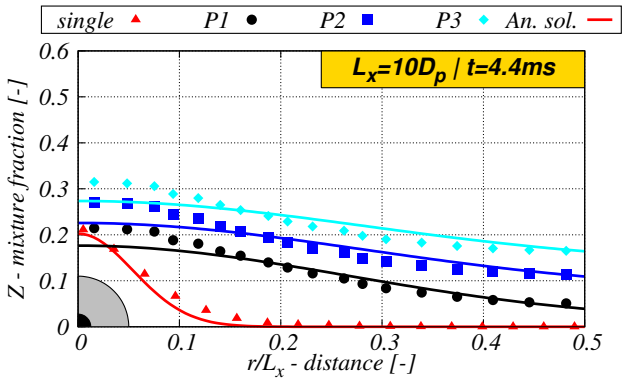

(b)

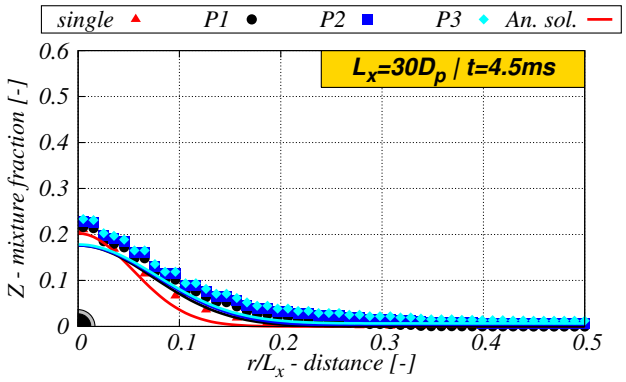

(c)

Abbildung 6.9: Mixture fraction profiles along the transverse direction in the wake of one particle (*single*) and an array of three (*P1...P3*) particles with spacing $L_x = 5D_p$ (a), $L_x = 10D_p$ (b) and $L_x = 30D_p$ (c) for $Re_p = 2$ at the time of maximum devolatilization rate. Symbols: DNS predictions, lines: asymptotic solution [58, 158].

6.4 Summary for Transient Evolution and Group Effects of Laminar Flows

Pulverized coal particle pyrolysis, ignition and volatile burning have been investigated by fully-resolved DNS. The processes are characterized for a wide range of conditions obtained from a reference LES study of a semi-industrial furnace [108]. For single particles, similar features are found as previously discussed in Chap. 5, for a lower particle Reynolds number Re_p. At the present elevated particle Reynolds number the formation of wake flames is observed, which becomes increasingly more relevant for flame interactions in ensembles of particles. Hence, when extending the analysis to multiple particles aligned in streamwise direction, such particle interactions are found to exist and to be strongly affected by the inter-particle distance L_x. In particular, different combustion regimes are observed when reducing L_x from large values, for which the particles burn independently (IFC regime), to small L_x, which results in strong interactions and group combustion (CGC). The regime transition is quantified by a global equivalence ratio, which spans from very lean (IFC) to very rich (CGC) combustion for the considered range of L_x and affects the particle surface temperature and devolatilization rate history. Available scaling laws for mixture fraction profiles along transverse planes in the vicinity of evaporating droplets [58] are applied to solid fuel and predict the mixture fraction distributions in the wake of the burning coal particles. The following Chap. 7 will extend the present analysis to consider the effects of large Re_p on volatile flame straining and extinction, as well as the effects of turbulent flow.

Chapter 7

Effects of Particle Reynolds Number and Turbulence on Volatile Combustion and Flame Interaction

In this chapter DNS is performed to characterize volatile combustion of isolated coal particles and closely spaced particle ensembles at high Reynolds numbers up to turbulent flow. Chapter 6 identified relevant PCC conditions from the reference LES of a pilot-scale furnace [106] and studied the transient behavior and near-particle scalar profiles of single particles and particle arrays that undergo heating, pyrolysis and volatile combustion by DNS. The main focus of Chap. 6 was the analysis of various coal combustion regimes that may result from a wide range of relative inter-particle spacings. The investigation was confined to a single low particle Reynolds number ($Re_p = 2$) resulting in laminar flow conditions. As the analysis of the reference LES revealed, though, high speed and locally turbulent flow also occur in industrial PCC furnaces. Therefore, in the present chapter, varying the inflow velocities, the effect of large particle Reynolds numbers and considerable levels of turbulence on the devolatilization and burning behavior of isolated particles and arrays of infinite particle layers are investigated, with a special focus on flame interaction. An attempt is also made to recover the single particle results with a standard steady laminar flamelet approach, investigating the limits of conventional flamelet modeling (cf. Sec. 2.4.2) and standard film theory on highly strained envelope flames. The results presented in this chapter have been published in *Fuel* 234:723-731 (2018) [130].

7.1 Computational Configuration

This chapter considers the same computational configuration presented in Chap. 6, mimicking the relevant conditions extracted from the reference LES of the IFRF coal furnace [108]. As reported in Chap. 6, the data extraction technique is based on the analysis of the gas phase statistics and time histories of coal particles from the reference (Euler-Lagrange) LES, to set the initial and boundary conditions for the DNS.

Chapter 6 considered a single particle Reynolds number, namely $Re_p = 2$. Here, a suitable range of particle Reynolds numbers to be studied was selected based on the analysis of the PDFs and CDFs of the devolatilizing particle ensemble inside the burner quarl from the reference LES. It was found that more than 90% of the particles are subjected to particle Reynolds numbers of less than 8, with 60% of the particles facing a range $1 \leqslant Re_p \leqslant 8$. The data also revealed that some particles may face substantially higher Re_p. But according to the CDF these occurrences are rather rare events with, for example, an extremely low probability ($\approx 2 \cdot 10^{-5}$) of particles facing $Re_p \geqslant 100$. For completeness, a DNS case with $Re_p = 100$ was also tested. The case revealed that, in such highly convective environments, the local strain rate is too high for ignition to occur and the particle is surrounded by areas of extremely high scalar dissipation rate that prevent any chemical reaction in the direct particle vicinity. Hence, the presentation of the results is limited to the range $1 \leqslant Re_p \leqslant 8$.

As discussed in Chap. 6, the analysis of the u'_{sgs}/U_{rel} ratio in the LES revealed that 95% of the particles experience values which are smaller than 0.97 and the most likely value of the normalized sub-grid turbulence intensity was 0.25. These typically laminar flow conditions were considered in Chap. 6. However, some particles facing sub-grid turbulence intensities of up to $u'_{sgs}/U_{rel} \approx 15$ were also found in the LES. These regions of high sub-grid turbulence intensity are mainly located in the highly sheared region between the two outer streams with large forward momentum and the inner quarl zone governed by recirculation in IFRF furnace #1 [108]. To reflect such occurrences of turbulence in the direct vicinity of the coal particle surface a study of fully-resolved turbulent flow around groups of coal particles is conducted in this chapter, cf. Sec. 7.2.2. As mentioned in Sec. 2.3.1.4, the turbulent (in-)flow conditions for DNS are obtained by generating artificial turbulence based on a von Karman spectrum using inverse Fourier transforms according to the method of Billson *et al.* [16], as explained in detail in Appendix A. Turbulence

generation is controlled by fixing the bounds of the desired turbulence spectrum by the integral length scale L_{int} and a total kinetic energy level representative of a velocity fluctuation level u', taken as the sub-grid velocity fluctuation from the LES u'_{sgs}. The range of integral scales that can be covered in the DNS is limited by the domain size and L_{int} is set to correspond to half the cross-stream (y-)extent of the DNS domain. Moreover, with the fully Eulerian approach used here, resolving the particles and the boundary layers around them but fixing their position in space, the energy levels of the flow can be strongly decreased by the "screen effect" [54]. Increasing the integral length scale may not affect the energetic structure of the flow any more, once the integral length scale is larger than the particle spacing. This is due to the mutual influence of neighboring particles with fixed positions, which limits the effective integral scale to the particle spacing. This intrinsic limitation of the approach was confirmed by Wang *et al.* [141] who performed fully-resolved simulations of fixed arrays of evaporating droplets and found that the mixture fraction distribution, its conditional scalar dissipation and PDF are all independent of the largest turbulent length scales. In order to capture more realistic turbulence modulation, the particles should be allowed to interact freely and to move with the flow. Such an Euler-Lagrange approach has already been adopted by Rieth et al. [106] who performed carrier-phase DNS of pulverized coal particles in a turbulent mixing layer. However, the present study requires full resolution of all scales in the vicinity of the particle, as individual particle ignition is primarily controlled by the small scales of the order of the particle distance and possible turbulence modulation by the screen effect is not expected to unduly influence the present analysis.

The velocity fluctuation level at the DNS inlet is varied from laminar to highly turbulent conditions and two representative values of u'_{sgs}/U_{rel} that reflect the LES sub-grid turbulence levels are discussed in Sec. 7.2.2. The first one is the most likely value extracted from the LES ($u'_{sgs}/U_{rel} = 0.25$) and the second one a highly turbulent condition with $u'_{sgs}/U_{rel} = 1.0$, which only applies to less than 5% of the particles in the LES.

The DNS domains used here share the same structure presented in Sec. 6.1.2. The central building block of all domains is a cube, the edge length of which corresponds to the inter-particle spacing L_x with a single particle of diameter D_p located at its center. The blocks can flexibly be combined with (pure gas) up- and downstream sections of size $1/2L_x \times L_x \times L_x$ to form particle clusters with varying particle number density and spacing. This allows, starting from the buildings blocks shown in Fig. 6.2, to obtain complex configurations as the 3x3x3 particle array shown in

Fig. 7.1. The ensembles considered here are closely spaced particles characterized by

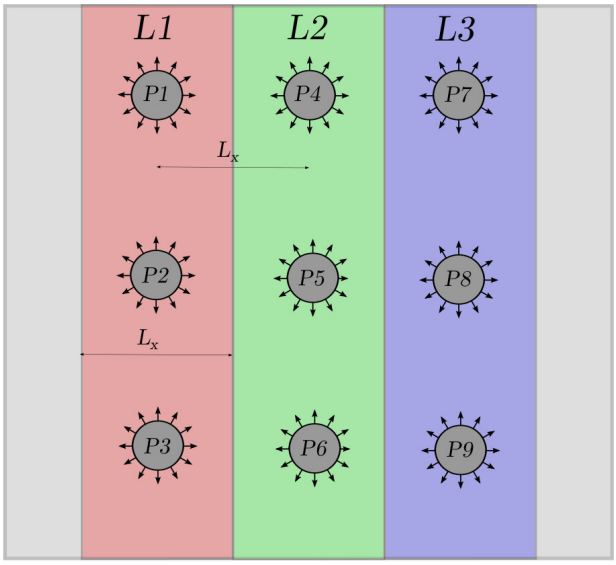

Abbildung 7.1: Particle array zones (layers) for data extraction.

$L_x = 5D_p$ and $L_x = 10D_p$ with $D_p = 100\mu m$, unless indicated otherwise. To perform a region-based analysis of the local mixing and reaction processes, different zones (layers) of the computational domain are identified as shown in Fig. 7.1 for the 3x3x3 particle array. The colored layers L1, L2 and L3 are centered about the axial positions of particle sets P1-P2-P3, P4-P5-P6 and P7-P8-P9 and used for the flame structure analysis in Sec. 7.2, whereas the gray areas for upstream flow development and the (far) downstream wake region are excluded. The boundary conditions are identical to the ones employed in Chap. 6, apart from (i) a variation of U_{rel} at the inlet to study the effect of particle Reynolds number Re_p and (ii) the application of turbulent inflow conditions to mimick turbulent flow at the sub-grid level in Sec. 7.2.2. The DNS is required to resolve all the scales at which relevant physics occur, i.e. (i) all flow scales including the Kolmogorov scale, (ii) the flame structure and (iii) the particle boundary layers. The full resolution of (ii) and (iii) has already been described in Chap. 6. To additionally consider (i) in the present study, the Kolmogorov scale η is calculated as $(\nu^3/\varepsilon)^{1/4}$, where ν is the kinematic viscosity near the surface of the burning particles and the dissipation rate is estimated as $\varepsilon = u'^3_{sgs}/L_{int}$. The conditions selected here to reproduce some of the extreme turbulence intensities that the coal particles face in the quarl region of the furnace are based on $Re_p = 8$ and $u'_{sgs}/U_{rel} \leqslant 1$, which leads to a Kolmogorov scale of size $\eta \geqslant D_p/2$. Here, the DNS resolution requirements for the Kolmogorov scale are easily fulfilled, as it is significantly larger than the smallest grid size required to resolve the flame structure

and the particle boundary layers such that all turbulent scales are well resolved. In addition to resolving all scales in the gas phase, heat transfer inside the particles is considered by solving Eq. (3.10) for the particle temperature and all particles are resolved with at least 3,600 internal cells.

7.2 Results

7.2.1 Effect of Particle Reynolds Number

7.2.1.1 Single Particle

Figure 7.2 shows OH mass fraction and temperature contours along with selected iso-lines of mixture fraction at the times of maximum devolatilization rate for a single coal particle at different values of Re_p. At low Reynolds number the envelope flame is nearly spherical such that after ignition the particle is heated uniformly from all sides ($Re_p = 1$). Increasing Re_p leads to increasingly more asymmetry of the mixing field, as can be seen from the progressively more elliptical iso-lines of Z. Volatile combustion is altered by the increased effect of convection, since the stand-off distance slightly decreases for increasing Re_p and combustion intensity is reduced, as indicated by the lower peak temperature and OH mass fraction values. The zone of maximum heat release (approximately characterized by the Y_{OH} profiles) is reduced at very high Re_p, where at $Re_p = 6$ the volatile flame ceases to fully enclose the particle and further reduces to a weak zone of elevated heat release in the wake of the particle at $Re_p = 8$. For these two elevated Reynolds numbers the reaction zone does not reach the upstream side of the particle at any time of the simulation, despite the fact that there are zones of mixture fraction values ranging from $Z_{st}/2$ to $2Z_{st}$, enclosing stoichiometric conditions. An attempt is made to model the trends of increased effects of strain on the volatile flames with increasing Re_p shown in Fig. 7.2 by steady laminar flamelet calculations (Sec. 2.4.2). The flamelet computations are performed by solving the standard flamelet equations (Eq. (2.21)), where both the boundary conditions at $Z = 0$ and $Z = Z_{max}$, as well as the profile of scalar dissipation rate in mixture fraction space, $\chi = \chi(Z)$, are extracted directly from the DNS and are therefore dependent on the considered Re_p and selected time instance. Data extraction is performed along the up- and downstream symmetry line, towards and away from the particle in the axial direction, at the times of maximum devolatilization rate, as shown in Fig. 7.2. Figure 7.3 shows the comparison of flamelet and DNS data for the reference case $Re_p = 2$. It can be observed that the

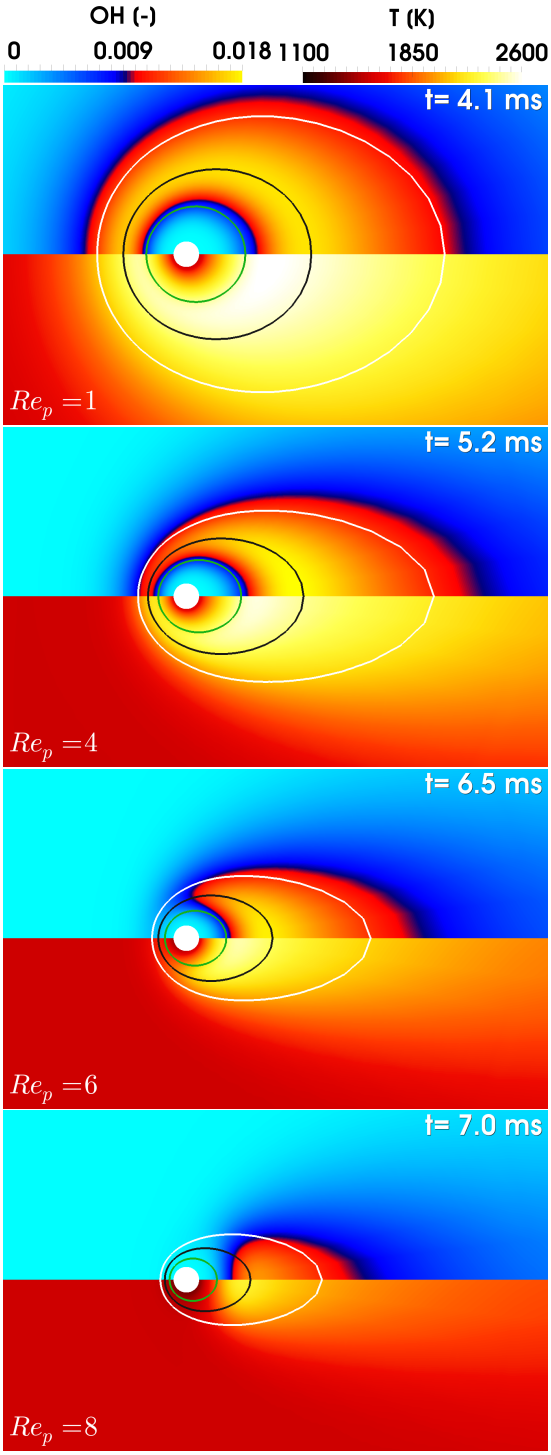

Abbildung 7.2: Mass fraction Y_{OH} (top of frame) and temperature (bottom of frame) contours, and mixture fraction iso-lines at $Z = Z_{st}$ (black), $Z = Z_{st}/2$ (white) and $Z = 2Z_{st}$ (green) at the times of maximum devolatilization rate for different particle Reynolds numbers Re_p.

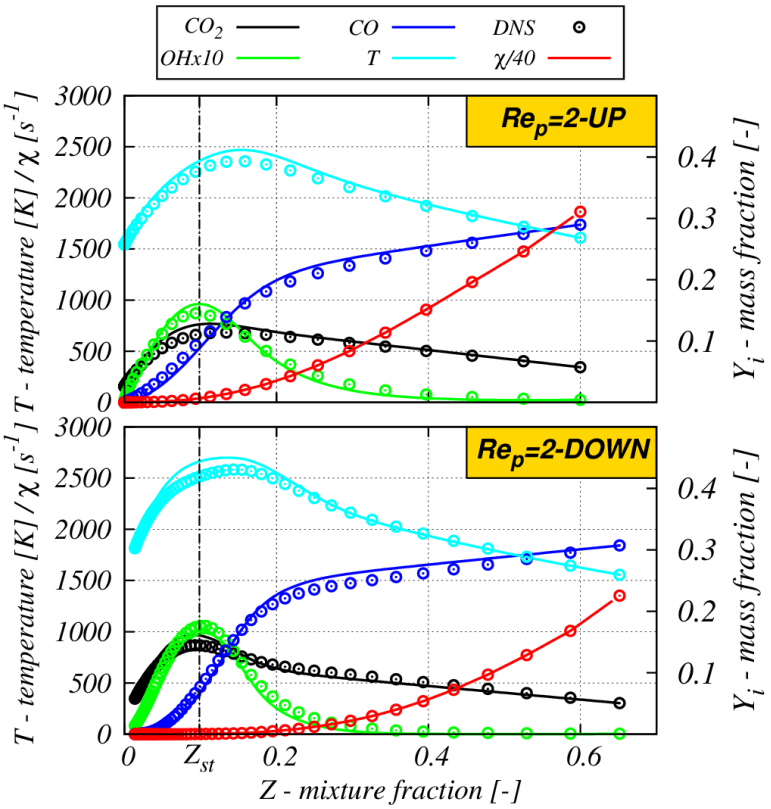

Abbildung 7.3: Results from steady laminar flamelet calculations (lines) compared with corresponding DNS data (circles) for particle Reynolds number $Re_p = 2$. The DNS profiles are extracted along the upstream (top) and downstream (bottom) axis of symmetry at the time of maximum devolatilization rate.

standard flamelet equations are well suited to represent the transport and chemical processes along the flame normal direction, as no major deviations can be observed. It is noted that the chemical state at the mixture fraction bounds and the scalar dissipation rate profiles, which have to be prescribed (cf. Sec. 2.4.2) but are generally unknown, are extracted here directly from the DNS data and used as inputs for the flamelet calculations. Therefore, the detailed information provided by the DNS can be of great value e.g. for flamelet modeling, allowing for *a priori* validation of pre-tabulated chemistry [134]. Figure 7.4 shows a similar comparison for Reynolds numbers $Re_p = 4$, $Re_p = 6$ and $Re_p = 8$, along the upstream symmetry line. While the cross-comparison of flamelet and DNS data for $Re_p = 4$ is still satisfactory, some deviations can already be observed, with the flamelet predicting an overall higher level of chemical conversion as indicated by the slightly higher temperature, CO_2 and OH mass fraction. This trend increases for $Re_p = 6$, where the DNS shows very little chemical conversion along the upstream symmetry line, Fig. 7.2,

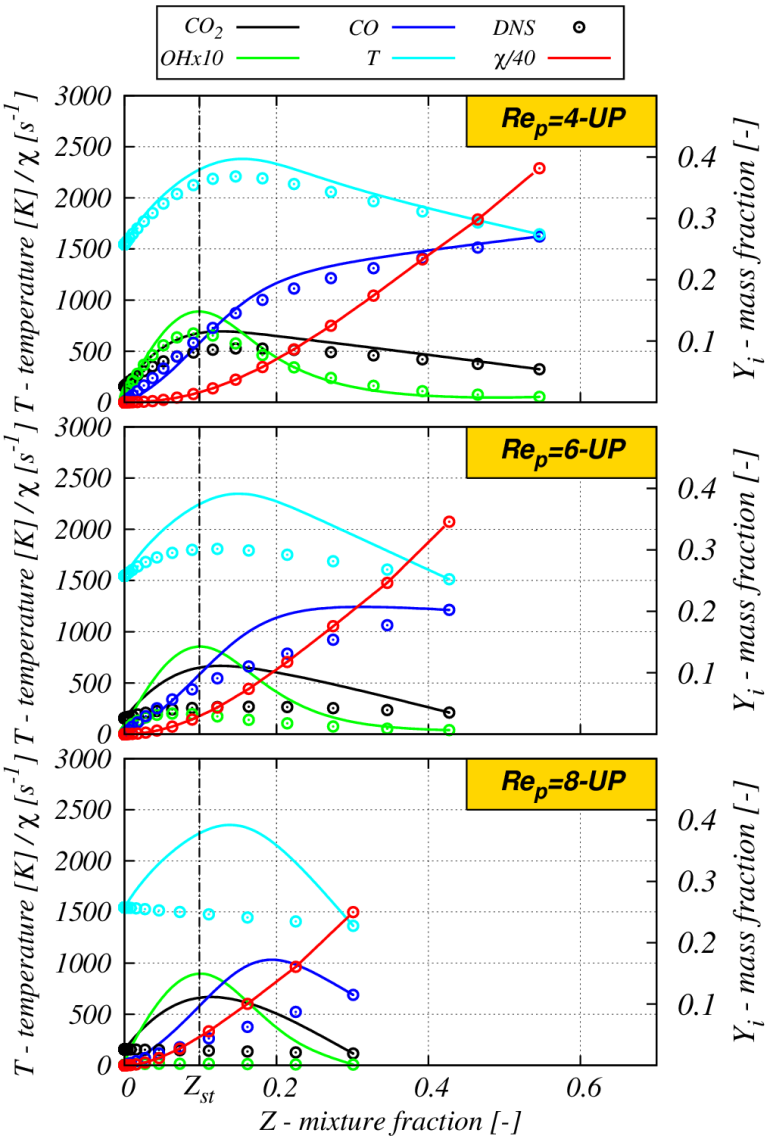

Abbildung 7.4: Results from steady laminar flamelet calculations (lines) compared with corresponding DNS data (circles) for particle Reynolds numbers $Re_p = 4$ (top), $Re_p = 6$ (middle) and $Re_p = 8$ (bottom). The DNS profiles are extracted along the upstream axis of symmetry at the times of maximum devolatilization rate.

but considerably higher temperature, CO_2 and OH mass fractions are predicted by the flamelet, Fig. 7.4 (middle). Similarly, upstream profiles extracted from the case with the even higher $Re_p = 8$ reveal almost no chemical conversion in the DNS, whereas the corresponding flamelet is found to be burning, Fig. 7.4 (bottom). The downstream profiles for $Re_p \geqslant 6$ (Fig. 7.5) exhibit similar discrepancies between DNS and the standard laminar flamelet approach. It is worth analyzing the cause of the deviations between the flamelet model and the DNS data. An obvious source

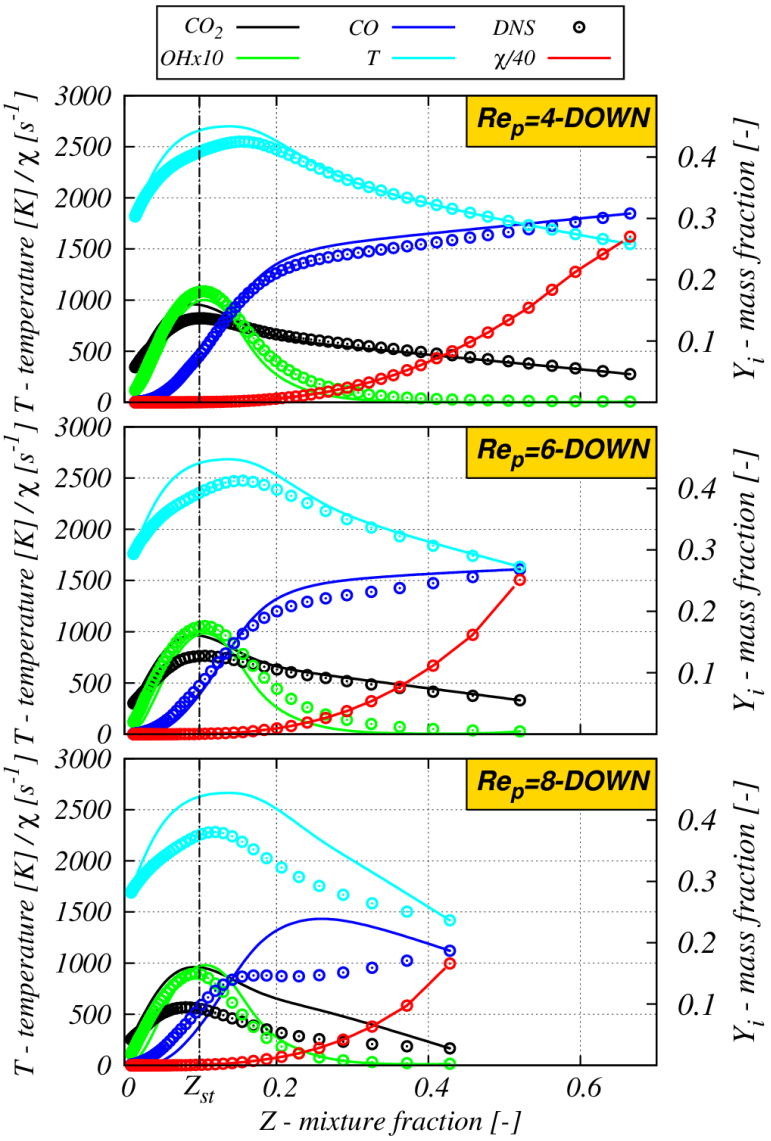

Abbildung 7.5: Results from steady laminar flamelet calculations (lines) compared with corresponding DNS data (circles) for particle Reynolds numbers $Re_p = 4$ (top), $Re_p = 6$ (middle) and $Re_p = 8$ (bottom). The DNS profiles are extracted along the downstream axis of symmetry at the times of maximum devolatilization rate.

of error is the fact that standard non-premixed flamelet results are compared to the DNS, where localized premixing can occur. To this end, it is interesting to extract the flame index ($FI = \nabla Y_{fuel} \cdot \nabla Y_{O_2}$) from the DNS data, where Y_{fuel} is taken to be the sum of all volatile species mass fractions and where opposed gradients of fuel and oxidizer (negative FI) indicate non-premixed combustion, whereas aligned gradients (positive FI) are representative of a premixed flame. Figure 7.6 presents the flame index analysis for two representative Reynolds numbers ($Re_p = 2$ and

$Re_p = 8$) at the instant of maximum devolatilization rate. Prior to ignition (not

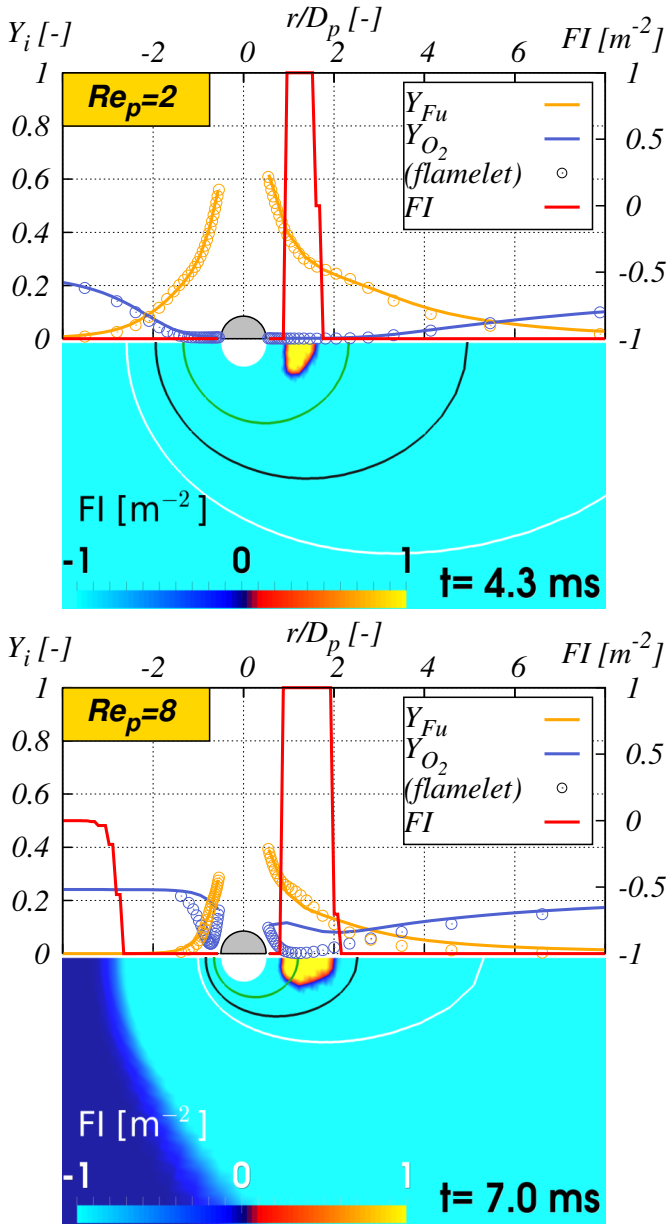

Abbildung 7.6: Analysis of flame index for particle Reynolds number $Re_p = 2$ (top) and $Re_p = 8$ (bottom). The upper frames show axial profiles of the fuel and oxygen mass fractions and the flame index calculated from the DNS results (lines) compared to the results from non-premixed laminar flamelet calculations (circles). The lower frames show flame index contours with the same mixture fraction iso-lines as in Fig. 7.2. The DNS line profiles are extracted along the axis of symmetry at the time of maximum devolatilization rate.

shown) the flame index contours indicate purely non-premixed behavior around the particle, since the fuel (oxidizer) mass fraction monotonously decreases (increases)

with increased distance from the particle surface, such that the gradients are opposed and FI is negative. Once ignition occurs and a volatile flame establishes, a small premixed zone (positive FI) is established in the particle wake for both Reynolds numbers, whereas the rest of the domain shows non-premixed behavior (negative FI) or -further away from the particle- no gradients at all ($FI = 0$), see the FI contours shown in Fig. 7.6. The reason for the formation of the small premixed region can be identified by inspecting the DNS line profiles of Y_{fuel} and Y_{O_2}, particularly for $Re_p = 8$, Fig. 7.6 (bottom, lines): While the fuel mass fraction keeps decreasing with increasing distance from the particle surface both up- and downstream of the particle, the oxidizer mass fraction behaves differently on the two sides of the particle. On the upstream side the fluid strain is too high for chemical reactions to occur, such that Y_{O_2} keeps increasing away from the particle in the DNS. However, the lower scalar dissipation rates on the downstream side allow for chemical conversion, such that Y_{O_2} locally decreases in the volatile flame zone, before increasing again at larger distances and the flame index changes sign. The situation is slightly different at the lower $Re_p = 2$, where a stable envelope flame forms around the particle and chemical reactions occur on both sides. In this case the oxidizer mass fraction (and its gradient) very close to the particle is near zero and the flame index becomes difficult to interpret. However, the DNS data also indicates largely non-premixed behavior for $Re_p = 2$, except for a very small premixed region in the particle wake, similar to the result for $Re_p = 8$. In agreement with the findings of Zhang *et al.* [157] the location where the volatile flame can ignite and stabilizes coincides with the position of transition between the two mixing regimes. As already discussed for Fig. 7.3 the cross-comparison of the flamelet (circles) and DNS (lines) profiles in Fig. 7.6 shows that for $Re_p = 2$ the non-premixed flamelet correctly predicts the DNS trends on both sides of the particle, despite the small premixed region downstream. In contrast, at $Re_p = 8$, the non-premixed flamelet over-predicts the rate of chemical reactions right at the particle, as can be seen from the significantly lower oxygen mass fractions compared with the DNS result, again irrespective of the particle side and the combustion regime indicated by the flame index. It can be concluded that small, localized deviations from the regime of non-premixed combustion do not seem to be the cause for the unfavourable performance of the non-premixed flamelet model at high Re_p. This finding is in line with the analysis conducted by Scholtissek *et al.* [112], who performed a multi-scale asymptotic scaling and regime analysis of flamelet equations and considered the effects of tangential diffusion. The authors found that highly strained and curved flames can be

dominated by multi-dimensional effects, which stem from local misalignment of the mixture fraction and reacting scalar fields. Such multi-dimensional effects are not present for planar or perfect spherically symmetric flames ($Re_p \rightarrow 0$), but dominate for elongated flames with curvature like the wake flames found at the highest Re_p here. In particular, when assuming a unity Lewis number, the multi-dimensionality can be related to a single dominant term [112]. This term is not present in the standard flamelet formulation (Eq. (2.21)) and a further detailed analysis of such effects would be warranted. However, the present study focuses on the effects of Reynolds number and turbulence in the DNS and a detailed flamelet analysis can be subject of future research. Figure 7.7 (bottom) shows a scatter plot of gas temperature vs. mixture fraction for $Re_p = 8$, now extracted from the entire DNS domain, at the time of maximum devolatilization. For convenience Fig. 7.7 (top) shows the same data for the reference case ($Re_p = 2$) that was already discussed in Chap. 6. The

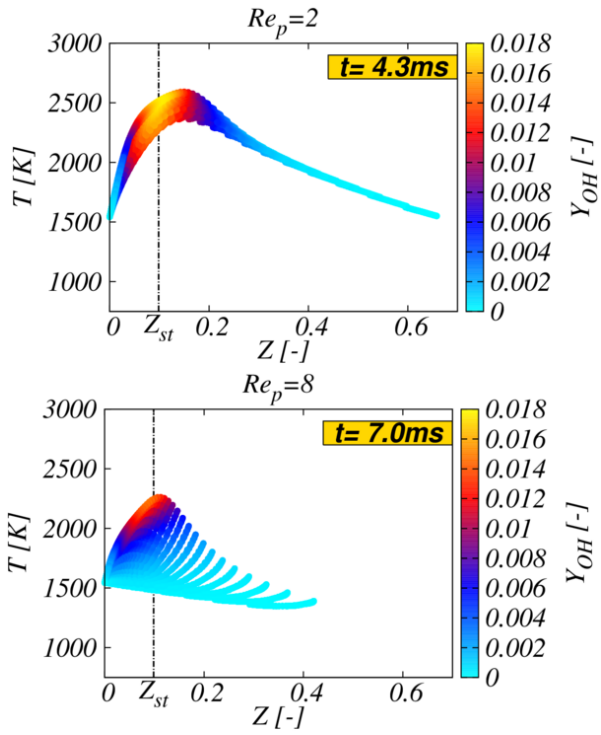

Abbildung 7.7: Scatter plot of gas temperature as a function of mixture fraction, colored by Y_{OH}, at the time of maximum devolatilization rate for a single particle with $Re_p = 8$.

cross-comparison of the two Re_p shows that lower peak mixture fraction values and maximum temperatures are reached at high Re_p. In addition, the range of chemical states that can be obtained at $Re_p = 8$ is significantly larger than at $Re_p = 2$, as can be seen from the wide span of gas temperatures at each Z for all intermediate

mixture fraction values. Figure 7.8 shows the temporal evolution of various quantities that govern the devolatilization and combustion process for the considered range of Re_p, namely particle surface temperature, devolatilization rate and maximum gas temperature (top), as well as particle surface mixture fraction and scalar dissipation rate (bottom). It can be observed that increasing Re_p leads to delayed ignition, as can be seen from the increased delay of the rise of the maximum gas temperature (green lines). As a consequence, the flame reaches the vicinity of the particle later, which delays gas-particle heat transfer and shifts both the increase in particle surface temperature (blue) and the related rise of the devolatilization rate (red) to late times. At high Re_p the flame remains confined to the wake region and in Fig. 7.8 it can also be seen that particularly for the highest $Re_p = 8$ all quantities reach far lower peak values than at low Re_p. This is due to the overall more gentle volatile release under these extreme flow conditions, which alter the particle heating and -in turn- devolatilization behavior. The evolution of the mixture fraction at the particle surface (black) is analogous to the particle surface temperature, in line with the temperature dependence of the devolatilization model. The scalar dissipation rate profiles (cyan) show a trend of first increasing and then decreasing overall profile magnitudes. Furthermore, for low Re_p the profiles of χ_{max} initially increase, followed by plateaus at intermediate times 2.5...4ms, during the wrapping process around the particle, before a further increase and then final decrease. A similar trend is found at the highest $Re_p = 8$, albeit shifted to late times and considerably less pronounced, as the flame never envelopes the particle in this case. The results presented in this section seem counter-intuitive at first, given standard (steady-state) film theory models for droplet and coal combustion, where increased convection results in sharper scalar gradients near the surface, which leads to stronger heat transfer towards, and faster mass release from the dispersed phase [131]. However, the fact that scalar gradients are steeper upstream, but lower downstream of the particle and that strong convection can lead to partial volatile flame extinction as shown in Fig. 7.2 cannot be captured by simple film models. A quantitative estimate of the extent of such modeling errors is obtained by comparing the present DNS results to standard film theory predictions based on Nusselt number correlations [131], relating the mass release rate of a coal particle in a convective flow to its value in quiescent conditions,

$$(\dot{m}_v)_{convective} = \frac{Nu}{2}(\dot{m}_v)_{quiescent}, \tag{7.1}$$

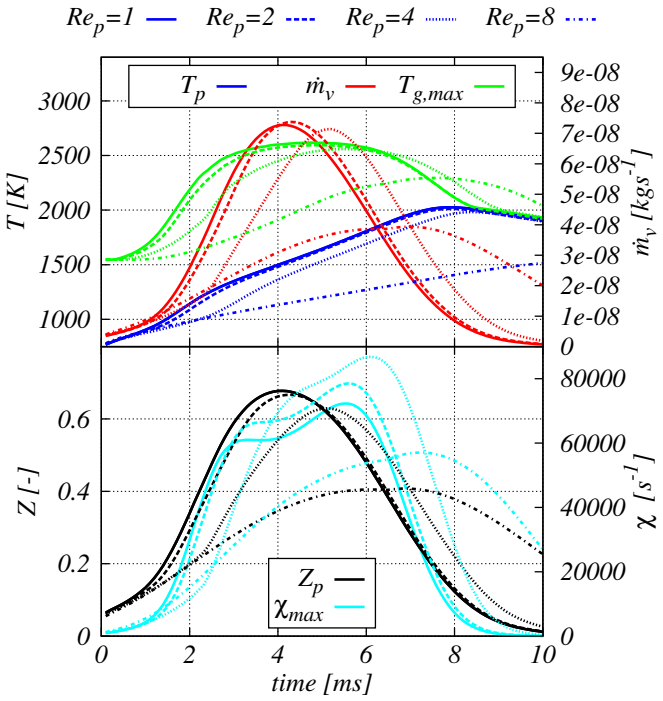

Abbildung 7.8: Temporal evolution of various quantities governing the devolatilization and burning process for a single particle at various Re_p. Top: Particle surface temperature (blue), devolatilization rate (red) and maximum gas temperature (green). Bottom: Mixture fraction (black) and scalar dissipation rate (cyan), both extracted at the particle surface.

where for the Nusselt number Nu the following approximation, obtained for the analogous problem of a burning droplet [32], can be used

$$Nu = 2 + \frac{0.555 Re_p^{1/2} Pr^{1/3}}{[1 + 1.232/(Re_p Pr^{4/3})]^{1/2}}. \tag{7.2}$$

In the present DNS the peak devolatilization rate $\dot{m}_{v,max}$ decreases to 54% of its reference value at quiescent conditions and the time for reaching $\dot{m}_{v,max}$ increases by 51% when increasing Re_p from 0 to 8. In contrast, using standard film theory (Eq. (7.1)) and a Nusselt number correlation (Eq. (7.2)) results in an increase of $\dot{m}_{v,max}$ across the same range of Re_p and a maximum deviation from the DNS result by 66% (for $Re_p = 8$). While these numbers may be strongly affected by the chosen simple models for the present comparison, they serve to illustrate that using simple subgrid models for LES may lead to significant errors and even qualitatively wrong trends.

7.2.1.2 Particle Array Combustion

Figure 7.9 shows OH and O_2 mass fraction contours for a row of three particles with inter-particle distance $L_x = 5D_p$ for different values of Re_p at the time of maximum devolatilization rate of the most upstream particle for each condition. The increase

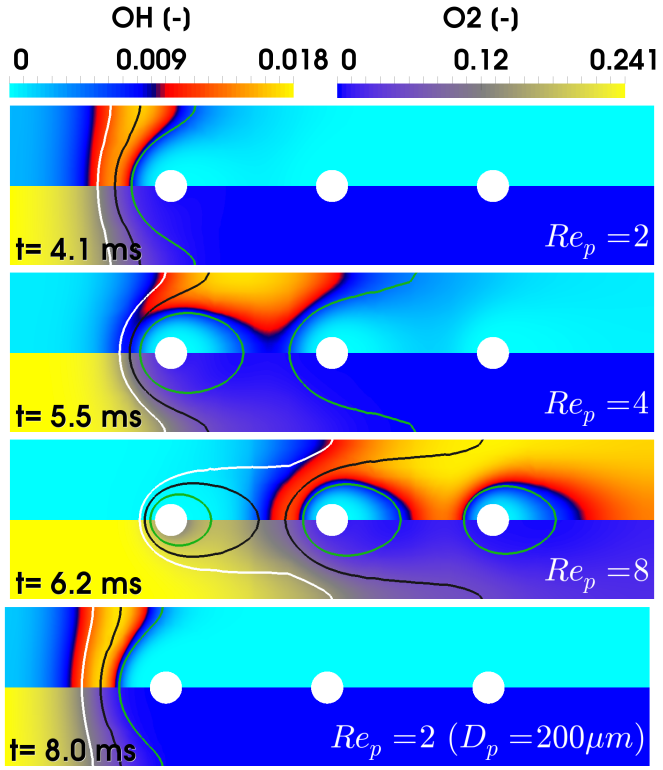

Abbildung 7.9: Row of three particles with $L_x = 5D_p$ for different Re_p obtained by changing the inflow velocity (top three frames) or the particle diameter (bottom frame). Y_{OH} (top of each frame), Y_{O_2} (bottom of each frame) contours at the time of maximum devolatilization rate of the first particle. Mixture fraction iso-lines as per Fig. 7.2.

of Re_p by a factor of four leads to increasingly steeper mixture fraction gradients and consequently higher scalar dissipation rates. As a result, scalar dissipation rates locally exceed extinction values, which leads to highly strained regions where no combustion can be sustained despite the presence of a stoichiometric mixture. This can be seen for $Re_p = 4$ where OH mass fractions at stoichiometry on the symmetry axis in front of particle 1 have significantly decreased compared with $Re_p = 2$, and the regions of maximum Y_{OH} are located near the cross-stream domain boundary, i.e. close to the next particle row in the cross-stream direction. Similar to what has been discussed for the single particle subject to various Re_p, Fig. 7.2, this is because local scalar dissipation rates rapidly decrease along the stoichiometric iso-line, from their

maximum at the upstream stagnation point to much lower values, here located near the boundary. However, despite significantly lower mixture fraction gradients (scalar dissipation rates) in the wake of particle 1, the region of high Y_{OH} does not reach the axis of symmetry since there is not enough O_2 left to burn. Similarly, the region between particles 2 and 3 and further downstream is completely devoid of oxygen and no flame can be sustained. Further doubling the particle Reynolds number from 4 to 8 results in a condition, where the stoichiometric region surrounding the foremost particle has ceased to overlap with the one from particle 2. Instead, the stoichiometric contours of particles 2 and 3 have merged to form a single bell-shaped structure around them. Despite the stoichiometric region completely enveloping the first particle, no significant chemical conversion can be observed. Different from the single particle subject to the same Re_p (bottom of Fig. 7.2), not even a wake flame can be found when the (same) particle is located in the front plane of an array at the present L_x. However, a large flame region wraps around particles 2 and 3 and touches the cross-stream domain boundary, i.e. the downstream flame interacts with the nearby particles of the array, which are located at the same axial position. As already discussed in Sec. 7.2.1 standard laminar flamelet models deliver increasingly less favorable predictions of the highly strained and curved flames observed here when Re_p is increased. Additionally, at the low inter-particle spacing tested here, interaction effects become important and no simple explanation of the observed flame structure based on standard flamelets can be given. In Fig. 7.9 (bottom) the same particle Reynolds number $Re_p = 2$ is established as previously in Fig. 7.9 (top). However, $Re_p = 2$ is now obtained by doubling the particle diameter to $D_{p,*} = 200\mu$m, but halving the inflow velocity, while the (relative) inter-particle spacing is kept fix at $L_x = 5D_{p,*}$. The results do not qualitatively change as can be observed by comparing Fig. 7.9 (bottom) and (top). However, the decrease of U_{rel} affects the characteristic time scale of the flow and therefore a longer period is required to reach identical conditions (4ms vs. 8ms).

7.2.2 Effect of Turbulence

After studying the effect of Re_p for laminar flow, DNS with turbulent inflow conditions are conducted. As discussed in Sec. 7.1 a wide range of inflow turbulence conditions is considered. However, for small to moderate turbulence levels u'/U_{rel} (including the most likely value $u'/U_{rel} = 0.25$ from the LES) the only impact of turbulence on the qualitative flame behaviour is a flapping motion of the particle wakes and reacting scalar fields, whereas the transient devolatilization behaviour

does not change substantially. To still reflect the impact that strong local sub-grid turbulence may have, the more extreme condition $u'/U_{rel} = 1.0$ is chosen for the majority of the results presented in this section and only the global impact of a more likely local turbulence level $u'/U_{rel} = 0.25$ is discussed at the end. Figure 7.10 shows a 2D slice through a 3^3 particles array at $L_x = 10D_p$ and $Re_p = 8$, which compares the contour of OH mass fraction for laminar and turbulent flow conditions with $u'/U_{rel} = 1$. The laminar case is shown at the time of maximum devolatilization

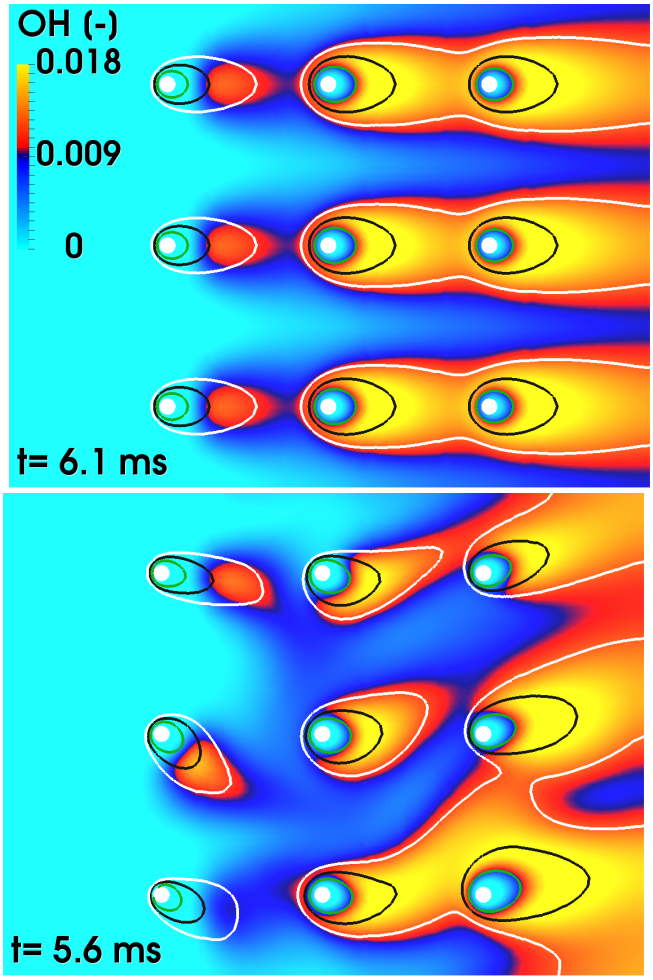

Abbildung 7.10: Array of 3^3 particles with $L_x = 10D_p$ and $Re_p = 8$ in laminar (top) and turbulent ($u'/U_{rel} = 1$, bottom) flow conditions. Y_{OH} contours at the time of maximum devolatilization rate of the first set of particles. Only the middle x-y-plane in the z-direction is shown. Mixture fraction iso-lines as per Fig. 7.2.

rate of the most upstream set of particles, whereas a snapshot of the turbulent case has been selected arbitrarily at a similar time and for comparable devolatilization rates. Considering the transient behavior of the laminar case (not shown) it is found that for the given L_x and Re_p the most downstream set of particles ignites first,

which is swiftly followed by the middle set of particles, such that stable volatile flames form around the two downstream particles of each row, with significant values of OH in the mixture fraction range $Z_{st}/2 \leqslant Z \leqslant 2Z_{st}$ (top of Fig. 7.10). This early ignition of the two downstream particle sets (at around 2...3ms) is later followed by ignition of the most upstream volatile flames which occurs at around 4...5ms. These front volatile flames are fully subjected to the incoming flow at high relative velocity, which heavily strains them and leads to partial flame extinction, as already discussed for the single particle at the same Re_p in the context of Fig. 7.2. The downstream particle sets reach their peak devolatilization rates at 5ms, followed by the peak rate of the upstream particles at 6.1ms, shown in Fig. 7.10, after which all particles deplete their volatiles until complete volatile flame extinction. Turbulence changes this transient behavior as follows: The turbulent eddies in the size range $\eta \leqslant l \leqslant L_{int}$ are typically larger than the extent of the flame structure such that the flames are mostly subjected to (relative to the particle diameter) large scale motions that cause them to flap around the particles. As can be seen in the turbulent snapshot (bottom of Fig. 7.10) this flapping motion can lead to the instantaneous detachment of the two downstream volatile flames which are stably joined to a single flame for each row in the laminar case. Furthermore, the turbulent motions can locally strain the flow around the first particle to such an extent, that the flame structure is strongly affected and local OH mass fractions decrease to half their peak value ($Y_{OH,max} \approx 0.018$) and less, see the lower left particle in Fig. 7.10 (bottom). Due to the randomness of turbulence also the inverse effect can occur, where the strain around the first particle set locally decreases below the typical values for the laminar case at this Re_p, such that higher OH concentrations can be sustained. To analyze how turbulence affects the probability of various chemical states in the gas phase within the array, Fig. 7.11 presents PDFs of the OH mass fraction conditional on mixture fraction for different zones in the computational domain, for the laminar (left column) and turbulent (right column) case. In addition, mean values of Y_{OH} conditional on mixture fraction are plotted as black lines. The top row of Fig. 7.11 shows data extracted from the entire computational domain, whereas the rows below show reduced datasets corresponding to the zones previously defined in Fig. 7.1. Comparing the conditional PDFs from the entire domain with the OH contours in Fig. 7.10 shows that for the laminar case two main branches of OH mass fraction can be identified. The upper branch corresponds to the stably burning flames around the downstream particle sets and the lower branch, where near-zero OH mass fractions occur even around Z_{st}, corresponds to the highly

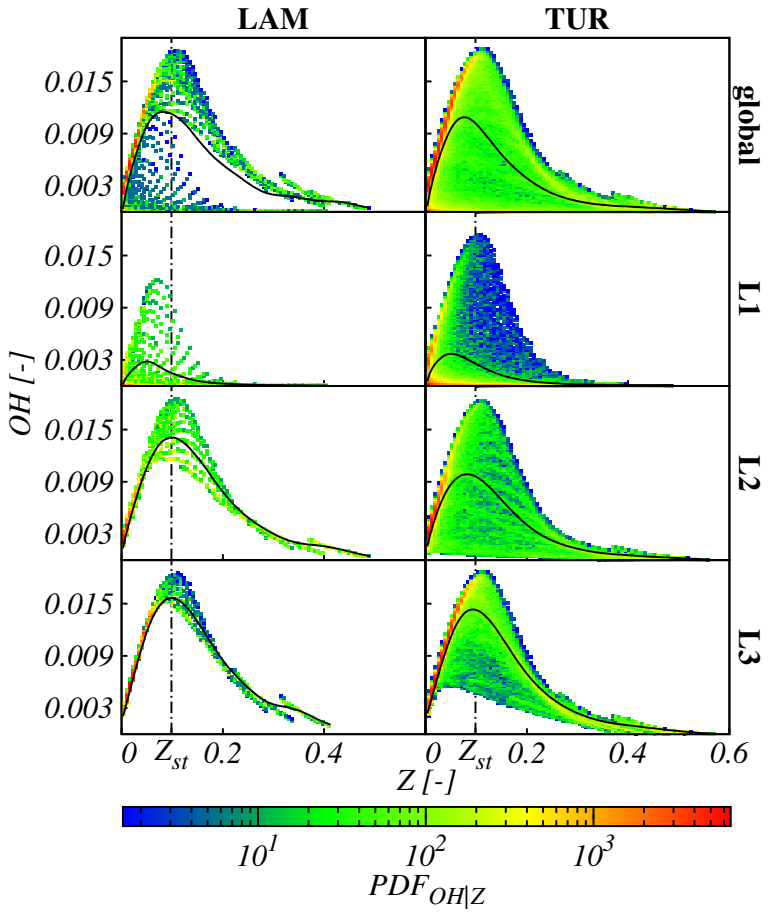

Abbildung 7.11: PDF of Y_{OH} conditional on mixture fraction (colormap) and conditional mean (black solid line) for different layers within an array of 3^3 particles for laminar (left) and turbulent ($u'/U_{rel} = 1$, right) conditions extracted at times corresponding to Fig. 7.10. The data for the top row is extracted from the entire computational domain, whereas the lower three rows correspond to the zones L1-L3 introduced in Fig. 7.1.

strained, partially extinguished flames around the upstream particle set. Comparing laminar and turbulent conditions it can be observed that the entire range of possible OH mass fractions between the two branches is filled for the turbulent case, whereas there are non-existing chemical states (white regions in the middle of the plot) for the laminar case. Overall, turbulence leads to increased strain rates such that Y_{OH} can locally decrease and as a net result the conditional mean value of OH across the entire domain is (mildly) decreased. Figure 7.11 (second row) compares the same quantities for zone L1 around the upstream particle set. Similar to Fig. 7.11 (first row) the laminar case shows a pattern, which reflects the fact that the conditional PDF corresponds to an ensemble of all possible flamelets between the fuel and oxidizer streams around the particles. Here, an (imaginary) curve through the set of

non-zero PDF counts for the highest OH values corresponds to a flamelet extracted along the downstream coordinate, where the highest chemical conversion occurs (see top of Fig. 7.10). Further curves with increasingly lower OH peak values can be identified, which correspond to flamelets extracted along all radial lines between the downstream and upstream axis of symmetry, where at this Re_p the upstream flamelet is fully extinguished (see also Fig. 7.2 at $Re_p = 8$). The äverage"flamelet for all radial lines extending from the nine particles at the most upstream location is represented by the conditional mean mass fraction curve. Moving to the turbulent case, it can be observed that turbulence leads to a wider distribution of chemical states for each mixture fraction, as can be seen from the larger number of blue values (low, but non-zero occurrences). As already discussed for Fig. 7.10, turbulence can both increase and decrease the local strain rate instantaneously and therefore hamper or support chemical conversion. Considering the conditional means in zone L1 it is found that turbulence slightly enhances the chemical conversion around the first particle set, as the conditional mean OH mass fraction increases from a peak of 0.003 (laminar) to approximately 0.004 (turbulent). It is important to note that at the chosen high Re_p the first set of particles burns pretty much independently of the two downstream particle sets. This is considerably different for the second particle set, the conditional PDFs of which are compared in Fig. 7.11 (third row). The second and third particle sets are enveloped by joint volatile flames for each particle row in the laminar case, but individual volatile flame burning can locally and instantaneously occur for turbulent conditions, as for example the central particle in Fig. 7.10 (bottom). This can further be observed in Fig. 7.11 (third row), where the laminar case shows only a single major burning branch and considerably less pattern formation compared to L1, corresponding to a stable envelope flame, whereas for turbulence almost any mass fraction of OH can occur for each mixture fraction. This is because instantaneously the turbulent volatile flames in zone L2 can extinguish, particularly on the upstream side (bottom of Fig. 7.10). As a result, the overall chemical conversion in zone L2 is significantly decreased and the peak conditional mean Y_{OH} reduces from 0.014 (laminar) to 0.010 (turbulent). The same effect can be observed in the most downstream zone L3. Turbulence leads to the occurrence of partially extinguished states on the upstream side of the particles, albeit less pronounced than in zone L2. As a result, a wider distribution of chemical states can be observed for turbulence, whereas a single flamelet suffices to describe the downstream laminar envelope flames. In L3 the difference of the peak conditional OH mass fraction is 0.016 (laminar) compared with 0.014 (turbulent). Naturally, the

impact of turbulence discussed in Figs. 7.10 and 7.11 is dependent on the chosen snapshot for the turbulent case. However, the discussed findings represent typical conditions, the net effect of which is a cumulative impact on the volatile release rate of particles at different downstream positions within the array. Figure 7.12 shows the cumulative volatile mass release m_v of different particles as a function of time for laminar and turbulent conditions. The continuous lines show the average volatile

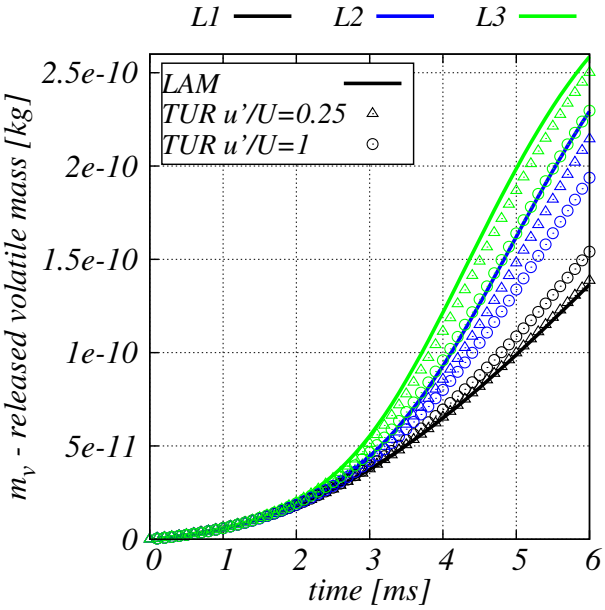

Abbildung 7.12: Temporal evolution of the cumulative volatile mass released from particles located in different layers (i.e. downstream positions, cf. Fig. 7.1) within the 3^3 particles array. Each layer is represented by the average mass released by its composing particles for laminar (lines) and turbulent (symbols) conditions.

mass released from a particle in layers L1 to L3 as defined in Fig. 7.1 for laminar and turbulent flow, where the turbulent results are given for $u'/U_{rel} = 1$ (circles) and for the mostly likely value from the LES, i.e. $u'/U_{rel} = 0.25$ (triangles). While m_v increases slightly earlier with turbulence for the most upstream particle layer L1, for both the middle (L2) and downstream (L3) particle layers the cumulative mass release is considerably delayed under the effect of turbulence. The decreased level of devolatilization in L2 and L3 is due to the altered degree of volatile flame interaction. The stably interacting laminar volatile flames lead to strong particle heating and fast devolatilization, whereas heat transfer to the downstream particles from their -typically weaker- single volatile flames is lower for turbulence, which in turn leads to a lower devolatilization rate. Conversely, for the most upstream particles in L1 that are only heated at their backside by a relatively faint wake flame for laminar

flow at the present Re_p (cf. Fig. 7.10, top), turbulence can lead to a more uniform and overall faster heating of the particles, which leads to a slightly earlier increase of the released volatile matter. However, due to the overall considerably weaker wake flames around the particles in L1 compared with L2 and L3 this effect is less pronounced. For L1 the transient behaviour of m_v is unaffected by small turbulence levels up to $u'/U_{rel} = 0.25$ and only a mild increase of the released volatile matter can be observed for the more extreme condition $u'/U_{rel} = 1$.

7.3 Summary for Particle Reynolds Number and Turbulence Effects

The present chapter completes the fully-resolved DNS study of pulverized coal particle pyrolysis and volatile combustion from Chap. 6 by investigating a wide range of typical particle Reynolds numbers Re_p and representative turbulence conditions from the reference LES [108]. For single particles, increasing Re_p leads to delayed ignition, gradually more prominent asymmetry of the volatile flame and a decreased combustion intensity, which results in a flame that ceases to envelope the particle for $Re_p \geqslant 6$ due to high upstream scalar dissipation rates. The attempt of modeling these conditions by steady laminar flamelet calculations based on local scalar dissipation rates extracted from the DNS shows that the standard flamelet model accurately captures the flame structure at low Re_p. However, at high Re_p the flames are dominated by curvature and multi-dimensional effects [112] and cannot be modeled with a standard flamelet formulation. It is also found that modeling the effect of convection on devolatilization by standard film theory may lead to qualitatively wrong trends and up to 66% error in the peak devolatilization rate when compared to the DNS results for $Re_p = 8$. Extending the analysis to multiple particles aligned in streamwise direction, the interaction among the particles is found to be strongly affected by Re_p, where very large Re_p tends to extinguish the volatile flame(s) around the upstream particles and leads to strong interactions of the flames around the downstream particle sets. Results for turbulent flow conditions show that a wide range of additional chemical states can be observed with respect to the corresponding laminar case. This is due to the randomness of turbulence, which alternately acts to increase or decrease the local strain, and to weaken or enhance particle interaction. A zonal analysis shows that, at the most upstream particle layer, turbulent motions can locally reduce the strain below the critical values that prevent combustion for the laminar case. As a result the chemical reactions in this region are slightly promoted

by turbulence, as indicated by an increased OH production. Conversely, the stable envelope flame around the remaining downstream particle layers in the laminar case is strongly perturbed by flapping turbulent motions, which leads to instantaneous flame detachments and local extinction events. The OH release is therefore instantaneously reduced as indicated by lower peak conditional means. These observed instantaneous differences result in an analogous cumulative impact on the heating rate history and volatile matter release of the respective particles. The DNS results presented here, as well as in Chap. 6, provide LES sub-grid information, and can be used for LES model development and validation.

Chapter 8

Fully-Resolved Simulations of Coal Particle Combustion Using a Detailed Multi-Step Approach for Heterogeneous Kinetics

The simulations performed in Chap. 5-7 were based on limiting -albeit reasonable- assumptions such as pre-fitted single-step devolatilization, simplified particle interior properties and a fixed (presumed) volatile composition based on relatively small hydrocarbons. This allowed the use of an effective but relatively affordable skeletal mechanism to describe the homogeneous chemistry. Furthermore, heterogeneous char conversion reactions were neglected. This simplified approach was validated in Chap. 5 and allowed to characterize the ignition and volatile burning behavior of single coal particles and particle arrays under different operating conditions by means of 3D fully resolved computations, as presented in Chaps. 6 and 7. However, the physico-chemical processes occurring inside the coal particle, the presence of heavy hydrocarbons in the mixture released by the particle, the effects of porosity and char combustion were omitted from the analysis. These phenomena, though, might have an impact on the observed coal particle burning behavior.

Therefore, significant level of model fidelity and generality are added here, in particular with regard to the particle interior description and heterogeneous kinetics. This is done by applying the detailed approach for heterogeneous coal conversion presented in Sec. 3.2. The approach uses a detailed multi-step mechanism for heterogeneous kinetics, coupled to detailed homogeneous chemistry. The mass release rate and species composition of the complex mixture of volatiles and heavy tars released

from the particle are dynamically predicted. A detailed description of the particle interior is also introduced, with time-evolving porosity and tortuosity that lead to an internal fluid flow of gas allowing for intra-particle oxygen diffusion that triggers the heterogeneous char reactions.

The improved model description results in a significantly higher computational cost and it is therefore applied here to 2D (laminar) flow only. In particular, fully-resolved simulations of the heating, ignition, volatile flame combustion and char conversion of single coal particles in convective gas environments are conducted, reproducing the same experimental setup and data taken as reference in Chap. 5.

The results presented in this chapter have been published in *Fuel* 240:75-83 (2019) [126].

8.1 Experimental and Computational Setup

The experiments by Molina & Shaddix [79] on single particle ignition presented in Sec. 5.1.1 are taken again as reference for the numerical simulations, this time attempting to predict the measurements applying the refined modeling approach presented in Sec. 3.2. Therefore, the computational setup considered here extends the one previously reported in Sec. 5.1.2. Figure 8.1 shows the two-dimensional, axisymmetric, multi-region domain, which is 100 particle diameters ($D_p = 0.1$mm) long, 33.5 D_p wide and set up as a 5° wedge, as rotational symmetry in laminar flow has been assumed. Differently to Chap. 5 that was based on a single-rate pyrolysis

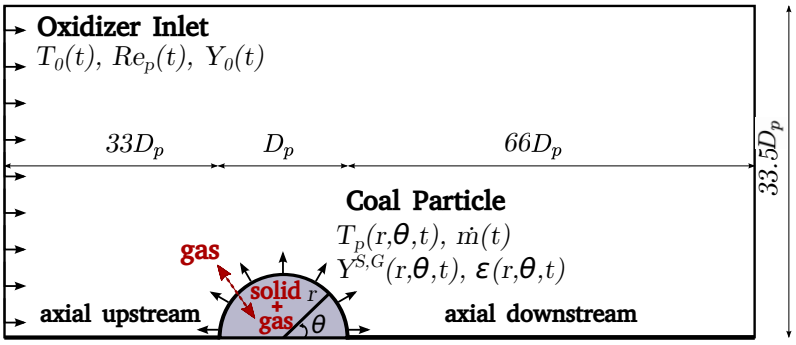

Abbildung 8.1: Computational domain for the resolved laminar simulation.

model (Eq. (3.12)) applied at the particle surface and neglected the particle interior flow and char conversion, the solid region is now modeled as a porous medium, characterized by the porosity ε (Eq.(3.33)), allowing for the presence of a fluid flow of gaseous species which are transported through the particle pores (Eqs. (3.19), (3.23)

and (3.25)). This allows not only for the release of the formed volatiles into the surrounding mixture, but also for the oxygen inflow through the particle pores that triggers the oxidation of the char. Therefore the composition inside the solid region varies in time as the coal thermal conversion proceeds. The assumed initial composition for the Pittsburgh seam high-volatile bituminous coal has been reported in Tab. 3.4 in terms of the reference coals COAL1, COAL2 and COAL3. These are used to describe the chemical-kinetic properties of the coal of interest by means of linear interpolation, cf. Sec. 3.2.4, dynamically predicting the rate and composition of the particle mass release. In particular, the species that the particle releases, include light volatile gases and heavy hydrocarbons representing tars which are modeled as lumped species (cf. Tab. 3.5). In order to accurately describe the oxidation of the resulting complex mixture, a version of the detailed POLIMI_TOT_1407 kinetic model, reduced down to 76 species and 973 homogeneous reactions, is used here (cf. Sec. 3.2.4). This is a key difference with respect to Chap. 5 where the particle was assumed to release hydrocarbons up to C_6H_6, allowing for a much more simplified description of the homogeneous gas-phase kinetics.

At the left boundary of the domain, mixtures of hot combustion products, cf. Tab. 5.1, are introduced as transient boundary conditions. These transient BCs are obtained, as for Chap. 5, from auxiliary Euler-Lagrange simulations of the Hencken burner [135], which resulted in the time-varying oxidizer temperatures $T_0(t)$ and particle Reynolds numbers $\mathrm{Re}_p = U_{rel}\, D_p/\nu = f(t)$ presented in Fig. 5.2. The initial values from the auxiliary simulations are also used to initialize the (particle exterior) computational domain for the fully-resolved simulation.

For the solid coal particle the same values of ρ^S=1400 kg/m^3, c_p^S=1680 J/(kg·K) and λ^S=0.3 W/(m·K) as in Chap. 5 are considered. As reported in [73], the heat of pyrolysis is less than 1% of the combustion heat and has therefore been neglected, whereas the heats of the heterogeneous reactions are calculated, considering the enthalpy of formation of the gas species only [73]. The initial particle porosity and tortuosity in Eqs. (3.33) and (3.35) are set to $\varepsilon_0 = 25\%$ and $\tau_0 = \sqrt{2}$ as estimated in [73]. The initial particle temperature T_p^0 is set to 350K after performing sensitivity analyses using the Euler-Lagrange set-up, exploring the effects of different boundary conditions at the furnace inlet. This T_p^0 is lower than the one previously reported in Chap. 5, where a significant particle pre-heat was assumed and a parameter study of T_p^0 was shown. However, subsequent Euler-Lagrange simulations predicted a significantly smaller pre-heat and $T_p^0 = 350$K is considered for all cases.

Based on the previous grid analyses (Sec. 5.1.2), the boundary layer around the

particle is fully resolved with 20 cells in the radial and more than 70 cells in the circumferential direction, with a characteristic cell width of $0.02D_p$ both in the external gas phase and in the particle interior. The envelope flame is also resolved with at least 20 cells. The simulations are performed with the customized OpenFOAM solver coupled with the *OpenSMOKE++* library, as described in Sec. 4.3.2. Note again that different sets of equations are solved in different areas of the multi-region domain: The standard gas phase conservation equations are solved for the particle exterior, while the complex intra-particle two-phase model described in Sec. 3.2 is solved for the particle interior (grey area in Fig. 8.1). A variable time step is used and a Courant number $\mathrm{Co} \leqslant 0.5$ is enforced for stability and accuracy in all simulations. The chemistry solver is subject to further sub-stepping and not affected by Co. Simulations are typically run on 24 Xeon cores, requiring about 80h of wall time to reach ignition and up to 200h until the 60 ms of physical time presented here are simulated.

8.2 Results

The sequence of ignition and burning of the coal particle is illustrated in Fig. 8.2, where the experimental condition N_2-21 of [79] is chosen as a representative example for all cases from Tab. 5.1. After an initial stage of particle heat-up that triggers the volatile matter release from the particle to the surroundings (not shown), homogeneous gas phase ignition occurs at 29.5ms, as indicated by the significant amounts of OH and elevated temperature that can first be observed in the particle wake (29.5ms) and which quickly envelope the entire particle (29.6ms). Up to this point the ignition sequence is identical to the one described for the simpler model, which did not account for the particle interior flow, was based on a single-step pyrolysis model and neglected char conversion. In that case, the envelope flame would continue to burn continuously at a small stand-off distance from the particle and extinguish after volatile depletion as observed in Sec. 5.2. However, with the present detailed porous-media model that includes char conversion a significantly different burning behavior is found. After ignition the volatile flame immediately consumes the light volatile gases available in the vicinity of the particle, whereas more time is required for the decomposition of the heavy tars. In addition, as more volatiles are produced inside the particle, they need to overcome the resistance of the porous medium before they can be released to the particle exterior gas phase. This effect is particularly strong for the heavy tar species, which are transported through the

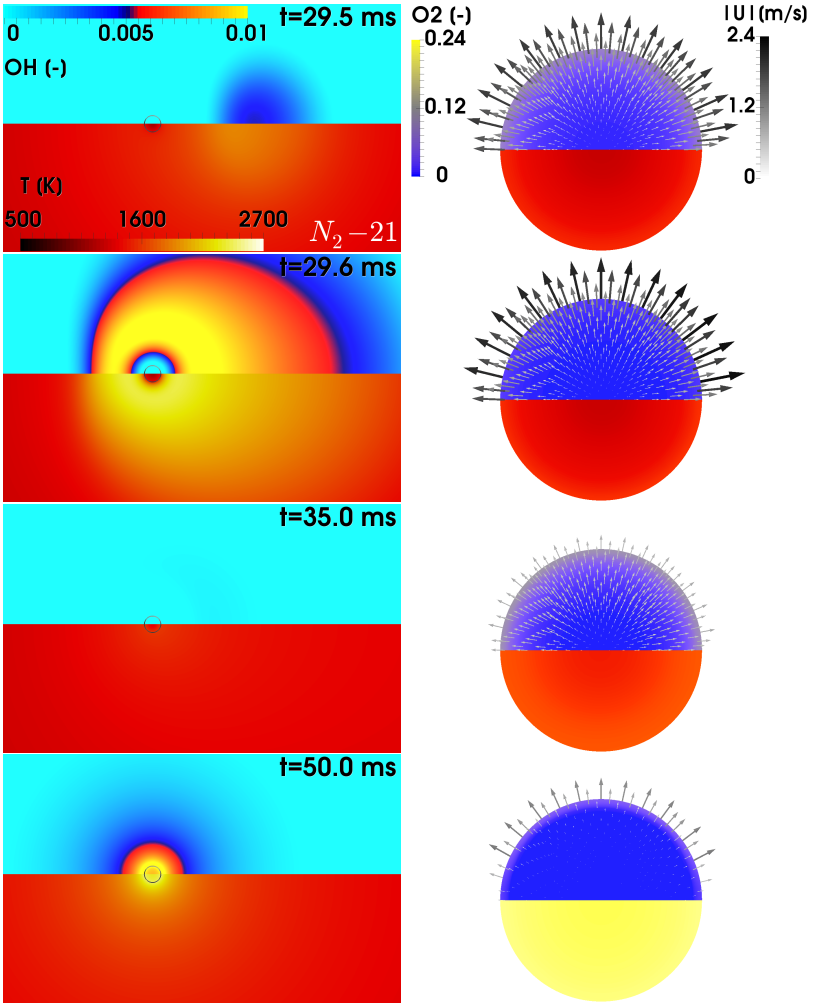

Abbildung 8.2: Selected time instants during ignition and combustion of a coal particle immersed in the N_2-21 mixture, where the particle surface is marked by a circle. **Left:** Mass fraction Y_{OH} (top frames) and temperature (bottom frames) contours *in the vicinity* of the particle, **Right:** Velocity vectors colored by magnitude, mass fraction Y_{O_2} (top frames) and temperature (bottom frames) contours for the *particle interior*.

particle pores more slowly. This delay causes the flame to slowly lose combustion intensity and the peak OH mass fractions and temperature observed at 29.6ms start to decrease until no elevated Y_{OH} and temperature indicative of a flame remain, see Fig. 8.2 (35ms). After this, due to the ongoing release of volatile matter and the decomposition of the large tars between 30 and 35ms, chemical reactions occur right at the particle surface and start to form further OH and to increase temperature again. From this moment onwards, the heterogeneous char reactions promote the formation of chemical species and heat release at the particle surface. The mass and heat provided at the surface diffuse away, both towards the surrounding gas

phase and into the particle interior, forming an extended circular region around the particle where chemical conversion occurs. This region continues to expand radially with its largest extent (roughly 1.5 particle diameters as judged by the OH contour) shown in Fig. 8.2 (50ms, left). After 50ms chemical reactions continuously reduce in intensity until no OH is left and the temperature field reduces to the single value of the furnace temperature (not shown), which indicates the end of the conversion process. On the right of Fig. 8.2 the O_2 mass fraction, temperature and velocity vectors in the particle interior for the same time instants are shown. It can be observed that ignition occurs when the particle temperature is approximately the same as the one of the surrounding gas phase and during a phase of high mass release (peak velocities of 2.4m/s) from the particle. During the subsequent phase of cool-down and radical depletion in the initial volatile flame the mass release from the particle decreases, while the particle is mildly heated by its (still hotter) surroundings. After 35ms the secondary (surface) ignition event happens, this time due to the heterogeneous conversion of the char, which leads to a continuous heat-up of the particle and again increased levels of mass release from the particle as shown in Fig. 8.2 (50ms, right). Since the velocity vectors shown in Fig. 8.2 represent the rate of overall mass release from the particle (irrespective of its nature of production) a closer look into the mass release contributions due to pyrolysis and char conversion is taken. Figure 8.3 shows the temporal evolution of (volume-averages of) some selected species in the particle interior. For ease of discussion the complex set of species from the detailed pyrolysis and char conversion model has been reduced to show the three reference coals, the overall mass of char, three selected light gas species (CO, CO_2 and O_2) and the sum of all tar species only. To judge the relative contributions from pyrolysis and char conversion, simulations with (solid lines) and without char reactions (dashed lines) are compared and case N_2-30 is chosen, as its elevated oxygen levels trigger more char conversion than the reference case N_2-21. During the first 20ms the composition of the solid coal, Fig. 8.3 (left), remains unchanged since the particle has not yet reached a sufficiently high temperature. From 20ms on devolatilization starts and reference coals COAL2 (representing bituminous coal) and COAL3 (lignitic coal) are rapidly consumed to produce more of COAL1 (hydrogen-rich coal), as well as volatile gases, tars and char. Between 23 and 30ms COAL1 is also consumed, while further char is formed. Up to around 33ms the curves from the simulations with and without char conversion completely overlap, while the simulation with char consumption continuously reduces the char mass after that, while it stays constant if char conversion is neglected.

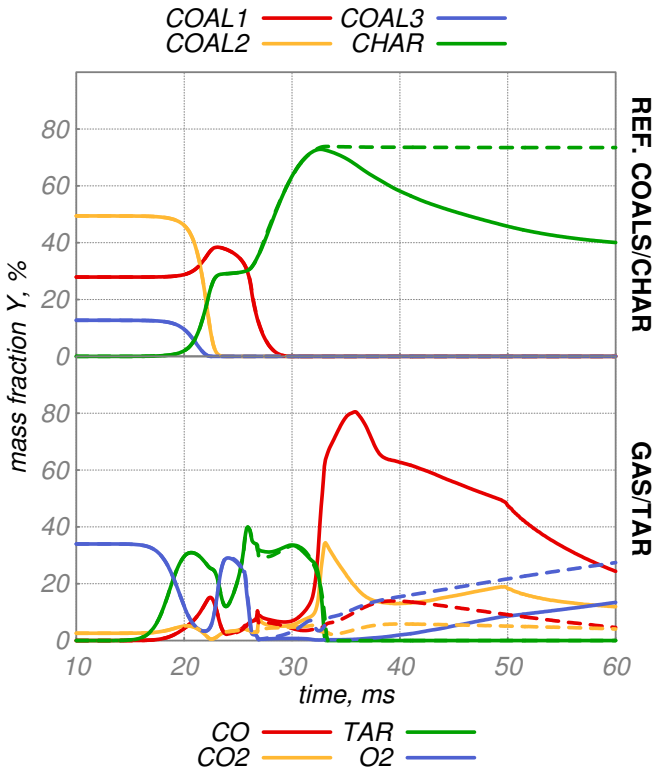

Abbildung 8.3: Temporal evolution of the particle interior fields, reference coals and char (top), selected volatile species and tars (bottom) for case N_2-30. Each line represents the volume-average of the distribution in the resolved particle interior. CO, CO_2 and O_2 are taken as representative species from the gas mixture and *char* and *tar* represent the sum of the complex mixture of various char and tar (cf. Tab. 3.5) species present in the detailed pyrolysis/char conversion submodel. The dashed lines refer to an identical simulation, but with char conversion switched off.

The (complex) time evolution of the gaseous species in the particle interior is shown in Fig. 8.3 (bottom). During the early stages (not included for legibility) the gas from the surrounding fluid phase rapidly diffuses through the pores inside the particle as O_2 and CO_2 have reached the nominal concentration of the external mixture by 10ms. Once the depletion of the reference coals begins, both light gas species such as CO and CO_2 and heavier tars are produced by pyrolysis and first released to the particle interior, before being ejected from the particle to the exterior gas phase, alongside the O_2 enclosed in the pores. As the (large) tar species are only formed during pyrolysis and subsequently depleted they are only present in the particle interior until the end of pyrolysis (33ms). In contrast, CO and CO_2 can be formed by char oxidation and are therefore present inside the particle at even later stages of the conversion process, while O_2 is consumed and stays near zero

between 25 and 35ms for the case with char conversion. With char conversion switched on, the levels of produced CO and CO_2, and consumed O_2 from around 30ms onwards are considerably higher than for the case without. The details of late-time char conversion (where particle shrinkage effects that are ignored by the present model, cf. Sec. 3.2.3, will increasingly play a role) are not critical for the considered experimental campaign that mainly focused on devolatilization and ignition. Therefore the simulations are run up to 60ms and then stopped. It is noted that at the end of the simulation that includes char conversion there still is a considerable amount of char and oxygen left (in a volume-averaged sense), which leads to further char conversion if the simulation is run longer. However, this process (accompanied by annealing reactions) is very slow possibly because a) the conversion/annealing reactions themselves are slow and/or b) despite the presence of elevated levels of O_2 at the particle surface there is no oxygen in the particle core that could convert the char, see Fig. 8.2 (right, 50ms). This can be further examined by investigating axial profiles of temperature and main chemical species along the centerline inside the particle and in its proximate vicinity at selected time instants as shown in Fig. 8.4, where the profiles of interest are plotted versus the axial coordinate normalized by the particle radius R_p. At 29.5ms the onset of homogeneous ignition can be recognized, as the gas temperature reaches ≈1900K at $x/R_p = 8$ and some OH starts to form at that location. Afterwards both the peak temperature and OH mass fraction rapidly propagate towards the particle surface, reaching a stand-off distance of about $1...2D_p$ at 29.6ms. At this time a significant amount of the reference coals has been consumed (especially in the outer layers of the particle where Y_{COAL} is already zero) to form the light volatile gases, the heavy tars ($Y_{TAR,max} > 30\%$ inside the particle) and the char that already represents more than 60% of the particle mass. At 35ms the reference coals have been fully depleted and the consequent drop in the release of volatile matter, causes the (near-)extinction behavior observed in Fig. 8.2. Moreover, the absence of an intense convective flux from the particle after the end of devolatilization now allows for oxygen to diffuse inside the particle, as the increased levels of Y_{O_2} in its outer layer suggest. The presence of oxygen triggers the conversion of the char, which is responsible for the temperature increase observed at 50ms, this time directly at the particle surface. The oxidation of the char occurs in the outer layers of the particle where both char and oxygen are consumed. As a consequence, oxygen cannot penetrate inside the core of the particle, which is mostly occupied by the char, that is therefore not further decomposed until the end of the simulation. Hence, in the inner particle region char conversion is diffusion-limited,

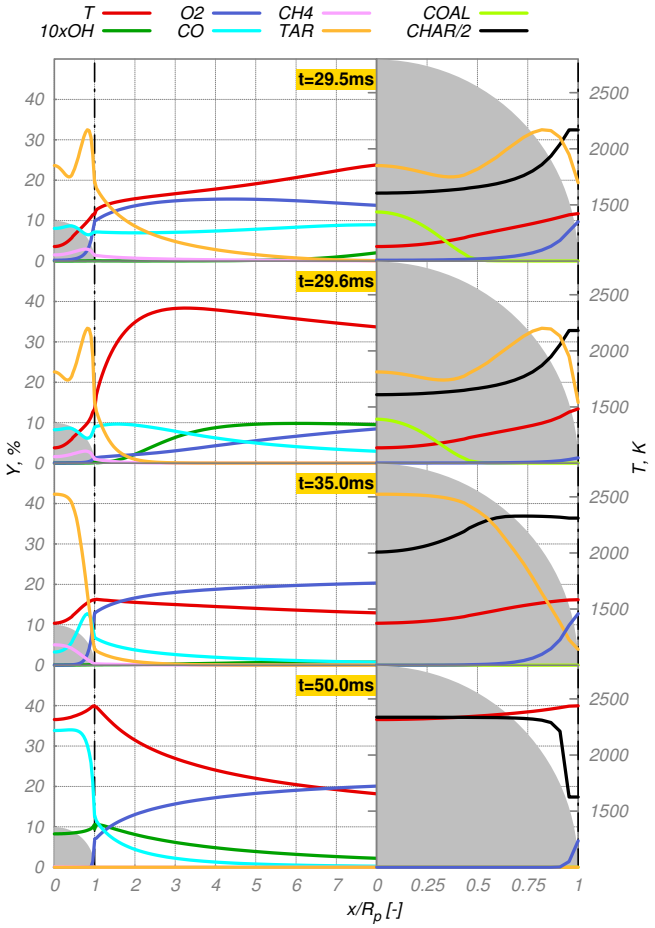

Abbildung 8.4: Downstream centerline profiles of temperature and main chemical species for case N_2-21, extracted at the same time instants selected for Fig. 8.2 (left). On the right selected profiles are zoomed in to better illustrate their distribution inside the particle.

since it is prevented by the lack of oxygen. The outer layers of the particle, however, still contain a substantial amount of oxygen, which should promote the conversion of the residual char. Yet, the significant amount of char present in that region, is consumed only slowly due to the slow kinetics of the char conversion/annealing reactions. The presence of both diffusion- and kinetically-limited char conversion at different locations inside the particle leads to the persisting volume-averaged char mass fraction at 60ms that was discussed in the context of Fig. 8.3.

Figure 8.5 shows the time evolution of the maximum gas and particle temperatures, mass release rate and released mass, as well as the volume-averaged particle conversion, porosity and tortuosity for the two mixtures balanced with N_2. As the particle heats up, the mass release increases slowly, becoming significant only at around 20ms. A drop in the release rate $\dot{m}$ after 20ms can be observed for both mix-

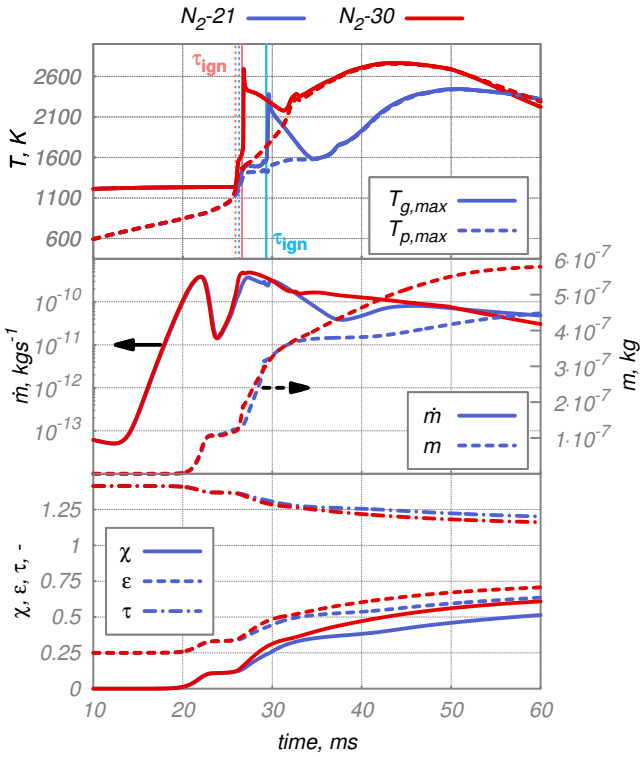

Abbildung 8.5: Temporal evolution of the maximum gas and particle temperature (top), particle mass release rate and released mass (middle) and volume-averaged conversion, porosity and tortuosity of the particle (bottom). A comparison of the two gas mixtures balanced with N_2 is shown. Vertical dotted and solid lines represent the ignition delay times evaluated by criteria based on the first increase of T_{max} and its maximum temporal gradient, respectively.

tures and coincides with the full consumption of reference coals COAL2 and COAL3 as shown in Fig. 8.3. Observing the gas temperature profiles the ignition behavior is affected by the oxygen concentration. For case N_2-30 the onset of ignition is sudden and unique, whereas the mixture with 21% O_2 shows a two-stage ignition process with a temperature plateau between 26 and 29ms, which corresponds to the final conversion period of COAL1.

After ignition, the gas temperature increases up to a peak value which is higher for the mixture containing more O_2 and, in general, for the mixtures balanced with N_2 rather than CO_2 (not shown in Fig. 8.5 for legibility). After reaching the peak gas temperature the volatile flame cools down, whereas the particle heats up until the temperature of the two phases is equilibrated (at 32ms for case N_2-30 and 35ms for N_2-21, see Fig. 8.5 (top)). Thereafter, the heat release resulting first from the combustion of the residual volatiles and then from char reactions increases the temperature of the gas phase in the immediate vicinity of the particle, and of the

particle itself. Hence, the temperatures of the two phases stay in equilibrium, first increasing and then decreasing again at late times. The late time behavior of the mass release rate and released mass in Fig. 8.5 (middle) show a continuous decrease of the mass release rate and almost constant values of the released mass towards the end of the simulation. Figure 8.5 (bottom) shows the temporal evolution of the coal conversion χ which, as defined in Eq. (3.32), relates the mass released from the coal particle, Fig. 8.5 (middle), to the initial particle mass. Only limited extents of particle conversion are obtained towards the end of the simulation, around 50% for case N_2-21 and 60% for case N_2-30. The particle porosity and tortuosity follow their assumed linear relationships with particle conversion, Eqs. (3.33) and (3.35), therefore they can influence particle burning mainly by means of their initial value. For example reducing the initial porosity from 25% to 10% of the particle volume leads to an increase in the ignition delay time of the 'N_2-21' mixture by 12% (not shown), as the augmented presence of solid matter increases the thermal inertia of the particle, which slows down the pyrolysis process. To confirm that the late time behavior discussed in Fig. 8.5 is indeed caused by char conversion, Fig. 8.6 shows a comparison of the same quantities with and without char conversion for case N_2-30, where more char conversion happens than for case N_2-21. As can be seen from the profiles up to 27ms, the cases with and without char conversion completely overlap, so the observed behavior is solely caused by pyrolysis. Between 27 and 33ms (after ignition) small, but non-zero differences between the profiles can be observed, where small levels of char conversion seem to cause slight deviations from the pure pyrolysis profiles. From 33ms onwards char conversion becomes significant and all quantities begin to deviate strongly. As a result, the case with char conversion shows significantly higher temperatures, more released mass, higher final particle conversion and porosity and lower final particle tortuosity than the case that neglects char reactions. Figure 8.7 shows the ignition delay time τ_{ign} predicted by the numerical simulations along with the experimental measurements, for each of the conditions presented in Tab. 5.1. The experimental values of τ_{ign} result from the acquisition of the CH* chemiluminescence signal. In Chap. 5, different ways of extracting ignition delay times from numerical simulations (based on species CH, OH and temperature) were compared and no significant influence of the chosen extraction method on τ_{ign} was found, similarly to what was found by Evans *et al.* [30] for autoigniting ethylene flames fed by hot air. The fact that the extraction criterion for ignition delay did not make any difference in Chap. 5 was probably related to the use of a single-step pyrolysis model, which results in monotonous temporal trends of the volatile release

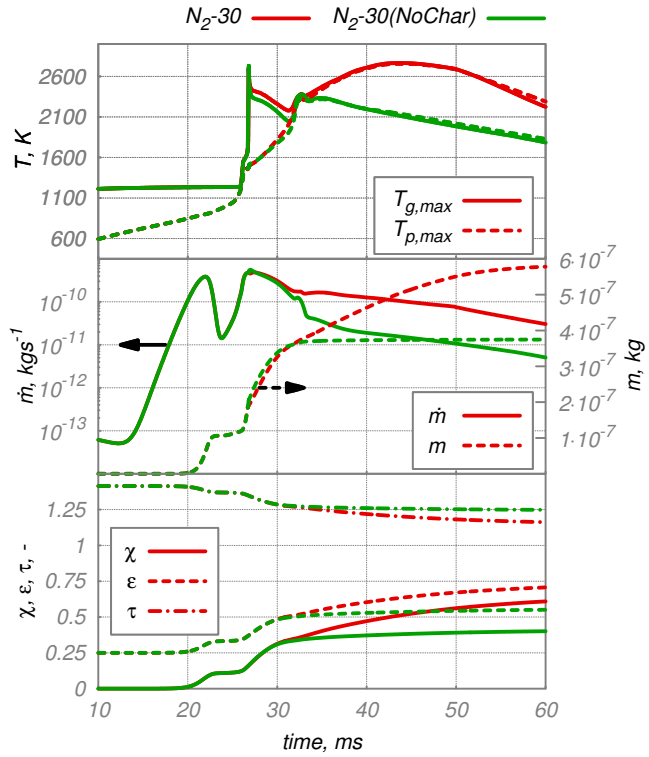

Abbildung 8.6: Temporal evolution of the maximum gas and particle temperature (top), particle mass release rate and released mass (middle) and volume-averaged conversion, porosity and tortuosity of the particle (bottom). A comparison of case N_2-30 with a case that exhibits the particle to the identical gas environment N_2-30, but with char conversion switched off is shown.

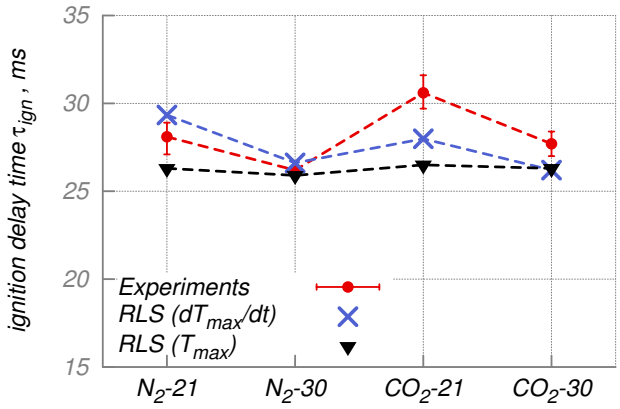

Abbildung 8.7: Ignition delay times measured in [79] and extracted from the resolved laminar simulation (RLS) based on T_{max} (triangles) or from its gradient (crosses). Vertical bars represent 98% confidence statistical error in the experiments.

rate and combustion quantities. In contrast, the complex pyrolysis model employed here leads to non-monotonous profiles with one and two-step ignition scenarios

as the ones shown in Figs 8.5 and 8.6. As a consequence, different methods of extracting ignition delay times may give different results even if applied to the same reference quantity. Here, the value of τ_{ign} extracted from the maximum (overall) gas temperature is compared to the value of τ_{ign} extracted from the maximum temporal gradient of gas temperature (which may differ from case to case, if multi-stage ignition occurs). The first criterion, indicated as 'T_{max}' in the legend of Fig. 8.7, evaluates the ignition delay time as the instant of the first increase of T_{max} from its base value (vertical dotted-lines in Fig. 8.5). The second criterion, indicated as 'dT_{max}/dt' in the legend of Fig. 8.7, defines τ_{ign} to lie at the interception of a line tangent to the (overall) maximum temporal gradient, with a horizontal line at the base value of T_{max} (vertical solid-lines in Fig. 8.5). In Fig. 8.7 it can be observed that irrespective of the chosen extraction method the simulation captures the measured ignition delay times very well. The experimental trend of decreasing ignition delay time with increased O_2 for a fixed balance gas is also captured by all simulations and the two extraction criteria, albeit this is more difficult to observe for the T_{max} criterion. However, the measured trend of increased ignition delay when changing from N_2 balance gas to CO_2 for a fixed oxygen concentration is only captured by the T_{max} criterion, whereas a slightly shorter τ_{ign} for CO_2 with 21% oxygen is found when using the temperature gradient criterion. It has been verified that pure homogeneous gas phase kinetics and thermodynamics actually slightly increase the ignition delay times for CO_2. As a matter of fact, the higher specific heat of CO_2 decreases the gas temperature delaying ignition in homogeneous mixtures. Moreover, increased levels of CO_2 have a chemical effect of depleting H radicals through the reverse reaction of CO oxidation ($H + CO_2 \rightarrow OH + CO$), as was also considered in [33]. In the present case, the heterogeneous chemistry of product release from the particle and the fuel/oxidizer mixing under strain partially hide these effects. Overall, it needs to be stated that the present detailed simulations provide a good representation of the experimental ignition delay, but since the predicted ignition delay times are all fairly similar, the trends with changing gas mixture -which are also small in the experiments- are difficult to corroborate for the selected set of cases.

8.3 Summary of the Detailed Multi-Step Approach for Coal Kinetics

The present chapter completes the study of ignition and combustion of pulverized coal particles by applying a multi-step model for heterogeneous kinetics coupled

to detailed homogeneous chemistry to fully-resolved simulations. The detailed approach is used to predict the behavior of single coal particles immersed in different hot gas environments mimicking the well-defined laminar flow experiments taken as reference also in Chap. 5. The latter was based on limiting assumptions on pyrolysis, the volatile composition and the particle interior properties and neglected char conversion. These limitations have been overcome here. A comprehensive model description is introduced for the particle interior, where a time-evolving porosity and tortuosity govern the particle internal fluid flow of gas formed during the thermal degradation of the coal, which allows for the consideration of char conversion. The model dynamically predicts the mass release rate and composition of species released from the particle by linear combination of a set of reference coals. The ignition sequence is investigated and shows a dependency of the particle burning behavior on the oxygen content in the surrounding gas. In the presence of lower oxygen concentrations, two-stage ignition phenomena are observed, which did not occur when using the single-step pyrolysis model in Chap. 5. The complex composition predicted by the porous-media model is analyzed and char conversion effects are discussed. Heterogeneous reactions result in considerably higher temperatures, enhanced mass release, and larger particle conversion along with a higher value of the final porosity. Slight deviations from the pure pyrolysis profiles are also found during the last stage of devolatilization, if char reactions are included. The predicted ignition delay times are in very good agreement with the experimental measurements even though, differently to Chap. 5, the complex profiles of the combustion quantities predicted by the detailed pyrolysis model lead to a mild dependence of the ignition delay time on the extraction method.

Chapter 9

Conclusion & Outlook

9.1 Conclusion

The aim of this thesis was to develop a comprehensive CFD model for the numerical simulation of pulverized coal combustion in order to gain new knowledge on coal ignition and particle burning, to improve the available database and to provide a reliable reference for alternative, simplified, numerical methods.

A direct numerical simulation framework was developed and applied to predict particle heating, devolatilization, fuel-oxidizer mixing, volatile ignition, combustion and char conversion in the immediate proximity of single particles and particle arrays. The presented study benefited from a fully resolved simulation approach complemented by detailed chemical kinetic models. This enabled accurate predictions of coal combustion characteristics, allowing for a thorough investigation of the factors that can affect the particles burning behavior in multiple configurations and under different operating conditions.

Fully-resolved modeling of coal conversion was achieved developing two main approaches with different levels of detail. The first approach used an Eulerian description of the reacting mixture carrying pulverized coal particles which affected the gas phase by means of boundary conditions at the interface. Particle heating and devolatilization were described by solving for intra-particle heat transfer and heat exchange between the particles and the surroundings, and by using the particle mean temperature to calculate the devolatilization rate from a single rate kinetic law. The volatile matter was then released at this rate by a pyrolysis boundary condition for the species mass transfer across the particle surface accounting for both convective and diffusive contributions. The assumed volatile composition included light gases and hydrocarbons up to C_6H_6, resulting in a rather simple description

for the tars and, hence, of the fuel stream. This allowed to use an effective but significantly reduced version of a detailed kinetic scheme for the homogeneous chemistry. Heterogeneous char reactions were neglected in this first instance. This simplified approach led to limited computational cost and offered the possibility to investigate a broad range of coal particle configurations by means of 3D fully resolved simulations. However, this first approach did not capture the physico-chemical phenomena occurring inside the porous coal particle, the detailed composition of the released volatile matter and the effect of char combustion.

To overcome these limitations a second modeling approach was introduced. It relied on a detailed, multi-step mechanism for heterogeneous kinetics coupled to detailed homogeneous chemistry, resulting in a significantly improved description of the volatiles and heavy tars released by the particle, i.e the fuel source. A complex model description was introduced for the particle interior, where a time-evolving porosity and tortuosity governed the particle internal fluid flow of gas formed during the thermal conversion of the coal which this time included char reactions as well. The model dynamically predicted the mass release rate and composition of species released from the particle by linear combination of a set of reference coals. The introduced complexity resulted in a significantly increased computational cost of this second approach, which limited its application in this work to 2D laminar computations only.

Initially the first approach was validated by investigating single coal particle ignition and volatile combustion in four different hot gas environments for which reliable experimental data are available [79]. Resolved laminar simulations of the flow, mixing and gas phase chemistry around the particle were performed. Results showed a good agreement with the experimental ignition delay times. The trends of ignition delay times for the investigated mixtures characterized by different oxygen levels and the use of N_2 and CO_2 as balance gas were predicted by the simulations in accordance with the experimental evidence. It was found that absolute values of predicted ignition delay time were functions of potential particle preheating, particle Reynolds number and the reference quantity employed for extraction of ignition delay, whereas the relative trends for different gas phase environments remained correct.

The same modeling technique was then applied to perform fully-resolved DNS of pulverized coal particles and particle arrays pyrolysis, ignition and volatile burning in laminar and turbulent flow for a wide range of conditions obtained from a reference LES study of a semi-industrial furnace [108]. The DNS domain represented a

characteristic cell size used for LES. The wake flames that established at sufficiently high particle Reynolds numbers led to significant particle interactions in case of particle ensembles. Such interactions were found to be strongly affected by the inter-particle distance L_x. In particular, different combustion regimes were observed when reducing L_x from large values, for which the particles burned independently (IFC regime), to small L_x, which resulted in strong interactions and group combustion (CGC). The regime transition was quantified by a global equivalence ratio, which spanned from very lean (IFC) to very rich (CGC) combustion for the considered range of L_x and affected the particle surface temperature and devolatilization rate history. Available scaling laws for mixture fraction profiles along transverse planes in the vicinity of evaporating droplets [58] were applied to solid fuel and predicted the mixture fraction distributions in the wake of the burning coal particles. Gradually increasing Re_p led, for single particles, to delayed ignition, more prominent asymmetry of the volatile flame and a decreased combustion intensity, eventually resulting in a flame that ceased to envelope the particle due to high upstream scalar dissipation rates. The attempt of modeling these conditions by steady laminar flamelet calculations based on local scalar dissipation rates extracted from the DNS showed that the standard flamelet model accurately captures the flame structure at low Re_p. However, at high Re_p the flames are dominated by curvature and multi-dimensional effects [112] and cannot be modeled with a standard flamelet formulation. Extending the analysis to multiple particles aligned in streamwise direction, the interaction among the particles was found to be strongly affected by Re_p, where very large Re_p tended to extinguish the volatile flame(s) around the upstream particles and led to strong interactions of the flames around the downstream particle sets. Results for turbulent flow conditions showed that a wide range of additional chemical states can be observed with respect to the corresponding laminar case. This is due to the randomness of turbulence, which alternately acts to increase or decrease the local strain, and to weaken or enhance particle interaction. A zonal analysis showed that, at the most upstream particle layer, turbulent motions could locally reduce the strain below the critical values that prevent combustion for the laminar case. As a result the chemical turnover in this region was slightly promoted by turbulence, as indicated by an increased OH production. Conversely, the stable envelope flame around the remaining downstream particle layers in the laminar case was strongly perturbed by flapping turbulent motions, which led to instantaneous flame detachments and local extinction events. The OH release was therefore instantaneously reduced as indicated by lower peak conditional means. These observed instantaneous differences

resulted in an analogous cumulative impact on the heating rate history and volatile matter release of the respective particles. The produced collection of DNS results for the representative conditions from the reference LES, provided sub-grid information, and can be used for further LES model development and validation.

Finally the detailed pyrolysis approach for the thermal conversion of the coal was applied, due to its computational cost, to the single particle setup only. Fully-resolved laminar simulations were performed attempting once again to predict the ignition delay times measured by Molina *et al.* [79]. The ignition sequence showed a dependency of the particle burning behavior on the oxygen content in the surrounding gas, which was not exhibited when using the simplified model. In the presence of lower oxygen concentrations, two-stage ignition phenomena were observed. The complex composition predicted by the porous-media model was analyzed and char conversion effects were discussed. Heterogeneous reactions resulted in considerably higher temperatures, enhanced mass release, and larger particle conversion along with a higher value of the final porosity. Slight deviations from the pure pyrolysis profiles were also found during the last stage of devolatilization, if char reactions were included. The predicted ignition delay times were in very good agreement with the experimental measurements, even though the more complex profiles of the combustion quantities predicted by the detailed pyrolysis model in comparison with the simplified approach, led to a mild dependence of the absolute values and the relative trends of the ignition delay time on the extraction method.

Ultimately, the complex modeling approach allowed to resolve high temperature and oxygen gradients that may be encountered when moving from the particle core to its surface, and that impact on the homogeneous and heterogeneous burning behavior. Therefore, the introduced model complication resulted to be fundamental for accurately modeling the physico-chemical phenomena occurring in- and outside the particle for the investigated conditions (particle diameter $D_p = 0.1\text{mm}$) already, and even bigger effects are expected for larger particles. Hence, the conducted investigation provided a useful reference to estimate which conditions represent stronger incentives for the higher CPU cost of the multi-step, detailed model compared with simpler model descriptions.

9.2 Outlook

The subject of the present study deserves further investigation and some improvements can be considered for future developments. Since this work aimed at characte-

rizing pulverized coal devolatilization and combustion in the proximity of individual particles and particle arrays, an accurate and comprehensive description of the immediate vicinity of the particles was fundamental, making a fully resolved Eulerian formulation the method of choice. However the fully resolved DNS presents two simplifications:

- the location of the particles is fixed, therefore the randomness of particle motion is neglected,
- the particle spacing is also fixed, which leads to screening of the turbulent scales that cannot exceed that size.

To overcome these limitations, carrier-phase DNS (CP-DNS) can be performed, resolving the flow and the mixing fields but treating the particles as point particles. In this way, it is possible to capture the dependence of fundamental particle processes such as drag or devolatilization on the particle size, by assuming an evolving particle size distribution. The latter can lead to significant advantages when attempting to predicting the burning behavior of coal in practical applications. Particles in pulverized coal furnaces show in fact broad size distributions including large particles, that are expected to have significant slip velocities and small particles, that heat up quickly and are crucial for ignition. Therefore a Lagrangian framework, with subgrid closures provided by the data collected in the present work, offers the potential to further improve the prediction of the pulverized coal combustion characteristics.

Additionally in the present work the particle size has also been assumed constant in time, i.e. particle shrinking was neglected during pyrolysis. Since the chemical reactions leading to the thermal conversion of coal occur throughout the entire particle volume, in most cases it is reasonable to solely consider an increase in particle porosity at constant particle diameter. This assumption can be strengthened by the circumstance of mostly uniform temperatures within the particles. However depending on the size of the particles and the heating rate to which they are exposed, considerable temperature and oxygen concentration differences may be encountered near the surface. In these cases to predict the thermochemical conversion of coal and the full char conversion in particular, modeling the decrease of the particle diameter in time might be crucial since the solid part eventually tends to became zero as only ashes remain. This can be achieved with the introduction of a moving mesh that, especially for larger particles and in the presence of high heating rates, promises to be worth the additional computational cost [39].

Independently from the discussed assumptions, the present study has highlighted the limits of the standard flamelet formulation and the standard film theory in predicting highly strained flames which are dominated by curvature and multi-dimensional effects [112]. To this end, the produced database offers the possibility to test improved flamelet models, for example including multi-dimensional and tangential diffusion effects [152] and introducing an additional progress variable tracking the progress of the chemical reactions, from non-reacting conditions (possibly indicating simple fuel and oxidizer mixing) to equilibrium conditions [134]. This would improve the combustion prediction of the flamelet models, especially in the turbulent recirculation regions that establish in pulverized coal applications.

Finally the continuous growth of the energy demand, along with fossil fuels limited availability and the associated greenhouse effects which are threatening the planet, forces the scientific community to address research efforts into alternative and renewable energy sources. In this scenario biomass represents a good alternative to keep industrial processes for power generation and chemicals production sustainable. Biomass is widely available, easily accessible and, once efficient supply chains are established, it can be introduced in the energy mix with reasonable operating costs. Most devices and technologies developed to extract energy from coal and fossil fuels in general can be converted to work with biomass. Thus, biomass represents a great opportunity for the differentiation of energy sources. On the other hand, predicting biomass thermal conversion also adds more modeling challenges, e.g. due to strongly non-spherical particles, high fuel variability and unknown kinetics. Therefore significant modeling efforts should aim at gaining a deeper understanding of biomass characterization.

Literaturverzeichnis

[1] The OpenFOAM Foundation, OpenFOAM v6 User Guide. https://cfd.direct/openfoam/user-guide.

[2] The International Energy Agency. https://www.iea.org, 2004.

[3] CRECK modeling group. http://CRECKmodeling.chem.polimi.it, 2018.

[4] IEA Clean Coal Centre. https://www.iea-coal.org/pulverised-coal-combustion-pcc/, 2018.

[5] The International Energy Agency, Coal 2018 - Analysis and Forecasts to 2023. https://www.iea.org/coal2018/, 2018.

[6] U.S. Energy Information Administration, International Energy Outlook. https://www.eia.gov/outlooks/ieo/, 2018.

[7] National Oceanic and Atmospheric Administration, U.S. Department of Commerce, temperature change and carbon dioxide change. https://www.ncdc.noaa.gov/global-warming/temperature-change, 2019.

[8] U.S. Energy Information Administration. https://www.eia.gov/tools/faqs/faq.php?id=73&t=11, 2019.

[9] U.S. Geological Survey. https://www.usgs.gov/, 2020.

[10] K. Annamalai, W. Ryan, and S. Dhanapalan. Interactive processes in gasification and combustion. Part III: Coal/char particle arrays, streams and clouds. *Prog. Energ. Combust. Sci.*, 20(6):487 – 618, 1994.

[11] S. Badzioch and P. G. Hawksley. Kinetics of thermal decomposition of pulverised coal particles. *Ind. Eng. Chem. Process Des. Develop.*, 9(4):521–530, 1970.

[12] C. Bailly and D. Juve. A stochastic approach to compute subsonic noise using linearized Euler's equations. In *5th AIAA/CEAS Aeroacoustics Conference and Exhibit*, 1999.

[13] S. Balusamy, M. M. Kamal, S. M. Lowe, B. Tian, Y. Gao, and S. Hochgreb. Laser diagnostics of pulverized coal combustion in O_2/N_2 and O_2/CO_2 conditions: velocity and scalar field measurements. *Exp. Fluids*, 56(5):108, 2015.

[14] M. Baum and P. Street. Predicting the combustion behaviour of coal particles. *Combust. Sci. Techn.*, 3:231–243, 1971.

[15] R. Bilger. Some aspects of scalar dissipation. *Flow Turbul. Combust.*, 72(2):93–114, 2004.

[16] M. Billson, L.-E. Eriksson, and L. Davidson. Jet noise prediction using stochastic turbulence modeling. In *9th AIAA/CEAS Aeroacoustics Conference, AIAA Paper 2003-3282*, 2003.

[17] T. Brosh, D. Patel, D. Wacks, and N. Chakraborty. Numerical investigation of localised forced ignition of pulverised coal particle-laden mixtures: A direct numerical simulation (DNS) analysis. *Fuel*, 145:50–62, 2015.

[18] A. Burcat and B. Rusic. Third millenium ideal gas and condensed phase thermochemical database for combustion (with update from active thermochemical tables). *Argonne National Laboratory, report No. ANL-05/20*, 2005.

[19] R. Cant and E. Mastorakos. *An Introduction to Turbulent Reacting Flows*. Imperial College Press, 2008.

[20] L. Chen and A. F. Ghoniem. Simulation of oxy-coal combustion in a 100 kWth test facility using RANS and LES: A validation study. *Energy Fuels*, 26(8):4783–4798, 2012.

[21] L. Chen, S. Z. Yong, and A. F. Ghoniem. Oxy-fuel combustion of pulverized coal: Characterization, fundamentals, stabilization and CFD modeling. *Prog. Energ. Combust. Sci.*, 38(2):156 – 214, 2012.

[22] P. Cheng. Two-dimensional radiating gas flow by a moment method. *AIAA Journal*, 2(9):1662–1664, Jan 1964.

[23] T. Coffee and J. Heimerl. Transport algorithms for premixed, laminar steady-state flames. *Combust. Flame*, 43:273 – 289, 1981.

[24] G. Comte-Bellot and S. Corrsin. Simple eulerian time correlation of full-and narrow-band velocity signals in grid-generated, 'isotropic' turbulence. *J. Fluid Mech.*, 48(2):273–337, 1971.

[25] C. T. Crowe, M. P. Sharma, and D. E. Stock. The Particle-Source-In Cell (PSI-CELL) Model for Gas-Droplet Flows. *J. Fluids Eng.*, 99(2):325–332, 06 1977.

[26] A. Cuoci, A. Frassoldati, T. Faravelli, and E. Ranzi. Opensmoke++: An object-oriented framework for the numerical modeling of reactive systems with detailed kinetic mechanisms. *Comp. Phys. Communic.*, 192:237–264, 2015.

[27] C. Curtiss and J. Hirschfelder. Transport properties of multicomponent gas mixtures. *J. Chem. Phys.*, 17:550–555, 1949.

[28] L. Davidson and S. Dahlström. Hybrid LES-RANS: An approach to make LES applicable at high Reynolds number. *Int. J. Comput. Fluid Dyn.*, 19(6):415–427, 2005.

[29] D. Dietzel, D. Messig, F. Piscaglia, A. Montorfano, G. Olenik, O. T. Stein, A. Kronenburg, A. Onorati, and C. Hasse. Evaluation of scale resolving turbulence generation methods for large eddy simulation of turbulent flows. *Comput. Fluids*, 93:116 – 128, 2014.

[30] M. J. Evans, P. R. Medwell, Z. F. Tian, A. Frassoldati, A. Cuoci, and A. Stagni. Ignition characteristics in spatially zero-, one- and two-dimensional laminar ethylene flames. *AIAA Journal*, 54(10):3255 – 3264, 2016.

[31] R. Eymard, G. Thierry, and R. Herbin. *Finite Volume Methods*, volume 7. 12 2000.

[32] G. Faeth. Current status of droplet and liquid combustion. *Prog. Energ. Combust. Sci.*, 3(4):191 – 224, 1977.

[33] S. Farazi, A. Attili, S. Kang, and H. Pitsch. Numerical study of coal particle ignition in air and oxy-atmosphere. *Proc. Combust. Inst.*, 37(3):2867 – 2874, 2019.

[34] S. Farazi, J. Hinrichs, M. Davidovic, T. Falkenstein, M. Bode, S. Kang, A. Attili, and H. Pitsch. Numerical investigation of coal particle stream ignition in oxy-atmosphere. *Fuel*, 241:477 – 487, 2019.

[35] S. Farazi, M. Sadr, S. Kang, M. Schiemann, N. Vorobiev, V. Scherer, and H. Pitsch. Resolved simulations of single char particle combustion in a laminar flow field. *Fuel*, 201:15 – 28, 2017.

[36] M. Field. Rate of combustion of size-graded fractions of char from a low-rank coal between 1200K and 2000K. *Combust. Flame*, 13(3):237–252, 1969.

[37] D. Genetti. An advanced model of coal devolatilization based on chemical structure. Master's thesis, Brigham Young University, 1999.

[38] D. Genetti, T. H. Fletcher, and R. Pugmire. Development and application of a correlation of ^{13}C NMR chemical structural analyses of coal based on elemental composition and volatile matter content. *Energy Fuels*, 13:60–68, 1999.

[39] G. Gentile, P. E. A. Debiagi, A. Cuoci, A. Frassoldati, E. Ranzi, and T. Faravelli. A computational framework for the pyrolysis of anisotropic biomass particles. *Chem. Eng. J.*, 321:458–473, 2017.

[40] M. Gharebaghi, R. Irons, L. Ma, M. Pourkashanian, and A. Pranzitelli. Large eddy simulation of oxy-coal combustion in an industrial combustion test facility. *Int. J. Greenh. Gas Control*, 5:S100–S110, 2011.

[41] S. Gordon and B. J. McBride. *Computer program for calculation of complex chemical equilibrium compositions, rocket performance, incident and reflected shocks, and Chapman-Jouguet detonations*. Washington : Scientific and Technical Information Office, National Aeronautics and Space Administration, 1971.

[42] B. Goshayeshi and J. C. Sutherland. A comparative study of thermochemistry models for oxy-coal combustion simulation. *Combust. Flame*, 162(10):4016–4024, 2015.

[43] P. Graeser and M. Schiemann. Emissivity of burning bituminous coal char particles - burnout effects. *Fuel*, 196:336 – 343, 2017.

[44] D. Grant, R. Pugmire, T. Fletcher, and A. Kerstein. Chemical model of coal devolatilization using percolation lattice statistics. *Energy Fuels*, 3:175–186, 1989.

[45] M. G. Gronli and M. C. Melaaen. Mathematical model for wood pyrolysiss-comparison of experimental measurements with model predictions. *Energy Fuels*, 14:791–800, 2000.

[46] K. Gustafson. Domain decomposition, operator trigonometry, Robin condition. *Contemp. Math.*, 218:432 – 437, 1998.

[47] J. H. Ferziger and M. Peric. *Computational Methods for Fluid Dynamics*, volume 3. 01 2002.

[48] T. Hara, M. Muto, T. Kitano, R. Kurose, and S. Komori. Direct numerical simulation of coal particle devolatilization and volatile combustion. *Combust. Flame*, 162:4391–4407, 2015.

[49] A. Harten. High resolution schemes for hyperbolic conservation laws. *J. Comput. Phys.*, 49(3):357 – 393, 1983.

[50] M. Hassanaly, H. Koo, C. F. Lietz, S. T. Chong, and V. Raman. A minimally-dissipative low-Mach number solver for complex reacting flows in openFOAM. *Comput. Fluids*, 162:11 – 25, 2018.

[51] L. Hu, L. Zhou, Y. Luo, and C. Xu. Measurement and simulation of swirling coal combustion. *Particuology*, 11(2):189–197, 2013.

[52] M. Hurskainen and P. Vainikka. Technology options for large-scale solid-fuel combustion. In J. Oakey, editor, *Fuel Flexible Energy Generation*, pages 177 – 199. Woodhead Publishing, Boston, 2016.

[53] S. M. Hwang, R. Kurose, F. Akamatsu, H. Tsuji, H. Makino, and M. Katsuki. Application of optical diagnostics techniques to a laboratory-scale turbulent pulverized coal flame. *Energy Fuels*, 19:382–392, 2005.

[54] W. Hwang and J. K. Eaton. Homogeneous and isotropic turbulence modulation by small heavy (St $\approx$ 50) particles. *J. Fluid Mech.*, 564:361–393, 2006.

[55] H. Jasak. *Error Analysis and Estimation for Finite Volume Method with Applications to Fluid Flow*. PhD thesis, Imperial College London, 1996.

[56] A. Kazakov and M. Frenklach. DRM 22. 1994. http://www.me.berkeley.edu/drm/, accessed 12/2015.

[57] F. Kee, R.J. ande Rupley, E. Meeks, and J. Miller. CHEMKIN-III: A FORTRAN chemical kinetics package for the analysis of gas-phase chemical and plasma kinetics. *Sandia Report*, SAND96-8216(UC-405), 5 1996.

[58] A. Klimenko and R. Bilger. Conditional moment closure for turbulent combustion. *Prog. Energy Combust. Sci.*, 25(6):595, 1999.

[59] R. Knappstein, G. Kuenne, L. G. Becker, F. di Mare, A. Sadiki, A. Dreizler, and J. Janicka. Large eddy simulation of a novel gas-assisted coal combustion chamber. *Flow, Turbul. Combust.*, 2018. https://doi.org/10.1007/s10494-018-9910-x.

[60] R. Knappstein, G. Kuenne, T. Meier, A. Sadiki, and J. Janicka. Evaluation of coal particle volatiles reaction by using detailed kinetics and FGM tabulated chemistry. *Fuel*, 201:39–52, 2017.

[61] K. Knill, T. Nakamura, and M. Morgan. The effect of mixing on NOx reduction by coal fuel staging. Report on the AP 19 investigation. Technical Report F 37/y/21, Int. Flame Res. Found. (IFRF), 1990.

[62] H. Kobayashi, J. B. Howard, and A. F. Sarofim. Coal devolatilization at high temperatures. *Proc. Combust. Inst.*, 16:411–425, 1977.

[63] A. Kolmogorov. The local structure of turbulence in incompressible viscous fluid for very large Reynolds' numbers. *Akademiia Nauk SSSR Doklady*, 30:301–305, 1941.

[64] A. N. Kolmogorov. Dissipation of energy in locally isotropic turbulence. *Akademiia Nauk SSSR Doklady*, 32:16, Apr. 1941.

[65] J. Köser, L. G. Becker, A.-K. Gossmann, B. Böhm, and A. Dreizler. Investigation of ignition and volatile combustion of single coal particles within oxygen-enriched atmospheres using high-speed OH-PLIF. *Proc. Combust. Inst.*, 36(2):2103 – 2111, 2017.

[66] R. H. Kraichnan. Diffusion by a random velocity field. *Phys. Fluids*, 13(1):22–31, 1970.

[67] J. Krueger, N. Haugen, D. Mitra, and T. Lovas. The effect of turbulent clustering on particle reactivity. *Proc. Combust. Inst.*, 36:2333 – 2340, 2017.

[68] R. Kurose and H. Makino. Large eddy simulation of a solid-fuel jet flame. *Combust. Flame*, 135:1–16, 2003.

[69] C. K. Law. Combustion at a crossroads: Status and prospects. *Proc. Combust. Inst.*, 31(1):1 – 29, 2007.

[70] K. Luo, H. Wang, J. Fan, and F. Yi. Direct numerical simulation of pulverized coal combustion in a hot vitiated co-flow. *Energy Fuels*, 26(10):6128–6136, 2012.

[71] Z. Luo and M. Agraniotis. *Low-rank Coals for Power Generation, Fuel and Chemical Production*. Woodhead Publishing, 2017.

[72] T. Maffei, G. Gentile, S. Rebughini, M. Bracconi, F. Manelli, S. Lipp, A. Cuoci, and M. Maestri. A multiregion operator-splitting CFD approach for coupling microkinetic modeling with internal porous transport in heterogeneous catalytic reactors. *Chem. Eng. J.*, 283:1392–1404, 2016.

[73] T. Maffei, R. Khatami, S. Pierucci, T. Faravelli, E. Ranzi, and Y. A. Levendis. Experimental and modeling study of single coal particle combustion in O_2/N_2 and oxy-fuel (O_2/CO_2) atmospheres. *Combust. Flame*, 160(11):2559–2572, 2013.

[74] F. C. Marincola. *Large Eddy Simulation of Coal Combustion*. PhD thesis, Imperial College London, 2013.

[75] F. Matthes. Energy transition in germany: a case study on a policy-driven structural change of the energy system. *Evolut. Inst. Econ. Rev.*, 14:141–169, 2017.

[76] J. McConnell, B. Goshayeshi, and J. C. Sutherland. An evaluation of the efficacy of various coal combustion models for predicting char burnout. *Fuel*, 201:53 – 64, 2017.

[77] D. Messig, M. Vascellari, and C. Hasse. Flame structure analysis and flamelet progress variable modeling of strained coal flames. *Combust. Theo. Mod.*, 21:700, 2017.

[78] M. F. Modest. *Radiative Heat Transfer*. Academic Press, 2003.

[79] A. Molina and C. R. Shaddix. Ignition and devolatilization of pulverized bituminous coal particles during oxygen/carbon dioxide coal combustion. *Proc. Combust. Inst.*, 31(2):1905–1912, 2007.

[80] M. Muto and N. Haugen. DNS for solid fuel flames, topical review. Workshop on Coal and Biomass Conversion (CBC), http://www.cbc.uni-due.de, 2018.

[81] M. Muto, H. Watanabe, R. Kurose, S. Komori, S. Balusamy, and S. Hochgreb. Large-eddy simulation of pulverized coal jet flame - effect of oxygen concentration on NOx formation. *Fuel*, 142:152–163, 2015.

[82] M. Muto, K. Yuasa, and R. Kurose. Numerical simulation of ignition in pulverized coal combustion with detailed chemical reaction mechanism. *Fuel*, 190:136 – 144, 2017.

[83] P. Nikrityuk, M. Gräbner, M. Kestel, and B. Meyer. Numerical study of the influence of heterogeneous kinetics on the carbon consumption by oxidation of a single coal particle. *Fuel*, 114:88–98, 2013.

[84] P. Nikrityuk and B. Meyer. *Gasification Processes: Modeling and Simulation*. 01 2014.

[85] S. Niksa. Rapid coal devolatilization as an equilibrium flash distillation. *AIChE Journal*, 34(5):790–802, 1988.

[86] S. Niksa. *Process Chemistry of Coal Utilization*. Woodhead Publishing Series in Energy. Woodhead Publishing, 2020.

[87] S. Niksa and A. R. Kerstein. Modeling the devolatilization behavior of various coals. In *1991 International Conference on Coal Science Proceedings*, pages 488 – 491. Butterworth-Heinemann, 1991.

[88] P.-Y. Oei, H. Hermann, P. Herpich, O. Holtemöller, B. Lünenbürger, and C. Schult. Coal phase-out in germany – implications and policies for affected regions. *Energy*, 196:117004, 2020.

[89] G. Olenik, O. T. Stein, and A. Kronenburg. LES of swirl-stabilised pulverised coal combustion in IFRF furnace no. 1. *Proc. Combust. Inst.*, 35(3):2819, 2015.

[90] A. D. Paulsen, M. S. Mettler, and P. J. Dauenhauer. The role of sample dimension and temperature in cellulose pyrolysis. *Energy Fuels*, 27:2126–2134, 2013.

[91] J. Pedel, J. Thornock, and P. Smith. Ignition of co-axial turbulent diffusion oxy-coal jet flames: Experiments and simulations collaboration. *Combust. Flame*, 160(6):1112, 2013.

[92] A. Peters and R. Weber. Mathematical modelling of a 2.4 MW swirling pulverized coal flame. *Combust. Sci. Techn.*, 122:131–182, 1997.

[93] N. Peters. Laminar flamelet concepts in turbulent combustion. *Symp. (Int.) Combust.*, 21(1):1231 – 1250, 1988.

[94] N. Peters. *Turbulent Combustion*. Cambridge Monographs on Mechanics. Cambridge University Press, 2000.

[95] N. Peters. Multiscale combustion and turbulence. *Proc. Combust. Inst.*, 32(1):1 – 25, 2009.

[96] R. Pletcher, J. Tannehill, and D. Anderson. *Computational Fluid Mechanics and Heat Transfer, Second Edition*. Series in Computational and Physical Processes in Mechanics and Thermal Sciences. Taylor & Francis, 1997.

[97] S. B. Pope. *Turbulent Flows*. Cambridge University Press, 2000.

[98] M. Rabacal, B. Franchetti, F. Cavallo-Marincola, F. Proch, M. Costa, C. Hasse, and A. M. Kempf. Large eddy simulation of coal combustion in a large-scale laboratory furnace. *Proc. Combust. Inst.*, 35(3):3609 – 3617, 2015.

[99] E. Ranzi, T. Faravelli, and F. Manenti. Chapter One - Pyrolysis, gasification, and combustion of solid fuels. In *Thermochemical Process Engineering*, volume 49 of *Adv. Chem. Eng.*, pages 1 – 94. Academic Press, 2016.

[100] E. Ranzi, A. Frassoldati, R. Grana, A. Cuoci, T. Faravelli, A. Kelley, and C. Law. Hierarchical and comparative kinetic modeling of laminar flame speeds of hydrocarbon and oxygenated fuels. *Prog. Engy Combust. Sci.*, 38(4):468–501, 2012.

[101] E. Ranzi, A. Frassoldati, A. Stagni, M. Peluchi, A. Cuoci, and T. Faravelli. Reduced kinetic schemes of complex reaction systems: Fossil and biomass-derived transportation fuels. *Int. J. Chem. Kin.*, 46(9):512–542, 2014.

[102] O. Reynolds. An experimental investigation of the circumstances which determine whether the motion of water shall be direct or sinuous, and of the law of resistance in parallel channels. *Philos. Trans. R. Soc. London*, 174:935–982, 1883.

[103] O. Reynolds. On the dynamical theory of incompressible viscous fluids and the determination of the criterion. *Philos. Trans. R. Soc. London, Ser. A*, 186:123–164, 1895.

[104] L. F. Richardson. Weather prediction by numerical process. *Q. J. R. Meteorolog. Soc.*, 48(203):282–284, 1922.

[105] M. Rieth, A. Clements, M. Rabaçal, F. Proch, O. Stein, and A. Kempf. Flamelet les modeling of coal combustion with detailed devolatilization by directly coupled CPD. *Proc. Combust. Inst.*, 36(2):2181 – 2189, 2017.

[106] M. Rieth, A. M. Kempf, A. Kronenburg, and O. T. Stein. Carrier-phase DNS of pulverized coal particle ignition and volatile burning in a turbulent mixing layer. *Fuel*, 212:364 – 374, 2018.

[107] M. Rieth, F. Proch, A. G. Clements, M. Rabacal, and A. M. Kempf. Highly resolved flamelet LES of a semi-industrial scale coal furnace. *Proc. Combust. Inst.*, 36:3371–3379, 2017.

[108] M. Rieth, F. Proch, M. Rabacal, B. M. Franchetti, F. C. Marincola, and A. M. Kempf. Flamelet LES of a semi-industrial pulverized coal furnace. *Combust. Flame*, 173:39 – 56, 2016.

[109] C. Saggese, A. Frassoldati, A. Cuoci, T. Faravelli, and E. Ranzi. A wide range kinetic modeling study of pyrolysis and oxidation of benzene. *Combust. Flame*, 160(7):1168–1190, 2013.

[110] C. Saggese, N. E. Sanchez, A. Frassoldati, A. Cuoci, T. Faravelli, M. U. Alzueta, and E. Ranzi. Kinetic modeling study of polycyclic aromatic hydrocarbons and soot formation in acetylene pyrolysis. *Energy Fuels*, 28(2):1489–1501, 2014.

[111] T. Sayadi, S. Farazi, S. Kang, and H. Pitsch. Transiesnt multiple particle simulations of char particle combustion. *Fuel*, 199:289 – 298, 2017.

[112] A. Scholtissek, W. L. Chan, H. Xu, F. Hunger, H. Kolla, J. H. Chen, M. Ihme, and C. Hasse. A multi-scale asymptotic scaling and regime analysis of flamelet equations including tangential diffusion effects for laminar and turbulent flames. *Combust. Flame*, 162(4):1507 – 1529, 2015.

[113] J. Smagorinsky. General circulation experiments with the primitive equations: I. The basic experiment. *Mon. Weather Rev.*, 91(3):99–164, 03 1963.

[114] G. P. Smith, D. M. Golden, M. Frenklach, N. W. Moriarty, B. Eiteneer, M. Goldenberg, C. T. Bowman, R. K. Hanson, S. Song, J. William C. Gardiner, V. V. Lissianski, and Z. Qin. GRI 3.0. 1999. http://combustion.berkeley.edu/gri-mech/, accessed 12/2015.

[115] I. W. Smith. The combustion rates of coal chars: a review. *Symp. (Int.) Combust.*, 19(1):1045–1065, 1982.

[116] P. Solomon and T. Fletcher. Impact of coal pyrolysis on combustion. *Proc. Combust. Inst.*, 25(1):463 – 474, 1994.

[117] P. R. Solomon and M. B. Colket. Coal devolatilization. *Symp. (Int.) Combust.*, 17(1):131 – 143, 1979.

[118] P. R. Solomon, D. G. Hamblen, R. M. Carangelo, M. A. Serio, and G. V. Deshpande. General model of coal devolatilization. *Energy Fuels*, 2(4):405–422, 1988.

[119] S. Sommariva, T. Maffei, G. Migliavacca, T. Faravelli, and E. Ranzi. A predictive multi-step kinetic model of coal devolatilization. *Fuel*, 89(2):318 – 328, 2010.

[120] A. Stagni, A. Frassoldati, A. Cuoci, T. Faravelli, and E. Ranzi. Skeletal mechanism reduction through species-targeted sensitivity analysis. *Combust. Flame*, 163:382–393, 2016.

[121] O. T. Stein, G. Olenik, A. Kronenburg, F. Marincola, B. Franchetti, A. M. Kempf, M. Ghiani, M. Vascellari, and C. Hasse. Towards comprehensive coal combustion modelling for LES. *Flow Turbul. Combust.*, 90:859, 2013.

[122] M. Stoellinger, B. Naud, D. Roekaerts, N. Beishuizen, and S. Heinz. PDF modeling and simulations of pulverized coal combustion - Part 2: Application. *Combust. Flame*, 160(2):396 – 410, 2013.

[123] S. Subramaniam. Lagrangian-eulerian methods for multiphase flows. *Prog. Energy Combust. Sci.*, 39(2):215 – 245, 2013.

[124] P. K. Sweby. High resolution schemes using flux limiters for hyperbolic conservation laws. *SIAM J. Numer. Anal.*, 21(5):995–1011, 1984.

[125] H. Tennekes and J. L. Lumley. *First Course in Turbulence*. The MIT press, 1978.

[126] G. Tufano, O. Stein, A. Kronenburg, G. Gentile, A. Stagni, A. Frassoldati, T. Faravelli, A. Kempf, M. Vascellari, and C. Hasse. Fully-resolved simulations of coal particle combustion using a detailed multi-step approach for heterogeneous kinetics. *Fuel*, 240:75 – 83, 2019.

[127] G. L. Tufano, O. T. Stein, A. Kronenburg, L. Deng, I. Wlokas, A. M. Kempf, M. Vascellari, and C. Hasse. Direct numerical simulation of coal particle devolatilization and volatile combustion. *7th Eur. Combust. Meet.*, 2015. P5-51.

[128] G. L. Tufano, O. T. Stein, A. Kronenburg, A. Frassoldati, T. Faravelli, L. Deng, A. M. Kempf, M. Vascellari, and C. Hasse. Resolved flow simulation of pulverized coal particle devolatilization and ignition in air- and O_2/CO_2-atmospheres. *Fuel*, 186:285–292, 2016.

[129] G. L. Tufano, O. T. Stein, B. Wang, A. Kronenburg, M. Rieth, and A. M. Kempf. Coal particle volatile combustion and flame interaction. Part I: Characterization of transient and group effects. *Fuel*, 229:262–269, 2018.

[130] G. L. Tufano, O. T. Stein, B. Wang, A. Kronenburg, M. Rieth, and A. M. Kempf. Coal particle volatile combustion and flame interaction. Part II: Effects of particle Reynolds number and turbulence. *Fuel*, 234:723–731, 2018.

[131] S. R. Turns. *An Introduction to Combustion: Concepts and Applications*. McGraw-Hill. 1999.

[132] D. van Krevelen. *Coal*. 3rd ed. Amsterdam: Elsevier. 1993.

[133] M. Vascellari, R. Arora, M. Pollack, and C. Hasse. Simulation of entrained flow gasification with advanced coal conversion submodels. Part I: Pyrolysis. *Fuel*, 113:654–669, 11 2013.

[134] M. Vascellari, G. L. Tufano, O. T. Stein, A. Kronenburg, A. M. Kempf, A. Scholtissek, and C. Hasse. A flamelet/progress variable approach for modeling coal particle ignition. *Fuel*, 201:29 – 38, 2017.

[135] M. Vascellari, H. Xu, and C. Hasse. Flamelet modeling of coal particle ignition. *Proc. Combust. Inst.*, 34(2):2445, 2013.

[136] H. Versteeg and W. Malalasekera. *An Introduction to Computational Fluid Dynamics: The Finite Volume Method*. Pearson Education, Limited, 2011.

[137] S. Vo, O. Stein, A. Kronenburg, and M. Cleary. Assessment of mixing time scales for a sparse particle method. *Combust. Flame*, 179:280, 2017.

[138] T. von Kármán. Progress in the statistical theory of turbulence. *Proc. Natl. Acad. Sci.*, 34(11):530–539, 1948.

[139] N. Vorobiev, M. Geier, M. Schiemann, and V. Scherer. Experimentation for char combustion kinetics measurements: Bias from char preparation. *Fuel Proces. Technol.*, 151:155 – 165, 2016.

[140] K. Wan, J. Xia, Z. Wang, M. Pourkashanian, and K. Cen. Large-eddy simulation of pilot-assisted pulverized-coal combustion in a weakly turbulent jet. *Flow, Turbul. Combust.*, 99(2):531–550, Sep 2017.

[141] B. Wang, H. Chu, A. Kronenburg, and O. T. Stein. A resolved simulation study on the interactions between droplets and turbulent flames using OpenFOAM. *High Performance Computing in Science and Engineering '17*, pages 205–220, 2018.

[142] B. Wang, A. Kronenburg, D. Dietzel, and O. T. Stein. Assessment of scaling laws for mixing fields in inter-droplet space. *Proc. Combust. Inst.*, 36(2):2451–2458, 2017.

[143] B. Wang, A. Kronenburg, G. L. Tufano, and O. T. Stein. Fully resolved DNS of droplet array combustion in turbulent convective flows and modelling for mixing fields in inter-droplet space. *Combust. Flame*, 189:347 – 366, 2018.

[144] J. Warnatz, U. Maas, and R. W. Dibble. *Combustion*. Springer, Berlin, Heidelberg. 2006. Physical and Chemical Fundamentals, Modeling and Simulation, Experiments, Pollutant Formation - 4th Edition.

[145] P. Warzecha and A. Boguslawski. Simulations of pulverized coal oxy-combustion in swirl burner using RANS and LES methods. *Fuel Proces. Technol.*, 119:130–135, 2014.

[146] R. Weber, J. Dugue, A. Sayre, A. A. F. Peters, and B. M. Visser. Technical Report F36/y/20, IFRF, 1992.

[147] R. Weber, J. Dugue, A. Sayre, and B. Visser. Quarl zone flow field and chemistry of swirling pulverized coal flames: Measurements and computations. *Symp. (Int.) Combust.*, 24(1):1373–1380, 1992.

[148] H. G. Weller, G. Tabor, H. Jasak, and C. Fureby. A tensorial approach to computational continuum mechanics using object-oriented techniques. *Computers in Physics*, 12(6):620–631, 1998.

[149] X. Wen, K. Luo, H. Jin, and J. Fan. Numerical investigation of coal flamelet characteristics in a laminar counterflow with detailed chemistry. *Fuel*, 195:232 – 242, 2017.

[150] X. Wen, K. Luo, Y. Luo, H. I. Kassem, H. Jin, and J. Fan. Large eddy simulation of a semi-industrial scale coal furnace using non-adiabatic three-stream flamelet/progress variable model. *Appl. Energy*, 183:1086 – 1097, 2016.

[151] X. Wen, Y. Luo, K. Luo, H. Jin, and J. Fan. LES of pulverized coal combustion with a multi-regime flamelet model. *Fuel*, 188:661 – 671, 2017.

[152] X. Wen, O. T. Stein, G. L. Tufano, A. Kronenburg, A. Scholtissek, and C. Hasse. Multi-dimensional and transient effects on flamelet modeling for turbulent pulverized coal combustion. *Fuel*, 255:115772, 2019.

[153] A. Williams, Pourkashanian, J. Jones, and N. Skorupska. *Combustion and Gasification of Coal*. Taylor and Francis New York, 2000.

[154] A. Williams, M. Pourkashanian, and J. M. Jones. The combustion of coal and some other solid fuels. *Proc. Combust. Inst.*, 28:2141–2162, 2000.

[155] F. Williams. Recent advances in theoretical descriptions of turbulent diffusion flames. *Turbulent mixing in nonreactive and reactive flows*, pages 189 – 208, 1975.

[156] K. Yamamoto, T. Murota, T. Okazaki, and M. Taniguchi. Large eddy simulation of a pulverized coal jet flame ignited by a preheated gas flow. *Proc. Combust. Inst.*, 33(2):1771–1778, 2011.

[157] W. Zhang, H. Watanabe, and T. Kitagawa. Direct numerical simulation of ignition of a single particle freely moving in a uniform flow. *Adv. Powder Technol.*, 28(11):2893–2902, 2017.

[158] M. Zoby, S. Navarro-Martinez, A. Kronenburg, and A. Marquis. Turbulent mixing in three-dimensional droplet arrays. *Int. J. Heat and Fluid Flow*, 32(3):499 – 509, 2011.

Anhang A

Turbulence Generation

In Chap. 7, DNS is performed to characterize volatile combustion of isolated coal particles and closely spaced particle ensembles in laminar and turbulent flow. In particular, the effect of large particle Reynolds number Re_p and considerable levels of turbulence on the devolatilization and burning behavior of arrays of infinite particle layers are investigated. The turbulent inflow conditions for DNS are obtained by generating artificial turbulence based on a von Karman spectrum using inverse Fourier transforms according to the method of Billson *et al.* [16]. The turbulent flow at the inlet needs to cover all turbulent scales, ranging from the smallest Kolmogorov scales to the largest integral length scale. This can be achieved by superimposing to a mean convective velocity $\overline{U}$, perpendicular to the inlet, a homogeneous isotropic turbulent velocity field with root-mean-square velocity U'. Such a method for generating synthetic turbulence (ST) was presented in [12, 16, 28] and it is based on calculating the perturbation from a turbulent energy spectrum. This approach was successfully validated in [29] by comparing the generated initial isotropic turbulence and its time evolution to experimental data provided by Comte-Bellot & Corrsin [24].

The turbulent fluctuation field is obtained combining random Fourier modes [66],

$$\boldsymbol{u}'(\boldsymbol{x},t) = 2\sum_{n=1}^{N} \hat{u}^n cos(\boldsymbol{\kappa}_n \boldsymbol{x} + \psi^n)\boldsymbol{\sigma}^n, \tag{A.1}$$

where $\boldsymbol{\kappa}_n$, $\hat{u}^n$, ψ^n and $\boldsymbol{\sigma}^n$ represent the wave number vector, the amplitude, phase and direction of the n-th Fourier mode, at time t and location $\boldsymbol{x}$. To enforce the isotropy of the generated turbulence, the wave number vector $\boldsymbol{\kappa}_n$ is randomly selected on a sphere with radius κ_n in a way that it is also orthogonal to the direction of the

respective Fourier mode

$$\boldsymbol{\kappa}_n \cdot \boldsymbol{\sigma}^n = 0. \tag{A.2}$$

The phase of each mode, ψ is randomly selected in the range 0 to 2π, whereas the amplitude $\hat{u}^n$ is calculated by means of a turbulent energy spectrum function, $E(\kappa)$,

$$\hat{u}^n = \sqrt{E(\kappa)\Delta\kappa}, \tag{A.3}$$

with $\Delta\kappa$ being the interval of wave numbers and the energy spectrum function $E(\kappa)$ prescribed as a modified von Karman spectrum [12, 138],

$$E(\kappa) = A_E \frac{\frac{2}{3}k}{\kappa_e} \frac{\left(\frac{\kappa}{\kappa_e}\right)^4)}{\left[1 + \left(\frac{\kappa}{\kappa_e}\right)^2\right]^{17/6}} e^{-2\left(\frac{\kappa}{\kappa_\eta}\right)^2}. \tag{A.4}$$

The turbulent kinetic energy k is calculated as $\frac{3}{2}U'^2$, A_E is a scaling factor to ensure that the intensity of the generated turbulence corresponds to the desired level, and κ_e and κ_η represent the wave number of the most energetic and the Kolmogorov scale eddy, respectively. Their expression reads,

$$\kappa_e = \frac{\alpha_e 9\pi}{55 L_{int}}, \tag{A.5}$$

$$\kappa_\eta = \left(\frac{\epsilon}{\nu^3}\right)^{1/4}, \tag{A.6}$$

where α_e is a scaling factor, here set to 1.4526 [12, 16], L_{int} is the prescribed integral length scale of the turbulent inflow, ν is its viscosity and ϵ is the turbulent energy dissipation defined as

$$\epsilon = \frac{U'^3}{L_{int}}. \tag{A.7}$$

Since the velocity fluctuations generated at every time step are independent from each other, a time filter was suggested by Billson *et al.* [16], based on Taylor hypothesis [19, 97], in order to establish a correlation between subsequent time instants t_{i-1} and t_i satisfying turbulence characteristics,

$$\boldsymbol{u}'(t_i) = e^{-\Delta t/\tau_a}\boldsymbol{u}'(t_{i-1}) + \sqrt{1 - e^{-2\Delta t/\tau_a}}\boldsymbol{u}'(t_i), \tag{A.8}$$

where τ_a represents the time interval that occurs before the autocorrelation of the generated velocity fluctuations decays to e^{-1}. This temporal scale can be estimated

as

$$\tau_a = \frac{L_{int}}{A_\tau \overline{\overline{U}}}. \tag{A.9}$$

Here A_τ ranges between 1 and 2.

Anhang B

Chemical Mechanisms

This section reports the chemical mechanisms, in Chemkin format, which have been used to produce the results presented in this thesis. These mechanisms are obtained by reducing a general detailed kinetic scheme, consisting of more than 450 species and ≈17,000 reactions referred to as POLIMI_TOT_1407 which was discussed in [100, 109, 110]. The reduction was performed by the CRECK modeling group to minimize the error in the range of operating conditions of interest for this work, cf. Sec 3.1.2.

The *kinetics* files are reported in the following sections, whereas the *thermo* and *transport* properties files are omitted for brevity, but can be found online [3], along with the general detailed kinetic scheme and all the relevant references for its reduction and validation.

CRECK 52

```
! Reduced version of the POLIMI TOT 1407 kinetic mechanism for gas-phase homogenous reactions
! of volatile species released from coal in CHEMKIN format.
! The reduction was performed by the CRECK modeling group and the obtained 52 species
! and 452 reactions mechanism was used in
! Tufano et al.: Fuel, 186:285-292 (2016), https://doi.org/10.1016/j.fuel.2016.08.073,
! Tufano et al.: Fuel, 229:262-269 (2018), https://doi.org/10.1016/j.fuel.2018.02.105,
! Tufano et al.: Fuel, 234:723-731 (2018), https://doi.org/10.1016/j.fuel.2018.07.054.
!
ELEMENTS
N
O
H
C
END
SPECIES
N2                  O2                  H2                  H2O                 H2O2
CO                  CO2                 CH2O                CH4                 CH3OH
CH3OOH              C2H2                CH2CO               C2H4                C2H6
C2H3CHO             C3H6                C4H4                CYC5H6              C6H4O2
C6H6                C6H5OH              CRESOL              C10H8               C10H7OH
DIBZFUR             O                   H                   OH                  HO2
CH                  HCO                 CH2                 CH2S                CH3
CH3O                CH3OO               C2H                 HCCO                C2H3
CH2CHO              CH3CO               C2H5                C3H3                CH2CHCH2
C4H5                CYC5H5              C6H5                C6H5O               RCRESOLO
RCRESOLC            C10H7O
END
REACTIONS
O2+H=O+OH                                                   9.6000e+14   -0.200     16625.00
H2+O=H+OH                                                   4.3300e+13    0.000     10000.00
O2+H(+M)=HO2(+M)                                            5.5800e+12    0.400         0.00
 LOW/    8.40e+17      -0.800          0.0/
TROE/           0.5000    1.000e-30    1.000e+30/
H2O/ 18.00/  H2/ 2.50/  N2/ 1.26/  CO/ 1.20/  CO2/ 2.40/
OH+HO2=O2+H2O                                               5.0000e+13    0.000      1000.00
H+HO2=2OH                                                   2.5000e+14    0.000      1900.00
O+HO2=O2+OH                                                 3.2500e+13    0.000         0.00
2OH=H2O+O                                                   3.5700e+04    2.400     -2110.00
H2+M=2H+M                                                   1.1150e+14    0.000     96081.00
H2/ 2.50/ H2O/ 12.00/ CO/ 1.90/ CO2/ 3.80/
O2+M=2O+M                                                   1.5500e+14    0.000    115120.00
H2/ 2.50/ H2O/ 12.00/ CO/ 1.90/ CO2/ 3.80/
H+OH+M=H2O+M                                                4.5000e+22   -2.000         0.00
H2O/ 16.00/ H2/ 2.00/ CO2/ 1.90/
H+HO2=O2+H2                                                 2.5000e+13    0.000       700.00
2HO2=O2+H2O2                                                2.1100e+12    0.000         0.00
2OH(+M)=H2O2(+M)                                            7.4000e+13   -0.370         0.00
 LOW/    1.30e+18      -0.900       -1700.0/
TROE/           0.7346    94.00    1756.    5182./
H2/ 2.00/  H2O/ 6.00/  CH4/ 2.00/  CO/ 1.50/  CO2/ 2.00/  C2H6/ 3.00/  N2/ 0.90/
O+OH+M=HO2+M                                                1.0000e+16    0.000         0.00
O2+CO=CO2+O                                                 2.5300e+12    0.000     47700.00
O2+HCO=CO+HO2                                               3.0000e+12    0.000         0.00
CO+O(+M)=CO2(+M)                                            9.6400e+10    0.000      3800.00
 LOW/    2.07e+26      -3.340        7610.0/
H2O/ 12.00/  H2/ 2.00/  CO/ 1.50/  CO2/ 2.00/
CO+OH=CO2+H                                                 9.6000e+11    0.140      7352.00
 DUPLICATE
CO+OH=CO2+H                                                 7.3200e+10    0.030       -16.00
 DUPLICATE
CO+HO2=CO2+OH                                               3.0000e+13    0.000     23000.00
H2O+CO=H2+CO2                                               2.0000e+11    0.000     38000.00
H+CH3(+M)=CH4(+M)                                           1.2000e+15   -0.400         0.00
 LOW/    6.40e+23      -1.800          0.0/
SRI/    0.4500   797.0000   979.0000   1.0000   0.0000/
H2/ 2.00/  CO/ 2.00/  CO2/ 3.00/  H2O/ 5.00/
2CH3(+M)=C2H6(+M)                                           2.5000e+13    0.000         0.00
 LOW/    2.33e+34      -5.030       -1200.0/
TROE/           0.3800    73.00    1180./
```

```
H2/ 2.00/  CO/ 2.00/  CO2/ 3.00/  H2O/ 5.00/
H+C2H5(+M)=C2H6(+M)                                    5.2100e+17   -0.990      1580.00
 LOW/    1.99e+41      -7.080       6685.0/
TROE/           0.8422    125.0    2219.    6882./
H2O/ 6.00/  C2H6/ 3.00/  CH4/ 2.00/  CO/ 1.50/
H+CH2CHCH2(+M)=C3H6(+M)                                1.0000e+14    0.000        0.00
 LOW/    1.33e+60     -12.000       5967.8/
TROE/           0.02000   1097.    1.097e+04   6860./
H2/ 2.00/  H2O/ 6.00/  CH4/ 2.00/  CO/ 1.50/  CO2/ 2.00/  C2H6/ 3.00/
H+C2H(+M)=C2H2(+M)                                     1.0000e+17   -1.000        0.00
 LOW/    3.75e+33      -4.800       1900.0/
TROE/           0.6464    132.0    1315.    5566./
H2/ 2.00/  H2O/ 6.00/  CH4/ 2.00/  CO/ 1.50/  CO2/ 2.00/  C2H6/ 3.00/
C2H4(+M)=H2+C2H2(+M)                                   8.0000e+12    0.440    88770.00
 LOW/    1.58e+51      -9.300      97800.0/
TROE/           0.7345    180.0    1035.    5417./
H2/ 2.00/  H2O/ 6.00/  CH4/ 2.00/  CO/ 1.50/  CO2/ 2.00/  C2H6/ 3.00/
H+C2H3(+M)=C2H4(+M)                                    6.0800e+12    0.270      280.00
 LOW/    1.40e+30      -3.860       3320.0/
TROE/           0.7820    207.5    2663.    6095./
H2/ 2.00/  H2O/ 6.00/  CH4/ 2.00/  CO/ 1.50/  CO2/ 2.00/  C2H6/ 3.00/
CH3+C2H3(+M)=C3H6(+M)                                  2.5000e+13    0.000        0.00
 LOW/    4.27e+58     -11.940       9770.0/
TROE/           0.1750   1341.    6.000e+04   1.014e+04/
H2/ 2.00/  H2O/ 6.00/  CH4/ 2.00/  CO/ 1.50/  CO2/ 2.00/  C2H6/ 3.00/
C4H4=C2H+C2H3                                          1.0000e+16    0.000   105000.00
C2H2+C2H3=C4H4+H                                       2.5000e+14   -0.710     6700.00
C4H5=C2H2+C2H3                                         7.5000e+12    0.000    40000.00
H+C2H3=H2+C2H2                                         3.0000e+13    0.000        0.00
H2+C2H4=H+C2H5                                         1.0000e+14    0.000    65000.00
2CH3=>H2+C2H4                                          5.0000e+14    0.000    32000.00
CH3+C2H3=CH4+C2H2                                      1.3330e+13    0.000        0.00
H+C4H5=C2H2+C2H4                                       1.0000e+13    0.000        0.00
H+C4H5=H2+C4H4                                         1.5000e+13    0.000        0.00
2C3H3=>C2H2+C4H4                                       1.0000e+11    0.000        0.00
C2H2+H(+M)=C2H3(+M)                                    1.0000e+13    0.000     2770.00
 LOW/    3.90e+16      0.000        -560.0/
H2/ 2.00/  CO/ 2.00/  CO2/ 3.00/  H2O/ 5.00/
C2H4+H(+M)=C2H5(+M)                                    1.7700e+13    0.000     2110.00
 LOW/    4.60e+18      0.000       1070.0/
TROE/           1.000   1.000e-15   95.00    200.0/
H2O/ 5.00/  CO2/ 3.00/  H2/ 2.00/  CO/ 2.00/
C4H5=C4H4+H                                            5.0000e+12    0.000    44000.00
C4H4+H=C2H4+C2H                                        2.0000e+13    0.000     2000.00
C4H5=C2H4+C2H                                          2.0000e+12    0.000    60000.00
2CH3=H+C2H5                                            1.4000e+14    0.000    14000.00
CH3+C2H3=H+CH2CHCH2                                    5.0000e+01    3.700     5677.00
CH2S+C3H3=C4H4+H                                       5.0000e+13    0.000        0.00
CH4+CH3=>C2H6+H                                        2.5000e+13    0.000    31000.00
C2H6=H2+C2H4                                           3.0000e+13    0.000    71000.00
2C2H2=C4H4                                             1.5000e+12    0.000    37400.00
CH2O+M=H2+CO+M                                         8.3000e+15    0.000    70000.00
H2O/ 16.00/ CO2/ 3.80/ H2/ 2.50/ CO/ 1.90/
CH2O+M=H+HCO+M                                         2.0000e+16    0.000    75600.00
H2O/ 16.00/ CO2/ 3.80/ H2/ 2.50/ CO/ 1.90/
CH3OH(+M)=OH+CH3(+M)                                   7.0000e+20   -1.300    92000.00
 LOW/    1.25e+14      0.850       67000.0/
O2+C2H2=OH+HCCO                                        2.0000e+07    1.500    30000.00
O2+CH4=HO2+CH3                                         9.0000e+13    0.000    56000.00
O2+CH2O=HO2+HCO                                        1.3000e+14    0.000    41000.00
O2+CH3OH=HO2+CH3O                                      2.5000e+12    0.000    55000.00
O2+C2H4=HO2+C2H3                                       1.0000e+14    0.000    60000.00
O2+C3H6=HO2+CH2CHCH2                                   3.0000e+13    0.000    43000.00
HCO+M=CO+H+M                                           1.2000e+17   -1.000    17000.00
CH4/ 2.80/ H2O/ 5.00/ CO2/ 3.00/ H2/ 1.90/ CO/ 1.90/
CH3O(+M)=CH2O+H(+M)                                    6.0000e+11    0.000    18000.00
 LOW/    1.20e+25      -2.700       30600.0/
CH3CO=CH2CO+H                                          1.0000e+14    0.000    49000.00
CH3CO+M=CO+CH3+M                                       2.5000e+15    0.000    14400.00
CH2CO+H=>CO+CH3                                        1.0000e+06    2.000     2000.00
CH2CO+H=H2+HCCO                                        3.6000e+14    0.000     8600.00
CH2CO+CH3=CH4+HCCO                                     3.7500e+12    0.000    13000.00
CH3OH+H=>H2O+CH3                                       6.5000e+11    0.000     5300.00
C2H2+O=>CH2CO                                          1.0000e+13    0.000    15000.00
```

C2H4+O=HCO+CH3	5.0000e+06	1.880	200.00
C3H6+O=>HCO+C2H5	1.0000e+13	0.000	3000.00
C4H4+O=HCO+C3H3	3.2000e+08	1.440	525.00
CH2O+O=>CO2+2H	2.0000e+13	0.000	5000.00
CH2CO+O=>2HCO	2.0000e+13	0.000	2300.00
CH2CO+O=>CO+CH2O	1.0000e+12	0.000	5000.00
C2H2+OH=>CO+CH3	1.5000e+11	0.000	0.00
CH2O+OH=>H2+CO2+H	1.0000e+11	0.000	0.00
CH2CO+OH=>CO2+CH3	1.0000e+13	0.000	0.00
CH2CO+OH=>CH2O+HCO	1.0000e+13	0.000	0.00
C4H4+OH=>CO+CH2CHCH2	3.0000e+13	0.000	0.00
C2H2+HO2=>CH2O+HCO	5.0000e+12	0.000	15000.00
C2H2+HCO=>CO+C2H3	5.0000e+11	0.000	6000.00
CO+CH3O=CO2+CH3	5.0000e+11	0.000	6500.00
O2+C2H2=>CO+CH2O	3.0000e+11	0.000	26000.00
O2+C2H4=>2CH2O	1.0000e+14	0.000	48000.00
O2+CH2CO=>CO2+CH2O	1.0000e+14	0.000	37000.00
O2+CH2CO=>CO+OH+HCO	3.0000e+14	0.000	40000.00
O2+C2H2=>2HCO	3.0000e+11	0.000	27000.00
O2+C2H4=>HCO+CH3O	1.0000e+14	0.000	43000.00
O2+CH3O=>CH2O+HO2	6.0000e+11	0.000	6500.00
O2+C2H5=>C2H4+HO2	1.0000e+12	0.000	3000.00
O2+CH3=O+CH3O	4.0000e+12	0.000	27000.00
O2+C2H=CO+HCO	2.0000e+14	0.000	7000.00
O2+C2H=CO2+CH	4.5000e+15	0.000	25000.00
O2+C2H3=O+CH2CHO	7.5000e+14	−0.610	5260.00
O2+C2H3=>CH2O+HCO	1.0000e+12	0.000	4000.00
O2+C2H3=>CH2CO+OH	6.0000e+11	0.000	1000.00
O2+C2H3=C2H2+HO2	6.0000e+09	0.000	0.00
O2+C2H5=>CH2O+CH3O	1.0000e+14	0.000	24000.00
O2+CH2CHO=>CO+CH2O+OH	6.0000e+10	0.000	0.00
O2+C4H5=>C2H2+CH2CO+OH	2.5000e+13	0.000	15000.00
O+CH3+M=>CH3O+M	5.0000e+16	0.000	0.00
O+C2H3=>CH2CHO	2.5000e+13	0.000	0.00
O+CH2CHCH2=>CH2O+C2H3	3.2500e+13	0.000	0.00
O+CH2CHO=>CH2O+HCO	5.0000e+13	0.000	0.00
OH+CH3=H+CH3O	5.1000e+11	0.000	13500.00
OH+CH3=H2+CH2O	6.0000e+12	0.000	0.00
OH+CH3=CH4+O	2.0000e+12	0.000	8000.00
OH+C2H3=H2O+C2H2	4.0000e+12	0.000	0.00
OH+C4H5=H2O+C4H4	2.0000e+12	0.000	0.00
OH+C4H5=>CH2CO+C2H4	3.0000e+12	0.000	0.00
OH+CH3CO=>H2O+CH2CO	3.0000e+12	0.000	0.00
OH+CH2CHO=>H2O+CH2CO	5.0000e+12	0.000	0.00
HO2+CH3=OH+CH3O	6.0000e+12	0.000	0.00
HO2+C2H3=>OH+CH2CHO	3.0000e+12	0.000	0.00
HO2+C2H5=>CH2O+OH+CH3	5.0000e+12	0.000	0.00
HO2+CH2CHCH2=>CH2O+OH+C2H3	3.5000e+11	0.000	0.00
O+HCO=CO2+H	3.0000e+13	0.000	0.00
H+HCO=H2+CO	5.0000e+13	0.000	0.00
OH+HCO=H2O+CO	5.0000e+13	0.000	0.00
HO2+HCO=H2O2+CO	4.0000e+11	0.000	0.00
HO2+HCO=>CO2+H+OH	3.0000e+13	0.000	0.00
2HCO=CO+CH2O	6.0000e+11	0.000	0.00
HCO+CH3=CO+CH4	1.0000e+13	0.000	0.00
H+CH3O=>H2+CH2O	2.0000e+13	0.000	0.00
OH+CH3O=>H2O+CH2O	1.5000e+13	0.000	0.00
HO2+CH3O=>H2O2+CH2O	1.5000e+12	0.000	0.00
HCO+CH3O=2CH2O	1.0000e+13	0.000	0.00
HCO+CH3O=>CO+CH3OH	1.0000e+13	0.000	0.00
CH3+CH3O=>CH2O+CH4	1.0000e+13	0.000	0.00
CH2CO+HO2=>CO+CH2O+OH	1.0000e+10	0.000	5000.00
CH2CHO=CH3CO	2.0000e+11	0.000	32000.00
CH2CHO=CH2CO+H	6.0000e+13	0.000	41000.00
C2H4+O=>H+CH2CHO	1.0000e+13	0.000	3000.00
C2H2+OH=>CH2CHO	5.0000e+11	0.000	0.00
O2+CH2CHO=>CH2CO+HO2	5.0000e+11	0.000	3000.00
CH4+CH2=2CH3	4.3000e+12	0.000	10034.00
CH4+CH2S=2CH3	4.3000e+13	0.000	0.00
CH4+CH=C2H4+H	6.0000e+13	0.000	0.00
CH3+M=H+CH2+M	1.0000e+16	0.000	90600.00
H2+CH2S=H+CH3	7.2000e+13	0.000	0.00
OH+CH3=H2O+CH2S	2.0000e+13	0.000	0.00
CH2+CH3=C2H4+H	4.2000e+13	0.000	0.00

CH2S+CH3=C2H4+H	2.0000e+13	0.000	0.00
CH+CH3=H+C2H3	3.0000e+13	0.000	0.00
CH2O+CH=CH2CO+H	9.5000e+13	0.000	−560.00
HCO+CH2=CO+CH3	2.0000e+13	0.000	0.00
H+CH2=H2+CH	1.7500e+14	0.000	−165.00
O+CH2=CO+2H	7.0000e+13	0.000	0.00
O+CH2=H2+CO	5.0000e+13	0.000	0.00
OH+CH2=CH2O+H	3.0000e+13	0.000	0.00
OH+CH2=H2O+CH	1.1000e+07	2.000	3000.00
O2+CH2=CH2O+O	5.0000e+13	0.000	9000.00
O2+CH2=H2O+CO	1.6000e+13	0.000	1500.00
O2+CH2=CO+H+OH	1.7000e+13	0.000	1500.00
CO2+CH2=CO+CH2O	1.1000e+11	0.000	1000.00
O2+CH2=CO2+2H	1.3200e+13	0.000	1500.00
2CH2=C2H2+2H	1.2000e+14	0.000	0.00
CH2S+M=CH2+M	1.0000e+13	0.000	0.00
H/ 20.00/ H2O/ 3.00/ C2H2/ 4.00/			
H+CH2S=H2+CH	3.0000e+13	0.000	0.00
O+CH2S=CO+2H	3.0000e+13	0.000	0.00
OH+CH2S=CH2O+H	3.0000e+13	0.000	0.00
O2+CH2S=CO+H+OH	3.1000e+13	0.000	0.00
CO2+CH2S=CO+CH2O	3.0000e+12	0.000	0.00
O+CH=CO+H	6.0000e+13	0.000	0.00
OH+CH=H+HCO	3.0000e+13	0.000	0.00
O2+CH=O+HCO	3.3000e+13	0.000	0.00
H2O+CH=CH2O+H	5.7000e+12	0.000	−760.00
CO2+CH=CO+HCO	3.4000e+12	0.000	705.00
C2H2+O=CO+CH2	3.5000e+03	2.800	500.00
C2H2+O=H+HCCO	5.0000e+06	2.000	1900.00
C2H2+CH2=H+C3H3	1.2000e+13	0.000	6600.00
C2H2+CH2S=H+C3H3	6.0000e+13	0.000	0.00
CH2CO(+M)=CO+CH2(+M)	1.5000e+14	0.000	76000.00
LOW/ 5.50e+15 0.000 59270.0/			
CH2CO=>H+HCCO	1.5000e+14	0.000	102400.00
CH2CO+O=CO2+CH2	1.5000e+12	0.000	1350.00
CH2CO+CH2=CO+C2H4	7.0000e+11	0.000	2000.00
CH2CO+CH2=CH3+HCCO	3.6000e+13	0.000	11000.00
CH2CO+CH3=CO+C2H5	1.5000e+11	0.000	7600.00
HCCO=CO+CH	6.5000e+12	0.000	59000.00
H+HCCO=CO+CH2S	1.5000e+14	0.000	0.00
O+HCCO=2CO+H	9.6000e+13	0.000	600.00
OH+HCCO=CO+H+HCO	1.0000e+13	0.000	0.00
O2+HCCO=2CO+OH	1.6000e+12	0.000	830.00
O2+HCCO=CO2+HCO	2.4000e+11	0.000	−854.00
CH2+HCCO=CO+C2H3	3.0000e+13	0.000	0.00
CH+HCCO=CO+C2H2	5.0000e+13	0.000	0.00
2HCCO=2CO+C2H2	1.0000e+13	0.000	0.00
HCCO+C3H3=CO+C4H4	1.0000e+12	0.000	0.00
O+C2H=CO+CH	1.0000e+13	0.000	0.00
OH+C2H=H+HCCO	2.0000e+13	0.000	0.00
O2+C2H=O+HCCO	2.3000e+13	0.000	0.00
O+C3H3=CH2O+C2H	3.0000e+13	0.000	0.00
O2+C3H3=CH2CO+HCO	2.0000e+10	0.000	2840.00
C3H6+H=H2+CH2CHCH2	1.0000e+07	2.000	4200.00
C2H4+OH=H2O+C2H3	2.0000e+13	0.000	6000.00
CH3OH+H=H2+CH3O	9.0000e+12	0.000	6100.00
CH2O+H=H2+HCO	4.5000e+14	0.000	7500.00
H2O+H=H2+OH	4.8000e+10	1.000	19000.00
H2O2+H=H2O+OH	2.4100e+13	0.000	3970.00
H2O2+H=H2+HO2	6.0250e+13	0.000	7950.00
CH4+H=H2+CH3	3.0000e+07	2.000	10000.00
C2H6+H=H2+C2H5	1.4300e+14	0.000	10500.00
CH2O+HO2=>H2O2+HCO	5.2000e+12	0.000	13000.00
C3H6+OH=>H2O+CH2CHCH2	1.6800e+06	2.000	−432.10
H2+C2H=C2H2+H	2.0000e+05	2.500	560.00
C2H2+OH=H2O+C2H	3.3700e+07	2.000	14000.00
CYC5H6=H+CYC5H5	1.5000e+15	0.000	81500.00
C2H4+C3H3=CYC5H6+H	5.0000e+10	0.000	20400.00
CYC5H6+H=>C2H2+CH2CHCH2	2.0000e+12	0.000	8000.00
CYC5H6+OH=>C2H2+C2H4+HCO	2.0000e+12	0.000	0.00
CYC5H6+OH=>C2H2+CH2CO+CH3	2.0000e+13	0.000	0.00
O2+CYC5H6=>2CO+C3H6	1.0000e+13	0.000	39000.00
O2+CYC5H6=>CO+HCO+CH2CHCH2	8.0000e+13	0.000	39000.00
CYC5H6+O=>HCO+C4H5	1.5000e+13	0.000	0.00

```
HO2+CYC5H5=>CO+OH+C4H5                                  3.3000e+13    0.000         0.00
HO2+CYC5H5=>CO+C2H4+OH+C2H                              1.5000e+13    0.000         0.00
HO2+CYC5H5=>C4H4+OH+HCO                                 3.0000e+12    0.000         0.00
OH+CYC5H5=>CO+C2H2+C2H4                                 2.0000e+14    0.250      4350.00
OH+CYC5H5=>CH2CO+H+C3H3                                 3.5000e+13    0.250      4350.00
O+CYC5H5=>CO+C4H5                                       1.0000e+14    0.000         0.00
CYC5H6+H=H2+CYC5H5                                      1.6000e+15    0.000      7925.00
 REV /  1.8000e+14  0.000  30000.00  /
CYC5H6+OH=>H2O+CYC5H5                                   1.0000e+14    0.000      1714.00
CYC5H5=>C2H2+C3H3                                       2.0000e+12    0.000     68000.00
C6H6+CYC5H5=>C10H8+CH3                                  3.0000e+12    0.000     23000.00
CH3+CYC5H5=>C2H3+C4H5                                   1.0000e+12    0.000      3000.00
2CYC5H5=>C10H8+2H                                       1.0000e+12    0.000      6000.00
CYC5H6+C4H5=>C6H6+CH2CHCH2                              1.0000e+12    0.000      6000.00
C6H6=H+C6H5                                             1.5000e+17    0.000    114000.00
O2+C6H6=HO2+C6H5                                        6.3000e+13    0.000     60000.00
C6H6+OH=>CO+CYC5H6+H                                    1.0000e+13    0.000      7000.00
2C3H3(+M)=C6H6(+M)                                      3.0000e+12    0.000         0.00
 LOW/    5.00e+17       0.000            0.0/
2C3H3=H+C6H5                                            3.0000e+12    0.000         0.00
CYC5H6+C6H6=>C10H8+H+CH3                                5.0000e+11    0.000     30000.00
C2H2+C4H5=C6H6+H                                        5.0000e+11    0.000      5000.00
C4H4+C4H5=>C6H6+C2H3                                    5.0000e+11    0.000      5000.00
C6H6+C4H5=>H2+C10H8+H                                   5.0000e+11    0.000      5000.00
O+C6H5=>CO+CYC5H5                                       1.0000e+14    0.000         0.00
2C4H5=C2H4+C6H6                                         2.0000e+12    0.000         0.00
C6H6+H=H2+C6H5                                          1.5000e+14    0.000     10000.00
C10H8+H=>C4H4+C6H5                                      5.0000e+12    0.000      2500.00
C6H6+OH=H2O+C6H5                                        1.0000e+12    0.000      5000.00
O2+CH3=CH3OO                                            2.0000e+12    0.000         0.00
CH3OOH=OH+CH3O                                          2.0000e+15    0.000     42500.00
H+CH3OO=CH3OOH                                          5.0000e+13    0.000         0.00
CH3OO=CH2O+OH                                           1.5000e+13    0.000     47000.00
OH+CH3OO=>HO2+CH3O                                      3.0000e+12    0.000         0.00
CH3+CH3OO=>2CH3O                                        3.0000e+13    0.000     -1200.00
HO2+CH3OO=O2+CH3OOH                                     4.0000e+10    0.000     -2600.00
HO2+CH3OO=>O2+H2O+CH2O                                  5.0000e+10    0.000         0.00
2CH3OO=>O2+2CH3O                                        2.0000e+11    0.000         0.00
2CH3OO=>O2+CH2O+CH3OH                                   1.0000e+10    0.000         0.00
CH3OO+CH2CHCH2=>CH2O+CH3O+C2H3                          7.5000e+10    0.000         0.00
CH2O+CH3OO=>H2+CO+CH2O+OH                               2.0000e+11    0.000     11000.00
CO+CH3OO=>CO2+CH3O                                      1.0000e+14    0.000     24000.00
C2H3CHO=>HCO+C2H3                                       3.0000e+16    0.000     90000.00
O2+C4H5=>C2H3CHO+HCO                                    2.5000e+13    0.000     15000.00
OH+C3H3=C2H3CHO                                         3.0000e+13    0.000         0.00
C2H3CHO+OH=>CO2+C2H4+H                                  1.1000e+13    0.000         0.00
C2H3CHO+HO2=>CH2O+CH2CO+OH                              5.0000e+12    0.000     15000.00
C2H4+HCO=>0.8CO+0.2C2H3CHO+0.2H+0.8C2H5                 7.0000e+11    0.000      6000.00
O2+CYC5H6=>CH2CO+C2H3CHO                                1.0000e+13    0.000     39000.00
O2+CH2CHCH2=>0.2CH2O+0.2C2H2+0.8C2H3CHO+OH              1.0000e+10    0.000      8000.00
HCO+C2H3=>C2H3CHO                                       4.0000e+12    0.000         0.00
C2H3CHO+H=>CH2O+C2H3                                    3.0000e+13    0.000      5000.00
C2H3CHO+H=>C2H4+HCO                                     1.0000e+13    0.000      5000.00
H+C6H5O(+M)=C6H5OH(+M)                                  4.0000e+14    0.000         0.00
 LOW/    3.00e+20       0.000            0.0/
TROE/             0.2000    1.000e-30    1.000e+30    1.000e-10/
H2O/ 6.00/  H2/ 2.00/  CO2/ 2.00/  CO/ 1.50/  CH4/ 2.00/  C2H6/ 3.00/
C6H5OH=OH+C6H5                                          5.0000e+16    0.000    115000.00
C6H5OH=CO+CYC5H6                                        2.5000e+13    0.000     72400.00
O2+C6H5OH=>CO+C2H2+CH2CO+H+HCO                          1.0000e+17    0.000     53000.00
C6H5OH+H=C6H6+OH                                        1.2000e+13    0.000      6000.00
C6H5OH+OH=>CO+CYC5H6+OH                                 4.0000e+12    0.000         0.00
C6H5O=>CO+CYC5H5                                        2.0000e+11    0.000     43920.00
H+C6H5O=CO+CYC5H6                                       2.0000e+14    0.000         0.00
OH+C6H5O=>CO+HCO+C4H5                                   5.0000e+12    0.000         0.00
OH+C6H5O=>HO2+C6H5                                      5.0000e+12    0.000         0.00
HO2+C6H5O=>CO+2C2H2+OH+HCO                              1.0000e+12    0.000      6000.00
O+C6H5O=>2CO+C4H5                                       1.0000e+14    0.000         0.00
O2+C6H5=O+C6H5O                                         2.6000e+13    0.000      6120.00
O2+C6H6=>OH+C6H5O                                       4.0000e+13    0.000     44000.00
C6H6+O=H+C6H5O                                          1.5000e+13    0.000      4000.00
C6H5OH+CYC5H5=CYC5H6+C6H5O                              3.0000e+12    0.000     25000.00
CH3+C6H5O=>CRESOL                                       3.3000e+12    0.000         0.00
CRESOL=>CH3+C6H5O                                       8.0000e+16    0.000     90000.00
```

H+RCRESOLO=CRESOL	1.5000e+14	0.000	0.00
H+RCRESOLC=CRESOL	1.5000e+14	0.000	0.00
CRESOL+H=C6H5OH+CH3	5.0000e+13	0.000	5000.00
RCRESOLO=>CO+C6H6+H	2.5000e+11	0.000	44000.00
RCRESOLO=>CO+0.5C2H4+CYC5H5	2.5000e+11	0.000	44000.00
RCRESOLC=RCRESOLO	1.0000e+11	0.000	30000.00
C3H3+RCRESOLC=>C10H7OH+2H	5.0000e+12	0.000	6000.00
CH2CHCH2+RCRESOLC=>H2+C10H7OH+2H	5.0000e+12	0.000	6000.00
H+C10H7O=C10H7OH	4.0000e+14	0.000	0.00
O+C6H5O=C6H4O2+H	1.0000e+14	0.000	0.00
C6H4O2+HO2=>2CO+CH2O+C2H2+HCO	5.0000e+12	0.000	13000.00
O2+C6H5=>C6H4O2+H	1.0000e+13	0.000	9000.00
O2+C10H8=>2CO+C2H2+H+C6H5	8.0000e+13	0.000	38000.00
C10H8+OH=>C10H7OH+H	2.0000e+11	0.000	0.00
C10H8+OH=>2C2H2+C6H5O	2.0000e+12	0.000	5000.00
C10H8+O=H+C10H7O	4.0000e+13	0.000	3000.00
C10H7OH+H=>C10H8+OH	2.2300e+13	0.000	7929.00
C4H5+C6H5=>C10H8+2H	5.0000e+12	0.000	1000.00
CYC5H6+C6H5=>C10H8+CH3	1.0000e+12	0.000	8000.00
C10H7OH+OH=H2O+C10H7O	1.0000e+14	0.000	630.00
2C6H5O=>H2O+DIBZFUR	4.0000e+13	0.000	11000.00
DIBZFUR+OH=>CO+C10H8+HCO	1.0000e+13	0.000	0.00
O2+CH2CO=>HO2+HCCO	5.1110e+06	2.000	38570.96
CH2CO+OH=H2O+HCCO	1.1980e+06	2.000	−3529.84
REV / 4.2800e+05 2.000 18970.16 /			
CH2CO+O=>OH+HCCO	4.0600e+06	2.000	1356.53
CH2CO+HO2=H2O2+HCCO	1.6160e+05	2.000	10613.33
REV / 3.4240e+04 2.000 163.33 /			
CH2CO+HCO=CH2O+HCCO	3.7890e+05	2.000	10951.12
REV / 3.4240e+05 2.000 3151.12 /			
CH2CO+CH2CHCH2=C3H6+HCCO	7.2200e+04	2.000	13700.03
REV / 1.2840e+05 2.000 4550.03 /			
CH2CO+C6H5=>C6H6+HCCO	4.0600e+04	2.000	−1345.18
CH2CO+CH3OO=>CH3OOH+HCCO	2.2830e+05	2.000	10885.67
CH2CO+C6H5O=>C6H5OH+HCCO	8.1010e+04	2.000	10961.70
CH2CO+RCRESOLO=>CRESOL+HCCO	8.1010e+04	2.000	10961.70
H2+C2H3=C2H4+H	9.4960e+05	2.000	8459.77
REV / 1.9250e+07 2.000 10409.77 /			
H2+CH3OO=>CH3OOH+H	1.0650e+06	2.000	17276.62
H2+C6H5O=>C6H5OH+H	3.7800e+05	2.000	17256.81
H2+RCRESOLO=>CRESOL+H	3.7800e+05	2.000	17256.81
CH4+OH=H2O+CH3	2.7960e+06	2.000	1566.11
REV / 3.9030e+05 2.000 15366.11 /			
CH4+HO2=H2O2+CH3	3.7710e+05	2.000	19906.34
REV / 3.1220e+04 2.000 756.34 /			
CH4+HCO=CH2O+CH3	8.8410e+05	2.000	20281.38
REV / 3.1220e+05 2.000 3781.38 /			
CH4+C2H5=C2H6+CH3	1.6090e+05	2.000	14621.99
REV / 3.5130e+05 2.000 7621.99 /			
CH4+CH2CHCH2=C3H6+CH3	1.6850e+05	2.000	23467.33
REV / 1.1710e+05 2.000 5617.33 /			
CH4+C2H3=C2H4+CH3	4.7480e+05	2.000	11093.60
REV / 3.1220e+05 2.000 11393.60 /			
CH4+CH3O=CH3OH+CH3	2.9960e+05	2.000	7323.34
REV / 1.9520e+04 2.000 5923.34 /			
CH4+C6H5=>C6H6+CH3	9.4730e+04	2.000	4854.35
CH4+CH3OO=>CH3OOH+CH3	5.3270e+05	2.000	20192.91
CH4+C6H5O=>C6H5OH+CH3	1.8900e+05	2.000	20262.59
CH4+RCRESOLO=>CRESOL+CH3	1.8900e+05	2.000	20262.59
O2+C2H2=>HO2+C2H	3.4080e+06	2.000	51633.86
C2H2+O=>OH+C2H	2.7070e+06	2.000	8781.96
C2H2+HO2=>H2O2+C2H	1.0780e+05	2.000	19844.40
C2H2+CH3=>CH4+C2H	7.8060e+04	2.000	11601.78
C2H2+HCCO=>CH2CO+C2H	8.5590e+04	2.000	12160.02
C2H4+O=>OH+C2H3	1.0830e+07	2.000	8781.96
C2H4+HO2=H2O2+C2H3	4.3100e+05	2.000	20242.54
REV / 5.4260e+04 2.000 792.54 /			
C2H4+HCO=CH2O+C2H3	1.0100e+06	2.000	20620.50
REV / 5.4260e+05 2.000 3820.50 /			
C2H4+C6H5=>C6H6+C2H3	1.0830e+05	2.000	5083.29
C2H6+OH=H2O+C2H5	3.5950e+06	2.000	−238.20
REV / 2.2980e+05 2.000 20561.80 /			
C2H6+O=>OH+C2H5	1.2180e+07	2.000	5025.57
C2H6+HO2=H2O2+C2H5	4.8490e+05	2.000	14841.16

```
 REV /  1.8390e+04  2.000  2691.16  /
C2H6+C6H5O=>C6H5OH+C2H5                                  2.4300e+05  2.000  15725.57
C3H6+O=>OH+CH2CHCH2                                      4.0600e+06  2.000   2579.54
C3H6+HO2=H2O2+CH2CHCH2                                   1.6160e+05  2.000  10460.93
 REV /  1.9250e+04  2.000  9160.93  /
C3H6+HCO=CH2O+CH2CHCH2                                   3.7890e+05  2.000  11521.15
 REV /  1.9250e+05  2.000  12871.15  /
H2O+HO2=H2O2+OH                                          5.3880e+05  2.000  28780.05
 REV /  3.1950e+05  2.000  -4169.95  /
H2O+HCO=CH2O+OH                                          1.2630e+06  2.000  28234.13
 REV /  3.1950e+06  2.000  -2065.87  /
H2O+CH2CHCH2=>C3H6+OH                                    2.4070e+05  2.000  31217.95
H2O+CH3O=CH3OH+OH                                        4.2800e+05  2.000  12484.97
 REV /  1.9970e+05  2.000  -2715.03  /
H2O+CH3OO=>CH3OOH+OH                                     7.6100e+05  2.000  27618.12
H2O+C6H5O=>C6H5OH+OH                                     2.7000e+05  2.000  26841.27
H2O+RCRESOLO=>CRESOL+OH                                  2.7000e+05  2.000  26841.27
H2O2+O=>OH+HO2                                           1.0830e+06  2.000  -1657.32
H2O2+CH3O=CH3OH+HO2                                      3.4240e+04  2.000  -2593.80
 REV /  2.6940e+04  2.000  15156.20  /
H2O2+C6H5=>C6H6+HO2                                      1.0830e+04  2.000  -3293.64
H2O2+CH3OO=>CH3OOH+HO2                                   6.0880e+04  2.000   6540.14
H2O2+C6H5O=>C6H5OH+HO2                                   2.1600e+04  2.000   7048.52
H2O2+RCRESOLO=>CRESOL+HO2                                2.1600e+04  2.000   7048.52
CH3OH+O=>OH+CH3O                                         6.7670e+05  2.000   4151.99
CH3OH+HCO=CH2O+CH3O                                      6.3150e+04  2.000  15131.22
 REV /  3.4240e+05  2.000  31.22  /
CH3OH+C6H5O=>C6H5OH+CH3O                                 1.3500e+04  2.000  14591.31
CH2O+O=>OH+HCO                                           1.0830e+07  2.000   1094.46
CH2O+C6H5=>C6H6+HCO                                      1.0830e+05  2.000   -847.84
CH2O+CH3OO=>CH3OOH+HCO                                   6.0880e+05  2.000  10073.62
CH2O+C6H5O=>C6H5OH+HCO                                   2.1600e+05  2.000  10621.42
CH2O+RCRESOLO=>CRESOL+HCO                                2.1600e+05  2.000  10621.42
O2+CYC5H6=>HO2+CYC5H5                                    1.7040e+07  2.000  40722.49
CYC5H6+O=>OH+CYC5H5                                      1.3530e+07  2.000   2579.54
CYC5H6+HO2=>H2O2+CYC5H5                                  5.3880e+05  2.000  11887.73
CYC5H6+CH3=>CH4+CYC5H5                                   3.9030e+05  2.000   4871.29
CYC5H6+C2H3=>C2H4+CYC5H5                                 6.7830e+05  2.000   4871.29
CYC5H6+HCCO=>CH2CO+CYC5H5                                4.2800e+05  2.000   5333.37
CYC5H6+CH3O=>CH3OH+CYC5H5                                4.2800e+05  2.000   1583.56
CYC5H6+C6H5=>C6H6+CYC5H5                                 1.3530e+05  2.000   -111.23
CYC5H6+CH3OO=>CH3OOH+CYC5H5                              7.6100e+05  2.000  12360.44
CYC5H6+RCRESOLO=>CRESOL+CYC5H5                           2.7000e+05  2.000  12549.65
C6H6+O=>OH+C6H5                                          2.1650e+07  2.000   8781.96
C6H6+HO2=>H2O2+C6H5                                      8.6200e+05  2.000  21656.36
C6H6+CH3=>CH4+C6H5                                       6.2450e+05  2.000  10654.35
C6H6+C2H3=>C2H4+C6H5                                     1.0850e+06  2.000  10583.29
C6H6+HCCO=>CH2CO+C6H5                                    6.8470e+05  2.000  13154.82
C6H6+CH3O=>CH3OH+C6H5                                    6.8470e+05  2.000   7759.09
C6H6+CH3OO=CH3OOH+C6H5                                   1.2180e+06  2.000  21049.51
 REV /  2.7070e+04  2.000  449.51  /
C6H6+C6H5O=>C6H5OH+C6H5                                  4.3200e+05  2.000  20602.87
C6H6+RCRESOLO=>CRESOL+C6H5                               4.3200e+05  2.000  20602.87
O2+C2H3CHO=>0.9CO+0.1C2H2+HO2+0.1HCO+0.9C2H3             1.0220e+07  2.000  38109.91
C2H3CHO+H=>H2+0.9CO+0.1C2H2+0.1HCO+0.9C2H3               1.4440e+07  2.000   2387.18
C2H3CHO+OH=>H2O+0.9CO+0.1C2H2+0.1HCO+0.9C2H3             2.3960e+06  2.000  -3343.83
C2H3CHO+O=>0.9CO+0.1C2H2+OH+0.1HCO+0.9C2H3               8.1200e+06  2.000   1094.46
C2H3CHO+HO2=>H2O2+0.9CO+0.1C2H2+0.1HCO+0.9C2H3           3.2330e+05  2.000   9982.61
C2H3CHO+CH3=>0.9CO+CH4+0.1C2H2+0.1HCO+0.9C2H3            2.3420e+05  2.000   3259.77
C2H3CHO+CH3O=>0.9CO+CH3OH+0.1C2H2+0.1HCO+0.9C2H3         2.5680e+05  2.000    161.62
C2H3CHO+CH3OO=>0.9CO+CH3OOH+0.1C2H2+0.1HCO+0.9C2H3       4.5660e+05  2.000  10438.75
C2H3CHO+C6H5O=>0.9CO+0.1C2H2+C6H5OH+0.1HCO+0.9C2H3       1.6200e+05  2.000  10621.42
C2H3CHO+RCRESOLO=>0.9CO+0.1C2H2+CRESOL+0.1HCO+0.9C2H3    1.6200e+05  2.000  10621.42
O2+C6H5OH=>HO2+C6H5O                                     8.5190e+06  2.000  45025.57
C6H5OH+H=>H2+C6H5O                                       1.2030e+07  2.000   6706.81
C6H5OH+OH=>H2O+C6H5O                                     1.9970e+06  2.000    841.27
C6H5OH+O=>OH+C6H5O                                       6.7670e+06  2.000   5025.57
C6H5OH+HO2=>H2O2+C6H5O                                   2.6940e+05  2.000  13998.52
C6H5OH+HCO=>CH2O+C6H5O                                   6.3150e+05  2.000  14921.42
C6H5OH+CH3=>CH4+C6H5O                                    1.9520e+05  2.000   8062.59
C6H5OH+C2H3=>C2H4+C6H5O                                  3.3910e+05  2.000   8102.87
C6H5OH+HCCO=>CH2CO+C6H5O                                 2.1400e+05  2.000   7461.70
C6H5OH+CH3O=>CH3OH+C6H5O                                 2.1400e+05  2.000   3791.31
C6H5OH+C6H5=>C6H6+C6H5O                                  6.7670e+04  2.000   2602.87
```

C6H5OH+CH3OO=>CH3OOH+C6H5O	3.8050e+05	2.000	15149.65
O2+CRESOL=>HO2+0.25RCRESOLO+0.75RCRESOLC	1.3630e+07	2.000	40722.49
CRESOL+H=>H2+0.25RCRESOLO+0.75RCRESOLC	1.9250e+07	2.000	3950.57
CRESOL+OH=>H2O+0.25RCRESOLO+0.75RCRESOLC	3.1950e+06	2.000	−2259.83
CRESOL+O=>OH+0.25RCRESOLO+0.75RCRESOLC	1.0830e+07	2.000	2579.54
CRESOL+HO2=>H2O2+0.25RCRESOLO+0.75RCRESOLC	4.3100e+05	2.000	11887.73
CRESOL+CH3=>CH4+0.25RCRESOLO+0.75RCRESOLC	3.1220e+05	2.000	4871.29
CRESOL+CH3O=>CH3OH+0.25RCRESOLO+0.75RCRESOLC	3.4240e+05	2.000	1583.56
CRESOL+CH3OO=>CH3OOH+0.25RCRESOLO+0.75RCRESOLC	6.0880e+05	2.000	12360.44
CRESOL+C6H5O=>C6H5OH+0.25RCRESOLO+0.75RCRESOLC	2.1600e+05	2.000	12549.65
C6H4O2+H=>H2+2CO+C2H2+C2H	8.4230e+07	2.000	10204.13
C6H4O2+OH=>H2O+2CO+C2H2+C2H	1.3980e+07	2.000	2076.14
C6H4O2+O=>2CO+C2H2+OH+C2H	4.7370e+07	2.000	8519.89
C6H4O2+HO2=>H2O2+2CO+C2H2+C2H	1.8860e+06	2.000	19508.20
C6H4O2+CH3=>2CO+CH4+C2H2+C2H	1.3660e+06	2.000	11317.39
C6H4O2+C6H5=>2CO+C2H2+C6H6+C2H	4.7370e+05	2.000	5078.14
C6H4O2+C6H5O=>2CO+C2H2+C6H5OH+C2H	9.4510e+05	2.000	20262.59
C10H7OH+H=>H2+C10H7O	2.4070e+07	2.000	6525.57
C10H7OH+O=>OH+C10H7O	1.3530e+07	2.000	5025.57
C10H7OH+CH3=>CH4+C10H7O	3.9030e+05	2.000	7525.57
END			

Detailed Pyrolysis Model

Solid Kinetics

```
! Kinetic mechanism for coal pyrolysis and char oxidation/gasification
! in CHEMKIN format.
! The mechanism was developed by Sommariva et al. (Fuel, 89(2):318-328, 2010) and
! Maffei et al. (Combust. Flame, 160(11):2559-2572, 2013).
! The following version has been used in
! Tufano et al.: Fuel 240:75-83 (2019), https://doi.org/10.1016/j.fuel.2018.11.139.
!
MATERIAL COAL

SOLID
ACQUA           GH2O            ASH             CHAR            GCOL            GCO2S
GCO2            GCO2TS          GCH2            GCOH2           GCH4            CHARH
GCOAL1          COAL1           GCOAL3          COAL3           GBTX2           COAL2
TAR1            TAR2            TAR3            CHARG


END

REACTIONS
COAL1=>GCOAL1+GCH2+CHAR+.5H2                    .5000E+10   .000   35000.0
COAL1=>GCOAL1+CH2+CHAR+.5H2                     .1000E+16   .000   65000.0
GCOAL1=>4CHARH+1.25CHAR+.75CH4+.5H2             .2000E+09   .000   40000.0
GCOAL1=>TAR1                                    .1000E+09   .000   40000.0
GCOAL1=>4CHARH+CHAR+CH4                         .1000E+15   .000   75000.0
GCOAL1=>0.25TETRALIN+0.625C12H8                 .1000E+15   .000   75000.0
TAR1=>0.25TETRALIN+0.625C12H8                   .2500E+13   .000   50000.0
TAR1+CHARH=>5CHARH+CHAR+CH4                     .2500E+11   .000   32500.0
TAR1+CHAR=>4CHARH+2CHAR+CH4                     .2500E+11   .000   32500.0
COAL2=>2.CHAR+3.94CHARH+.25COAL1+.02GBTX2+.31GCH4+.11GCH2+.11GCOH2+.15GCO2S+.41GH2O+.18GCOL+.265
      H2   .6000E+11   .000   36000.0
COAL2=>1.81CHAR+3.73CHARH+.21COAL1+.08GBTX2+.27CH4+.50CO+.1H2O+.3GCOH2+.48H2+0.1GCOL   .4000E+19
        .000   63000.0
COAL2=>TAR2                                     .5000E+11   .000   36000.0
COAL2=>0.3055555556C10H7CH3+0.3944444444BIN1B+0.25C11H12O4                                .4000E
      +18   .000   63000.0
TAR2=>0.3055555556C10H7CH3+0.3944444444BIN1B+0.25C11H12O4                                 .2400E
      +10   .000   39000.0
TAR2+CHARH=>7.CHARH+1.5CHAR+GH2O+.5CH4          .4500E+09   .000   30000.0
TAR2+GCO2TS=>GCO2TS+.15GCO2S+1.94CHAR+4.CHARH+.25COAL1+.02GBTX2+.3GCH4+.05GCH2+.1GCOH2+.4GH2O+.2
      GCOL+.335H2   .1500E+12   .000   30000.0
COAL3=>2.73CHAR+1.8CHARH+.22COAL1+.04GBTX2+.2CH3O+.1GCH4+.11GCH2+.2H2+.6GCOH2+2.2GH2O+.1CO2+.38
      GCO2+.02GCO2TS+GCOL   .2000E+11   .000   33000.0
COAL3=>GCOAL3                                   .5000E+19   .000   61000.0
GCOAL3=>1.0CHARH+2.23CHAR+1.9CO+.25CH3O+.17CH4+.74CH2+.5CO2+.65GCOH2+.08GBTX2+.21COAL1+1.2H2O
      +.48H2   .1200E+09   .000   30000.0
COAL3=>TAR3+GCO2+H2O                            .1600E+10   .000   33000.0
COAL3=>0.1192411924C10H7CH3+0.1539295393BIN1B+0.3170731707C9H10O2+0.3414634146C11H12O4+CO2+H2O
                                .2000E+19   .000   61000.0
TAR3=>0.1192411924C10H7CH3+0.1539295393BIN1B+0.3170731707C9H10O2+0.3414634146C11H12O4
                                .5000E+10   .000   32500.0
TAR3+CHARH=>4CHARH+2.5CHAR+.2GCH4+2GCOH2+.8H2+.3GCH2   .1400E+12   .000   30000.0
GBTX2=>0.5C10H7CH3+0.75TETRALIN                                    .4000E+13   .000   48000.0
GCH4=>CH4                                       .1000E+04   .000   17000.0
GCH2=>CH2                                       .1000E+04   .000   17000.0
GCO2=>CO2                                       .1000E+04   .000   18000.0
GCO2S=>CO2                                      .1000E+03   .000   18000.0
GCO2S=>.01GCO2S+.99CO2                          .5000E+12   .000   65000.0
GH2O=>H2O                                       .1000E+04   .000   18000.0
GH2O=>.01GH2O+.99H2O                            .5000E+14   .000   60000.0
GCOH2=>GCOL+H2                                  .1500E+10   .000   57000.0
GCOL=>CO                                        .3000E+03   .000   20000.0
CHARH=>2CHAR+0.5H2                              .1000E+12   .000   80000.0
CHAR=>CHARG                                    3.0000E+03   .000   50167.0
  DUPLICATE
CHAR=>CHARG                                    1.0000E+11   .000   109890.0
```

```
 DUPLICATE
ASH=>ASH                                          .1000E+01   .000      .0
ACQUA=>H2O                                        .1000E+01  1.000   7100.0
CHARH+0.75O2=>0.5H2O+CO+CHAR                     1.2033E+10   .000  28667.0
FORD / O2 0.78 /
CHAR+O2=>CO2                                     7.3000E+10   .000  32250.0
CHAR+0.5O2=>CO                                   3.2816E+11   .000  38223.0
FORD / O2 0.78 /
CHARG+O2=>CO2                                    2.3000E+10   .000  37028.0
CHARG+0.5O2=>CO                                  1.3345E+10   .000  43000.0
FORD / O2 0.78 /
CHARH+0.5H2O=>H2+0.5CO+1.5CHAR                   4.6000E+11   .000  46345.0
FORD / H2O 1.0 /
CHAR+H2O=>H2+CO                                  1.5000E+12   .000  53034.0
CHARG+H2O=>H2+CO                                 2.9000E+11   .000  53989.0
CHARH+0.5CO2=>0.5H2O+0.5CO+2CHAR                 3.0000E+12   .000  55184.0
FORD / CO2 1.0 /
CHAR+CO2=>2CO                                    4.0000E+12   .000  59962.0
CHARG+CO2=>2CO                                   1.0000E+12   .000  61395.0
 !
 ! ABSTRACTION REACTIONS
 !
END
```

Gas Kinetics

```
! Reduced version of the POLIMI TOT 1407 kinetic mechanism for gas-phase homogenous reactions
! of volatile species released from coal in CHEMKIN format.
! The reduction was performed by the CRECK modeling group and the obtained 76 species
! and 973 homogeneous reactions mechanism was used in
! Tufano et al.: Fuel 240:75-83 (2019), https://doi.org/10.1016/j.fuel.2018.11.139.
!
ELEMENTS
C
H
O
N
K
END

SPECIES
N2                  O2                  H2                  H2O                 H2O2
CO                  CO2                 CH2O                CH4                 CH3OH
CH3OOH              C2H2                CH2CO               C2H4                C2H6
PC3H4               AC3H4               C2H3CHO             C4H4                CYC5H6
C6H4O2              C6H5OH              C6H5CHO             C6H5C2H             C8H10O3
INDENE              C9H10O2             C10H8               C10H7OH             C10H10
TETRALIN            C10H7CHO            C10H7CH3            CH3C10H6OH          C11H12O4
C12H8               C16H10              BIN1B               O                   H
OH                  HO2                 CH                  HCO                 CH2S
CH2                 CH3                 CH3O                CH3OO               C2H
HCCO                C2H3                CH2CHO              C2H5                C3H3
CH2CHCH2            CH3COCH2            C4H5                CYC5H5              C6H5
C6H5O               C6H4CH3             RCRESOLO            C6H4C2H             C6H5C2H2
INDENYL             C10H7               C10H7O              RTETRALIN           RTETRAOO
C10H7CH2            C10H6CH3            CH3C10H6O           C12H7               C14H9
C16H9
END


REACTIONS

O2+H=O+OH                                         9.6000e+14  -0.200   16625.00
H2+O=H+OH                                         4.3300e+13   0.000   10000.00
O2+H(+M)=HO2(+M)                                  5.5800e+12   0.400       0.00
 LOW/     8.40e+17      -0.800          0.0/
TROE/            0.5000    1.000e-30    1.000e+30/
H2O/ 18.00/  H2/ 2.50/  N2/ 1.26/  CO/ 1.20/  CO2/ 2.40/
OH+HO2=O2+H2O                                     5.0000e+13   0.000    1000.00
H+HO2=2OH                                         2.5000e+14   0.000    1900.00
O+HO2=O2+OH                                       3.2500e+13   0.000       0.00
2OH=H2O+O                                         3.5700e+04   2.400   -2110.00
```

```
H2+M=2H+M                                                    1.1150e+14    0.000     96081.00
 H2/ 2.50/ H2O/ 12.00/ CO/ 1.90/ CO2/ 3.80/
O2+M=2O+M                                                    1.5500e+14    0.000    115120.00
 H2/ 2.50/ H2O/ 12.00/ CO/ 1.90/ CO2/ 3.80/
H+OH+M=H2O+M                                                 4.5000e+22   -2.000         0.00
 H2O/ 16.00/ H2/ 2.00/ CO2/ 1.90/
H+HO2=O2+H2                                                  2.5000e+13    0.000       700.00
2HO2=O2+H2O2                                                 2.1100e+12    0.000         0.00
2OH(+M)=H2O2(+M)                                             7.4000e+13   -0.370         0.00
 LOW/    1.30e+18      -0.900       -1700.0/
TROE/            0.7346    94.00    1756.    5182./
 H2/ 2.00/  H2O/ 6.00/  CH4/ 2.00/  CO/ 1.50/  CO2/ 2.00/  C2H6/ 3.00/  N2/ 0.90/
O+OH+M=HO2+M                                                 1.0000e+16    0.000         0.00
O2+CO=CO2+O                                                  2.5300e+12    0.000     47700.00
O2+HCO=CO+HO2                                                3.0000e+12    0.000         0.00
CO+O(+M)=CO2(+M)                                             9.6400e+10    0.000      3800.00
 LOW/    2.07e+26      -3.340        7610.0/
H2O/ 12.00/  H2/ 2.00/  CO/ 1.50/  CO2/ 2.00/
CO+OH=CO2+H                                                  9.6000e+11    0.140      7352.00
 DUPLICATE
CO+OH=CO2+H                                                  7.3200e+10    0.030       -16.00
 DUPLICATE
CO+HO2=CO2+OH                                                3.0000e+13    0.000     23000.00
H2O+CO=H2+CO2                                                2.0000e+11    0.000     38000.00
H+CH3(+M)=CH4(+M)                                            1.2000e+15   -0.400         0.00
 LOW/    6.40e+23      -1.800         0.0/
SRI/    0.4500   797.0000   979.0000   1.0000   0.0000/
 H2/ 2.00/  CO/ 2.00/  CO2/ 3.00/  H2O/ 5.00/
2CH3(+M)=C2H6(+M)                                            2.5000e+13    0.000         0.00
 LOW/    2.33e+34      -5.030       -1200.0/
TROE/            0.3800    73.00    1180./
 H2/ 2.00/  CO/ 2.00/  CO2/ 3.00/  H2O/ 5.00/
H+C2H5(+M)=C2H6(+M)                                          5.2100e+17   -0.990      1580.00
 LOW/    1.99e+41      -7.080        6685.0/
TROE/            0.8422    125.0    2219.    6882./
 H2O/ 6.00/  C2H6/ 3.00/  CH4/ 2.00/  CO/ 1.50/
H+CH2CHCH2=H2+AC3H4                                          1.8100e+13    0.000         0.00
H+C2H(+M)=C2H2(+M)                                           1.0000e+17   -1.000         0.00
 LOW/    3.75e+33      -4.800        1900.0/
TROE/            0.6464    132.0    1315.    5566./
 H2/ 2.00/  H2O/ 6.00/  CH4/ 2.00/  CO/ 1.50/  CO2/ 2.00/  C2H6/ 3.00/
C2H4(+M)=H2+C2H2(+M)                                         8.0000e+12    0.440     88770.00
 LOW/    1.58e+51      -9.300       97800.0/
TROE/            0.7345    180.0    1035.    5417./
 H2/ 2.00/  H2O/ 6.00/  CH4/ 2.00/  CO/ 1.50/  CO2/ 2.00/  C2H6/ 3.00/
H+C2H3(+M)=C2H4(+M)                                          6.0800e+12    0.270       280.00
 LOW/    1.40e+30      -3.860        3320.0/
TROE/            0.7820    207.5    2663.    6095./
 H2/ 2.00/  H2O/ 6.00/  CH4/ 2.00/  CO/ 1.50/  CO2/ 2.00/  C2H6/ 3.00/
H+C3H3(+M)=AC3H4(+M)                                         1.0000e+17   -0.800       315.00
 LOW/    3.50e+33      -4.900        2225.0/
TROE/            0.7090    134.0    1784.    5740./
 H2/ 2.90/  H2O/ 8.60/  CH4/ 2.90/  CO/ 2.10/  CO2/ 2.90/  C2H6/ 4.30/
H+C3H3(+M)=PC3H4(+M)                                         1.0000e+17   -0.800       315.00
 LOW/    3.50e+33      -4.900        2225.0/
TROE/            0.7090    134.0    1784.    5740./
 H2/ 2.90/  H2O/ 8.60/  CH4/ 2.90/  CO/ 2.10/  CO2/ 2.90/  C2H6/ 4.30/
C4H4=C2H+C2H3                                                1.0000e+16    0.000    105000.00
C2H2+C2H3=C4H4+H                                             2.5000e+14   -0.710      6700.00
C4H5=C2H2+C2H3                                               7.5000e+12    0.000     40000.00
H+C2H3=H2+C2H2                                               3.0000e+13    0.000         0.00
H2+C2H4=H+C2H5                                               1.0000e+14    0.000     65000.00
2CH3=>H2+C2H4                                                5.0000e+14    0.000     32000.00
CH3+C2H3=CH4+C2H2                                            1.3330e+13    0.000         0.00
CH4+C2H4=>CH3+C2H5                                           3.0000e+13    0.000     62000.00
2C2H2=C2H+C2H3                                               1.7000e+14    0.000     92000.00
C2H2+C2H4=2C2H3                                              2.4000e+13    0.000     68360.00
H+C4H5=C2H2+C2H4                                             1.0000e+13    0.000         0.00
H+C4H5=H2+C4H4                                               1.5000e+13    0.000         0.00
C2H2+AC3H4=C2H+CH2CHCH2                                      5.0000e+14    0.000     73000.00
C2H2+C2H6=C2H3+C2H5                                          2.0000e+14    0.000     60000.00
C2H2+C4H4=C2H+C4H5                                           1.0000e+14    0.000     95000.00
2C2H4=C2H3+C2H5                                              4.8000e+14    0.000     71500.00
2C3H3=>C2H2+C4H4                                             1.0000e+11    0.000         0.00
```

```
AC3H4=PC3H4                                                    6.0260e+53  -12.180    84276.00
C2H2+H(+M)=C2H3(+M)                                            1.0000e+13    0.000     2770.00
 LOW/     3.90e+16       0.000        -560.0/
H2/ 2.00/  CO/ 2.00/  CO2/ 3.00/  H2O/ 5.00/
C2H4+H(+M)=C2H5(+M)                                            1.7700e+13    0.000     2110.00
 LOW/     4.60e+18       0.000        1070.0/
TROE/            1.000    1.000e-15    95.00    200.0/
H2O/ 5.00/  CO2/ 3.00/  H2/ 2.00/  CO/ 2.00/
AC3H4+H(+M)=CH2CHCH2(+M)                                       1.2000e+11    0.690     3007.00
 LOW/     5.66e+33       -5.000       4448.0/
C4H5=C4H4+H                                                    5.0000e+12    0.000    44000.00
C4H4+H=C2H4+C2H                                                2.0000e+13    0.000     2000.00
C4H5=C2H4+C2H                                                  2.0000e+12    0.000    60000.00
2CH3=H+C2H5                                                    1.4000e+14    0.000    14000.00
CH3+C2H3=H+CH2CHCH2                                            5.0000e+01    3.700     5677.00
PC3H4+H=C2H2+CH3                                               2.0000e+05    2.500     1000.00
CH2S+C3H3=C4H4+H                                               5.0000e+13    0.000        0.00
CH4+CH3=>C2H6+H                                                2.5000e+13    0.000    31000.00
C2H6=H2+C2H4                                                   3.0000e+13    0.000    71000.00
2C2H2=C4H4                                                     1.5000e+12    0.000    37400.00
2AC3H4=>C2H4+C4H4                                              5.0000e+11    0.000    25000.00
CH2O+M=H2+CO+M                                                 8.3000e+15    0.000    70000.00
H2O/ 16.00/ CO2/ 3.80/ H2/ 2.50/ CO/ 1.90/
CH2O+M=H+HCO+M                                                 2.0000e+16    0.000    75600.00
H2O/ 16.00/ CO2/ 3.80/ H2/ 2.50/ CO/ 1.90/
CH3OH(+M)=OH+CH3(+M)                                           7.0000e+20   -1.300    92000.00
 LOW/     1.25e+14       0.850        67000.0/
O2+C2H2=OH+HCCO                                                2.0000e+07    1.500    30000.00
O2+AC3H4=>CH2O+CH2CO                                           1.0000e+15    0.000    41000.00
O2+CH4=HO2+CH3                                                 9.0000e+13    0.000    56000.00
O2+CH2O=HO2+HCO                                                1.3000e+14    0.000    41000.00
O2+CH3OH=HO2+CH3O                                              2.5000e+12    0.000    55000.00
O2+C2H4=HO2+C2H3                                               1.0000e+14    0.000    60000.00
O2+C2H6=HO2+C2H5                                               1.0000e+14    0.000    50000.00
HCO+M=CO+H+M                                                   1.2000e+17   -1.000    17000.00
CH4/ 2.80/ H2O/ 5.00/ CO2/ 3.00/ H2/ 1.90/ CO/ 1.90/
CH3O(+M)=CH2O+H(+M)                                            6.0000e+11    0.000    18000.00
 LOW/     1.20e+25       -2.700       30600.0/
CH2CO+H=>CO+CH3                                                1.0000e+06    2.000     2000.00
CH2CO+H=H2+HCCO                                                3.6000e+14    0.000     8600.00
CH2CO+CH3=CH4+HCCO                                             3.7500e+12    0.000    13000.00
CH3OH+H=>H2O+CH3                                               6.5000e+11    0.000     5300.00
C2H2+O=>CH2CO                                                  1.0000e+13    0.000    15000.00
C2H4+O=HCO+CH3                                                 5.0000e+06    1.880      200.00
PC3H4+O=CO+C2H4                                                5.0000e+12    0.000     2102.00
AC3H4+O=>CO+C2H4                                               2.0000e+13    0.000        0.00
C4H4+O=HCO+C3H3                                                3.2000e+08    1.440      525.00
C4H4+O=>CO+0.5PC3H4+0.5AC3H4                                   2.0000e+12    0.000     5000.00
CH2O+O=>CO2+2H                                                 2.0000e+13    0.000     5000.00
CH2CO+O=>2HCO                                                  2.0000e+13    0.000     2300.00
CH2CO+O=>CO+CH2O                                               1.0000e+12    0.000     5000.00
C2H2+OH=>CO+CH3                                                1.5000e+11    0.000        0.00
CH2O+OH=>H2+CO2+H                                              1.0000e+11    0.000        0.00
CH2CO+OH=>CO2+CH3                                              1.0000e+13    0.000        0.00
CH2CO+OH=>CH2O+HCO                                             1.0000e+13    0.000        0.00
AC3H4+OH=>0.5CH2O+0.5CH2CO+0.5CH3+0.5C2H3                      5.0000e+11    0.000     1000.00
C4H4+OH=>CO+CH2CHCH2                                           3.0000e+13    0.000        0.00
C2H2+HO2=>CH2O+HCO                                             5.0000e+12    0.000    15000.00
C2H2+HCO=>CO+C2H3                                              5.0000e+11    0.000     6000.00
CH2O+HCO=CO2+CH3                                               5.0000e+11    0.000     6000.00
CO+CH3O=CO2+CH3                                                5.0000e+11    0.000     6500.00
O2+C2H2=>CO+CH2O                                               3.0000e+11    0.000    26000.00
O2+C2H4=>2CH2O                                                 1.0000e+14    0.000    48000.00
O2+CH2CO=>CO2+CH2O                                             1.0000e+14    0.000    37000.00
O2+CH2CO=>CO+OH+HCO                                            3.0000e+14    0.000    40000.00
O2+C2H2=>2HCO                                                  3.0000e+11    0.000    27000.00
O2+C2H4=>HCO+CH3O                                              1.0000e+14    0.000    43000.00
O2+CH3O=>CH2O+HO2                                              6.0000e+11    0.000     6500.00
O2+C2H5=>C2H4+HO2                                              1.0000e+12    0.000     3000.00
O2+CH3=O+CH3O                                                  4.0000e+12    0.000    27000.00
O2+C2H=CO+HCO                                                  2.0000e+14    0.000     7000.00
O2+C2H=CO2+CH                                                  4.5000e+15    0.000    25000.00
O2+C2H3=O+CH2CHO                                               7.5000e+14   -0.610     5260.00
O2+C2H3=>CH2O+HCO                                              1.0000e+12    0.000     4000.00
```

O2+C2H3=>CH2CO+OH	6.0000e+11	0.000	1000.00
O2+C2H3=C2H2+HO2	6.0000e+09	0.000	0.00
O2+C2H5=>CH2O+O+CH3	1.0000e+13	0.000	27000.00
O2+C2H5=>CH2O+CH3O	1.0000e+14	0.000	24000.00
O2+CH2CHO=>CO+CH2O+OH	6.0000e+10	0.000	0.00
O2+C4H5=>CO+0.4CH2O+0.3PC3H4+0.3AC3H4+0.6OH+0.4C2H3	7.0000e+13	0.000	15000.00
O2+C4H5=>C2H2+CH2CO+OH	1.5000e+13	0.000	15000.00
O+CH3+M=>CH3O+M	5.0000e+16	0.000	0.00
O+C2H3=>CH2CHO	2.5000e+13	0.000	0.00
O+CH2CHCH2=>CH2O+C2H3	3.2500e+13	0.000	0.00
O+CH2CHO=>CH2O+HCO	5.0000e+13	0.000	0.00
OH+CH3=H+CH3O	5.1000e+11	0.000	13500.00
OH+CH3=H2+CH2O	6.0000e+12	0.000	0.00
OH+CH3=CH4+O	2.0000e+12	0.000	8000.00
OH+C2H=>0.7C2H2+0.3CH2CO+0.7O	1.0000e+12	0.000	13000.00
OH+C2H3=H2O+C2H2	4.0000e+12	0.000	0.00
OH+C4H5=H2O+C4H4	2.0000e+12	0.000	0.00
OH+C4H5=>CH2CO+C2H4	3.0000e+12	0.000	0.00
OH+CH2CHO=>H2O+CH2CO	5.0000e+12	0.000	0.00
HO2+CH3=OH+CH3O	6.0000e+12	0.000	0.00
HO2+C2H3=>OH+CH2CHO	3.0000e+12	0.000	0.00
HO2+C2H5=>CH2O+OH+CH3	5.0000e+12	0.000	0.00
HO2+CH2CHCH2=>CH2O+OH+C2H3	3.5000e+11	0.000	0.00
O+HCO=CO2+H	3.0000e+13	0.000	0.00
H+HCO=H2+CO	5.0000e+13	0.000	0.00
OH+HCO=H2O+CO	5.0000e+13	0.000	0.00
HO2+HCO=H2O2+CO	4.0000e+11	0.000	0.00
HO2+HCO=>CO2+H+OH	3.0000e+13	0.000	0.00
2HCO=CO+CH2O	6.0000e+11	0.000	0.00
HCO+CH3=CO+CH4	1.0000e+13	0.000	0.00
H+CH3O=>H2+CH2O	2.0000e+13	0.000	0.00
OH+CH3O=>H2O+CH2O	1.5000e+13	0.000	0.00
HO2+CH3O=>H2O2+CH2O	1.5000e+12	0.000	0.00
HCO+CH3O=2CH2O	1.0000e+13	0.000	0.00
HCO+CH3O=>CO+CH3OH	1.0000e+13	0.000	0.00
CH3+CH3O=>CH2O+CH4	1.0000e+13	0.000	0.00
2CH3O=>CH2O+CH3OH	2.0000e+12	0.000	0.00
CH2CO+HO2=>CO+CH2O+OH	1.0000e+10	0.000	5000.00
CH2CHO=CH2CO+H	6.0000e+13	0.000	41000.00
C2H4+O=>H+CH2CHO	1.0000e+13	0.000	3000.00
C2H2+OH=>CH2CHO	5.0000e+11	0.000	0.00
O2+CH2CHO=>CH2CO+HO2	5.0000e+11	0.000	3000.00
CH4+CH2=2CH3	4.3000e+12	0.000	10034.00
CH4+CH2S=2CH3	4.3000e+13	0.000	0.00
CH4+CH=C2H4+H	6.0000e+13	0.000	0.00
CH3+M=H+CH2+M	1.0000e+16	0.000	90600.00
H2+CH2S=H+CH3	7.2000e+13	0.000	0.00
OH+CH3=H2O+CH2S	2.0000e+13	0.000	0.00
CH2+CH3=C2H4+H	4.2000e+13	0.000	0.00
CH2S+CH3=C2H4+H	2.0000e+13	0.000	0.00
CH+CH3=H+C2H3	3.0000e+13	0.000	0.00
CH2O+CH=CH2CO+H	9.5000e+13	0.000	−560.00
HCO+CH2=CO+CH3	2.0000e+13	0.000	0.00
H+CH2=H2+CH	1.7500e+14	0.000	−165.00
O+CH2=CO+2H	7.0000e+13	0.000	0.00
O+CH2=H2+CO	5.0000e+13	0.000	0.00
OH+CH2=CH2O+H	3.0000e+13	0.000	0.00
OH+CH2=H2O+CH	1.1000e+07	2.000	3000.00
O2+CH2=CH2O+O	5.0000e+13	0.000	9000.00
O2+CH2=H2O+CO	1.6000e+13	0.000	1500.00
O2+CH2=CO+H+OH	1.7000e+13	0.000	1500.00
CO2+CH2=CO+CH2O	1.1000e+11	0.000	1000.00
O2+CH2=CO2+2H	1.3200e+13	0.000	1500.00
2CH2=C2H2+2H	1.2000e+14	0.000	0.00
CH+CH2=C2H2+H	4.0000e+13	0.000	0.00
CH2S+M=CH2+M	1.0000e+13	0.000	0.00
H/ 20.00/ H2O/ 3.00/ C2H2/ 4.00/			
H+CH2S=H2+CH	3.0000e+13	0.000	0.00
O+CH2S=CO+2H	3.0000e+13	0.000	0.00
OH+CH2S=CH2O+H	3.0000e+13	0.000	0.00
O2+CH2S=CO+H+OH	3.1000e+13	0.000	0.00
CO2+CH2S=CO+CH2O	3.0000e+12	0.000	0.00
O+CH=CO+H	6.0000e+13	0.000	0.00
OH+CH=H+HCO	3.0000e+13	0.000	0.00

O2+CH=O+HCO	3.3000e+13	0.000	0.00
H2O+CH=CH2O+H	5.7000e+12	0.000	−760.00
CO2+CH=CO+HCO	3.4000e+12	0.000	705.00
C2H2+O=CO+CH2	3.5000e+03	2.800	500.00
C2H2+O=H+HCCO	5.0000e+06	2.000	1900.00
C2H2+CH2=H+C3H3	1.2000e+13	0.000	6600.00
C2H2+CH2S=H+C3H3	6.0000e+13	0.000	0.00
CH2CO(+M)=CO+CH2(+M)	1.5000e+14	0.000	76000.00
LOW/ 5.50e+15 0.000 59270.0/			
2CH2CO=CO2+AC3H4	7.5000e+09	0.000	27700.00
2CH2CO=>2CO+C2H4	7.5000e+10	0.000	40000.00
CH2CO=>H+HCCO	1.5000e+14	0.000	102400.00
CH2CO+O=CO2+CH2	1.5000e+12	0.000	1350.00
CH2CO+CH2=CO+C2H4	7.0000e+11	0.000	2000.00
CH2CO+CH2=CH3+HCCO	3.6000e+13	0.000	11000.00
CH2CO+CH3=CO+C2H5	1.5000e+11	0.000	7600.00
CH2CO+CH3=AC3H4+OH	1.5000e+11	0.000	32300.00
CH2CO+CH3=PC3H4+OH	3.0000e+10	0.000	39000.00
HCCO=CO+CH	6.5000e+12	0.000	59000.00
H+HCCO=CO+CH2S	1.5000e+14	0.000	0.00
O+HCCO=2CO+H	9.6000e+13	0.000	600.00
OH+HCCO=CO+H+HCO	1.0000e+13	0.000	0.00
O2+HCCO=2CO+OH	1.6000e+12	0.000	830.00
O2+HCCO=CO2+HCO	2.4000e+11	0.000	−854.00
CH2+HCCO=CO+C2H3	3.0000e+13	0.000	0.00
CH+HCCO=CO+C2H2	5.0000e+13	0.000	0.00
2HCCO=2CO+C2H2	1.0000e+13	0.000	0.00
HCCO+C2H3=CO+PC3H4	4.0000e+13	0.000	0.00
HCCO+C3H3=CO+C4H4	1.0000e+12	0.000	0.00
O+C2H=CO+CH	1.0000e+13	0.000	0.00
OH+C2H=H+HCCO	2.0000e+13	0.000	0.00
O2+C2H=O+HCCO	2.3000e+13	0.000	0.00
O+C3H3=CH2O+C2H	3.0000e+13	0.000	0.00
O2+C3H3=CH2CO+HCO	2.0000e+10	0.000	2840.00
HCO+C3H3=CO+PC3H4	2.5000e+13	0.000	0.00
C2H4+OH=H2O+C2H3	2.0000e+13	0.000	6000.00
CH3OH+H=H2+CH3O	9.0000e+12	0.000	6100.00
CH2O+H=H2+HCO	4.5000e+14	0.000	7500.00
AC3H4+H=H2+C3H3	5.0000e+07	2.000	5000.00
AC3H4+OH=H2O+C3H3	2.0000e+07	2.000	1000.00
PC3H4+H=H2+C3H3	1.0000e+07	2.000	5000.00
PC3H4+OH=H2O+C3H3	8.0000e+06	2.000	1000.00
PC3H4+CH3=CH4+C3H3	2.2200e+00	3.500	5600.00
AC3H4+CH3=CH4+C3H3	4.0000e+13	0.000	16000.00
H2O+H=H2+OH	4.8000e+10	1.000	19000.00
H2O2+H=H2O+OH	2.4100e+13	0.000	3970.00
H2O2+H=H2+HO2	6.0250e+13	0.000	7950.00
CH4+H=H2+CH3	3.0000e+07	2.000	10000.00
C2H6+H=H2+C2H5	1.4300e+14	0.000	10500.00
CH2O+HO2=>H2O2+HCO	5.2000e+12	0.000	13000.00
H2+C2H=C2H2+H	2.0000e+05	2.500	560.00
C2H2+OH=H2O+C2H	3.3700e+07	2.000	14000.00
CYC5H6=H+CYC5H5	1.5000e+15	0.000	81500.00
C2H2+AC3H4=CYC5H6	4.0000e+11	0.000	22000.00
C2H2+PC3H4=CYC5H6	5.0000e+10	0.000	22000.00
C2H4+C3H3=CYC5H6+H	5.0000e+10	0.000	20400.00
CYC5H6+H=>C2H2+CH2CHCH2	2.0000e+12	0.000	8000.00
CYC5H6+OH=>C2H2+C2H4+HCO	2.0000e+12	0.000	0.00
CYC5H6+OH=>C2H2+CH2CO+CH3	2.0000e+13	0.000	0.00
O2+CYC5H6=>CO+HCO+CH2CHCH2	8.0000e+13	0.000	39000.00
CYC5H6+O=>HCO+C4H5	1.5000e+13	0.000	0.00
CYC5H6+O=>CH2CO+AC3H4	3.0000e+12	0.000	0.00
CYC5H6+O=>CH2CO+PC3H4	3.0000e+12	0.000	0.00
HO2+CYC5H5=>CO+OH+C4H5	3.3000e+13	0.000	0.00
HO2+CYC5H5=>CO+C2H4+OH+C2H	1.5000e+13	0.000	0.00
HO2+CYC5H5=>C4H4+OH+HCO	3.0000e+12	0.000	0.00
OH+CYC5H5=>CO+C2H2+C2H4	2.0000e+14	0.250	4350.00
OH+CYC5H5=>CH2CO+H+C3H3	3.5000e+13	0.250	4350.00
O+CYC5H5=>CO+C4H5	1.0000e+14	0.000	0.00
O+CYC5H5=>AC3H4+HCCO	5.0000e+12	0.000	0.00
O+CYC5H5=>PC3H4+HCCO	5.0000e+12	0.000	0.00
CYC5H6+H=H2+CYC5H5	1.6000e+15	0.000	7925.00
REV / 1.8000e+14 0.000 30000.00 /			
CYC5H6+OH=>H2O+CYC5H5	1.0000e+14	0.000	1714.00

```
CYC5H5=>C2H2+C3H3                                          2.0000e+12    0.000     68000.00
CYC5H6+CYC5H5=>H2+C10H8+H                                  3.0000e+12    0.000     23000.00
CH3+CYC5H5=>C2H3+C4H5                                      1.0000e+12    0.000      3000.00
2CYC5H5=>C10H8+2H                                          1.0000e+12    0.000      6000.00
AC3H4+C2H3=>CYC5H6+H                                       5.0000e+11    0.000      3000.00
PC3H4+C2H3=>CYC5H6+H                                       5.0000e+11    0.000      3000.00
2C3H3=H+C6H5                                               3.0000e+12    0.000         0.00
O+C6H5=>CO+CYC5H5                                          1.0000e+14    0.000         0.00
C10H8+H=>C4H4+C6H5                                         5.0000e+12    0.000      2500.00
O2+CH3=CH3OO                                               2.0000e+12    0.000         0.00
CH3OOH=OH+CH3O                                             2.0000e+15    0.000     42500.00
H+CH3OO=CH3OOH                                             5.0000e+13    0.000         0.00
CH3OO=CH2O+OH                                              1.5000e+13    0.000     47000.00
OH+CH3OO=>HO2+CH3O                                         3.0000e+12    0.000         0.00
CH3+CH3OO=>2CH3O                                           3.0000e+13    0.000     -1200.00
HO2+CH3OO=O2+CH3OOH                                        4.0000e+10    0.000     -2600.00
HO2+CH3OO=>O2+H2O+CH2O                                     5.0000e+10    0.000         0.00
CH3O+CH3OO=>CH2O+CH3OOH                                    6.0000e+11    0.000         0.00
2CH3OO=>O2+2CH3O                                           2.0000e+11    0.000         0.00
2CH3OO=>O2+CH2O+CH3OH                                      1.0000e+10    0.000         0.00
CH3OO+CH2CHCH2=>CH2O+CH3O+C2H3                             7.5000e+10    0.000         0.00
CH3OOH+CH3O=>CH2O+CH3OH+OH                                 1.5000e+11    0.000      6500.00
CH2O+CH3OO=>H2+CO+CH2O+OH                                  2.0000e+11    0.000     11000.00
CO+CH3OO=>CO2+CH3O                                         1.0000e+14    0.000     24000.00
CH3COCH2=CH2CO+CH3                                         1.0000e+14    0.000     31000.00
O2+CH3COCH2=>CH2O+CH2CO+OH                                 8.0000e+11    0.000         0.00
C2H3CHO=>HCO+C2H3                                          3.0000e+16    0.000     90000.00
O2+C4H5=>C2H3CHO+HCO                                       2.5000e+13    0.000     15000.00
OH+C3H3=C2H3CHO                                            3.0000e+13    0.000         0.00
PC3H4+OH=>C2H3CHO+H                                        6.0000e+11    0.000      1000.00
C2H3CHO+OH=>CO2+C2H4+H                                     1.1000e+13    0.000         0.00
C2H3CHO+HO2=>CH2O+CH2CO+OH                                 5.0000e+12    0.000     15000.00
C2H4+HCO=>0.8CO+0.2C2H3CHO+0.2H+0.8C2H5                    7.0000e+11    0.000      6000.00
O2+CYC5H6=>CH2CO+C2H3CHO                                   1.0000e+13    0.000     39000.00
O2+CH2CHCH2=>0.2CH2O+0.2C2H2+0.8C2H3CHO+OH                 1.0000e+10    0.000      8000.00
HCO+C2H3=>C2H3CHO                                          4.0000e+12    0.000         0.00
C2H3CHO+H=>CH2O+C2H3                                       3.0000e+13    0.000      5000.00
C2H3CHO+H=>C2H4+HCO                                        1.0000e+13    0.000      5000.00
C6H5CHO=>HCO+C6H5                                          5.0000e+16    0.000     97000.00
C6H5CHO+O=>CO+OH+C6H5                                      1.0000e+13    0.000      3000.00
H+C6H5O(+M)=C6H5OH(+M)                                     4.0000e+14    0.000         0.00
 LOW/    3.00e+20       0.000            0.0/
TROE/            0.2000    1.000e-30    1.000e+30    1.000e-10/
H2O/ 6.00/  H2/ 2.00/  CO2/ 2.00/  CO/ 1.50/  CH4/ 2.00/  C2H6/ 3.00/
C6H5OH=OH+C6H5                                             5.0000e+16    0.000    115000.00
C6H5OH=CO+CYC5H6                                           2.5000e+13    0.000     72400.00
O2+C6H5OH=>CO+C2H2+CH2CO+H+HCO                             1.0000e+17    0.000     53000.00
C6H5OH+OH=>CO+CYC5H6+OH                                    4.0000e+12    0.000         0.00
C6H5O=>CO+CYC5H5                                           2.0000e+11    0.000     43920.00
H+C6H5O=CO+CYC5H6                                          2.0000e+14    0.000         0.00
OH+C6H5O=>CO+HCO+C4H5                                      5.0000e+12    0.000         0.00
OH+C6H5O=>HO2+C6H5                                         5.0000e+12    0.000         0.00
HO2+C6H5O=>CO+2C2H2+OH+HCO                                 1.0000e+12    0.000      6000.00
O+C6H5O=>2CO+C4H5                                          1.0000e+14    0.000         0.00
O2+C6H5=O+C6H5O                                            2.6000e+13    0.000      6120.00
C6H5OH+CYC5H5=CYC5H6+C6H5O                                 3.0000e+12    0.000     25000.00
RCRESOLO=>CO+0.5C2H4+CYC5H5                                2.5000e+11    0.000     44000.00
2RCRESOLO=>C6H5CHO+OH+C6H4CH3                              2.5000e+12    0.000      6000.00
O2+C6H4CH3=O+RCRESOLO                                      2.0000e+12    0.000      9500.00
PC3H4+OH=>0.15CO+0.15C2H5+0.85CH3COCH2                     1.6000e+12    0.000      1000.00
C4H4+C2H=C6H5                                              3.0000e+11    0.000         0.00
CYC5H5+RCRESOLO=>CO+C10H7CH3+2H                            5.0000e+12    0.000      6000.00
C2H2+INDENE=>C10H7CH3                                      3.0000e+11    0.000     30000.00
INDENE+H=>0.5PC3H4+0.5AC3H4+C6H5                           2.5000e+12    0.000      3000.00
INDENE+OH=>CO+C2H4+C6H5                                    6.0000e+12    0.000         0.00
INDENE+OH=>H2O+INDENYL                                     1.5000e+14    0.000      4000.00
INDENE+O=>CO+C2H3+C6H5                                     6.0000e+12    0.000         0.00
2C4H4=>H2+C6H5C2H                                          1.0000e+14    0.000     44000.00
C10H8=H+C10H7                                              5.0000e+15    0.000    116000.00
CYC5H6+CYC5H5=>INDENE+CH3                                  1.3000e+25   -3.935     23108.00
H+INDENYL=INDENE                                           1.5000e+14    0.000         0.00
H+C6H4C2H=C6H5C2H                                          1.0000e+14    0.000         0.00
H+C12H7=C12H8                                              1.0000e+14    0.000         0.00
H+C16H9=C16H10                                             1.0000e+14    0.000         0.00
```

H+C10H7CH2=C10H7CH3	1.0000e+14	0.000	0.00
H+C10H6CH3=C10H7CH3	1.0000e+14	0.000	0.00
H+C10H7O=C10H7OH	4.0000e+14	0.000	0.00
H+C10H7O=>CO+INDENE	5.0000e+13	0.000	0.00
OH+C10H7O=>HO2+C10H7	5.0000e+12	0.000	0.00
O+C6H5O=C6H4O2+H	1.0000e+14	0.000	0.00
H+CH3C10H6O=CH3C10H6OH	3.0000e+15	0.000	0.00
H+C6H5C2H2=H2+C6H5C2H	2.0000e+14	0.000	0.00
C10H6CH3=C10H7CH2	1.0000e+10	0.000	39000.00
CH3+C10H7=C10H7CH3	5.0000e+13	0.000	0.00
CH3C10H6OH=OH+C10H6CH3	1.0000e+17	0.000	110000.00
C10H7OH=>OH+C10H7	5.0000e+16	0.000	115000.00
C10H7CHO=>HCO+C10H7	5.0000e+16	0.000	97000.00
C6H4O2+HO2=>2CO+CH2O+C2H2+HCO	5.0000e+12	0.000	13000.00
CYC5H6+C12H8=>C16H10+H+CH3	2.5000e+11	0.000	31000.00
2CYC5H6=>2H2+C10H8	2.0000e+11	0.000	35000.00
2INDENE=>0.5C2H4+C16H10+H+CH3	2.5000e+11	0.000	33000.00
INDENE+C10H8=>C2H2+C16H10+H+CH3	2.5000e+11	0.000	41000.00
O2+C6H4O2=>2CO+C2H2+HO2+C2H	1.4000e+14	0.000	56200.00
O2+C10H7CH3=HO2+C10H7CH2	2.0000e+14	0.000	43000.00
C10H7CH3+CH3=CH4+C10H7CH2	2.0000e+13	0.000	14000.00
O2+C6H4C2H=>2CO+C6H5	2.0000e+12	0.000	3000.00
O2+C10H7=>CO+C6H5C2H+HCO	1.0000e+12	0.000	3000.00
O2+C14H9=>CO+C12H8+HCO	1.0000e+12	0.000	9000.00
O2+C14H9=>2CO+C10H8+C2H	2.0000e+12	0.000	3000.00
O2+C12H7=>2CO+C10H7	2.0000e+12	0.000	3000.00
O2+C16H9=>2CO+C14H9	2.0000e+12	0.000	3000.00
O2+C6H5=>C6H4O2+H	1.0000e+13	0.000	9000.00
O2+INDENYL=>CO+C6H5C2H+OH	5.0000e+11	0.000	17500.00
O2+C10H7=O+C10H7O	2.6000e+13	0.000	6120.00
O2+C10H6CH3=O+CH3C10H6O	2.0000e+12	0.000	9500.00
O2+C10H7CH2=>C10H7CHO+OH	1.0000e+13	0.000	26500.00
O2+C6H5C2H=>CO+HCO+C6H5	3.0000e+11	0.000	22000.00
O2+C10H8=>2CO+C2H2+H+C6H5	8.0000e+13	0.000	38000.00
O2+INDENE=>CO+CH2CO+H+C6H5	8.0000e+13	0.000	38000.00
C10H8+OH=>C10H7OH+H	2.0000e+11	0.000	0.00
C10H8+OH=>CO+PC3H4+C6H5	2.0000e+12	0.000	5000.00
C10H8+OH=>CO+AC3H4+C6H5	2.0000e+12	0.000	5000.00
C10H8+OH=>2C2H2+C6H5O	2.0000e+12	0.000	5000.00
C10H8+OH=>CO+INDENE+H	2.0000e+12	0.000	5000.00
C10H8+OH=>H2O+C10H7	5.0000e+13	0.000	4000.00
C6H5C2H+OH=>CH2CO+C6H5	5.0000e+12	0.000	2000.00
C12H8+OH=>CH2CO+C10H7	2.1800e−04	4.500	−1000.00
C12H8+OH=>CO+C10H7CH2	1.0000e+13	0.000	7000.00
C16H10+OH=>CH2CO+C14H9	2.1800e−04	4.500	−1000.00
OH+C6H5C2H2=H2O+C6H5C2H	1.5000e+13	0.000	0.00
OH+C10H7=>C10H7OH	5.0000e+13	0.000	0.00
OH+C10H7=H+C10H7O	5.0000e+13	0.000	0.00
O+C10H7CH2=C10H7CHO+H	3.0000e+14	0.000	0.00
O+INDENYL=CO+C6H5C2H2	1.0000e+14	0.000	0.00
O+C10H7CH2=CH2O+C10H7	8.0000e+13	0.000	0.00
C10H7CH3+O=H+CH3C10H6O	1.5000e+13	0.000	4500.00
C10H7CHO+O=>CO+OH+C10H7	1.0000e+13	0.000	3000.00
C10H8+O=H+C10H7O	4.0000e+13	0.000	3000.00
INDENE+O=>C2H2+C6H5CHO	1.0000e+13	0.000	3000.00
HO2+INDENYL=>CO+CH2CHO+C6H5	1.0000e+13	0.000	0.00
HO2+C10H7CH2=>C10H7CHO+H+OH	2.5000e+14	0.000	0.00
HO2+C10H7CH2=>CH2O+OH+C10H7	8.0000e+13	0.000	0.00
C10H7CH3+HO2=>H2O2+C10H7CH2	1.0000e+11	0.000	14000.00
HO2+C10H7O=>H2O+2CO+C6H5C2H	1.0000e+12	0.000	6000.00
C10H6CH3=>PC3H4+C6H4C2H	4.5000e+13	0.000	72500.00
C10H7CH2=>C2H2+INDENYL	6.0000e+13	0.000	70000.00
C6H5C2H2=>C2H2+C6H5	4.0000e+13	0.000	68000.00
CH3C10H6O=>CO+C10H8+H	5.0000e+11	0.000	44000.00
C10H7O=CO+INDENYL	1.2500e+11	0.000	45000.00
C10H7CH3+H=C10H8+CH3	1.2000e+13	0.000	5000.00
CH3C10H6OH+H=C10H7OH+CH3	1.2000e+13	0.000	5000.00
C10H7CHO+H=C10H8+HCO	1.2000e+13	0.000	5000.00
CH3C10H6OH+H=C10H7CH3+OH	4.0000e+13	0.000	3000.00
C6H5C2H+H=C6H5C2H2	3.0000e+12	0.000	5000.00
C10H7OH+H=>C10H8+OH	2.2300e+13	0.000	7929.00
C2H2+C6H5=C6H5C2H+H	2.0000e+12	0.000	8000.00
C10H7OH+CH3=C10H7CH3+OH	1.5000e+12	0.000	15000.00
C6H5C2H+CH3=>INDENE+H	3.0000e+11	0.000	7600.00

INDENE+CH3=>H2+C10H8+H	3.0000e+11	0.000	7600.00
C10H8+C2H=>C12H8+H	3.0000e+11	0.000	8000.00
C12H8+C2H=>C14H9	3.0000e+11	0.000	8000.00
C6H5C2H+C2H=>C10H7	3.0000e+11	0.000	8000.00
C6H5C2H+C2H3=>C10H8+H	1.0000e+12	0.000	6000.00
C6H5C2H+CH2CHCH2=>C10H8+CH3	5.0000e+11	0.000	18000.00
H2+INDENYL=>INDENE+H	1.0000e+12	0.000	13000.00
C2H2+C6H5C2H=>C10H8	2.0000e+11	0.000	25500.00
C2H2+C6H4CH3=INDENE+H	1.0000e+12	0.000	5000.00
C2H2+C6H4C2H=>C10H7	1.0000e+12	0.000	5000.00
C2H2+C6H5C2H2=>C10H8+H	1.0000e+12	0.000	5000.00
C2H2+C10H7=C12H8+H	1.0000e+12	0.000	5000.00
C2H2+C10H6CH3=>C12H8+CH3	1.0000e+12	0.000	5000.00
C2H2+C14H9=C16H10+H	1.0000e+12	0.000	5000.00
C2H2+C16H9=>0.5C16H10+0.5BIN1B+H	1.0000e+12	0.000	5000.00
C2H2+INDENYL=>C10H7CH2	1.0000e+12	0.000	20000.00
C2H2+C10H7CH2=>C12H8+CH3	1.0000e+12	0.000	20000.00
CH3+C10H7CH2=>C2H4+C10H8	3.0000e+12	0.000	0.00
CH3+C10H7=H+C10H7CH2	1.5000e+13	0.000	0.00
C3H3+C6H5=>INDENE	5.0000e+12	0.000	3000.00
C3H3+C6H4CH3=>C10H8+2H	5.0000e+12	0.000	3000.00
C3H3+C6H4C2H=>0.5C10H8+0.5C12H8	5.0000e+12	0.000	3000.00
C3H3+C6H5C2H2=>C10H7CH3	5.0000e+12	0.000	3000.00
C3H3+C14H9=>0.75C16H10+0.25BIN1B+2H	5.0000e+12	0.000	3000.00
C3H3+C16H9=>0.25C16H10+0.75BIN1B+2H	5.0000e+12	0.000	3000.00
C4H5+C6H5=>C10H8+2H	5.0000e+12	0.000	1000.00
C4H5+C6H4CH3=>C10H7CH3+2H	5.0000e+12	0.000	1000.00
C4H5+C12H7=>C16H10+2H	5.0000e+12	0.000	1000.00
CYC5H5+C6H5=>C10H7CH3	2.0000e+12	0.000	3000.00
CYC5H5+C10H7CH2=>H2+C16H10+2H	2.0000e+12	0.000	6000.00
CYC5H5+C10H6CH3=>H2+C16H10+2H	2.0000e+12	0.000	3000.00
CYC5H5+C12H7=>0.75C16H10+0.25BIN1B+2H	2.0000e+12	0.000	3000.00
CYC5H5+C14H9=>0.5C16H10+0.5BIN1B+H+CH3	2.0000e+12	0.000	3000.00
CYC5H5+C16H9=>BIN1B+H+CH3	2.0000e+12	0.000	3000.00
C6H5+C10H7=>C16H10+2H	5.0000e+12	0.000	0.00
C6H5+C10H7CH2=>C16H10+H+CH3	2.0000e+12	0.000	3000.00
C6H5+C10H6CH3=>C16H10+H+CH3	5.0000e+12	0.000	0.00
C6H5+C12H7=>0.5C16H10+0.5BIN1B+2H	5.0000e+12	0.000	0.00
C6H4CH3+INDENYL=>1.5H2+C16H10+H	2.0000e+12	0.000	3000.00
C6H4CH3+C10H7=>C16H10+H+CH3	5.0000e+12	0.000	0.00
C6H4CH3+C10H7CH2=>H2+0.75C16H10+0.25BIN1B+H+CH3	2.0000e+12	0.000	3000.00
C6H4CH3+C10H6CH3=>H2+0.75C16H10+0.25BIN1B+H+CH3	5.0000e+12	0.000	0.00
C6H4CH3+C12H7=>0.5C16H10+0.5BIN1B+H+CH3	5.0000e+12	0.000	0.00
2C6H4C2H=>C16H10	5.0000e+12	0.000	0.00
C6H4C2H+C6H5C2H2=>C16H10+2H	5.0000e+12	0.000	0.00
C6H4C2H+INDENYL=>0.75C16H10+0.25BIN1B+2H	5.0000e+12	0.000	3000.00
C6H4C2H+C10H7=>0.5C16H10+0.5BIN1B+2H	5.0000e+12	0.000	0.00
C6H4C2H+C10H7CH2=>0.5C16H10+0.5BIN1B+H+CH3	2.0000e+12	0.000	3000.00
C6H4C2H+C10H6CH3=>0.5C16H10+0.5BIN1B+H+CH3	5.0000e+12	0.000	0.00
2C6H5C2H2=>H2+C16H10+2H	5.0000e+12	0.000	0.00
C6H5C2H2+INDENYL=>H2+0.75C16H10+0.25BIN1B+2H	5.0000e+12	0.000	3000.00
C6H5C2H2+C10H7=>H2+0.5C16H10+0.5BIN1B+2H	5.0000e+12	0.000	0.00
C6H5C2H2+C10H7CH2=>H2+0.5C16H10+0.5BIN1B+H+CH3	2.0000e+12	0.000	3000.00
C6H5C2H2+C10H6CH3=>H2+0.5C16H10+0.5BIN1B+H+CH3	5.0000e+12	0.000	0.00
2INDENYL=>0.75C16H10+0.25BIN1B+H+CH3	2.0000e+12	0.000	6000.00
INDENYL+C10H7=>0.5C16H10+0.5BIN1B+H+CH3	2.0000e+12	0.000	3000.00
C6H5C2H+C3H3=>C10H7CH2	4.0000e+11	0.000	19000.00
C16H10+C3H3=>H2+0.25C16H10+0.75BIN1B+H	4.0000e+11	0.000	19000.00
C10H7CH3+CYC5H5=>2H2+C16H10+H	4.0000e+11	0.000	19000.00
CYC5H6+C6H5=>C10H8+CH3	1.0000e+12	0.000	8000.00
C10H8+C6H5=>H2+C16H10+H	1.0000e+12	0.000	8000.00
C10H7CH3+C6H5=>H2+C16H10+CH3	1.0000e+12	0.000	8000.00
C10H7CH3+C6H4CH3=>3H2+0.5C16H10+0.5BIN1B+H	4.0000e+11	0.000	19000.00
CYC5H6+C6H4C2H=>C12H8+CH3	1.0000e+12	0.000	8000.00
C6H5C2H+C6H4C2H=>C16H10+H	1.0000e+12	0.000	8000.00
INDENE+C6H4C2H=>C16H10+CH3	1.0000e+12	0.000	8000.00
C10H8+C6H4C2H=>0.75C16H10+0.25BIN1B+CH3	1.0000e+12	0.000	8000.00
C10H7CH3+C6H4C2H=>H2+0.5C16H10+0.5BIN1B+CH3	1.0000e+12	0.000	8000.00
CYC5H6+C6H5C2H2=>H2+C12H8+CH3	1.0000e+12	0.000	8000.00
C6H5C2H+C6H5C2H2=>H2+C16H10+H	1.0000e+12	0.000	8000.00
INDENE+C6H5C2H2=>H2+C16H10+CH3	1.0000e+12	0.000	8000.00
C10H8+C6H5C2H2=>H2+0.75C16H10+0.25BIN1B+CH3	1.0000e+12	0.000	8000.00
C10H7CH3+C6H5C2H2=>2H2+0.5C16H10+0.5BIN1B+CH3	1.0000e+12	0.000	8000.00
C10H7CH3+INDENYL=>2H2+0.25C16H10+0.75BIN1B+CH3	4.0000e+11	0.000	19000.00

C6H5C2H+C10H7=>0.75C16H10+0.25BIN1B+CH3	1.0000e+12	0.000	8000.00
C6H5C2H+C10H7CH2=>H2+0.5C16H10+0.5BIN1B+CH3	4.0000e+11	0.000	19000.00
C6H5C2H+C10H6CH3=>H2+0.5C16H10+0.5BIN1B+CH3	1.0000e+12	0.000	8000.00
CYC5H6+C12H7=>C16H10+CH3	1.0000e+12	0.000	8000.00
C6H5C2H+C12H7=>0.25C16H10+0.75BIN1B+CH3	1.0000e+12	0.000	8000.00
CYC5H6+C14H9=>H2+0.5C16H10+0.5BIN1B+CH3	1.0000e+12	0.000	8000.00
BIN1B+OH=>0.25C16H10+0.75BIN1B+HCO	3.5000e+13	0.500	9600.00
C10H7OH+OH=H2O+C10H7O	1.0000e+14	0.000	630.00
C6H5+C14H9=>H2+BIN1B+2H	5.0000e+12	0.000	0.00
C6H5+C16H9=>0.5H2+1.1BIN1B+2H	5.0000e+12	0.000	0.00
C6H4C2H+C12H7=>BIN1B+2H	5.0000e+12	0.000	0.00
C6H5C2H2+C12H7=>H2+BIN1B+2H	5.0000e+12	0.000	0.00
INDENYL+C10H7CH2=>2H2+BIN1B+2H	1.0000e+12	0.000	6000.00
INDENYL+C10H6CH3=>2H2+BIN1B+2H	2.0000e+12	0.000	3000.00
INDENYL+C12H7=>BIN1B+H+CH3	2.0000e+12	0.000	3000.00
2C10H7=>H2+BIN1B+2H	5.0000e+12	0.000	0.00
C10H7+C10H7CH2=>H2+BIN1B+H+CH3	2.0000e+12	0.000	3000.00
C10H7+C10H6CH3=>H2+BIN1B+H+CH3	5.0000e+12	0.000	0.00
C6H5C2H+INDENYL=>H2+0.8BIN1B+CH3	4.0000e+11	0.000	19000.00
C10H7CH3+C10H7=>2H2+BIN1B+CH3	1.0000e+12	0.000	8000.00
TETRALIN=>CH2CHCH2+C6H4CH3	1.0000e+14	0.000	76500.00
TETRALIN=>C2H4+C2H3+C6H5	1.0000e+13	0.000	76500.00
TETRALIN=>H2+C10H10	5.0000e+13	0.000	70000.00
C10H10=>H2+C10H8	1.0000e+14	0.000	69000.00
2C6H5O=>2CO+C10H10	1.2500e+12	0.000	6000.00
C10H10+H=>RTETRALIN	1.0000e+13	0.000	2500.00
C10H10+OH=>C2H3CHO+C6H4CH3	5.0000e+12	0.000	0.00
RTETRALIN=>INDENE+CH3	1.5000e+13	0.000	30500.00
RTETRALIN=>H2+C10H8+H	2.0000e+13	0.000	30500.00
RTETRALIN=>C10H10+H	3.0000e+14	0.000	41000.00
O2+RTETRALIN=>H2+2CO+C2H4+C6H5	2.5000e+11	0.000	1000.00
O2+RTETRALIN=>C10H10+HO2	5.0000e+11	0.000	3000.00
TETRALIN+H=>2C2H4+C6H5	8.0000e+12	0.000	5000.00
C10H8+H=>0.5C10H7+0.5RTETRALIN	5.0000e+12	0.000	2500.00
O2+RTETRALIN=RTETRAOO	1.5000e+12	0.000	0.00
REV / 1.0000e+13 0.000 32000.00 /			
RTETRAOO=>C10H10+HO2	1.0000e+11	0.000	21000.00
RTETRAOO=>C2H4+C6H5CHO+HCO	2.0000e+11	0.000	25000.00
O2+C6H5C2H2=>C6H5CHO+HCO	6.0000e+10	0.000	3000.00
C9H10O2=>0.5C10H8+2CH2CHO	3.3000e+15	0.000	72000.00
C9H10O2+H=>0.5CO+0.5C2H4+C6H5OH+0.5HCO+0.5C2H5	1.0000e+13	0.000	5000.00
C11H12O4=>CO+C2H2+C8H10O3	7.0000e+15	0.000	88000.00
C11H12O4+H=>CO+C8H10O3+C2H3	1.0000e+13	0.000	5000.00
C8H10O3+H=>0.5C6H5OH+0.5C8H10O3+CH3O	1.0000e+13	0.000	5000.00
O2+CH2CO=>HO2+HCCO	5.1110e+06	2.000	38570.96
CH2CO+OH=H2O+HCCO	1.1980e+06	2.000	−3529.84
REV / 4.2800e+05 2.000 18970.16 /			
CH2CO+O=>OH+HCCO	4.0600e+06	2.000	1356.53
CH2CO+HO2=H2O2+HCCO	1.6160e+05	2.000	10613.33
REV / 3.4240e+04 2.000 163.33 /			
CH2CO+HCO=CH2O+HCCO	3.7890e+05	2.000	10951.12
REV / 3.4240e+05 2.000 3151.12 /			
CH2CO+C2H5=C2H6+HCCO	6.8950e+04	2.000	6224.33
REV / 3.8520e+05 2.000 7924.33 /			
CH2CO+C2H3=C2H4+HCCO	2.0350e+05	2.000	3378.60
REV / 3.4240e+05 2.000 12378.60 /			
CH2CO+C3H3=AC3H4+HCCO	8.1010e+04	2.000	12917.53
REV / 2.5680e+06 2.000 11417.53 /			
CH2CO+CH3O=CH3OH+HCCO	1.2840e+05	2.000	451.05
REV / 2.1400e+04 2.000 7751.05 /			
CH2CO+CH3OO=>CH3OOH+HCCO	2.2830e+05	2.000	10885.67
CH2CO+C6H5O=>C6H5OH+HCCO	8.1010e+04	2.000	10961.70
CH2CO+INDENYL=>INDENE+HCCO	4.0600e+04	2.000	14117.10
CH2CO+C10H7=>C10H8+HCCO	2.5620e+04	2.000	−1345.18
CH2CO+C10H6CH3=>C10H7CH3+HCCO	4.0600e+04	2.000	−1345.18
H2+C2H3=C2H4+H	9.4960e+05	2.000	8459.77
REV / 1.9250e+07 2.000 10409.77 /			
H2+CH3OO=>CH3OOH+H	1.0650e+06	2.000	17276.62
H2+C6H5O=>C6H5OH+H	3.7800e+05	2.000	17256.81
H2+C10H7=>C10H8+H	1.1950e+05	2.000	2710.27
H2+C10H6CH3=>C10H7CH3+H	1.8950e+05	2.000	2710.27
CH4+OH=H2O+CH3	2.7960e+06	2.000	1566.11
REV / 3.9030e+05 2.000 15366.11 /			
CH4+HO2=H2O2+CH3	3.7710e+05	2.000	19906.34

```
 REV /  3.1220e+04  2.000  756.34  /
CH4+HCO=CH2O+CH3                                  8.8410e+05   2.000    20281.38
 REV /  3.1220e+05  2.000  3781.38  /
CH4+C2H5=C2H6+CH3                                 1.6090e+05   2.000    14621.99
 REV /  3.5130e+05  2.000  7621.99  /
CH4+C2H3=C2H4+CH3                                 4.7480e+05   2.000    11093.60
 REV /  3.1220e+05  2.000  11393.60  /
CH4+CH3O=CH3OH+CH3                                2.9960e+05   2.000     7323.34
 REV /  1.9520e+04  2.000  5923.34  /
CH4+CH3OO=>CH3OOH+CH3                             5.3270e+05   2.000    20192.91
CH4+C6H5O=>C6H5OH+CH3                             1.8900e+05   2.000    20262.59
CH4+INDENYL=>INDENE+CH3                           9.4730e+04   2.000    23948.69
CH4+C10H7=>C10H8+CH3                              5.9770e+04   2.000     4854.35
CH4+C10H6CH3=>C10H7CH3+CH3                        9.4730e+04   2.000     4854.35
O2+C2H2=>HO2+C2H                                  3.4080e+06   2.000    51633.86
C2H2+O=>OH+C2H                                    2.7070e+06   2.000     8781.96
C2H2+HO2=>H2O2+C2H                                1.0780e+05   2.000    19844.40
C2H2+HCO=>CH2O+C2H                                2.5260e+05   2.000    20386.31
C2H2+CH3=>CH4+C2H                                 7.8060e+04   2.000    11601.78
C2H2+C2H5=>C2H6+C2H                               4.5970e+04   2.000    14929.22
C2H2+C2H3=>C2H4+C2H                               1.3570e+05   2.000    11601.78
C2H2+C3H3=>AC3H4+C2H                              5.4010e+04   2.000    23085.73
C2H2+HCCO=>CH2CO+C2H                              8.5590e+04   2.000    12160.02
C2H2+CH3O=>CH3OH+C2H                              8.5590e+04   2.000     7522.23
C2H2+CH3OO=>CH3OOH+C2H                            1.5220e+05   2.000    20386.31
C2H2+C6H5O=>C6H5OH+C2H                            5.4010e+04   2.000    20602.87
C2H2+INDENYL=>INDENE+C2H                          2.7070e+04   2.000    24161.27
C2H2+C10H7=>C10H8+C2H                             1.7080e+04   2.000     5307.08
C2H2+C10H6CH3=>C10H7CH3+C2H                       2.7070e+04   2.000     5307.08
C2H4+O=>OH+C2H3                                   1.0830e+07   2.000     8781.96
C2H4+HO2=H2O2+C2H3                                4.3100e+05   2.000    20242.54
 REV /  5.4260e+04  2.000  792.54  /
C2H4+HCO=CH2O+C2H3                                1.0100e+06   2.000    20620.50
 REV /  5.4260e+05  2.000  3820.50  /
C2H4+C2H5=C2H6+C2H3                               1.8390e+05   2.000    14929.22
 REV /  6.1050e+05  2.000  7629.22  /
C2H4+C3H3=AC3H4+C2H3                              2.1600e+05   2.000    22861.94
 REV /  4.0700e+06  2.000  12361.94  /
C2H4+CH3O=CH3OH+C2H3                              3.4240e+05   2.000     7574.27
 REV /  3.3910e+04  2.000  5874.27  /
C2H4+CH3OO=>CH3OOH+C2H3                           6.0880e+05   2.000    20532.03
C2H4+C6H5O=>C6H5OH+C2H3                           2.1600e+05   2.000    20602.87
C2H4+INDENYL=>INDENE+C2H3                         1.0830e+05   2.000    24306.99
C2H4+C10H7=>C10H8+C2H3                            6.8310e+04   2.000     5083.29
C2H4+C10H6CH3=>C10H7CH3+C2H3                      1.0830e+05   2.000     5083.29
C2H6+OH=H2O+C2H5                                  3.5950e+06   2.000     -238.20
 REV /  2.2980e+05  2.000  20561.80  /
C2H6+O=>OH+C2H5                                   1.2180e+07   2.000     5025.57
C2H6+HO2=H2O2+C2H5                                4.8490e+05   2.000    14841.16
 REV /  1.8390e+04  2.000  2691.16  /
C2H6+HCO=CH2O+C2H5                                1.1370e+06   2.000    15417.09
 REV /  1.8390e+05  2.000  5917.09  /
C2H6+C3H3=AC3H4+C2H5                              2.4300e+05   2.000    18129.22
 REV /  1.3790e+06  2.000  14929.22  /
C2H6+CH3O=CH3OH+C2H5                              3.8520e+05   2.000     3901.46
 REV /  1.1490e+04  2.000  9501.46  /
C2H6+CH3OO=>CH3OOH+C2H5                           6.8490e+05   2.000    15458.07
C2H6+C6H5O=>C6H5OH+C2H5                           2.4300e+05   2.000    15725.57
C2H6+INDENYL=>INDENE+C2H5                         1.2180e+05   2.000    18958.07
C2H6+C10H7=>C10H8+C2H5                            7.6850e+04   2.000     2129.22
C2H6+C10H6CH3=>C10H7CH3+C2H5                      1.2180e+05   2.000     2129.22
H2O+HO2=H2O2+OH                                   5.3880e+05   2.000    28780.05
 REV /  3.1950e+05  2.000  -4169.95  /
H2O+HCO=CH2O+OH                                   1.2630e+06   2.000    28234.13
 REV /  3.1950e+06  2.000  -2065.87  /
H2O+CH3O=CH3OH+OH                                 4.2800e+05   2.000    12484.97
 REV /  1.9970e+05  2.000  -2715.03  /
H2O+CH3OO=>CH3OOH+OH                              7.6100e+05   2.000    27618.12
H2O+C6H5O=>C6H5OH+OH                              2.7000e+05   2.000    26841.27
H2O+INDENYL=>INDENE+OH                            1.3530e+05   2.000    31744.79
H2O+C10H7=>C10H8+OH                               8.5390e+04   2.000     7946.24
H2O+C10H6CH3=>C10H7CH3+OH                         1.3530e+05   2.000     7946.24
H2O2+O=>OH+HO2                                    1.0830e+06   2.000    -1657.32
H2O2+HCO=>CH2O+HO2                                1.0100e+05   2.000     6335.02
```

H2O2+C3H3=AC3H4+HO2	2.1600e+04	2.000	9542.01
REV / 3.2330e+06 2.000 18492.01 /			
H2O2+CH3O=CH3OH+HO2	3.4240e+04	2.000	−2593.80
REV / 2.6940e+04 2.000 15156.20 /			
H2O2+CH3OO=>CH3OOH+HO2	6.0880e+04	2.000	6540.14
H2O2+C6H5O=>C6H5OH+HO2	2.1600e+04	2.000	7048.52
H2O2+INDENYL=>INDENE+HO2	1.0830e+04	2.000	9550.95
H2O2+C10H7=>C10H8+HO2	6.8310e+03	2.000	−3293.64
H2O2+C10H6CH3=>C10H7CH3+HO2	1.0830e+04	2.000	−3293.64
CH3OH+O=>OH+CH3O	6.7670e+05	2.000	4151.99
CH3OH+HCO=CH2O+CH3O	6.3150e+04	2.000	15131.22
REV / 3.4240e+05 2.000 31.22 /			
CH3OH+C3H3=AC3H4+CH3O	1.3500e+04	2.000	16145.45
REV / 2.5680e+06 2.000 7345.45 /			
CH3OH+CH3OO=>CH3OOH+CH3O	3.8050e+04	2.000	14853.15
CH3OH+C6H5O=>C6H5OH+CH3O	1.3500e+04	2.000	14591.31
CH3OH+INDENYL=>INDENE+CH3O	6.7670e+03	2.000	18289.21
CH3OH+C10H7=>C10H8+CH3O	4.2700e+03	2.000	559.09
CH3OH+C10H6CH3=>C10H7CH3+CH3O	6.7670e+03	2.000	559.09
CH2O+O=>OH+HCO	1.0830e+07	2.000	1094.46
CH2O+C3H3=AC3H4+HCO	2.1600e+05	2.000	13290.78
REV / 7.5780e+06 2.000 19590.78 /			
CH2O+CH3OO=>CH3OOH+HCO	6.0880e+05	2.000	10073.62
CH2O+C6H5O=>C6H5OH+HCO	2.1600e+05	2.000	10621.42
CH2O+INDENYL=>INDENE+HCO	1.0830e+05	2.000	13285.87
CH2O+C10H7=>C10H8+HCO	6.8310e+04	2.000	−847.84
CH2O+C10H6CH3=>C10H7CH3+HCO	1.0830e+05	2.000	−847.84
O2+PC3H4=>HO2+C3H3	1.0220e+08	2.000	51633.86
PC3H4+O=>OH+C3H3	8.1200e+07	2.000	8781.96
PC3H4+HO2=>H2O2+C3H3	3.2330e+06	2.000	18492.01
PC3H4+HCO=>CH2O+C3H3	7.5780e+06	2.000	19590.78
PC3H4+C2H5=>C2H6+C3H3	1.3790e+06	2.000	14929.22
PC3H4+C2H3=>C2H4+C3H3	4.0700e+06	2.000	12361.94
PC3H4+C3H3=>AC3H4+C3H3	1.6200e+06	2.000	23845.90
PC3H4+HCCO=>CH2CO+C3H3	2.5680e+06	2.000	11417.53
PC3H4+CH3O=>CH3OH+C3H3	2.5680e+06	2.000	7345.45
PC3H4+CH3OO=>CH3OOH+C3H3	4.5660e+06	2.000	19891.31
PC3H4+C6H5O=>C6H5OH+C3H3	1.6200e+06	2.000	20602.87
PC3H4+INDENYL=>INDENE+C3H3	8.1200e+05	2.000	23666.28
PC3H4+C10H7=>C10H8+C3H3	5.1230e+05	2.000	6067.25
PC3H4+C10H6CH3=>C10H7CH3+C3H3	8.1200e+05	2.000	6067.25
O2+AC3H4=>HO2+C3H3	1.0220e+08	2.000	51633.86
AC3H4+O=>OH+C3H3	8.1200e+07	2.000	8781.96
AC3H4+CH3OO=>CH3OOH+C3H3	4.5660e+06	2.000	19891.31
AC3H4+C6H5O=>C6H5OH+C3H3	1.6200e+06	2.000	20602.87
AC3H4+INDENYL=>INDENE+C3H3	8.1200e+05	2.000	23666.28
AC3H4+C10H7=>C10H8+C3H3	5.1230e+05	2.000	6067.25
AC3H4+C10H6CH3=>C10H7CH3+C3H3	8.1200e+05	2.000	6067.25
O2+CYC5H6=>HO2+CYC5H5	1.7040e+07	2.000	40722.49
CYC5H6+O=>OH+CYC5H5	1.3530e+07	2.000	2579.54
CYC5H6+HO2=>H2O2+CYC5H5	5.3880e+05	2.000	11887.73
CYC5H6+HCO=>CH2O+CYC5H5	1.2630e+06	2.000	12360.44
CYC5H6+CH3=>CH4+CYC5H5	3.9030e+05	2.000	4871.29
CYC5H6+C2H5=>C2H6+CYC5H5	2.2980e+05	2.000	7658.07
CYC5H6+C2H3=>C2H4+CYC5H5	6.7830e+05	2.000	4871.29
CYC5H6+C3H3=>AC3H4+CYC5H5	2.7000e+05	2.000	14730.58
CYC5H6+HCCO=>CH2CO+CYC5H5	4.2800e+05	2.000	5333.37
CYC5H6+CH3O=>CH3OH+CYC5H5	4.2800e+05	2.000	1583.56
CYC5H6+CH3OO=>CH3OOH+CYC5H5	7.6100e+05	2.000	12360.44
CYC5H6+INDENYL=>INDENE+CYC5H5	1.3530e+05	2.000	15681.39
CYC5H6+C10H7=>C10H8+CYC5H5	8.5390e+04	2.000	−111.23
CYC5H6+C10H6CH3=>C10H7CH3+CYC5H5	1.3530e+05	2.000	−111.23
CH3OOH+H=>H2+CH3OO	4.8130e+06	2.000	4126.62
CH3OOH+OH=>H2O+CH3OO	7.9880e+05	2.000	−981.88
CH3OOH+O=>OH+CH3OO	2.7070e+06	2.000	2579.54
CH3OOH+HO2=>H2O2+CH3OO	1.0780e+05	2.000	10890.14
CH3OOH+HCO=>CH2O+CH3OO	2.5260e+05	2.000	11773.62
CH3OOH+CH3=>CH4+CH3OO	7.8060e+04	2.000	5392.91
CH3OOH+C2H5=>C2H6+CH3OO	4.5970e+04	2.000	7658.07
CH3OOH+C2H3=>C2H4+CH3OO	1.3570e+05	2.000	5432.03
CH3OOH+C3H3=>AC3H4+CH3OO	5.4010e+04	2.000	15291.31
CH3OOH+HCCO=>CH2CO+CH3OO	8.5590e+04	2.000	4785.67
CH3OOH+CH3O=>CH3OH+CH3OO	8.5590e+04	2.000	1453.15
CH3OOH+C6H5O=>C6H5OH+CH3OO	5.4010e+04	2.000	12549.65

CH3OOH+INDENYL=>INDENE+CH3OO	2.7070e+04	2.000	15316.26
CH3OOH+C10H7=>C10H8+CH3OO	1.7080e+04	2.000	449.51
CH3OOH+C10H6CH3=>C10H7CH3+CH3OO	2.7070e+04	2.000	449.51
O2+C2H3CHO=>0.9CO+0.1C2H2+HO2+0.1HCO+0.9C2H3	1.0220e+07	2.000	38109.91
C2H3CHO+H=>H2+0.9CO+0.1C2H2+0.1HCO+0.9C2H3	1.4440e+07	2.000	2387.18
C2H3CHO+OH=>H2O+0.9CO+0.1C2H2+0.1HCO+0.9C2H3	2.3960e+06	2.000	−3343.83
C2H3CHO+O=>0.9CO+0.1C2H2+OH+0.1HCO+0.9C2H3	8.1200e+06	2.000	1094.46
C2H3CHO+HO2=>H2O2+0.9CO+0.1C2H2+0.1HCO+0.9C2H3	3.2330e+05	2.000	9982.61
C2H3CHO+HCO=>0.9CO+CH2O+0.1C2H2+0.1HCO+0.9C2H3	7.5780e+05	2.000	10438.75
C2H3CHO+CH3=>0.9CO+CH4+0.1C2H2+0.1HCO+0.9C2H3	2.3420e+05	2.000	3259.77
C2H3CHO+C2H5=>0.9CO+0.1C2H2+C2H6+0.1HCO+0.9C2H3	1.3790e+05	2.000	5917.09
C2H3CHO+C2H3=>0.9CO+0.1C2H2+C2H4+0.1HCO+0.9C2H3	4.0700e+05	2.000	3259.77
C2H3CHO+C3H3=>0.9CO+0.1C2H2+AC3H4+0.1HCO+0.9C2H3	1.6200e+05	2.000	12730.05
C2H3CHO+HCCO=>0.9CO+0.1C2H2+CH2CO+0.1HCO+0.9C2H3	2.5680e+05	2.000	3698.82
C2H3CHO+CH3O=>0.9CO+CH3OH+0.1C2H2+0.1HCO+0.9C2H3	2.5680e+05	2.000	161.62
C2H3CHO+CH3OO=>0.9CO+CH3OOH+0.1C2H2+0.1HCO+0.9C2H3	4.5660e+05	2.000	10438.75
C2H3CHO+C6H5O=>0.9CO+0.1C2H2+C6H5OH+0.1HCO+0.9C2H3	1.6200e+05	2.000	10621.42
C2H3CHO+INDENYL=>0.9CO+0.1C2H2+INDENE+0.1HCO+0.9C2H3	8.1200e+04	2.000	13651.00
C2H3CHO+C10H7=>0.9CO+0.1C2H2+C10H8+0.1HCO+0.9C2H3	5.1230e+04	2.000	−1408.57
C2H3CHO+C10H6CH3=>0.9CO+0.1C2H2+C10H7CH3+0.1HCO+0.9C2H3	8.1200e+04	2.000	−1408.57
O2+C6H5CHO=>CO+HO2+C6H5	1.3630e+07	2.000	38109.91
C6H5CHO+H=>H2+CO+C6H5	1.9250e+07	2.000	2387.18
C6H5CHO+OH=>H2O+CO+C6H5	3.1950e+06	2.000	−3343.83
C6H5CHO+HO2=>H2O2+CO+C6H5	4.3100e+05	2.000	9982.61
C6H5CHO+HCO=>CO+CH2O+C6H5	1.0100e+06	2.000	10438.75
C6H5CHO+CH3=>CO+CH4+C6H5	3.1220e+05	2.000	3259.77
C6H5CHO+C2H5=>CO+C2H6+C6H5	1.8390e+05	2.000	5917.09
C6H5CHO+C2H3=>CO+C2H4+C6H5	5.4260e+05	2.000	3259.77
C6H5CHO+C3H3=>CO+AC3H4+C6H5	2.1600e+05	2.000	12730.05
C6H5CHO+HCCO=>CO+CH2CO+C6H5	3.4240e+05	2.000	3698.82
C6H5CHO+CH3O=>CO+CH3OH+C6H5	3.4240e+05	2.000	161.62
C6H5CHO+CH3OO=>CO+CH3OOH+C6H5	6.0880e+05	2.000	10438.75
C6H5CHO+C6H5O=>CO+C6H5OH+C6H5	2.1600e+05	2.000	10621.42
C6H5CHO+INDENYL=>CO+INDENE+C6H5	1.0830e+05	2.000	13651.00
C6H5CHO+C10H7=>CO+C10H8+C6H5	6.8310e+04	2.000	−1408.57
C6H5CHO+C10H6CH3=>CO+C10H7CH3+C6H5	1.0830e+05	2.000	−1408.57
O2+C6H5OH=>HO2+C6H5O	8.5190e+06	2.000	45025.57
C6H5OH+H=>H2+C6H5O	1.2030e+07	2.000	6706.81
C6H5OH+OH=>H2O+C6H5O	1.9970e+06	2.000	841.27
C6H5OH+O=>OH+C6H5O	6.7670e+06	2.000	5025.57
C6H5OH+HO2=>H2O2+C6H5O	2.6940e+05	2.000	13998.52
C6H5OH+HCO=>CH2O+C6H5O	6.3150e+05	2.000	14921.42
C6H5OH+CH3=>CH4+C6H5O	1.9520e+05	2.000	8062.59
C6H5OH+C2H5=>C2H6+C6H5O	1.1490e+05	2.000	10525.57
C6H5OH+C2H3=>C2H4+C6H5O	3.3910e+05	2.000	8102.87
C6H5OH+C3H3=>AC3H4+C6H5O	1.3500e+05	2.000	18602.87
C6H5OH+HCCO=>CH2CO+C6H5O	2.1400e+05	2.000	7461.70
C6H5OH+CH3O=>CH3OH+C6H5O	2.1400e+05	2.000	3791.31
C6H5OH+CH3OO=>CH3OOH+C6H5O	3.8050e+05	2.000	15149.65
C6H5OH+INDENYL=>INDENE+C6H5O	6.7670e+04	2.000	18649.65
C6H5OH+C10H7=>C10H8+C6H5O	4.2700e+04	2.000	2602.87
C6H5OH+C10H6CH3=>C10H7CH3+C6H5O	6.7670e+04	2.000	2602.87
C6H4O2+H=>H2+2CO+C2H2+C2H	8.4230e+07	2.000	10204.13
C6H4O2+OH=>H2O+2CO+C2H2+C2H	1.3980e+07	2.000	2076.14
C6H4O2+O=>2CO+C2H2+OH+C2H	4.7370e+07	2.000	8519.89
C6H4O2+HO2=>H2O2+2CO+C2H2+C2H	1.8860e+06	2.000	19508.20
C6H4O2+HCO=>2CO+CH2O+C2H2+C2H	4.4210e+06	2.000	20047.18
C6H4O2+CH3=>2CO+CH4+C2H2+C2H	1.3660e+06	2.000	11317.39
C6H4O2+C2H5=>2CO+C2H2+C2H6+C2H	8.0440e+05	2.000	14621.99
C6H4O2+C2H3=>2CO+C2H2+C2H4+C2H	2.3740e+06	2.000	11317.39
C6H4O2+C3H3=>2CO+C2H2+AC3H4+C2H	9.4510e+05	2.000	22732.70
C6H4O2+HCCO=>2CO+C2H2+CH2CO+C2H	1.4980e+06	2.000	11871.57
C6H4O2+CH3O=>2CO+CH3OH+C2H2+C2H	1.4980e+06	2.000	7271.30
C6H4O2+CH3OO=>2CO+CH3OOH+C2H2+C2H	2.6640e+06	2.000	20047.18
C6H4O2+C6H5O=>2CO+C2H2+C6H5OH+C2H	9.4510e+05	2.000	20262.59
C6H4O2+INDENYL=>2CO+C2H2+INDENE+C2H	4.7370e+05	2.000	23802.97
C6H4O2+C10H7=>2CO+C2H2+C10H8+C2H	2.9890e+05	2.000	5078.14
C6H4O2+C10H6CH3=>2CO+C2H2+C10H7CH3+C2H	4.7370e+05	2.000	5078.14
O2+C10H7CHO=>CO+HO2+C10H7	1.3630e+07	2.000	38109.91
C10H7CHO+H=>H2+CO+C10H7	1.9250e+07	2.000	2387.18
C10H7CHO+OH=>H2O+CO+C10H7	3.1950e+06	2.000	−3343.83
C10H7CHO+HO2=>H2O2+CO+C10H7	4.3100e+05	2.000	9982.61
C10H7CHO+HCO=>CO+CH2O+C10H7	1.0100e+06	2.000	10438.75
C10H7CHO+CH3=>CO+CH4+C10H7	3.1220e+05	2.000	3259.77

C10H7CHO+C2H5=>CO+C2H6+C10H7	1.8390e+05	2.000	5917.09
C10H7CHO+C2H3=>CO+C2H4+C10H7	5.4260e+05	2.000	3259.77
C10H7CHO+C3H3=>CO+AC3H4+C10H7	2.1600e+05	2.000	12730.05
C10H7CHO+HCCO=>CO+CH2CO+C10H7	3.4240e+05	2.000	3698.82
C10H7CHO+CH3O=>CO+CH3OH+C10H7	3.4240e+05	2.000	161.62
C10H7CHO+CH3OO=>CO+CH3OOH+C10H7	6.0880e+05	2.000	10438.75
C10H7CHO+C6H5O=>CO+C6H5OH+C10H7	2.1600e+05	2.000	10621.42
C10H7CHO+INDENYL=>CO+INDENE+C10H7	1.0830e+05	2.000	13651.00
C10H7CHO+C10H7=>CO+C10H8+C10H7	6.8310e+04	2.000	−1408.57
C10H7CHO+C10H6CH3=>CO+C10H7CH3+C10H7	1.0830e+05	2.000	−1408.57
O2+CH3C10H6OH=>HO2+CH3C10H6O	5.9630e+06	2.000	40722.49
CH3C10H6OH+H=>H2+CH3C10H6O	8.4230e+06	2.000	3950.57
CH3C10H6OH+OH=>H2O+CH3C10H6O	1.3980e+06	2.000	−2259.83
CH3C10H6OH+O=>OH+CH3C10H6O	4.7370e+06	2.000	2579.54
CH3C10H6OH+HO2=>H2O2+CH3C10H6O	1.8860e+05	2.000	11887.73
CH3C10H6OH+HCO=>CH2O+CH3C10H6O	4.4210e+05	2.000	12360.44
CH3C10H6OH+CH3=>CH4+CH3C10H6O	1.3660e+05	2.000	4871.29
CH3C10H6OH+C2H5=>C2H6+CH3C10H6O	8.0440e+04	2.000	7658.07
CH3C10H6OH+C2H3=>C2H4+CH3C10H6O	2.3740e+05	2.000	4871.29
CH3C10H6OH+C3H3=>AC3H4+CH3C10H6O	9.4510e+04	2.000	14730.58
CH3C10H6OH+HCCO=>CH2CO+CH3C10H6O	1.4980e+05	2.000	5333.37
CH3C10H6OH+CH3O=>CH3OH+CH3C10H6O	1.4980e+05	2.000	1583.56
CH3C10H6OH+CH3OO=>CH3OOH+CH3C10H6O	2.6640e+05	2.000	12360.44
CH3C10H6OH+C6H5O=>C6H5OH+CH3C10H6O	9.4510e+04	2.000	12549.65
CH3C10H6OH+INDENYL=>INDENE+CH3C10H6O	4.7370e+04	2.000	15681.39
CH3C10H6OH+C10H7=>C10H8+CH3C10H6O	2.9890e+04	2.000	−111.23
CH3C10H6OH+C10H6CH3=>C10H7CH3+CH3C10H6O	4.7370e+04	2.000	−111.23
O2+INDENE=>HO2+INDENYL	1.0220e+07	2.000	40722.49
INDENE+H=>H2+INDENYL	1.4440e+07	2.000	4212.94
INDENE+O=>OH+INDENYL	8.1200e+06	2.000	2579.54
INDENE+HO2=>H2O2+INDENYL	3.2330e+05	2.000	10400.95
INDENE+HCO=>CH2O+INDENYL	7.5780e+05	2.000	11485.87
INDENE+CH3=>CH4+INDENYL	2.3420e+05	2.000	5648.69
INDENE+C2H5=>C2H6+INDENYL	1.3790e+05	2.000	7658.07
INDENE+C2H3=>C2H4+INDENYL	4.0700e+05	2.000	5706.99
INDENE+C3H3=>AC3H4+INDENYL	1.6200e+05	2.000	15566.28
INDENE+HCCO=>CH2CO+INDENYL	2.5680e+05	2.000	4517.10
INDENE+CH3O=>CH3OH+INDENYL	2.5680e+05	2.000	1389.21
INDENE+CH3OO=>CH3OOH+INDENYL	4.5660e+05	2.000	11816.26
INDENE+C6H5O=>C6H5OH+INDENYL	1.6200e+05	2.000	12549.65
INDENE+C10H7=C10H8+INDENYL	5.1230e+04	2.000	724.47
REV / 2.1650e+05 2.000 24824.47 /			
INDENE+C10H6CH3=C10H7CH3+INDENYL	8.1200e+04	2.000	724.47
REV / 1.8950e+05 2.000 24824.47 /			
O2+C6H5C2H=>HO2+C6H4C2H	1.7040e+07	2.000	51633.86
C6H5C2H+H=>H2+C6H4C2H	2.4070e+07	2.000	10480.03
C6H5C2H+OH=>H2O+C6H4C2H	3.9940e+06	2.000	2267.44
C6H5C2H+O=>OH+C6H4C2H	1.3530e+07	2.000	8781.96
C6H5C2H+HO2=>H2O2+C6H4C2H	5.3880e+05	2.000	19844.40
C6H5C2H+HCO=>CH2O+C6H4C2H	1.2630e+06	2.000	20386.31
C6H5C2H+CH3=>CH4+C6H4C2H	3.9030e+05	2.000	11601.78
C6H5C2H+C2H5=>C2H6+C6H4C2H	2.2980e+05	2.000	14929.22
C6H5C2H+C2H3=>C2H4+C6H4C2H	6.7830e+05	2.000	11601.78
C6H5C2H+C3H3=>AC3H4+C6H4C2H	2.7000e+05	2.000	23085.73
C6H5C2H+HCCO=>CH2CO+C6H4C2H	4.2800e+05	2.000	12160.02
C6H5C2H+CH3O=>CH3OH+C6H4C2H	4.2800e+05	2.000	7522.23
C6H5C2H+CH3OO=>CH3OOH+C6H4C2H	7.6100e+05	2.000	20386.31
C6H5C2H+C6H5O=>C6H5OH+C6H4C2H	2.7000e+05	2.000	20602.87
C6H5C2H+INDENYL=>INDENE+C6H4C2H	1.3530e+05	2.000	24161.27
C6H5C2H+C10H7=>C10H8+C6H4C2H	8.5390e+04	2.000	5307.08
C6H5C2H+C10H6CH3=>C10H7CH3+C6H4C2H	1.3530e+05	2.000	5307.08
O2+C10H8=>HO2+C10H7	2.7260e+07	2.000	51633.86
C10H8+H=>H2+C10H7	3.8510e+07	2.000	10160.27
C10H8+O=>OH+C10H7	2.1650e+07	2.000	8781.96
C10H8+HO2=>H2O2+C10H7	8.6200e+05	2.000	21656.36
C10H8+HCO=>CH2O+C10H7	2.0210e+06	2.000	21452.16
C10H8+CH3=>CH4+C10H7	6.2450e+05	2.000	10654.35
C10H8+C2H5=>C2H6+C10H7	3.6770e+05	2.000	14929.22
C10H8+C2H3=>C2H4+C10H7	1.0850e+06	2.000	10583.29
C10H8+C3H3=>AC3H4+C10H7	4.3200e+05	2.000	22067.25
C10H8+HCCO=>CH2CO+C10H7	6.8470e+05	2.000	13154.82
C10H8+CH3O=>CH3OH+C10H7	6.8470e+05	2.000	7759.09
C10H8+CH3OO=>CH3OOH+C10H7	1.2180e+06	2.000	21049.51
C10H8+C6H5O=>C6H5OH+C10H7	4.3200e+05	2.000	20602.87

C10H8+C10H6CH3=C10H7CH3+C10H7	2.1650e+05	2.000	4288.60
REV / 1.1950e+05 2.000 4288.60 /			
O2+C10H7OH=>HO2+C10H7O	1.7040e+07	2.000	45025.57
C10H7OH+H=>H2+C10H7O	2.4070e+07	2.000	6525.57
C10H7OH+O=>OH+C10H7O	1.3530e+07	2.000	5025.57
C10H7OH+HO2=>H2O2+C10H7O	5.3880e+05	2.000	15025.57
C10H7OH+HCO=>CH2O+C10H7O	1.2630e+06	2.000	15525.57
C10H7OH+CH3=>CH4+C10H7O	3.9030e+05	2.000	7525.57
C10H7OH+C2H5=>C2H6+C10H7O	2.2980e+05	2.000	10525.57
C10H7OH+C2H3=>C2H4+C10H7O	6.7830e+05	2.000	7525.57
C10H7OH+C3H3=>AC3H4+C10H7O	2.7000e+05	2.000	18025.57
C10H7OH+HCCO=>CH2CO+C10H7O	4.2800e+05	2.000	8025.57
C10H7OH+CH3O=>CH3OH+C10H7O	4.2800e+05	2.000	3925.57
C10H7OH+CH3OO=>CH3OOH+C10H7O	7.6100e+05	2.000	15525.57
C10H7OH+C6H5O=>C6H5OH+C10H7O	2.7000e+05	2.000	15725.57
C10H7OH+INDENYL=>INDENE+C10H7O	1.3530e+05	2.000	19025.57
C10H7OH+C10H7=>C10H8+C10H7O	8.5390e+04	2.000	2025.57
C10H7OH+C10H6CH3=>C10H7CH3+C10H7O	1.3530e+05	2.000	2025.57
C10H7CH3+H=>H2+C10H7CH2	7.2200e+06	2.000	3950.57
C10H7CH3+OH=>H2O+C10H7CH2	1.1980e+06	2.000	−2259.83
C10H7CH3+O=>OH+C10H7CH2	4.0600e+06	2.000	2579.54
C10H7CH3+HCO=>CH2O+C10H7CH2	3.7890e+05	2.000	12360.44
C10H7CH3+C2H5=>C2H6+C10H7CH2	6.8950e+04	2.000	7658.07
C10H7CH3+C2H3=>C2H4+C10H7CH2	2.0350e+05	2.000	4871.29
C10H7CH3+C3H3=>AC3H4+C10H7CH2	8.1010e+04	2.000	14730.58
C10H7CH3+HCCO=>CH2CO+C10H7CH2	1.2840e+05	2.000	5333.37
C10H7CH3+CH3O=>CH3OH+C10H7CH2	1.2840e+05	2.000	1583.56
C10H7CH3+CH3OO=>CH3OOH+C10H7CH2	2.2830e+05	2.000	12360.44
C10H7CH3+C6H5O=>C6H5OH+C10H7CH2	8.1010e+04	2.000	12549.65
C10H7CH3+INDENYL=>INDENE+C10H7CH2	4.0600e+04	2.000	15681.39
C10H7CH3+C10H7=>C10H8+C10H7CH2	2.5620e+04	2.000	−111.23
C10H7CH3+C10H6CH3=>C10H7CH3+C10H7CH2	4.0600e+04	2.000	−111.23
O2+C10H7CH3=>HO2+C10H6CH3	2.3850e+07	2.000	51633.86
C10H7CH3+H=>H2+C10H6CH3	3.3690e+07	2.000	10160.27
C10H7CH3+OH=>H2O+C10H6CH3	5.5920e+06	2.000	−53.76
C10H7CH3+O=>OH+C10H6CH3	1.8950e+07	2.000	8781.96
C10H7CH3+HO2=>H2O2+C10H6CH3	7.5430e+05	2.000	21656.36
C10H7CH3+HCO=>CH2O+C10H6CH3	1.7680e+06	2.000	21452.16
C10H7CH3+CH3=>CH4+C10H6CH3	5.4640e+05	2.000	10654.35
C10H7CH3+C2H5=>C2H6+C10H6CH3	3.2180e+05	2.000	14929.22
C10H7CH3+C2H3=>C2H4+C10H6CH3	9.4960e+05	2.000	10583.29
C10H7CH3+C3H3=>AC3H4+C10H6CH3	3.7800e+05	2.000	22067.25
C10H7CH3+HCCO=>CH2CO+C10H6CH3	5.9920e+05	2.000	13154.82
C10H7CH3+CH3O=>CH3OH+C10H6CH3	5.9920e+05	2.000	7759.09
C10H7CH3+CH3OO=>CH3OOH+C10H6CH3	1.0650e+06	2.000	21049.51
C10H7CH3+C6H5O=>C6H5OH+C10H6CH3	3.7800e+05	2.000	20602.87
O2+C12H8=>HO2+C12H7	2.7260e+07	2.000	51633.86
C12H8+H=>H2+C12H7	3.8510e+07	2.000	10480.03
C12H8+OH=>H2O+C12H7	6.3900e+06	2.000	2267.44
C12H8+O=>OH+C12H7	2.1650e+07	2.000	8781.96
C12H8+HO2=>H2O2+C12H7	8.6200e+05	2.000	19844.40
C12H8+HCO=>CH2O+C12H7	2.0210e+06	2.000	20386.31
C12H8+CH3=>CH4+C12H7	6.2450e+05	2.000	11601.78
C12H8+C2H5=>C2H6+C12H7	3.6770e+05	2.000	14929.22
C12H8+C2H3=>C2H4+C12H7	1.0850e+06	2.000	11601.78
C12H8+C3H3=>AC3H4+C12H7	4.3200e+05	2.000	23085.73
C12H8+HCCO=>CH2CO+C12H7	6.8470e+05	2.000	12160.02
C12H8+CH3O=>CH3OH+C12H7	6.8470e+05	2.000	7522.23
C12H8+CH3OO=>CH3OOH+C12H7	1.2180e+06	2.000	20386.31
C12H8+C6H5O=>C6H5OH+C12H7	4.3200e+05	2.000	20602.87
C12H8+INDENYL=>INDENE+C12H7	2.1650e+05	2.000	24161.27
C12H8+C10H7=>C10H8+C12H7	1.3660e+05	2.000	5307.08
C12H8+C10H6CH3=>C10H7CH3+C12H7	2.1650e+05	2.000	5307.08
O2+C16H10=>HO2+C16H9	4.7710e+07	2.000	51633.86
C16H10+H=>H2+C16H9	6.7390e+07	2.000	10480.03
C16H10+OH=>H2O+C16H9	1.1180e+07	2.000	2267.44
C16H10+O=>OH+C16H9	3.7890e+07	2.000	8781.96
C16H10+HO2=>H2O2+C16H9	1.5090e+06	2.000	19844.40
C16H10+HCO=>CH2O+C16H9	3.5360e+06	2.000	20386.31
C16H10+CH3=>CH4+C16H9	1.0930e+06	2.000	11601.78
C16H10+C2H5=>C2H6+C16H9	6.4350e+05	2.000	14929.22
C16H10+C2H3=>C2H4+C16H9	1.8990e+06	2.000	11601.78
C16H10+C3H3=>AC3H4+C16H9	7.5610e+05	2.000	23085.73
C16H10+HCCO=>CH2CO+C16H9	1.1980e+06	2.000	12160.02

C16H10+CH3O=>CH3OH+C16H9	1.1980e+06	2.000	7522.23
C16H10+CH3OO=>CH3OOH+C16H9	2.1310e+06	2.000	20386.31
C16H10+C6H5O=>C6H5OH+C16H9	7.5610e+05	2.000	20602.87
C16H10+INDENYL=>INDENE+C16H9	3.7890e+05	2.000	24161.27
C16H10+C10H7=>C10H8+C16H9	2.3910e+05	2.000	5307.08
C16H10+C10H6CH3=>C10H7CH3+C16H9	3.7890e+05	2.000	5307.08
O2+C10H10=>C10H8+H+HO2	2.3850e+07	2.000	40722.49
C10H10+H=>H2+C10H8+H	3.3690e+07	2.000	3950.57
C10H10+OH=>H2O+C10H8+H	5.5920e+06	2.000	−2259.83
C10H10+O=>C10H8+H+OH	1.8950e+07	2.000	2579.54
C10H10+HO2=>H2O2+C10H8+H	7.5430e+05	2.000	11887.73
C10H10+HCO=>CH2O+C10H8+H	1.7680e+06	2.000	12360.44
C10H10+CH3=>CH4+C10H8+H	5.4640e+05	2.000	4871.29
C10H10+C2H5=>C2H6+C10H8+H	3.2180e+05	2.000	7658.07
C10H10+C2H3=>C2H4+C10H8+H	9.4960e+05	2.000	4871.29
C10H10+C3H3=>AC3H4+C10H8+H	3.7800e+05	2.000	14730.58
C10H10+HCCO=>CH2CO+C10H8+H	5.9920e+05	2.000	5333.37
C10H10+CH3O=>CH3OH+C10H8+H	5.9920e+05	2.000	1583.56
C10H10+CH3OO=>CH3OOH+C10H8+H	1.0650e+06	2.000	12360.44
C10H10+C6H5O=>C6H5OH+C10H8+H	3.7800e+05	2.000	12549.65
C10H10+INDENYL=>INDENE+C10H8+H	1.8950e+05	2.000	15681.39
C10H10+C10H7=>2C10H8+H	1.1950e+05	2.000	−111.23
C10H10+C10H6CH3=>C10H8+C10H7CH3+H	1.8950e+05	2.000	−111.23
O2+TETRALIN=>HO2+RTETRALIN	2.7260e+07	2.000	40722.49
TETRALIN+H=>H2+RTETRALIN	3.8510e+07	2.000	3950.57
TETRALIN+OH=>H2O+RTETRALIN	6.3900e+06	2.000	−2259.83
TETRALIN+O=>OH+RTETRALIN	2.1650e+07	2.000	2579.54
TETRALIN+HO2=>H2O2+RTETRALIN	8.6200e+05	2.000	11887.73
TETRALIN+HCO=>CH2O+RTETRALIN	2.0210e+06	2.000	12360.44
TETRALIN+CH3=>CH4+RTETRALIN	6.2450e+05	2.000	4871.29
TETRALIN+C2H5=>C2H6+RTETRALIN	3.6770e+05	2.000	7658.07
TETRALIN+C2H3=>C2H4+RTETRALIN	1.0850e+06	2.000	4871.29
TETRALIN+C3H3=>AC3H4+RTETRALIN	4.3200e+05	2.000	14730.58
TETRALIN+HCCO=>CH2CO+RTETRALIN	6.8470e+05	2.000	5333.37
TETRALIN+CH3O=>CH3OH+RTETRALIN	6.8470e+05	2.000	1583.56
TETRALIN+CH3OO=>CH3OOH+RTETRALIN	1.2180e+06	2.000	12360.44
TETRALIN+C6H5O=>C6H5OH+RTETRALIN	4.3200e+05	2.000	12549.65
TETRALIN+INDENYL=>INDENE+RTETRALIN	2.1650e+05	2.000	15681.39
TETRALIN+C10H7=>C10H8+RTETRALIN	1.3660e+05	2.000	−111.23
TETRALIN+C10H6CH3=>C10H7CH3+RTETRALIN	2.1650e+05	2.000	−111.23
O2+C9H10O2=>CH2CO+0.5C10H8+HO2+CH2CHO	6.8150e+06	2.000	38109.91
C9H10O2+H=>H2+CH2CO+0.5C10H8+CH2CHO	9.6270e+06	2.000	2387.18
C9H10O2+OH=>H2O+CH2CO+0.5C10H8+CH2CHO	1.5980e+06	2.000	−3343.83
C9H10O2+O=>CH2CO+0.5C10H8+OH+CH2CHO	5.4130e+06	2.000	1094.46
C9H10O2+HO2=>H2O2+CH2CO+0.5C10H8+CH2CHO	2.1550e+05	2.000	9982.61
C9H10O2+HCO=>CH2O+CH2CO+0.5C10H8+CH2CHO	5.0520e+05	2.000	10438.75
C9H10O2+CH3=>CH4+CH2CO+0.5C10H8+CH2CHO	1.5610e+05	2.000	3259.77
C9H10O2+C2H5=>CH2CO+C2H6+0.5C10H8+CH2CHO	9.1930e+04	2.000	5917.09
C9H10O2+C2H3=>CH2CO+C2H4+0.5C10H8+CH2CHO	2.7130e+05	2.000	3259.77
C9H10O2+C3H3=>CH2CO+AC3H4+0.5C10H8+CH2CHO	1.0800e+05	2.000	12730.05
C9H10O2+HCCO=>2CH2CO+0.5C10H8+CH2CHO	1.7120e+05	2.000	3698.82
C9H10O2+CH3O=>CH3OH+CH2CO+0.5C10H8+CH2CHO	1.7120e+05	2.000	161.62
C9H10O2+CH3OO=>CH3OOH+CH2CO+0.5C10H8+CH2CHO	3.0440e+05	2.000	10438.75
C9H10O2+C6H5O=>CH2CO+C6H5OH+0.5C10H8+CH2CHO	1.0800e+05	2.000	10621.42
C9H10O2+INDENYL=>CH2CO+INDENE+0.5C10H8+CH2CHO	5.4130e+04	2.000	13651.00
C9H10O2+C10H7=>CH2CO+1.5C10H8+CH2CHO	3.4160e+04	2.000	−1408.57
C9H10O2+C10H6CH3=>CH2CO+0.5C10H8+C10H7CH3+CH2CHO	5.4130e+04	2.000	−1408.57
O2+C8H10O3=>2CO+C2H2+0.5PC3H4+0.5AC3H4+HO2+CH3O	8.5190e+06	2.000	45025.57
C8H10O3+H=>H2+2CO+C2H2+0.5PC3H4+0.5AC3H4+CH3O	1.2030e+07	2.000	6525.57
C8H10O3+OH=>H2O+2CO+C2H2+0.5PC3H4+0.5AC3H4+CH3O	1.9970e+06	2.000	−474.43
C8H10O3+O=>2CO+C2H2+0.5PC3H4+0.5AC3H4+OH+CH3O	6.7670e+06	2.000	5025.57
C8H10O3+HO2=>H2O2+2CO+C2H2+0.5PC3H4+0.5AC3H4+CH3O	2.6940e+05	2.000	15025.57
C8H10O3+HCO=>2CO+CH2O+C2H2+0.5PC3H4+0.5AC3H4+CH3O	6.3150e+05	2.000	15525.57
C8H10O3+CH3=>2CO+CH4+C2H2+0.5PC3H4+0.5AC3H4+CH3O	1.9520e+05	2.000	7525.57
C8H10O3+C2H5=>2CO+C2H2+C2H6+0.5PC3H4+0.5AC3H4+CH3O	1.1490e+05	2.000	10525.57
C8H10O3+C2H3=>2CO+C2H2+C2H4+0.5PC3H4+0.5AC3H4+CH3O	3.3910e+05	2.000	7525.57
C8H10O3+C3H3=>2CO+C2H2+0.5PC3H4+1.5AC3H4+CH3O	1.3500e+05	2.000	18025.57
C8H10O3+HCCO=>2CO+C2H2+CH2CO+0.5PC3H4+0.5AC3H4+CH3O	2.1400e+05	2.000	8025.57
C8H10O3+CH3O=>2CO+CH3OH+C2H2+0.5PC3H4+0.5AC3H4+CH3O	2.1400e+05	2.000	3925.57
C8H10O3+CH3OO=>2CO+CH3OOH+C2H2+0.5PC3H4+0.5AC3H4+CH3O	3.8050e+05	2.000	15525.57
C8H10O3+C6H5O=>2CO+C2H2+0.5PC3H4+0.5AC3H4+C6H5OH+CH3O	1.3500e+05	2.000	15725.57
C8H10O3+INDENYL=>2CO+C2H2+0.5PC3H4+0.5AC3H4+INDENE+CH3O	6.7670e+04	2.000	19025.57
C8H10O3+C10H7=>2CO+C2H2+0.5PC3H4+0.5AC3H4+C10H8+CH3O	4.2700e+04	2.000	2025.57
C8H10O3+C10H6CH3=>2CO+C2H2+0.5PC3H4+0.5AC3H4+C10H7CH3+CH3O	6.7670e+04	2.000	2025.57

O2+C8H10O3=>CO+C2H2+CH2CO+0.5C4H4+HO2+CH3O	8.5190e+06	2.000	45025.57
C8H10O3+H=>H2+CO+C2H2+CH2CO+0.5C4H4+CH3O	1.2030e+07	2.000	6525.57
C8H10O3+OH=>H2O+CO+C2H2+CH2CO+0.5C4H4+CH3O	1.9970e+06	2.000	−474.43
C8H10O3+O=>CO+C2H2+CH2CO+0.5C4H4+OH+CH3O	6.7670e+06	2.000	5025.57
C8H10O3+HO2=>H2O2+CO+C2H2+CH2CO+0.5C4H4+CH3O	2.6940e+05	2.000	15025.57
C8H10O3+HCO=>CO+CH2O+C2H2+CH2CO+0.5C4H4+CH3O	6.3150e+05	2.000	15525.57
C8H10O3+CH3=>CO+CH4+C2H2+CH2CO+0.5C4H4+CH3O	1.9520e+05	2.000	7525.57
C8H10O3+C2H5=>CO+C2H2+CH2CO+C2H6+0.5C4H4+CH3O	1.1490e+05	2.000	10525.57
C8H10O3+C2H3=>CO+C2H2+CH2CO+C2H4+0.5C4H4+CH3O	3.3910e+05	2.000	7525.57
C8H10O3+C3H3=>CO+C2H2+CH2CO+AC3H4+0.5C4H4+CH3O	1.3500e+05	2.000	18025.57
C8H10O3+HCCO=>CO+C2H2+2CH2CO+0.5C4H4+CH3O	2.1400e+05	2.000	8025.57
C8H10O3+CH3O=>CO+CH3OH+C2H2+CH2CO+0.5C4H4+CH3O	2.1400e+05	2.000	3925.57
C8H10O3+CH3OO=>CO+CH3OOH+C2H2+CH2CO+0.5C4H4+CH3O	3.8050e+05	2.000	15525.57
C8H10O3+C6H5O=>CO+C2H2+CH2CO+0.5C4H4+C6H5OH+CH3O	1.3500e+05	2.000	15725.57
C8H10O3+INDENYL=>CO+C2H2+CH2CO+0.5C4H4+INDENE+CH3O	6.7670e+04	2.000	19025.57
C8H10O3+C10H7=>CO+C2H2+CH2CO+0.5C4H4+C10H8+CH3O	4.2700e+04	2.000	2025.57
C8H10O3+C10H6CH3=>CO+C2H2+CH2CO+0.5C4H4+C10H7CH3+CH3O	6.7670e+04	2.000	2025.57

END

Anhang C

OpenFOAM Customized Code

This section provides examples of how OpenFOAM source code has been extended in order to include customized pyrolysis boundary conditions describing the release and mixing of volatile matter at the particle surface.

In particular Eqs. (3.12) and (3.13) are implemented in the *classes* "MYArrheniusFlowRateInletVelocity.H" and "MYuniformFixedValue.H" to calculate the devolatilization rate and accordingly set the velocity and species mass fraction at the particle surface, respectively.

Species Mass Fraction BC

In the modeling approach presented in Sec. 3.1 devolatilization is described by a generic boundary condition at the particle surface that accounts for both convective and diffusive phenomena during pyrolysis (Eq. (3.13)), repeated here for convenience,

$$\dot{m}_i = Y_i \dot{m}_v - \rho_g S_p D_g \frac{\partial Y_i}{\partial n}. \tag{C.1}$$

It consists of a linear combination of the species mass fraction Y_i and its derivative evaluated normal to the particle surface (third type or Robin boundary [46]). The relationship can be rearranged to obtain an expression for Y_i to be set at the particle boundary. Isolating the derivative term leads to

$$\frac{\partial Y_i}{\partial n} = Y_i \frac{\dot{m}_v}{\rho_g S_p D_g} - Y_i^p \frac{\dot{m}_v}{\rho_g S_p D_g}, \tag{C.2}$$

where Y_i^p is the mass fraction of the species i according to the assumed particle volatile composition (Tab. 3.3), so that

$$\dot{m}_i = Y_i^p \cdot \dot{m}_v. \tag{C.3}$$

A 1^{st} order approximation is used for the derivative at the particle surface,

$$\frac{\partial Y_i}{\partial n} \approx \frac{Y_{i_{face}} - Y_{i_{center}}}{\Delta x/2}, \tag{C.4}$$

where $Y_{i_{face}}$ and $Y_{i_{center}}$ are the values of Y_i at the face (corresponding to the particle surface) and at the center of the first computational cell of width Δx.

Substituting in Eq. (C.2) and solving for the cell face value of Y_i, which is the value that has to be set at the particle surface,

$$Y_{i_{face}} \left(1 - \frac{\dot{m}_v \Delta x}{2\rho_g S_p D_g}\right) = Y_{i_{center}} - Y_i^p \frac{\dot{m}_v \Delta x}{2\rho_g S_p D_g}, \tag{C.5}$$

$$Y_{i_{face}} = \frac{1}{1 - \frac{\dot{m}_v \Delta x}{2\rho_g S_p D_g}} \cdot Y_{i_{center}} - \frac{\frac{\dot{m}_v \Delta x}{2\rho_g S_p D_g}}{1 - \frac{\dot{m}_v \Delta x}{2\rho_g S_p D_g}} \cdot Y_i^p. \tag{C.6}$$

Introducing the quantity

$$A = \frac{\dot{m}_v \Delta x}{2\rho_g S_p D_g}, \tag{C.7}$$

Eq. (C.6) finally becomes

$$Y_{i_{face}} = \frac{A}{A-1} \cdot Y_i^p - \frac{1}{A-1} \cdot Y_{i_{center}}. \tag{C.8}$$

The obtained expression is implemented in OpenFOAM customized *class* "MYuniformFixedValue.H". Listing C.1 in particular shows the excerpt of the member function which updates at each time step the value of the species mass fraction in object, at each location of the particle boundary. This allows to obtain the instantaneous distribution of the species mass fraction at the coal particle surface.

```
// * * * * * * * * * * * * * * * * * * Member Functions  * * * * * * * * * * * * * * * * * * //
void Foam::MYuniformFixedValue::updateCoeffs()
{
    if (updated())
    {
        return;
    }

        const scalar t = db().time().timeOutputValue();

// * Read flow rate: phi
        const surfaceScalarField& phi =
        db().lookupObject<surfaceScalarField>(phiName_);
        const fvsPatchField<scalar>& phip =
        patch().patchField<surfaceScalarField, scalar>(phi);

// * Read assumed particle composition for species i: Yp
        Field<scalar> Yp(patch().deltaCoeffs().size(),uniformValue_->value(t));

// * Read viscosity: mup
        const Foam::fvPatchField<scalar>& mup =
          patch().lookupPatchField<volScalarField, scalar>(muName_);

// * Read Schmidt number from a "transportProperties" dictionary: Scp
const dictionary& transportProperties = db().lookupObject<IOdictionary>
(
   "transportProperties"
);
dimensionedScalar Schm(transportProperties.lookup(ScName_));
scalar Scp=Schm.value();

// * Define A considering that:
// - rho*D=mu/Sc
// - patch().magSf() is the surface area of the boundary cell face
// - 1/patch().deltaCoeffs() represents the distance from the boundary
//   of the center of the first computational cell at the given location
// - patchInternalField() is the value of the field in object at the center
//   of the first computational cell at that location

scalarField A = (phip/patch().magSf())*(1/patch().deltaCoeffs())/(mup/Scp);

        Field<scalar>::operator=
        (
        A/(A-1) * Yp - 1/(A-1) * patchInternalField()
        );
}
```

Listing C.1: Excerpt from "MYuniformFixedValue.C"

Velocity BC

In the modeling approach presented in Sec. 3.1 the time evolution of volatile release is captured by using a single kinetic rate law (Eq. (3.12)), repeated here for convenience,

$$\dot{m}_v = A_v e^{-\frac{E_v}{R_u \overline{T}_p}} (m_v^* - m_v), \tag{C.9}$$

with the Arrhenius rate parameters, namely the pre-exponential factor A_v and the devolatilization activation energy E_v, that in this work are either CPD-fitted as for the Pittsburgh bituminous coal (Tab. 3.1), or fitted to specific pyrolysis kinetics measurements as for the employed Saar hvBb (Tab. 3.2).

The heating rate history of the particle is obtained by solving for intra-particle heat transfer and heat exchange between the particle and its surroundings (Eqs. (3.10) and (3.11)). The particle mean temperature $\overline{T}_p$ is then used in Eq. (C.9) to calculate the devolatilization rate.

The model also requires the mass of volatiles which has been already released m_v in order to compare it to the available volatile mass m_v^*. The former is obtained by integrating over the particle surface and in time the mass flow rate given by Eq. (C.9), whereas for the latter the particle volatile matter content is either provided by CPD results (Sec. 5.1.2), or calculated based on the coal density ρ_c, its proximate analysis, and a Q-factor correction (Sec. 6.1.2).

The presented single kinetic rate model for devolatilization is implemented in the OpenFOAM customized *class* "MYArrheniusFlowRateInletVelocity.H". Listing C.2 reports the member function which calculates the rate of devolatilization and accordingly updates the value of the velocity at the particle boundary.

```
// * * * * * * * * * * * * * * * * * * Member Functions  * * * * * * * * * * * * * * * * * * //

void Foam::MYArrheniusFlowRateInletVelocity::updateCoeffs()
{
    if (updated())
    {
        return;
    }

    const scalar t = db().time().timeOutputValue();
    const Time& time_ = db().time();

    // * Read neighbor mesh, i.e. the particle region
    const fvMesh& parMesh = time_.lookupObject<fvMesh>("regionSolidPARTICLE");

    // * Read the mean value of the particle temperature importing the field
    //    TpmeanField from the particle region (uniform field including the
    //    calculated mean temperature inside the region)
```

```
    volScalarField TpmeanField =
20  parMesh.objectRegistry::lookupObject<volScalarField>("TpmeanField");
    const scalar Tpmean = TpmeanField[0];
22
     // * Read the field ReleasedVolatileMass which at the boundary
24   //   uniformly assumes the value of volatile mass which has been already
    released
     const label patchi = patch().index();
26   const volScalarField& ReleasedVolatileMass =
     db().lookupObject<volScalarField>("ReleasedVolatileMass");
28   fvPatchScalarField& ReleasedVolatileMassp =
     const_cast<fvPatchScalarField&>(VolatileMass.boundaryField()[patchi]);
30   const scalar m_v = ReleasedVolatileMassp[0];

32   const scalar R_u = 8.3144621;// universal gas constant R_u = 8.3144621 J/(K
    mol)

34  // * Read coal particle geometrical and physical properties
    //   - scaling factor for particle wedge
36   const scalar dwedge = wedAng_->value(t)/360.0;
    //   - particle radius
38   const scalar r_par  = parR_->value(t);
    //   - particle volume (sphere)
40   const scalar V_par  = 4.0/3.0*constant::mathematical::pi*pow(r_par,3);
    //   - volatile matter yet to be released
42   const scalar Dvolmass = (rhoPar_->value(t) * V_par * dwedge * volPer_->value(t
    )) - m_v;
    //   - Arrhenius rate
44   const scalar kp = Av_->value(t) * exp(-Ev_->value(t) / R_u / Tpmean);
    //   - devolatilization rate
46   const scalar flowRate=kp*Dvolmass;

48  // * Output relevant devolatilization information
Info << "Initial particle mass (m*) ---> "
50      << rhoPar_->value(t) * V_par * dwedge << endl ;
Info << "Initial particle volatile content (m*_v) ---> "
52      << rhoPar_->value(t) * V_par * dwedge * volPer_->value(t) << endl ;
Info << "Volatile matter devolatilized from the particle (m_v)  ---> "
54      << m_v << endl ;
Info << "Volatile matter still in the particle (m*_v-m_v)---> "
56      << Dvolmass << " kg"  << endl ;
Info << "Devolatilizazion RATE ---> "
58      << flowRate << " kg/s" << endl ;

60  // * Calculate the velocity at the boundary corresponding to
    //   the given devolatilization rate
62  const scalar avgU = -flowRate/gSum(patch().magSf());

64  tmp<vectorField> n = patch().nf();

66
    if (phiName_ == "none")
68  {
        // volumetric flow-rate
70      operator==(n*avgU);
```

```
    }
    else
    {
        const surfaceScalarField& phi =
            db().lookupObject<surfaceScalarField>(phiName_);

        if (phi.dimensions() == dimVelocity*dimArea)
        {
            // volumetric flow-rate
            operator==(n*avgU);
        }
        else if (phi.dimensions() == dimDensity*dimVelocity*dimArea)
        {
            if (rhoName_ == "none")
            {
                // volumetric flow-rate
                operator==(n*avgU);
            }
            else
            {
                // mass flow-rate
                const fvPatchField<scalar>& rhop =
                    patch().lookupPatchField<volScalarField, scalar>(rhoName_);

                operator==(n*avgU/rhop);
            }
        }
        else
        {
            FatalErrorIn
            (
                "MYArrheniusFlowRateInletVelocity::updateCoeffs()"
            )   << "dimensions of " << phiName_ << " are incorrect" << nl
                << "    on patch " << this->patch().name()
                << " of field " << this->dimensionedInternalField().name()
                << " in file " << this->dimensionedInternalField().objectPath()
                << nl << exit(FatalError);
        }
    }

    fixedValueFvPatchField<vector>::updateCoeffs();
}
```

Listing C.2: Excerpt from "MYArrheniusFlowRateInletVelocity.C"

Anhang D

Data Storage

Tabelle 4.1: Case and code used to produce the results published in Tufano *et al.* [128] on fully-resolved DNS of coal particle ignition in air- and O2/CO2-atmospheres. The corresponding code/data repository is itv-publications/2016_Tufano_FUE The main directory for the RAW data storage is /itv/storage/ITV-DATABASE/ITV/PUBLICATIONS/JOURNAL/2016_Tufano_FUE.

Tufano *et al.* [128], 2016_Tufano_FUE		
Data on storage	Case	Code
N2-21*Tp500	Fully-resolved DNS of coal particle ignition in the mixture containing 21% O_2 and balanced with N2. The initial particle temperature is 500K to account for pre-heating	"coalReactingFoam" on GIT SHA: 911abe37
N2-30*Tp500	Mixture containing 30% O_2 and balanced with N_2. Otherwise same settings as $N2-21*$	"coalReactingFoam" on GIT SHA: 911abe37
CO2-21*Tp500	Mixture containing 21% O_2 and balanced with CO_2. Otherwise same settings as $N2-21*$	"coalReactingFoam" on GIT SHA: 911abe37
CO2-30*Tp500	Mixture containing 30% O_2 and balanced with CO_2. Otherwise same settings as $N2-21*$	"coalReactingFoam" on GIT SHA: 911abe37
N2-21*Tp300/400	Same settings as $N2-21*$ but different initial particle temperature	"coalReactingFoam" on GIT SHA: 911abe37
Pre-/Post-processing tools		
Utility name	Description	Code
$MYdecompose--ManualAuto$	creates a list-file for radial decomposition	"master" on GIT SHA: 911abe37
$takeMax$	writes out the overall maximum value per each time step for selected properties	"master" on GIT SHA: 911abe37
$MYboundaryValue$	writes out surface (mean) values of selected properties in time	"master" on GIT SHA: 911abe37
$ignitionCH.py$ (Python)	calculates the cumulative CH profile based on the particle trajectory	"master" on GIT SHA: 911abe37
$ignDelTim.m$ (Matlab)	calculates the ignition delay time based on different criteria and indicators	"master" on GIT SHA: 911abe37

Tabelle 4.2: Case and code used to produce the results published in Tufano *et al.* [129] on fully-resolved DNS of coal particle volatile combustion and flame interaction, with focus on the characterization of transient and group effects. The corresponding code/data repository is itv-publications/2018_Tufano_FUE The main directory for the RAW data storage is /itv/storage/ITV-DATABASE/ITV/PUBLICATIONS/JOURNAL/2018_Tufano_FUE.

Tufano *et al.* [129], 2018_Tufano_FUE		
Data on storage	Case	Code
1P-LAM/*	DNS of single coal particle volatile combustion in laminar flow at Re_p=2. The upstream extent of the computational domain is 20 particle diameter D_p	"reactingPccFoam" on GIT SHA: 32fb177d
XP-LAM/Lx=**Y**Dp/*	DNS of a **X**-particles array volatile combustion in laminar flow at Re_p=2. The inter-particle distance L_x =**Y**D_p	"reactingPccFoam" on GIT SHA: 32fb177d
Pre-/Post-processing tools		
Utility name	Description	Code
toBuildDomain (Bash)	generates the domain composing multiple repetitions of an elementary mesh	"master" on GIT SHA: 32fb177d
$MYdecompose-$ $-ManualAuto$	creates a list-file for radial decomposition	"master" on GIT SHA: 32fb177d
$takeMax$	writes out the overall maximum value per each time step for selected properties	"master" on GIT SHA: 32fb177d
$MYboundaryValue$ $-xP$	writes out surface (mean) values of selected properties in time at the surface of the particles	"master" on GIT SHA: 32fb177d
$MYcalcCondMean$	calculates the mean of a property, e.g. Y_{OH}, conditioned to another property, e.g. mixture fraction Z, for different regions and using different binning resolutions	"master" on GIT SHA: 32fb177d
$MYcalcPDF$	calculates the probability density function (PDF) of a property, e.g. Z, for different regions and using different binning resolutions	"master" on GIT SHA: 32fb177d
$MYgetIntFields$	writes out the internal field for selected properties to produce scatter plots	"master" on GIT SHA: 32fb177d
$MYgetRhoDavg$	calculates average density and Favre average (density weighted) of the diffusion coefficient D in specified regions	"master" on GIT SHA: 32fb177d

Tabelle 4.3: Case and code used to produce the results published in Tufano *et al.* [130] on fully-resolved DNS of coal particle volatile combustion and flame interaction, with focus on the effects of particle Reynolds number and turbulence. The corresponding code/data repository is itv-publications/2018_Tufano_FUE The main directory for the RAW data storage is /itv/storage/ITV-DATABASE/ITV/PUBLICATIONS/JOURNAL/2018_Tufano_FUE_II.

Tufano *et al.* [130], 2018_Tufano_FUE_II		
Data on storage	Case	Code
1P-LAM/*/ *Rep=**X***	DNS of single coal particle volatile combustion in laminar flow at different Re_p=**X**. The upstream extent of the computational domain is 20 particle diameter D_p	"reactingPccFoam" on GIT SHA: 5614d280
3P-LAM/Lx=5Dp/ *Rep=**X***	DNS of a 3-particles array volatile combustion in laminar flow at Re_p=**X**. The inter-particle distance L_x =$5D_p$	"reactingPccFoam" on GIT SHA: 5614d280
27P-LAM/Lx=10Dp/ *Rep=8*	DNS of a 27-particles array volatile combustion in laminar flow at Re_p=8. The inter-particle distance L_x =$10D_p$	"reactingPccFoam" on GIT SHA: 5614d280
27P-TUR/Lx=10Dp/ *Rep=8*	DNS of a 27-particles array volatile combustion in turbulent flow at Re_p=8 and u'/U=0.25 or 1. The inter-particle distance L_x =$10D_p$	"reactingPccFoam" on GIT SHA: 5614d280
FLT/DNSchiZs=1/ *Rep=**X***	Flamelet calculations for the regions UP-/DOWN- stream of a single coal particle at Re_p=**X**	"coalFlameletFoam" on GIT SHA: 5614d280
Pre-/Post-processing tools (additional to Tab.4.2)		
Utility name	Description	Code
$MYcalcPDF2D$	calculates the 2D probability density function (PDF) of a property, e.g. Y_{OH}, conditioned to another property, e.g. mixture fraction Z, for different regions and using different binning resolutions	"master" on GIT SHA: 5614d280
$MYcalcFI$	calculates the Flame index FI as a field based on the definition $FI = \nabla Y_{Fu} \cdot \nabla Y_{O_2}$	"master" on GIT SHA: 5614d280
$MYboundaryValue Layers$	writes out cumulative volatile mass released from particles located in different layers (i.e. downstream positions).	"master" on GIT SHA: 5614d280

Tabelle 4.4: Case and code used to produce the results published in Tufano *et al.* [126] in which a comprehensive and predictive model for the thermal degradation of coal is coupled to resolved laminar simulations in order to predict the ignition delay time of single coal particles in air- and O2/CO2-atmospheres. The corresponding code/data repository is itv-publications/2019_Tufano_FUE The main directory for the RAW data storage is /itv/storage/ITV-DATABASE/ITV/PUBLICATIONS/JOURNAL/2019_Tufano_FUE.

Tufano *et al.* [126], 2019_Tufano_FUE		
Data on storage	Case	Code
N2-21	Fully-resolved DNS of coal particle ignition in the mixture containing 21% O_2 and balanced with N2. The initial particle temperature is 350K to account for pre-heating. The initial porosity and tortuosity are $\epsilon_0 = 25\%$ and $\tau_0 = \sqrt{2}$	"coalSMOKE_MR" on GIT SHA: c7a25b45
N2-30	Mixture containing 30% O_2 and balanced with N_2. Otherwise same settings as $*N2-21*$	"coalSMOKE_MR" on GIT SHA: c7a25b45
CO2-21	Mixture containing 21% O_2 and balanced with CO_2. Otherwise same settings as $*N2-21*$	"coalSMOKE_MR" on GIT SHA: c7a25b45
CO2-30	Mixture containing 30% O_2 and balanced with CO_2. Otherwise same settings as $*N2-21*$	"coalSMOKE_MR" on GIT SHA: c7a25b45
N2-21+SurfRad	Same settings as $*N2-21*$ but accounting for the radiative heat flux Q_r at the particle surface	"coalSMOKE_MR" on GIT SHA: c7a25b45
Pre-/Post-processing tools		
Utility name	Description	Code
bioSMOKE_createFile	pre-processing routine to create all required species files in the 0 folder	"master" on GIT SHA: c7a25b45
takePartAvgMR	post-processing routine to calculate volume averaged properties inside the particle	"master" on GIT SHA: c7a25b45
takePartCenterMR	calculates selected properties at the particle center	"master" on GIT SHA: c7a25b45
takePartOutLayerMR	calculates selected properties at the outest particle layer	"master" on GIT SHA: c7a25b45
takeMaxMR	writes out the overall maximum of selected properties per each time step in different regions	"master" on GIT SHA: c7a25b45
ignitionCH.py (Python)	calculates the cumulative CH profile based on the particle trajectory	"master" on GIT SHA: c7a25b45
ignDelTim.m (Matlab)	calculates the ignition delay time with different criteria and indicators	"master" on GIT SHA: c7a25b45